UNITED KINGDOM · CHINA · MALAYSIA

DEPARTMENT OF CHEMICAL AND ENVIRONMENTAL ENGINEERING
Low Carbon Energy and Resources Technologies (LCERT)

Development of Three-Dimensional Mesoporous Biocarbon Materials for Energy-Related Applications

By

Suleiman Sani

Supervised by Dr Chenggong Sun, Dr Xin Liu, and Prof Colin Snape

Faculty of Engineering

University of Nottingham

A thesis submitted to the University of Nottingham for the degree of Doctor of Philosophy

November 2022

Abstract

The massive fossil fuel combustion in the post-industrial era to meet the world's energy consumption has caused an increase in CO_2 concentration in the environment. The use of various renewable energy technologies such as wind, nuclear, and solar have demonstrated excellent potential to reduce the rate of CO_2 emissions. However, these energy technologies with renewable energies are not rapid enough to mitigate the impact of CO_2 on climate change due to the low utilization ratio and erratic electricity supply. Among the carbon capture technologies, mesoporous carbons as supports to prepare polyethyleneimine (PEI)-modified sorbents for CO_2 capture have attracted considerable attention due to significant sources of raw materials, high pore volume, organized pore geometry, and high efficiency and selectivity for CO_2. This project aims to utilize the second and third most abundant biomass (chitosan and lignin) as renewable carbon sources to prepare bio-carbon materials with regulatable bimodal 3-dimensional (3D) interconnected mesoporous structures and evaluate their performance for CO_2 capture.

Firstly, a series of ordered mesoporous carbons with large mesopore sizes ranging from 9.6 to 14.1 nm and pore volumes ranging from 0.50 to 1.80 cm^3/g were synthesized using lignin as a renewable and sustainable polymeric precursor and spherical siliceous mesostructured cellular foam (MCFs) as a template in a solvothermal process. The prepared lignin carbon materials showed a quasi-spherical porous morphology and were highly characterized by the rarely seen dominance of a three-dimensional large mesopore system that had a narrow pore size distribution centered at 20–25 nm with high surface areas of up to 960 m^2/g and mesopore volumes of up to 1.50 cm^3/g. The results also showed that the large-pore mesoporous

framework could be readily tuned by varying the carbonization/activation temperature and the silica-to-lignin ratio by mass.

Secondly, ordered mesoporous carbon materials were synthesized using mesoporous silica SBA-15 as a template and lignin as a carbon precursor. The SBA-15-derived mesoporous carbons showed several exciting features: a 2-dimensional hexagonal structure, rod-like morphology, and a high surface area of up to 1076 m^2/g with a moderate pore volume in the range of 0.29-0.66 cm^3/g, and continuous evolution of average pore size from 3.87 to 4.01 nm.

Thirdly, nitrogen-rich mesoporous materials were prepared in a solvothermal approach using biocompatible chitosan as both carbon and nitrogen sources and spherical siliceous mesostructured cellular foam (MCFs) as the templates. The pore structure, morphology, and chemical composition of the obtained materials were thoroughly characterized using nitrogen adsorption-desorption isotherms, scanning electron microscopy, transmission electron microscopy, and CHN elemental analysis. The results showed that the as-prepared mesoporous carbons had a high surface area in the range of 312-983 m^2/g, large pore volume in the range of 0.22-1.32 cm^3/g, a bimodal distribution of mesopore sizes in the range of 5-6.3 and 9-21.6 nm, and high nitrogen content of up to 10.48 wt%.

Finally, amine-impregnated mesoporous carbon sorbents have been considered one of the most promising sorbents for CO_2 capture from streams with low CO_2 concentrations. A series of novel solid amine adsorbents were prepared by impregnating polyethyleneimine (PEI) on mesoporous carbons prepared using low-cost bio-waste material “lignin” as a carbon precursor via a facile templating method. The results demonstrated that the mesoporous carbon with 3D interconnected porous structure and large pore size and pore volume exhibited excellent CO_2 adsorption

capture of 2.90-3.13 mmol/g at a temperature operating window of 75-90 °C under CO_2 partial pressure of 0.15 bar, being significantly higher than PEI impregnated sorbents prepared by using mesoporous carbon with 2D porous structures and also one of the best amongst other amine-impregnated adsorbents reported in the literature. The well-developed 3D interconnected mesoporous structure, high pore volume (up to 1.80 cm^3/g), and large pore size permit the facile dispersion and immobilization of PEI within their pores and high availability of amine groups, which influences the high adsorption performance. In addition, the extended adsorption-desorption tests showed that the CO_2 adsorbed by the PEI-impregnated adsorbent could be easily regenerated at 110 °C. It exhibited excellent cycling stability. Thus, these results indicate that the PEI-impregnated mesoporous adsorbents are ideal candidates for post-combustion CO_2 capture.

Acknowledgments

First and foremost, ultimate praises and thanks to Almighty God for His showers of blessings throughout these research years and the successful completion of this work.

I would like to express my sincere gratitude to my research supervisors, Dr. Cheng-Gong Sun, Dr. Xin Liu, and Prof. Colin Snape, for their help and invaluable guidance on my experimental work in this PhD project. Special thanks to my primary supervisor, Dr. Cheng-Gong Sun, for being patient and tolerant in many discussions on my experimental work. His vision, kindness, scientific and personal knowledge profoundly motivated and inspired me throughout my whole Ph.D. life. In addition, I would like to thank Dr. Xin Liu for his friendship, great sense of humor, endless hours of training, and technical assistance given to me in the laboratory.

I would like to thank the Nigeria Government for funding my research through the Petroleum Technology Development Fund (PTDF). Also, I thank my internal examiner Dr. Begum Tokay, Dr. Lee Stevens for his assistance with BET, Mr. Nigel Neate for his help with the FEG-SEM, Dr. Micheal Fay for the aid with FEG-TEM, Dr. Craig Stoppiello for XPS, and Dr. David Furniss for the use of the FTIR. I would also like to thank the laboratory technician, Adrian Quinn, for his technical support and for ensuring I managed to get my research conducted promptly and safely.

I would like to say thanks to my friends and research colleagues, Umar Musa, Dr. Andrew Gill, Ahmed Ibrahim, Wei Lee, Mengbin Li, Mohammed Alamo, Arthur Ellis, Lewis Tuck, Dr. Shaima Al-Bazzaz, Xu Yang, Dr. Clement Uguna, and Dr. Suleiman Baba for their constant encouragement.

Finally, I am grateful to all my family members for their unwavering love and support, especially my late parents (Rest in Peace).

Content

List of Figures

List of Tables

Chapter 1 General Introduction

1.1 Background

The rise of carbon dioxide (CO_2) emissions over the past decades, mainly caused by the dominant combustion of fossil fuels (Figure 1.1), has raised serious concerns about the environment and ecosystem on the earth because of its greenhouse effect (Cox et al., 2000; Plaza et al., 2008), leading to a detrimental impact on the global climate, sea level, and land desertification (Davis et al., 2010; Satterthwaite et al., 200). According to the National Oceanic and Atmospheric Admiration's Mauna Loa Observatory, the concentration of CO_2 in the atmosphere has increased from 280 to 415 ppm, the highest level ever reported (Global Monitoring Laboratory, 2020; Kamran and Park, 2021; Riahi et al., 2003). As a result, it has attracted global political attention, with countries worldwide agreeing on a plan to control the emission of CO_2 (Mac Dowell et al., 2017).

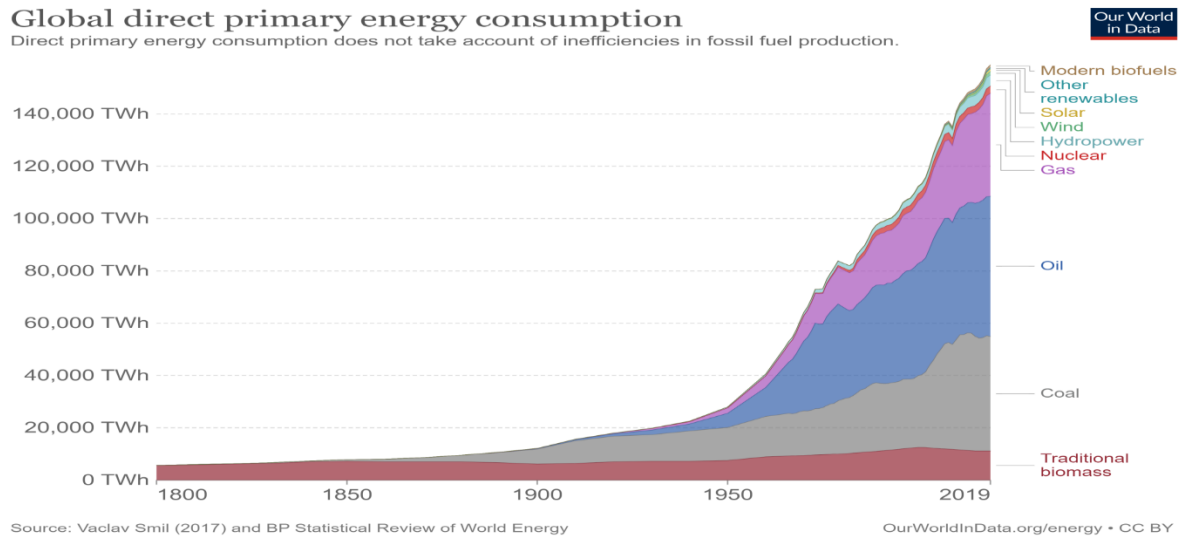

Figure 1.1 The trend of world energy consumption by different sources (Vaclav, 2017).

The United Nation's Environment Programme (UNEP) predicted in its emissions report that the atmospheric concentration of CO_2 would increase to 570 ppm with an average temperature rise of 3.2 ℃, and the annual CO_2 emissions must be reduced to 7.6% in order to keep global warming below 1.5 ℃ (United Nation Environmental Programme, 2019). Moreover, reports by the Intergovernmental Panel on Climate Change warned that if the temperature rose to approximately 1.5 in the future, it would lead to species extinctions, with about 4, 6, and 8% of vertebrates, insects, and plants, respectively, among the 105,000 species studied to disappear (Tollefson, 2018). The British Petroleum Energy Outlook predicts that this trend of increasing atmospheric CO_2 concentration will not be altered in the next couple of decades because fossil fuels such as coal, natural gas, and oil will still be the main power source despite the promising development of renewable energy (solar, nuclear and hydropower) (British Petroleum Report, 2014). Among these sources, a disproportionate amount of CO_2 is produced from large stationary emission sources like coal-fired power plants, industries (chemical, petrochemical, cement, iron, and steel), and anthropogenic sources, corresponding to over 50% of the total CO_2 emission (Kamran and Park, 2021; Sumida et al., 2011; Olivier et al., 2016). Thus, the Intergovernmental Panel on Climate Change recognized the carbon capture and storage (CCS) technique as a major technology to drastically reduce CO_2 emissions (Metz et al., 2005). At present, a wide variety of technologies such as absorption in liquids (Bishnoi and Rochelle, 2000; Agbonghae et al., 2014; Perdikaki et al.,2016), adsorption on solids (Trickett et al., 2017; Favros et al., 2019) cryogenic distillation (Olajire, 2010) and membrane technology (Labropoulos et al., 2015) have been proposed for the capture of CO_2 from the flue gas. Among those CCS technologies, chemical absorption using aqueous amine solutions (e.g., monoethanolamine or methyldiethanolamine), which reacts with

CO_2 to produce carbamates, is the state-of-the-art technology in the industry for effective CO_2 capture (Wang et al., 2011; Pires et al., 2011; Figueroa et al., 2008; Yang et al., 2008). Although amine scrubbing technology shows over 98% capture efficiency and selectivity at very low CO_2 concentration (Rochelle, 2009), several disadvantages exist, such as high corrosion of equipment, large capital, and operational cost, high energy consumption for solvent regeneration, and thermal and oxidative degradation (Oschatz and Antonietti 2018). Therefore, this necessitates the search for alternative, less energy-intensive methods that can still exhibit similar CO_2 capture efficiencies.

To alleviate these issues, solid adsorbent-based capture or adsorption-based technologies have been considered and widely studied as potential alternative post-combustion carbon capture technologies (Sun et al., 2015; Azmi and Azeez, 2019). Different types of solid adsorbents have been developed and widely investigated, including zeolites, metal-organic frameworks (MOFs), activated carbons, and covalent organic frameworks (COFs) (Trickett et al., 2017; Jiang et al., 2019; Chen et al.,2017; Puthiaraj and Ahn, 2017). Although the likes of zeolites and MOFs adsorbents had shown high CO_2 adsorption capacity up to 3.7 mmol/g at 40 ℃ and 0.15 bar (Bae et al., 2013) and 74.2 wt% at 298 K and 50 bar (Furukawa et al., 2010), respectively, their major drawback is low tolerance to water vapor present in the flue gas, which limits their CO_2 adsorption capacities and makes them unsuitable for carbon capture.

Recently, amine-functionalized solid adsorbents have attracted considerable attention due to their high CO_2 adsorption capacity of up to 27 mmol/g (Mishra et al., 2012), high selectivity for carbon dioxide due to the introduction of amine species, and low energy input (2– 2.5 MJ kg/CO_2) for adsorbent regeneration at 80-120 ℃ (Hack et al., 2022). Generally, amine-functionalized solid adsorbents can be produced via chemical

grafting (Bezerra et al., 2014; Hou et al., 2018) and physical impregnation (Drage et al., 2008; Jung et al., 2016, Meng et al., 2019). Chemical grafting by forming a chemical bond between the aminosilanes and hydroxyl groups on porous silica surfaces results in amine adsorbents with high thermal and chemical stability. However, the synthetic methods are complicated, and most of the sorbents suffer from low CO_2 adsorption capacity under flue gas conditions (low pressure and high temperature) due to the limited functional groups in the support for chemical reactions, the number of amine groups capable of grafting is limited. In comparison, physical impregnation has been more preferred;d from the perspective of industrial application because of its simplicity, lower cost, higher amine loading levels, and capability for large-scale production (Ma et al., 2009; Zhang et al., 2017). Various porous supports, especially mesoporous materials, including carbon-based porous materials and mesoporous silicas (Maroto-Valer et al., 2008; Wang et al., 2011, Liu et al., 2017), have been considered potential candidates for preparing PEI-functionalized solid adsorbents (Samanta et al., 2011; Son et al., 2008; Liu et al., 2019; Sun et al., 2018; Alkhabbaz et al., 2014; Tang et al., 2013; Wang et al., 2012; Wang et al., 2013a; Wang et al., 2015; Gibson et al., 2015; Kong and Liu 2019).

Mesoporous carbons are particularly attractive as support for preparing PEI-functionalized adsorbents. One significant advantage of mesoporous carbon supports over silica materials is their excellent thermal and electrical conductivity, making them potential candidates for potential applications in electric swing adsorption (ESA). Differing from the conventional temperature swing adsorption process (TSA), the electrical current could be directly passed through the adsorbents to regenerate the adsorbents via “in-situ” heating by the Joule effect, which could potentially reduce the regeneration energy consumption (Wang et al., 2016; Gibson et al., 2015).

This PhD project aims to utilize the advantages of precursor chemistries and preparation methods to develop mesoporous carbon materials with controllable and physicochemical properties using biomass. These appealing mesoporous carbons can be synthesized through templated carbonization method with high surface areas, large pore volume, and ordered mesoporous structures. The second and third most abundant and low-cost biomass (chitosan and lignin) were selected as the carbon precursors to prepare ordered mesoporous carbons under a controlled carbonization process. Among them, lignin is a carbon-rich precursor accounting for over 60%, with 70-100 million tons produced annually (Jedrzejczk et al., 2021; Chatterjee and Saito, 2015), while chitosan served as both carbon and nitrogen precursor for the resultant carbon materials. The results showed that the prepared mesoporous carbon materials had large mesopore size, large pore volume, high nitrogen content, and large surface area. The performance of the mesoporous carbon materials as the porous supports for preparing polyamine CO_2 adsorbents was then evaluated with success, as highlighted by CO_2 high adsorption capacities with fast adsorption kinetics performance obtained at modest to high adsorption temperatures at low CO_2 partial pressure.

1.2 Aims and objectives

The PhD research aims to develop novel technology strategies to prepare bio-carbon materials with regulatable bimodal 3-dimensional (3D) and 2D interconnected mesoporous structures and evaluate their performance for carbon capture applications with or without further functionalization. This addresses the following objectives of the Ph.D.;

I. Investigate the potential of lignin for producing 3D interconnected cellular bio-carbon materials with hard templating methods (using meso-cellular siliceous foams (MCFs) as the hard templates under different conditions).

II. To develop 2D interconnected mesoporous carbon materials using SBA-15 as a hard template.

III. To investigate the potential of chitosan for producing 3D interconnected cellular bio-carbon materials with hard templating methods (using meso-cellular siliceous foams (MCFs) as the hard templates under different conditions).

IV. To characterize the resultant mesoporous bio-carbon materials using a range of characterization tools, such as BET analysis, Scanning Electron Microscopy (SEM), and Thermogravimetric (TGA) analysis to reveal textural properties, morphology solid phase structure, respectively.

V. Performance evaluation of the functionalized bio-carbon materials for CO_2 capture under different conditions.

1.3 Thesis structure

The Ph.D. thesis is divided into eight (8) chapters, which are organized as follows;

Chapter 2 provides a review of porous carbon materials and their classifications, focusing on the recent developments in synthesizing mesoporous carbon materials with well-ordered mesopores, and amine-functionalized ordered mesoporous carbons for CO_2 capture application.

Chapter 3 provides detailed experimental methodologies, such as the materials/chemicals used for the synthesis of the ordered mesoporous carbons materials, and the experimental procedure involved to investigate the characteristics and performance of the samples.

Chapter 4 presents a facile and efficient hard templating approach for synthesizing 3D ordered spherical mesoporous carbon materials with large mesopore size and volume, using kraft lignin as an environmentally friendly single precursor and spherical mesocellular foam (MCF) silica as the hard scaffolding template. The 3D-connected porous structure of MCF silica is expected to benefit the development of 3D-ordered mesopores for the lignin-derived mesoporous carbons. Furthermore, the role of lignin carbonization/activation temperature, lignin-to-silica ratio, and the textural parameters of the MCF template in governing the development of mesoporous carbon framework was examined.

Chapter 5 describes synthesizing a series of ordered mesoporous carbons based on a hard templating approach using SBA-15 as a hard template and lignin as a renewable carbon precursor. Such an approach allowed the investigation of different carbonization temperatures and silica-to-lignin mass ratios. In addition, the textural properties of these carbon materials were characterized by nitrogen adsorption-desorption isotherms and scanning electron microscopy (SEM).

Chapter 6 adopted a green and straightforward hard template method for synthesizing nitrogen-rich mesoporous carbon materials using chitosan as a carbon precursor and nitrogen source and spherical mesocellular foams (MCF) silica as hard templates. The resulting carbons were characterized by nitrogen adsorption isotherm, high-resolution transmission electron microscopy (HR-TEM), scanning electron microscopy (SEM), elemental analysis, X-ray photoelectron spectroscopy (XPS), and Fourier transform infrared spectroscopy (FTIR). Furthermore, the effect of carbonization temperature and different chitosan-to-silica ratios on the structural and textural properties of the carbons was thoroughly investigated.

Chapter 7, the mesoporous carbons derived from lignin were selected as the porous support to prepare supported PEI adsorbents for CO_2 capture. The mesoporous carbon was prepared through a facile hard template route using an abundantly available bio-waste “lignin” as carbon precursor and spherical mesocellular foam (MCF) silica with 3D connected porous structure and large pore size and pore volume as the hard template. The effects of pore structure, PEI loading, and adsorption temperature on CO2 adsorption of the PEI-impregnated mesoporous carbon materials were studied.

Chapter 8 provides general discussions, conclusions of the research, and possible recommendations for future studies.

CHAPTER 2 Literature Review

2.1 Porous carbon materials

Porous carbon materials belong to a class of materials that contain a significant amount of carbon (up to 50 wt%) with a different interconnected network of pore structures (Zhang et al., 2021, Casanova et al., 2022). They have received great scientific and technological interest because of their unique ability to interact with atoms, ions, and molecules both at their surfaces and throughout their bulk (Xia et al., 2010), which makes them useful in many applications, including catalysis (Zhao et al., 2021), water and air purification, energy storage (Xue et al., 2020), and gas storage (Zhang and Lu, 2020). Generally, these materials include mesoporous carbons (Gang et al., 2021), activated carbons (Kumar and Gupta, 2020), graphene (Iqbal et al., 2020), carbon nanotubes (Notarianni et al., 2016), and even biochar materials (Shaheen et al., 2019). Porous carbon materials are often uniquely characterized by their large surface area, high pore volume, and tunable pore size (Benzigar et al., 2018; Lu and Schuth, 2006). In particular, activated carbon is the most commonly applied material in the field of adsorption (Kumar and Gupta, 2020; Chuenchom et al., 2012) due to its high surface area of up to 3250 m^2/g, high pore volume of up to 1.9 cm^3/g, and low cost (Hayashi et al., 2000; Correa et al., 2017; de Souza et al., 2020; Quan et al., 2020). Among the huge family of porous carbon materials, mesoporous carbons stand out due to their large accessible pore networks, high surface area (up to 1530 m^2/g), and well-ordered mesopore structure with adjustable pore sizes (2-50 nm), which are necessary for advanced applications, including the separation of large molecules (Gang et al., 2021), and catalysis (Wei et al., 2014). Graphene and carbon nanotubes have good mechanical and thermal stabilities, as well as a high surface

area. They have also shown high potential as supercapacitors (Brownson and Banks, 2012; Notarianni et al., 2016) and sensors (Raju et al., 2014).

2.2 Classification of porous carbon materials

The pore structures of porous carbon materials play a vital role in their behavior. These pores can be classified according to pore size, pore shape, and accessibility to surroundings.

2.2.1 Classification by pore size

The pore size is an essential parameter in classifying porous carbon materials because it can be adjusted according to practical application requirements (Wang et al., 2021). Pore size is meaningful when the geometrical shape of the pores (e.g., spherical, cylindrical) is known and well-defined. The pore system of these materials can be classified according to the International Union of Pure and Applied Chemistry (IUPAC) as microporous, mesoporous, and macroporous carbon materials (Zhou et al., 2021). The pore system of these materials can be classified according to the International Union of Pure and Applied Chemistry (IUPAC) as microporous, mesoporous, and macroporous carbon materials (Zhou et al., 2021).

Microporous carbon materials (d<2 nm): These materials have very narrow pores with less than 2 nm diameter. The typical materials are activated carbon and carbon molecular sieves. The microporous nature of these materials makes them suitable for the adsorption of very small gas molecules such as CO_2 (Lee et al., 2004a; Poole, 2005).

Mesoporous carbon materials (2 nm < d < 50 nm): Ordered mesoporous carbons, aerogels, fullerenes, carbon nanotubes, and graphenes are the typical materials found in this category (Xin and Song, 2015). These materials have pores big enough to accommodate large molecules such as vitamins and dyes, which might be due to the existence of wider pores in the mesopore range (Ryoo et al., 2001).

Macroporous carbon material (d > 50 nm): This type of carbon material has a large pore size, and a prominent example is carbon foam, which can be used as matrices for heavy oil recovery and biomedical liquids (Inagaki et al., 2015; Baumann et al., 2003).

2.2.2 Classification by pore geometrical shape

According to Zdravkov et al. (2007), pores are divided based on their geometrical shapes.

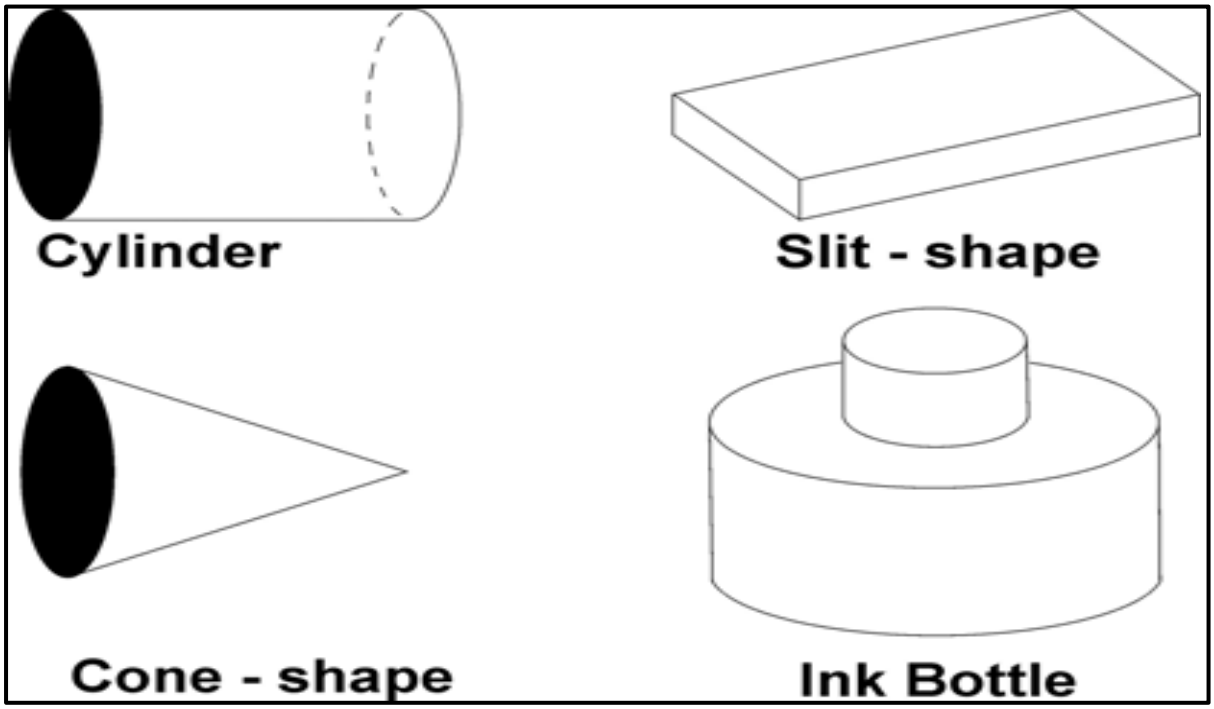

Figure 2.1 Pore shape classification (Zdravkov et al., 2007).

The pore-shape classification is presented in Figure 2.1. It includes cylinder, spherical, cone-shape, ink bottle, and slit-shaped. The pore shapes are usually based on model systems for simplicity and irregularity in geometry. The pore-modeled systems are defined in terms of various geometric bodies such as cylinders, spherical (mesoporous carbons), and slits (activated carbons).

2.2.3 Classification according to pore's accessibility to surroundings

The pore system of porous carbon materials can also be classified according to their accessibility to the surroundings, as presented in Figure 2.2. The open pores (b, c, d, and e) are the ones that connect two neighboring pores with the external surface of the material. These pores are accessible to ions or molecules in the surroundings. The open pores are further divided into blind pores (b and f), which may be opened only at one end, and through pores (e), which are opened at two ends.

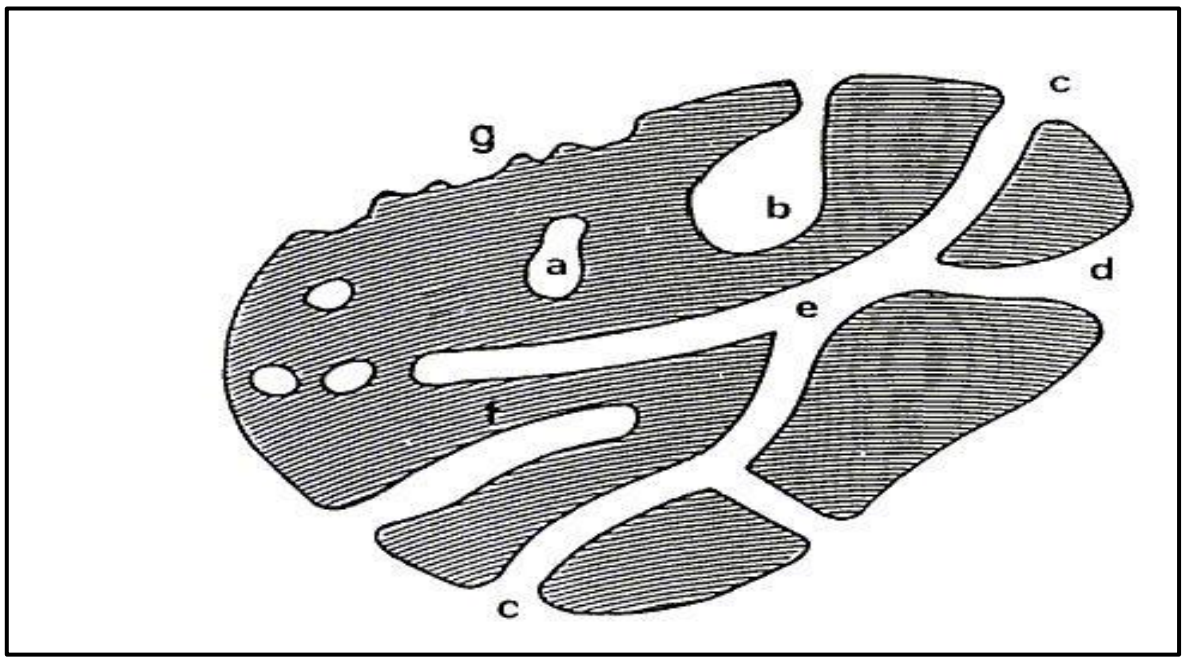

Figure 2.2 Pore classification based on their availability to surroundings (Rouquerol et al., 1994).

Open pores are much more preferred in functional applications, such as adsorption and catalysis involving penetration, due to their interconnectivity, leading to high porosity of up to 99% (Liu et al., 2020a). The closed pores (a) are isolated from connecting with the surroundings. They are not associated with the adsorption and permeability of molecules. However, they enhance the mechanical strength of solid materials in sonic and thermal insulation (Lu & Zhoa, 2004; Zdravkov et al., 2007).

2.3 Microporous carbon materials.

2.3.1 Preparation methods of microporous carbons.

Conventional microporous carbon materials, such as activated carbons, have a high degree of porosity with an extended surface area, while up to 90% may be composed of carbon (Heidarinejad et al., 2019). It is obtained from the thermal treatment of various carbonaceous materials under different conditions. Activated carbon is a versatile material that has been produced in large quantities (about 100000 t annually) and used widely in various industrial and environmental sectors (Bansal and Goya, 2005). Basically, activated carbon has been synthesized using classic activation methods, such as physical and chemical activation (Liang et al., 2008). The physical activation method is a two-step process. The first step involves carbonizing the raw carbonaceous precursor material (e.g., woody biomass) at a temperature within the range of 700-1000 ˚C in an inert atmosphere. The heat treatment removes volatile matter and water vapor, leading to the formation of solid char with high carbon content and some level of porosity (McDougall, 1991; Bansal and Goya, 2005). The second step is the physical activation (oxidation) of the carbonized material in the presence of suitable oxidizing gases such as CO_2 (Yuliusman et al., 2017), steam (Zhou et al.,

2018), or air (Ledesmaa et al., 2018). According to Molina-Sabio et al. (1996) and Manocha (2003), carbon dioxide and steam are the most commonly used gases for physical activation due to their low cost and availability and easy-to-control endothermic reactions, as illustrated below.

$$C + H_2O \rightarrow CO + H_2 \quad 2.1$$

$$C + CO_2 \rightarrow 2CO \quad 2.2$$

$$CO + 3H_2 \rightarrow CH_4 + H_2O \quad 2.3$$

Thus, the objective of the activation process is to enlarge the diameter of the pores which are formed during the carbonization process and to increase the accessibility of pore structure and adsorption capacity, thereby resulting in developed activated carbon with a large surface area (Manocha, 2003; Pallares et al., 2018). A series of different kinds of ACs have been synthesized from different biomasses such as soya (Rana et al., 2017; Sun et al., 2021), coconut shell (Yue et al., 2018), and corn straws (Qiu et al., 2018). In the study conducted by Zhou and his co-workers, they prepared activated carbon using waste tea as a carbon precursor and steam as oxidizing gas through physical activation. The maximum surface area, total pore volume, and pore diameter reached were 995 m^2/g, 0.68 cm^3/g, and 3.19 nm, respectively (Zhou et al., 2018). Parelles et al. (2018) synthesized activated carbon from barley straw using a physical activation approach with carbon dioxide and steam as activating agents. They found that the highest BET surface area and micropore volume by CO_2 were 789 m^2/g and 0.3268 cm^3/g, while steam activation was 552 m^2/g and 0.2304 cm^3/g, respectively.

Activated carbons can also be readily manufactured via chemical activation. It involves the impregnation of biomass with acids or strong bases such as phosphoric acid (H_3PO_4), sodium hydroxide (NaOH), potassium hydroxide (KOH), and zinc chloride ($ZnCl_2$), which results in the degradation and removal of tar particles from the biomass material (Xuan et al., 2017; Chen et al., 2017b; Islam et al., 2017; Yorgun and Yildiz, 2015). The chemically impregnated biomass material is then subjected to heat treatment at relatively modest activation temperatures (typically at ca. 600˚C) in the absence of air. Aqueous washing of the resultant activated carbons is required to remove the soluble reaction products and remaining unreacted activating agents (if any), which may occupy the pores. Upon activation, the chemically impregnated biomass material yields porous structured activated carbon with an extended surface area (Danish and Ahmad, 2018; Norwicki et al., 2010). KOH is the most widely used activation agent among various chemical agents. The mechanism of KOH activation involves a series of chemical reactions, as shown in Equations 2.4 to 2.7 (Wang and Kaskel et al., 2012).

At 360 ^oC, KOH melts and decomposes to produce water (steam) and K_2O, enhancing the subsequent reactions at a solid-liquid interface. The reaction between KOH and carbon (Eq. 2.4) starts at an approximate temperature range of 400 to 600 ˚C, forming carbamate K_2CO_3, metallic K, and H_2 (Lozano-Castello et al. 2007). At temperatures above 700 ˚C, C and K_2CO_3 are further combined (Eq. 2.5), and the chemical etching effect of K_2CO_3 occurs, releasing gaseous products such as H_2, CO, and CO_2, which facilitates the development of pores. The expansion of carbon lattice due to reacting with metallic K leads to the formation of micropores.

$$6KOH + 2C \rightarrow 2K_2CO_3 + 2K + 3H_2 \qquad 2.4$$

$K_2CO_3 + C \rightarrow K_2O + 2CO$ 2.5

$K_2CO_3 \rightarrow K_2O + CO_2$ 2.6

$2K + CO_2 \rightarrow K_2O + CO$ 2.7

Xuan et al. (2017) reported the synthesis of activated carbons with a high BET surface area of 2100.8 m^2/g and pore volume of 1.02 cm^3/g, using Torreya Grandi's shell as a carbon precursor through carbonization and KOH activation under N_2. Lately, Chen et al. (2019a) reported mixing alkali to produce porous carbon materials with high adsorption capacity. Surprisingly, mixing NaOH and KOH as chemical activating agents in a ratio of 1:1 exhibited a high BET surface area and rhodamine B adsorption capacity of 1993 m^2/g and 1558 mg/g, respectively. Compared to physical activation, the chemical activation method is more preferred due to its numerous benefits, such as lower activation temperature, which saves energy and increases the carbon yield, higher surface area, and less activation time (Lillo-Ródenas et al., 2003). However, the major limitation of the chemical activation process is the cost and corrosiveness of chemical reagents. It could require an additional step of removing impurities like zinc and phosphorus depending on the chemical used to form the activated carbon (Macia-Agullo et al., 2004).

Ordered microporous carbons were synthesized by using mainly zeolites as sacrificial hard templates. The zeolites-templated microporous carbons had good properties such as narrow pore size distribution, good stability, and high selectivity with large surface areas (Nishihara and Kyotani, 2018, Perego and Millini, 2013). Hirotomo et al. (2018) demonstrated the possibility of achieving a higher BET surface area of zeolite-templated carbon by using computer simulation to compare the physical properties with the experimental data. Unexpectedly, the order microporous carbons obtained

from using zeolite as the hard template achieved high surface areas of up to 3935 m^2/g, and the simulation study predicts an increased BET surface area of 4845 m^2/g.

Despite the promising applications of microporous carbon materials (activated carbons) in adsorption, catalysis, and electrochemistry, they still suffer from a series of limitations arising mainly from their small pore sizes, including; (a) slow mass transfer of molecules due to small pore sizes, reducing their mass transfer efficiency and diffusion kinetics and ultimately limiting the access of molecules to the surface of the adsorbent, and (b) collapse of porous structures at elevated temperature (Lee et al., 2003; Liang et al., 2008). In addition, previous research (Wang and Yang 2012) reported that excellent BET surface area alone is insufficient for determining the high performance of porous carbon materials in various applications. For example, Wang and Yang (2012) fabricated a series of carbon materials with different surface areas (1361-3840 m^2/g) and with/without N-doping (6-7 wt % N) with turnable micropores using zeolite Y as a hard template and furfuryl alcohol as the precursor. Although the carbon materials had high surface areas because of the large pore openings and straight channels of the zeolite, however, the pores of the zeolites are relatively small to accommodate bulky molecules.

2.3.2 Potential applications of microporous carbons.

Microporous carbon materials with unique properties, varying pore sizes, and porosity have different porous structures that determine their potential application opportunities as sorbents for gas storage, supports for catalytic processes, and water purification and electrode materials for supercapacitors (Tian et al., 2020).

Adsorption of microporous carbon materials in gases: The enrichment of molecules, atoms, or ions in the vicinity of an interface is known as adsorption, and

the adsorbed solid material is termed an adsorbent (Saha and Kienbaum, 2019). According to Lu and Zhoa (2004) and Nalwa (2003), as an adsorbent, a specific set of performance criteria is required from porous carbon materials, including the following:

High adsorption capacity: Fundamental properties of porous carbon materials, such as high surface area, well-developed structure, and large pore volume, are important because they determine how the adsorbent can be an excellent media adsorbate. For instance, a significant amount of micropores (especially ultra micropores < 0.7 nm) are needed in activated carbons because high-density CO_2 is preferably captured at low pressure (Presser et al., 2011; Li et al., 2016).

High selectivity: The pore size and pore size distribution make selectivity highly desired for multicomponent mixture separation.

Favorable adsorption kinetics: The pore size- macro-, meso-, and microporosity are essential parameters that determine the adsorption kinetics of the adsorbent. Favorable adsorption kinetics implies that the adsorption rate is fast and depends on the requirement of a particular application.

Good mechanical properties: Porous carbon adsorbents should exhibit mechanical strength and be robust enough to resist crushing and erosion in adsorption chambers.

Good stability and durability: Porous carbon adsorbents are often subjected to harmful chemicals, high pressure, and thermal environments. Good strength in those environments is required to ensure the lifetime for use and re-use without losing properties. These materials have been applied as adsorbents to remove CO_2, CH_4, and H_2. Li et al. (2016a) prepared porous carbon spheres from starch as raw materials via the activation method. The resultant carbons displayed a large surface area of 3350 m^2/g, a pore volume of 1.75 cm^3/g, and a great adsorption capacity of 10.7 mmol/g, and 21.2 mmol/g for CH_4 and CO_2, respectively. Alabadi et al. (2015) found

that the activated carbon materials prepared from biomass (gelatin and starch mixture) by employing KOH activation possess a high surface of 1636-1957 m^2/g, abundant micropores with a pore size of 1.95 nm, and CO_2 uptake of 7.49 mmol/g (1 bar, 273 K). Choma et al. (2015) reported that a series of KOH-activated carbons manufactured from sulfonated styrene-divinylbenzene resin through carbonization and subsequent activation showed a specific surface area in the range of 730–3870 m^2 g^{-1}, total pore volume in the range of 0.44–2.07 cm^3/g and micropore volume in the range of 0.30–1.59 cm^3/g. Significantly, the carbon activated obtained using the KOH/C ratio of 4 exhibited CH_4 adsorption of 1.68 mmol/g at 293 K and 1.1 bar.

Hydrogen (H_2), as an application example for porous carbon materials, is an ideal, clean energy source that can be produced via coal gasification to syngas and then to hydrogen through the process of a water-gas shift reaction. This is considered a promising method for cheap H_2 due to coal's low cost and wide availability. The success of such an H_2 production approach greatly depends on safe carbon dioxide sequestration. Nevertheless, the major challenge for H_2 energy application is storage (Li et al., 2020; Lu and Zhoa, 2004). It has been reported that porous carbon materials exhibited interesting performance as storage materials for H_2 energy applications due to their large surface area, pore volume, and low cost. Sevilla et al. (2011) fabricated activated carbon spheres with a high surface area (up to 2700 m^2 g^{-1}) and micropore size range (0.7–2 nm), through the KOH activation of hydrothermally carbonized organic materials (furfural, glucose, starch, cellulose, and eucalyptus sawdust) as precursors. They showed high hydrogen uptakes up to 6.4 wt% at 20 bar and 77K.

Therefore, it is well known that microporous carbons are essential for the adsorption of small gas molecules such as CO_2 with a molecular diameter of 3.34×10^{-8} cm

(Khalil et al., 2019). However, when the absorbate is a big molecule such as dye (for example, methyl orange: 1.31 × 0.55 × 0.18 nm, and methylthionine chloride: 1.26 × 0.77 × 0.65 nm) only mesopores are needed for such adsorption (Xin and Song, 2015). Producing carbons with well-developed mesopores is essential for large molecule adsorption and specific functional applications, including drug delivery, biomedicals, and catalysis. Thus, emerging interest and desire have been directed toward the synthesis of mesoporous carbon for the improvement of the performance of microporous carbon and the development of new application areas.

2.4 Mesoporous carbons (MCs)

Mesoporous carbons (MCs) are a group of nanostructured carbon materials that have either ordered or disordered structures with narrow or wide mesopore size distributions within the range of 2 to 50 nm (Xin and Song, 2015). Disordered mesoporous carbons were prepared using various methods such as the carbonization of polymer blends (Ozaki et al., 1997), catalytic activation using metals (Tamai et al., 1996), and carbonization of aerogels (Ma et al., 2012; Moreno-Castilla). For instance, Pekala et al. (1992) synthesized mesoporous carbon aerogels exhibiting high porosities (> 80%) and high surface areas (>400 m^2/g) through the carbonization of organic aerogels using resorcinol-formaldehyde. Moreno-Castilla et al. (2002) reported the synthesis of Titania/Carbon composite aerogels by mixing titanium alkoxide during a sol-gel synthesis process. The samples were heated at 500 and 900 ˚C in a helium atmosphere, which produced a mesoporous carbon with a bimodal pore size distribution having surface areas in the range of 200-700 m^2/g. Ordered mesoporous carbons (OMCs) have uniform mesopore arrangements and a periodic array of carbon frameworks. OMCs have recently attracted significant interest due to their well-ordered porous structure, controlled pore size, excellent textural properties, and morphologies

(Baek et al., 2021). The presence of mesoporosity makes them indispensable for vast potential advanced applications varying from adsorption and separation (Briao et al., 2017; Xia et al., 2017; Chen et al*.,* 2016), drug delivery (Saha et al., 2014), catalysis (Ahn et al*.,* 2001 and Kim et al., 2010), water treatment (Naushad et al., 2017; Gai et al*.,* 2018) to energy storage in batteries and supercapacitors as electrode materials (Herou et al., 2019).

2.4.1 Synthesis of Ordered Mesoporous Carbons.

The template carbonization route has attracted much attention for the preparation of ordered mesoporous carbon with the advantage of high control over pore size and shape distribution compared to the mesoporous carbon materials prepared from catalyst-assisted activation and carbonization, which usually showed a disordered mesoporous carbon structure with wide pore size distribution (Khalili et al., 2000; Zhong and Sels, 2018). Generally, ordered mesoporous carbon can be synthesized by two of the most common strategies, either by the hard or soft template method, as shown in Figure 2.3. Typically, the templated synthesis route of OMC involves the following steps (1) template preparation, (2) template-directed fabrication of the desired materials (via direct synthesis, hydrothermal synthesis, etc.), and (3) removal of the template (Savic et al., 2018).

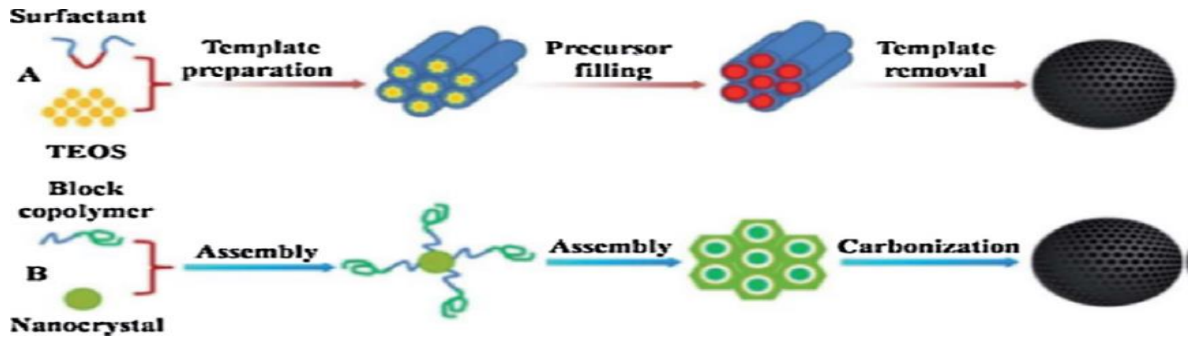

Figure 2.3: Schematic of a hard template method (A) and soft template method (B) (Zhong and Sels, 2018).

2.4.1.1 Soft Template Method

Soft templating is the direct synthesis of ordered mesoporous carbons using amphiphilic block copolymers or surfactants as structural directing agents with precursors. It involves the following steps; (a) polymerization of the carbon precursor with the surfactant and solvent (such as water or ethanol) to form highly crossed-linked networks, (b) removal of the templates, (c) carbonization at high temperature to obtain mesoporous carbon (Ma et al., 2013; Chauhan, 2021; Enterria and Figueiredo, 2016). The order mesoporous framework structure can be obtained by intermolecular interactions (electrostatic interactions, hydrogen, and covalent bonding) between the amphiphilic block copolymer surfactants and carbon precursors. The organic-inorganic interactions are significant because they determine the mesoporous carbon's structural morphology. The three major classes of surfactants used as soft templates are anionic, non-ionic, and cationic (Petkovich and Stein, 2013). These surfactants are grouped based on the charge head in a neutral pH solution. The cationic surfactants have no more than one amine group, representing the hydrophilic head group and at least one hydrophobic tail (Rosen and Kunjappu, 2012). Anionic surfactants have a vast diversity of head groups attached to the hydrophobic tail, including carboxylates, phosphates, and sulfates. Typically, ionic surfactants interact with precursors via electrostatic interactions and generate either micropores or small mesopores (2-4 nm) (Soler-Illia et al., 2002). Non-ionic surfactants are considered the most popular class of surfactants. A typical example includes Pluronic P123 (poly (ethylene oxide)-block-poly (propylene oxide)-block-poly (ethylene oxide), pluronic F127 Poly(ethylene glycol)-block-poly(propylene glycol)-block-poly(ethylene glycol) diacrylate, poly(ethylene oxide)-block-poly(styrene) (PEO-b-PCL) (Ma et., 2013; Petkovich and Stein, 2013). The assembly processes between non-ionic surfactants

and precursors occur via van der Waals interactions and hydrogen bonding, resulting in mesopores from a few to over 10 nm (Soler-Illia et al., 2002).

2.4.1.2 Hard Template Method

The hard template method is considered to be an effective method for synthesizing ordered mesoporous carbon materials, and significant advances have been made over the years. Based on the structural and textural properties of the host template, various morphologies and porosity can be adjusted by using the hard template method. The typical synthesis procedure of the OMC using ordered mesoporous silica material as a hard template is shown in Figure 2.4. It involves the following steps: (1) the preparation of mesoporous silica with controlled pore structure; (2) the filling of the template pores with an appropriate carbon precursor via either wet impregnation or chemical vapor deposition; (3) the carbonization of the organic-inorganic composite; and (4) the removal of the mesoporous silica template by etching in HF or NaOH (Ryoo et al., 1999; Ryoo et al., 2001; Knox et al., 1986, and Liang et al., 2008). The porous structures of the resultant OMCs are usually the reverse replica of the mesoporous silica templates. Consequently, the pore shape and pore size distribution depend primarily on the structure of the mesoporous silica template materials.

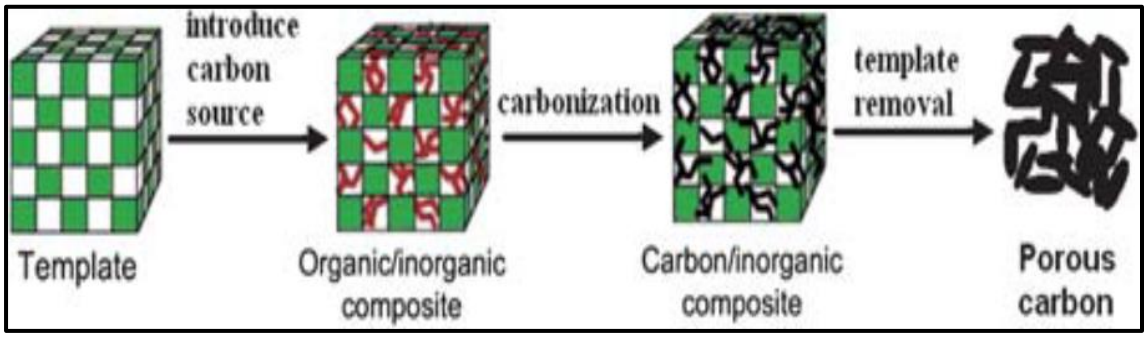

Figure 2.4 Schematic illustration of a hard-templated method for synthesizing mesoporous carbon using a porous inorganic template (Kyotani, 2006).

Several hard templates such as clays, zeolites, colloidal silicas, opals, MgO, ZnO, and mesoporous silicas have been used for the preparation of various micro or mesoporous carbon materials with different pore sizes and structures (Sandi et al., 1999; Benzigar et al., 2018; Ma et al., 2002; Klinthongchai et al., 2020; Morishata et al. 2006). Ordered mesoporous silica is mainly used among these rigid materials because of its particular structural characteristics, stability, and reproducible preparation (Entterria and Figueiredo, 2016). In addition, both the mesostructures of the silicate templates can be replicated, and the morphology can be entirely retained by choosing a suitable mesoporous silica template with the required morphology (Lee et al., 1999; Lee et al., 2001; Ryoo et al., 1999). The works by Ryoo et al. (1999) first paved the road for new opportunities in the synthesis of OMCs using well-ordered mesoporous silica materials with two-dimensional (2D) and three-dimensional (3D) structures, such as MCM-48 (Kruk et al., 2000a), MCF (Lee et al., 2001; Lee et al., 2004b; Lukens and Stucky., 2002; and Lee et al., 2002b), SBA-15 (Jun et al., 2000), MSU-1 (Alvarez and Fuertes, 2004), MSU-H (Kim and Pinnavaia, 2001), HMS (Lee et al., 2000), and KIT-6 (Kleitz et al., 2003) as inorganic templates.

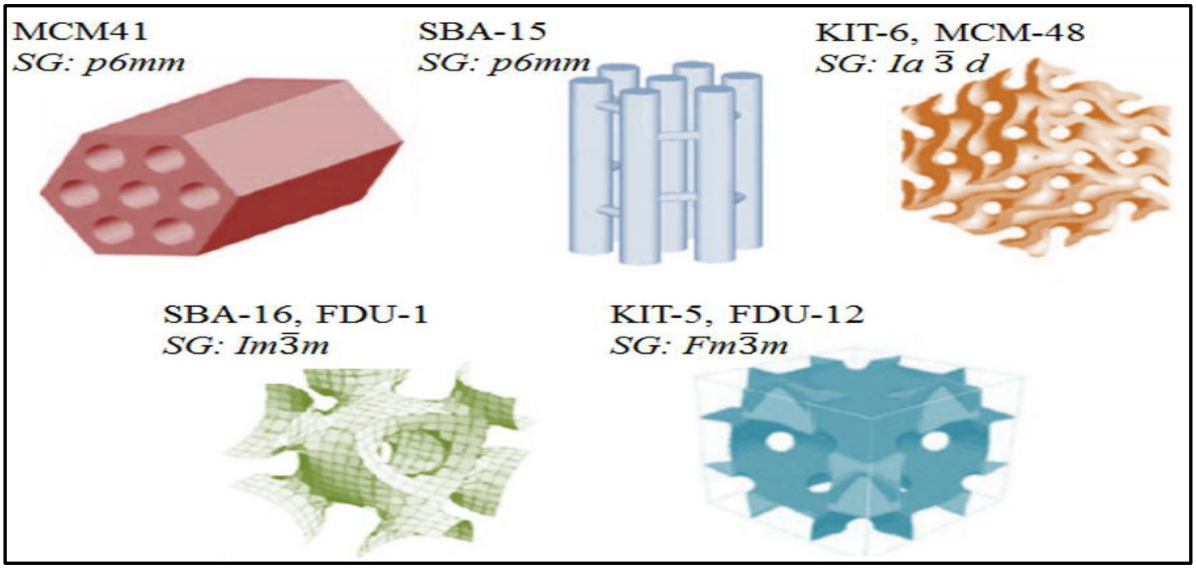

Figure 2.5 Various mesoporous silica templates (Savic et al. 2018)

2.4.2 Factors governing the preparation of ordered mesoporous carbon materials.

Carbon precursors, templates, and catalysts are the three main constituents that play a vital role and significantly impact the structure and pore size of the OMCs (Ma et al., 2019; Benzigar et al., 2018).

2.4.2.1 Type of Carbon Precursors

The choice and nature of a suitable carbon precursor is the most crucial factor because it affects the final carbon framework, physicochemical properties, porosity, and surface functionality (Joo et al., 2006). For selecting carbon precursors, several factors to be considered include low cost, high carbon, high density, renewability, high solubility, and availability (Bae et al., 2014; Tay et al., 2009). So far, the two kinds of carbon precursors mainly used to synthesize mesoporous carbons are synthetic polymeric precursors and biomass-based precursors. For hard templates (mesoporous silica and colloidal silica) and soft templates (F127), phenolic resins such as phenol, resorcinol, and phloroglucinol have been often selected for the preparation of OMCs. (Inagaki et al., 2016, Fang et al., 2010; Lee and Oh, 2002; Saha et al., 2012). This is because these monomers have many phenolic hydroxyl groups that can form strong hydrogen bonds with the polyethylene oxide (PEO) chains of the PEO–PPO–PEO block copolymers, which can lead to the formation of micelles. These micelles can partly produce mesopores in the resulting carbon materials (Saha et al., 2012; Xin and Song, 2015). The reactivity of different monomers increases with the amount of hydroxyl groups and follows a trend of phloroglucinol > resorcinol > phenol. Under different reaction conditions and at room temperature, the polymerization of different monomers with formaldehyde to prepare mesoporous carbons are compared. For

instance, at a low acid concentration of 10^{-2} mol/L, Liang and Dai (2006) found that the polymerization of phenol was exceptionally slow in the presence of F127 with hydrochloric acid, and the resultant formaldehyde/phenol polymer produced porous carbon with a low BET surface area (<5 m^2/g). Resorcinol polymerized faster compared to phenol at room temperatures. Phloroglucinol was found to polymerize much faster than phenol and resorcinol. It took around 30 min for the phase separation reaction of phloroglucinol polymerization to occur. The superiority of phloroglucinol as an excellent precursor for synthesis at low acid concentrations might be attributed to the presence of an abundance of a hydroxyl group in its oligomers compared to those of phenol and resorcinol (Liang and Dai, 2006). Polybenzoxazines could also be used as carbon precursors (Zhang et al., 2018a; Brawe et al., 2017).

Biomass is an abundant, environmentally benign, and renewable material derived from plant and animal sources, which contains varying amounts of cellulose, hemicellulose, lignin, sugar, starches, proteins, and inorganic constituents (Vassilev. et al. 2010; Nizamuddin et al., 2017). Of all these compounds, lignin, cellulose, and hemicellulose are the three major components of biomass. Biomass containing a combination of these three components is known as lignocellulose biomass (Suhas et al., 2007). Lignin, cellulose, and hemicellulose are strongly intermeshed and chemically bonded by either non-covalent forces or covalent linkage (Saidur 2011). In addition, typical biomass contains about 50 wt% of carbon, 42 wt% of oxygen, and 5 wt% of hydrogen (Zhang et al., 2010). Compared with polymer precursors, biomass-derived carbon precursors have the advantages of being readily available, inexpensive, and green. The most widely used biomass materials are lignin, sugar cane, fish scale, wood fiber, watermelon, grape, hemicellulose, chitosan, peanut shells, coconut shells, corn hubs, and banana peel (Tian et al., 2020; Zhang et al., 2018a).

Various seed biomass such as soya bean, colza, peanut, and sunflower seed has also been employed as carbon sources to synthesize mesoporous carbon materials via grinding impregnation (Wang et al., 2011a). It has been reported that organic compounds such as sucrose (Lee et al., 2002a), aromatic hydrocarbons (Kim et al., 2004), mesophase pitch (Qiao et al., 2006), furfuryl alcohol (Joo et al., 2001), and polyacrylonitrile (PAN) (Kruk et al., 2005) are also suitable carbon sources for the synthesis of mesoporous carbons.

2.4.2.2 Use of Catalyst.

Properly using a catalyst can minimize the activation energy of chemical reactions, leading to a high reaction efficiency. Regarding synthesizing mesoporous carbons using the soft template approach, acidic or basic catalysts are essential. For instance, HCl or NaOH is usually employed as a catalyst for the polymerization reaction of phloroglucinol or resorcinol precursors with formaldehyde (Liu et al., 2010; Tanaka et al., 2005). This strong acid catalyst (HCl) and alkali catalyst (NaOH) have limitations due to their corrosiveness to the equipment and environment. Lu et al. (2008) found that amino acids can serve as an alternative to these commonly used catalysts. Using glutamic acid as a catalyst, well-ordered mesoporous carbons with a high surface area of up to 720 m^2/g and pore volume of up to 0.61 cm^3/g with a hexagonal structure were obtained via self-assembly of resorcinol-formaldehyde polymer and surfactant F127 (Lu et al., 2008).

In the case of the hard template method, although there are several types of carbon precursors, some organic compounds, such as sucrose, need to be polymerized with sulphuric acid as a catalyst (Ryoo et al., 1999).

2.4.2.3 Type of template

A proper template should interact strongly with the carbon precursor and be removed easily. In this section, the synthesis of mesoporous carbons based on soft and hard templating methods is discussed according to the textural properties and morphologies of the final carbon materials.

2.4.2.3.1 Soft templates

Generally, ordered mesoporous carbons can be prepared in soft templating via the evaporation-induced self-assembly (EISA) method or hydrothermal process (Inagaki et al., 2016. Liang et al. (2004) first synthesized highly ordered mesoporous carbon films via a solvent-induced structural annealing self-assembly approach using polystyrene-block-poly(4-vinylpyridine) (PS-P4VP) as a soft template and N,N-Dimethylformamide (DMF) as the solvent. Later, Tanaka et al. (2005) fabricated ordered mesoporous carbon materials (COU-1) with a BET surface area of 1354 m^2/g, pore volume of 0.74 cm^3/g, and pore size of 5.9 nm via the self-assembly of resorcinol/formaldehyde and triethyl orthoacetate as carbon co-precursors and triblock copolymer Pluronic F-127 as a surfactant. Ghimbeu et al. (2014) synthesized a series of ordered carbon powders and films based on the self-assembly of phloroglucinol/ glyoxylic acid precursors with a triblock copolymer Pluronic F127 template in an organic medium and without a catalyst. The synthesized carbon films and powders showed high surface areas (up to 800 m^2/g), high porous volume (up to 1 cm^3/g^{-1}), pore size (0.6 nm to 7 nm) and various pore morphologies (hexagonal, cubic, and ink-bottle) by tuning the mass ratio of the precursor to the template. Zhang et al. (2017a) reported the synthesis of hexagonal cylindrical ordered mesoporous carbons with a large pore size (up to 8 nm), pore volume (up to 0.96 cm^3/g), and surface area (up to 1057 m^2/g) based on the assembly of biomass-derived tannin as carbon precursor

with F127 as a soft template. Li et al. (2012) reported the synthesis of hexagonal ordered mesoporous carbons (OMC-Ts) via a soft templating and catalytic method by using resorcinol and formaldehyde mixture as precursors, Pluronic F127 as the template F127, and $Fe(NO_3)_3.9H_2O$ as a catalyst. By adjusting the pyrolysis temperature of resorcinol and formaldehyde from 700 to 1000 ˚C, the resultants OMC-Ts showed a high surface area of up to 808 m^2/g, pore-volume of up to 0.66 cm^3/g and pore diameter of up to 4.8 nm, respectively. Sterk et al. (2012) described the fabrication of OMCs by using triblock copolymer F127 as a soft template and phenolic resin as a carbon precursor in the presence of tetraethyl orthosilicate (TEOS). In this case, silver nitrate was introduced into the prepared mixture to enhance the microporosity development. The specific surface area and pore volume were in the range of 353 to 779 m^2/g and 0.19 to 0.65 cm^3/g, respectively. Feng and co-workers fabricated highly ordered mesoporous carbons (OMCs) with a 2D hexagonal mesostructured via a facile hydrothermal method using β-cyclodextrin as a renewable and environmentally-friendly carbon precursor. The resulting OMCs exhibit a high surface area of ~781 m^2/g, a uniform pore size (~4.5 nm), and a pore volume of 0.41 cm^3/g (Feng et al., 2014). Liu and Kong synthesized activated ordered mesoporous carbon (AOMC) with a very high surface area (2903 m^2/g) and large mesopore volume of 3.40 cm^3/g via the soft template route. In their synthesis, the phloroglucinol-formaldehyde precursor was self-assembled with triblock copolymer pluronic F-127 to form a polymeric composite, which was carbonized at 800 ˚C under an N_2 atmosphere to produce OMC. The activation of the resultant OMC with sodium amide led to the AOMC. Monolithic mesoporous carbons were also fabricated via a simple autoclaving method using citric acid as a catalyst. The citric acid assisted in maintaining the structural order of the resultant OMCs by enhancing the hydrogen bonding interactions

between the triblock copolymer F127 template and resorcinol–formaldehyde resins precursor. The obtained mesoporous carbons showed a hexagonal pore structure with pore sizes of up to 5 nm and a BET surface area of up to 758 m^2/g (Liu et al., 2012).

2.4.2.3.2 Hard templates

In hard template methods, ordered mesoporosity in carbon materials can be achieved via the nanocasting technique by ordered-mesoporous silica, colloidal particles, or opals as hard templates (Inagaki et al., 2016). Historically, Ryoo et al. (1999) first reported OMC synthesis using mesoporous silica molecular sieve MCM-48 as a hard template, sucrose as a carbon precursor, and sulphuric acid as a carbon precursor the polymerization catalyst. The resultant carbon material had a BET surface area and pore size of 1380 m^2/g and 3.0 nm, respectively. Nevertheless, the pore structure of the resultant carbon was not a precise replica of the MCM-48 template due to structural transformation after the template removal. Lee et al. (1999) reported that when phenol-formaldehyde was used as a carbon precursor, aluminum was implanted onto MCM-48 to create strong acid catalytic sites for the polymerization of phenol and formaldehyde. The obtained carbon material with regular three-dimensional interconnected (3D) pore channels was a faithful replica of the MCM-48 template after a series of impregnation/drying steps and carbonization at a temperature above 600 ˚C. In 2000, Jun and co-workers used SBA-15 as a template instead of MCM-48 and sucrose as a carbon precursor to produce an ordered mesoporous carbon exhibiting the exact symmetry as the template SBA-15. It had a specific surface area of 1520 m^2/g, a total pore volume of 1.3 cm^3/g, and a pore diameter of 4.5 nm. Therefore, the report on the study of the synthesis of ordered mesoporous carbon materials using different hard templates and carbon precursors is rapidly growing. Fuertes (2004)

employed SBA-15 as a template to develop OMC materials with paratoluene sulfonic acid and furfuryl alcohol as carbon sources. By adjusting the synthesis temperature of SBA-15 between 90 and 150 ℃, the pore diameter of the obtained OMCs can be tuned from 3.0 to 5.2 nm, while the BET surface area, and pore volume, can be tuned within the range of 1500-1800 m^2/g, and 1.1-1.5 cm^3/g, respectively. Considering the advantages of nanocasted porous carbon materials, Lin et al. (2006) also reported the synthesis of mesoporous carbon with a high surface area and ordered structure via a nanocasting process at 900 ℃ using mesoporous MCM-41 silica as a template and sucrose as a carbon precursor. The results showed that the templated carbon had a BET surface area of 1200 m^2/g, a pore volume of 1.0 cm^3/g, and a bimodal porosity centered at around 4 nm and 46 nm. In another report, Gokulakrishnan et al. (2011) produced an OMC with hexagonal arrays of rods by using SBA-15 as a template and 2,3-dihydroxynaphthalene as a fused-aromatic carbon precursor. The impregnation of 2,3-dihydroxynaphthalene inside the mesopores of the silica template leads to the conversion into carbon via dehydration reaction of the surface silanols and hydroxyl groups and carbonization at 900 ℃ under an inert atmosphere. The pore size analysis shows that the resulting material possessed a specific surface area of 724 m^2/g and a monomodal pore size distribution of 3.4 nm. Schuster et al. (2012) reported that spherical OMCs with the bimodal pore size distribution of large and small mesopores of 6 nm and 3.1 nm, respectively, can be prepared through the hard template method by using a mixture of phenol and formaldehyde as carbon source and spherical silica as a template. The material exhibited a high BET surface area of 2445 m^2/g and a total pore volume of 2.63 cm^3/g. Schuster et al. (2012) reported that the hard templating synthesis procedure using phenol and formaldehyde mixture precursor and spherical silica as hard templates yielded spherical OMC nanoparticles with a high specific

surface area of 2445 m^2/g, total pore volume of 2.32 cm^3/g and a bimodal pore size distribution with pores centered at 6 and 3.2 nm. Liu et al. (2011) synthesized a series of OMC materials using triblock copolymer (P123), glycol as a structure-directing agent and carbon source, and TEOS as a silica source. A rod-like OMC material was obtained when the HCl concentrations were 1 and 3 mol/L, while when the HCl concentrations were 1.5, 2, and 2.5 mol/L, OMCs materials with flower-type, plate-like, and gyroid-shaped were produced. The OMCs showed surface area, pore volume, and pore size of 970-1312 m^2/g, 1.09-2.20 cm^3/g, and 4.7-6.5 nm, respectively.

The hard templating method can also be used to prepare well-ordered nitrogen-containing mesoporous carbon materials with tunable pore diameters by using precursors containing N atoms. Mane et al. (2012) demonstrated the preparation of highly ordered nitrogen-containing mesoporous carbons (NMC-G) using a low-cost, naturally occurring gelatin as a carbon and nitrogen precursor and 2D hexagonal SBA-15 with different pore sizes obtained at different aging temperatures (100-130 ˚C) as the hard template. The NMC-G materials showed excellent textural properties such as high specific surface areas (764–804 m^2/g), large pore volumes (1.14–1.40 cm^3/g), and mesopore sizes (3.54–4.89 nm). Gao et al. (2016) reported the synthesis of nitrogen-containing ordered mesoporous carbons (NOMC) via a solvent-free approach by directly heating amino acids inside the porous networks of SBA-15. It was found that the strong interactions between the different types of amino acids with the SBA-15 template at carbonization temperatures (700-900 ˚C) led to nitrogen-containing ordered mesoporous carbons with high surface areas (700–1400 m^2/g), large pore volumes (0.9–2.5 cm^3/g), and uniform mesopore sizes (4.3–10.0 nm). Liu and co-workers reported that mesoporous nitrogen-doped carbon (N-MC) with highly

ordered two-dimensional hexagonal structures could be prepared using diaminobenzene (DAB) as carbon and nitrogen sources, ammonium peroxydisulfate (APDS) as an oxidant, and SBA-15 as a hard template (Liu et al., 2010a). By varying the synthesis temperature of the template (70-100 ℃), the pore diameter of the N-MC materials was in the range of 3.4 to 4.2 nm, while the BET surface area of the N-MC with a nitrogen content of 26.5 wt.% was in the range of 281.8 to 535.2 m^2/g. The C/N molar ratio of the samples was in the range of 3.25 to 3.65 by varying the mole ratio of DAB/APDS precursors at a synthesis temperature of 80 ℃, while the pore size of the N-MC was in the range of 4.12 to 3.66 nm. Sanchez-Sanchez et al. (2014) prepared nitrogen and oxygen-doped OMC materials via the polymerization of polyamide precursor formed from 3-aminobenzoic acid with an SBA-15 template carbonized at 900 ℃. The results showed that OMCs with very narrow pore size distributions and nitrogen and oxygen contents as large as 6 and 6.4–11.5 wt.% were obtained. Liang et al. (2019) also demonstrated a simple hard template synthesis of nitrogen and oxygen co-doped mesoporous carbons using KIT-6 as a template, $Fe(NO_3)_3$ as a catalyst, and polyvinylpyrrolidone (PVP) as the source of C, N, and O, and KOH activated. The resulting N/O-OMC replicates the morphology of KIT-6, and the specific surface area and pore volume of the sample increased from 516 m^2/g and 0.56 cm^3/g to 1403 m^2/g and 1.29 cm^3/g after KOH activation, indicating that activation could effectively improve the specific surface area and pore volume. To incorporate more nitrogen atoms into a porous carbon structure, Vinu (2008) fabricated two-dimensional mesoporous carbon nitride (MCN) materials with tunable pore diameters from SBA-15 silicas with different pore diameters as hard templates through a simple polymerization reaction between ethylenediamine (EDA) and carbon tetrachloride (CTC) using a hard template route. The authors found that the pore diameter of the

MCN materials can be easily tuned from 4.2 to 6.4 nm by an easy adjustment of the pore diameter of the SBA silica templates. The carbon-to-nitrogen ratio of the MCN materials decreases from 4.3 to 3.3, with an increasing EDA to CTC weight ratio from 0.3 to 0.9. Meanwhile, the BET surface area and pore volume of the MCN samples can be adjusted within the range of 505-830 m^2/g and 0.55-1.25 cm^3/g, respectively.

MgO has also been employed as a template due to its structural and thermal stabilities. Zhu and Akiyama (2016) reported the synthesis of disordered amorphous mesoporous carbon by a facile hard templating approach. In their synthesis, the MgO template, which served as a pore-expanding agent, was incorporated into the cotton cellulose-derived carbon by absorbing an $Mg(NO_3)_2$ solution into cellulose fibers with subsequent drying and carbonization steps. After washing and removing the MgO template by dilute acid solution, the resultant carbon had a specific surface area of up to 1260 m^2/g and a pore size of 3-5 nm. Meng and Park (2012) reported the preparation of a series of micro/mesoporous carbons from a weak acid cation exchange resin (CER) by the carbonization of Mg acetate ($Mg(CH_3COO)_2 \cdot 4H_2O$) according to a 0, 0.5, 1, 2, 3, 4:1 (Mg acetate/CER mass ratio). By dissolving the MgO template, the obtained porous materials showed a BET surface area within the range of 326–1276 m^2/g and pore volumes of 0.258–0.687 cm^3/g.

Three-dimensional interconnected mesoporous carbons with a large pore volume were also prepared through hard templating with colloidal silica. For example, Gierszal and Jaroniec (2006) reported the synthesis of mesoporous carbon with an extremely large pore volume of 6 cm^3/g, surface area of 1800 m^2/g, and narrow bimodal pore size distribution. The OMC was obtained via carbonization of resorcinol-formaldehyde resin as carbon precursor and colloidal silica particles with 24 nm diameter as a

template. Wang et al. (2013a) reported the development of ordered mesoporous carbon via a combined hard templating approach with the sol-gel method employing colloidal silica as a template and resorcinol-formaldehyde as a carbon precursor. The MC showed a high surface area, pore volume, and pore size of 757 m^2/g, 3.61 cm^3/g, and 29.3 nm, respectively. In summary, mesoporous carbons with different physicochemical properties have been successfully synthesized using different hard templates and carbon precursors, and some typical examples are presented in Table 2.1.

2.4.3 The influence of operating parameters

In addition to carbon precursors and templates, operating parameters such as carbonization temperature and mass ratio between template-to-carbon precursors are vital factors determining the mesoporous carbon's porosity and textural structure.

Carbonization temperature. Carbonization is a process of thermal decomposition of polymer molecules in a corresponding temperature range by removing non-carbon elements (H, S, and O) in the form of volatiles to form an enriched carbon framework (Nor et al., 2013; Teng et al., 1998). During the carbonization process, carbonization temperature directly affects pore structure, chemical composition, structural evolution, and strength of carbonization products. Based on conventional thermal heating, low carbonization temperature (typically < 600 ℃) results in carbons with ill-defined mesostructured and cannot form enough mechanical strength due to incomplete carbonization (Shon et al., 2016; Lee et al., 2007). Usually, the carbonization temperature is in the range of 700 to 800 °C to ensure the full development of porosity and surface area. While temperatures that are too high, like above 900 °C, are time

and energy-consuming processes that can result in a decrease in surface area and pore volume with a large amount of ash content and eventually lead to the blockage of the pores due to structural shrinkage (Hendrawan, 2019; Zhou et al., 2021).

Table 2.1 Summary of the textural properties of the mesoporous carbon materials synthesized with hard templating method under different synthesis conditions.

Material	Structure	Template	Temperature (˚C)	Carbon precursor	Surface area (m^2/g)	Pore volume (cm^3/g)	Pore size (nm)	Reference
CMK-3-130	Rod-like	SBA-15	900	Sucrose	1823	2.23	5.8	Yu et al., 2002
MFC60-130	well-ordered porous structure	SBA-15	900	C_{60} in 1-chloronaphthalene	680	0.75	4.89	Benzigar et al., 2018
CAS40-1.75	spherical	Colloidal silica	900	Chitosan	1101	4.31	19.8	Olejniczak et al., 2013
Mesoporous carbons	Spherical	Colloidal silica	800	Resolcinol-formaldehyde	587-999	1.4-3.1	10.5-18.9	Wang et al., 2013
MCS-1.5	spherical	Colloidal silica	700	Resolcinol-formaldehyde	1097	2.68	10.8	Chen et al., 2020
CDMC	Spherical	Colloidal silica	900	Chitosan	871	3.04	18.4	Peng et al., 2019
SOMC-600	Rod-like	SBA-15	600	Soybean oil	882	-	3.5	Liu et al., 2020
FOMC-1	Carbon-rods	SBA-15	900	finger citron essential oil	889	1.13	3.9	Fang et al., 2016
SNU-2	hexagonal	HMS + $AlCl_3$	700	phenol and formaldehyde	1056	0.69	0.6-2	Lee et al., 2002
Mesoporous nitrogen-doped materials	Hollow	KIT-6	850	(1-methyl-1Hpyrrole-2-yl)methanol (MPM)	782-1152	0.91-1.02	3.4-3.9	Park et al., 2014
NHPC-3D	Macroporous structure	Colloidal silica spheres	800	dopamine	1056	2.56	2.5	Tang et al., 2015.

For instance, Yu et al. (2014) reported the gradual change in the mesopore size for the materials NOMC-600, NOMC-700, and NOMC-80, implying that ordered mesoporosity is well preserved with increasing carbonization temperature. The materials showed an increasing tendency of BET surface area and pore volume from 583 m^2/g and 0.16 cm^3/g to 631 m^2/g and 0.19 cm^3/g when the temperature increases from 600 to 800 °C.

The template-to-carbon ratio by mass is the weight between the silica template and the precursor, affecting carbon's ordered structure and textural characteristics. A low template-to-carbon mass results in an ordered structure replication with developed porosity. A high template-to-carbon ratio can cause carbon overloading on the silica template's external surface, leading to a detrimental effect on the development of porosity (Shao et al., 2022; Lezanska et al., 2018). Janus studied the impact of different mass ratios on SBA/furfuryl alcohol-derived mesoporous carbons (Janus et al., 2020). The results exhibited an increase in surface area and pore volume at a low mass ratio of 0.5-1.25 from 858 to 1203 m^2/g and 0.91 to 1.45 cm^3/g. However, a gradual drop in BET surface area and pore volume was noticed as the mass ratio was increased from 1.50 to 2.00.

2.4.4 Comparison of the soft template with hard template synthesis

One of the significant drawbacks of the soft templating approach is that it is difficult to gain control over the condensation reaction, as it depends on the sol-gel chemistry where the mesoporosity of the final carbon product is sensitive to the relatively rigid reaction conditions, such as pH value, hydrogen bonding between the template and the precursor, temperature, functionalization of the template with the polymeric unit and humidity (Crepaldi et al., 2003; Grosso et al., 2001). During the synthesis process,

the narrow temperature range favors a relatively low crystallinity, which leads to materials produced through the soft templating method in an amorphous or semi-crystalline phase. Depending on the target application of the mesostructured product, shortcomings of the amorphous phases include reducing the catalytic efficiency of the material and decreasing the conductivity of the electrode materials. Although the amorphous phase could be avoided during the carbonization process, it is challenging to preserve a well-ordered mesoporous structure after heat treatment at high temperatures (Savic et al., 2018). Other disadvantages include formaldehyde has dominated as a highly toxic and volatile precursor. Exploring other monomers and various carbon precursors besides the phenolic resins is necessary.

The benefit of the soft template approach is the ease of the one-step synthetic procedure for producing mesoporous carbon materials and the easy removal of the templating surfactant. Still, it is challenging to gain morphological control desired product. The soft templating method is low-cost, flexible, and suitable for large-scale industrial applications such as adsorption and catalysis. The mesostructured products are of high-quality standard with controllable pore sizes (Tian et al., 2020; Ma et al., 2013; Chauhan, 2021).

In general, the hard templating method is the most desirable technique for synthesizing OMC materials because of the following advantages; (a) makes the synthesis of OMCs easy to control and is highly applicable due to the fixed solid states of the templates (Chu et al., 2019), (b) high crystallinity of the final OMC products, (c) high-quality final products with ordered mesoporous structure (Lee et al., 2004b; Yamada et al., 2007; Wan et al., 2008; Lee & Park, 2012). Some drawbacks still exist

for the hard templating strategy. Besides, compared to the soft template, the hard templating method is multistep and time-consuming since the silica template preparation can take a couple of days. Another downside of the hard templating approach is the usage of hydrogen fluoride for template removal, and the cost of the synthesis procedure is high (Chauhan et 2021).

2.4.5 Applications of mesoporous carbon materials.

Mesoporous carbon is a promising material having diverse applications. It can be used as an electrode material in energy storage and conversion. In 2011, Lei and co-workers used mesoporous carbon nanospheres (MSC) with a specific surface area of 2396 m^2/g and pore volume of 2.9 cm^3/g to prepare supercapacitor electrodes. The MSC electrodes not only showed a high specific capacitance of 180 F/g and energy densities of 62.8 W h/kg and 9.1 W h/kg at power densities of 0.16 kW/kg and 32 kW/kg, respectively but also displayed an excellent cyclability, with 78% energy density and more than 90% power density remaining after 700 cycles at a current density of 3.0 A g^{-1}. Some studies revealed that heteroatom doping is an effective method of enhancing the pseudocapacitive interactions between electrolyte ions and surface active sites of the heteroatom and improving the wettability and conductivity of the mesoporous carbon electrodes (Han et al., 2019; Yang et al., 2017). Song et al. (2014) prepared nitrogen-doped ordered mesoporous carbon with a large BET surface area as high as 1374 m^2/g and a large pore size of 7.4 nm. The obtained nitrogen-doped OMC was used as electrode material for the supercapacitor, exhibited excellent cycling stability, and delivered a reversible specific capacitance as high as 308 F/g^{-1} in a 1 mol/L H_2SO_4 aqueous electrolyte, of which 58% of the capacity is due to pseudo-capacitance. Wang et al. (2013c) prepared nitrogen-rich ordered mesoporous carbon (N-OMC) by soft templating and direct pyrolysis of ammonia. The resultant N-OMC

had a large surface area (up to 1400 m^2/g), high nitrogen content (up to 9.3 wt%), and a good capacitance of 6.8 $\mu F/cm^2$ as electrode materials for symmetric electric double-layer capacitors.

Mesoporous carbon materials have also drawn significant attention in catalysis due to their high structural stability. Liu et al. (2017a) reported the synthesis of hierarchical 3D porous carbon (3DC) via a copolymer-silica assembly route, using silica as a hard template and styrene-co-acrylonitrile polymer has been as both a carbon source and a soft template. The resultant 3DC material had a high surface area of 550.5 m^2/g, which allows the facile dispersion of Pt nanoparticles on the carbon support. In addition, the 3DC-supported Pt electrocatalyst exhibited excellently in the oxygen reduction reaction (ORR). Yan et al. (2014) reported the synthesis of mesoporous carbon with a BET surface area between 400-500 m^2/g dispersed with palladium particles (Pd) to produce Pd/MC catalysts by the impregnation method. They found that 5% Pd/MC gave 82.2% selectivity to cyclohexanone oxime at the nitrocyclohexane conversion of 99.4% under the mild reaction condition of 0.5 MPa and 323 K. Park et al. (2014) demonstrated the synthesis of mesoporous nitrogen-doped carbon using (1-methyl-1H-pyrrole-2-yl) methanol as a precursor and 3D mesoporous cubic KIT-6 as a template. The results revealed that the mesoporous carbons had nitrogen content in the range of 0.5 to 10.0 at%, with pore diameters of 3.4−4.0 nm, a surface area of 780-1150 m^2/g and a pore volume of 0.91-1.02 cm^3/g. These materials showed high catalytic activities for electrochemical oxygen reduction to obtain H_2O_2 with high selectivity of over 90 %.

2.5 Amine functionalized OMCs for CO_2 capture applications

2.5.1 Overview of different carbon capture technologies

The basic types of technologies related to CO_2 capture are pre-combustion, oxy-fuel combustion, and post-combustion carbon capture, as illustrated in Figure 2.6. A proper CO_2 capture approach significantly depends on the combustion method, generating plant, and the fuel used (Leung et al., 2014). The operating conditions such as temperature, pressure, and material differ for each CO_2 capture type, making them economically viable only in large-scale plants (Yu et al., 2017).

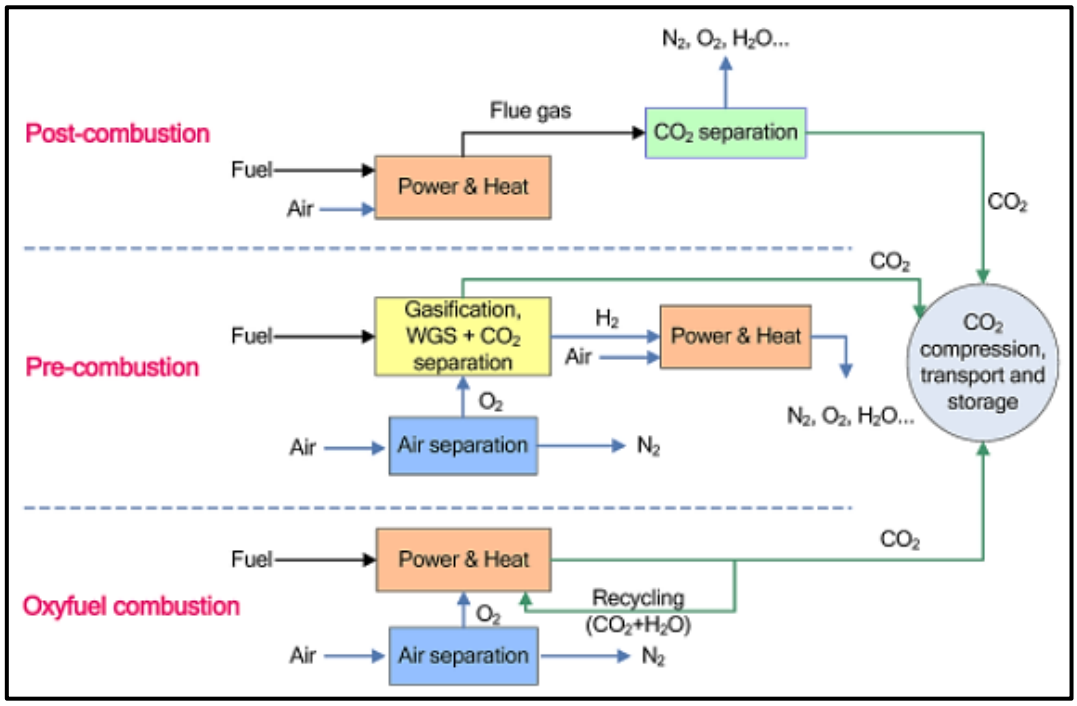

Figure 2.6 Main separation processes for post-combustion, pre-combustion, and oxy-combustion. (Vaseghi et al., 2012).

Pre-combustion technologies. Pre-combustion CO_2 capture is the technique used to capture CO_2 from fossil fuel (coal) or biomass fuel before the combustion process (Theo et al., 2016). Typically, this technique is applied to integrated

gasification combined cycle (IGCC) power plants, as depicted in Figure 2.5. The synthesis gas of high temperature (>1000 ℃) and pressure (15-150 atm) is generated via gasification of the fuel such as biomass, coal, and natural gas, as presented in Equation 2.8. Then the synthesis gas forms more H_2 through a water-gas shift reaction with steam, where CO is converted to CO_2, as shown in Equation 2.9 (Babu et al., 2015; Bert Metz, 2005). After the particulate matter removal, the CO_2 could be separated from the gas stream and H_2, contributing to power generation (Scholes et al., 2010).

$$\text{Coal/Biomass} \rightarrow CO + H_2 \quad (2.8)$$

$$CO + H_2O \rightarrow CO_2 + H_2 \quad (2.9)$$

Pre-combustion capture has the following technical advantages: (1) hydrogen/synthesis gas is generated as an alternative fuel that can be used in cement, iron, and steel industries for power production purposes with minimum CO_2 emissions; (2) less energy is required due to high gas volume (15-60 % dry basis), high pressure (2-7 MPa), and high-temperature range of 200-400 ℃; (3) low water consumption is needed in this technique, which makes it easy for capture (Jansen et al., 2015; Wall, 2007; Zhu et al., 2010). Generally, it is a well-established acid-gas removal process with excellent efficiency that produces syngas containing 64-73 mol% H_2 and 20-23 mol% CO_2 (Zhu et al., 2010). However, there are drawbacks to the commercial availability of integrated gasification combined cycle (IGCC) and water gas shift reaction processes, which are expensive and challenging. The issue of high energy loss might arise due to adsorbent regeneration (Pires et al., 2011).

Oxy-fuel combustion technologies. CO_2 capture by oxy-fuel combustion technology has attracted considerable attention due to the minimal emission of pollutants, and low capture cost compared with the other two CCS technologies (Theo et al., 2016; Yin and Yan, 2016). According to International Energy Agency (IEA) (Wu et al., 2018), oxy-fuel combustion technology has been anticipated to be commercially feasible in coal-power plants, due to its simplicity of implementation and compatibility with a wide variety of fuels. In oxyfuel combustion, the fuel is combusted in pure oxygen rather than air, producing a flue gas stream consisting mainly of CO_2 and water vapor (Rubin et al., 2012). The CO_2 can be easily purified and ready for compression and storage, upon the removal of particulate matter (fly ash) with an electrostatic precipitator (ESP) and the removal of water vapor and small quantities of other gaseous impurities, such as sulfur dioxide (SO_2) and nitrogen oxides (NO_x), by cooling, compression and liquefaction processes (Carrasco-Maldonado et al., 2016). The major performance barrier of oxy-fuel technology is the high cost of air separation for oxygen production and the prevention of air ingress during oxy-fuel combustion (Pfaff and Kather, 2009).

Post-combustion technologies. The main goal of the post-combustion method is to separate and capture CO_2 from flue gas produced after fuel combustion (e.g., coal and biomass) (Zou et al., 2017). Fuel combustion produces a flue gas stream typically consisting of N_2, CO_2, and other small components such as water vapors, CO, NO_x, and SO_x. Pre-treatments are required to remove impurities, and the flue gas is then transferred to the CO_2 separation system at atmospheric pressure and temperatures (40-80 ℃) (Gardarsdottir et al., 2015). This carbon capture process is considered to have the best prospects for application, due to its unique capability to retrofit onto

virtually any existing fuel combustion plant, although it may not be the most cost-effective technology compared to oxy-fuel and precombustion capture. Removing impurities from the captured CO_2 in this technology is the main issue, due to the low amount of CO_2 in the flue gas (15% and 4% in coal-fired and natural gas-fired systems, respectively) (Bui et al., 2014; Zhang et al., 2018). Post-combustion carbon capture techniques have been so far the most investigated next-generation capture technology, although other technologies, such as membrane separation and cryogenics are also under development at various scales (Ahmed et al., 2020; Samanta et al., 2012).

Currently, the state-of-the-art method for post-combustion capture is chemical absorption, due to several advantages such as technology maturity at commercial scales, high CO_2 capture efficiency (typically, over 98%), and selectivity at very low CO_2 concentrations (Rochelle,2008; Liu et al., 2016). Among many technologies, amine scrubbing with an aqueous amine such as monoethanolamine (MEA) and diethylenetetramine (DETA) is the most demonstrated capture technology for power plant CO2 capture applications, as presented in Figure 2.7. The flue gas is passed via an absorbing column containing the solvent, absorbing the CO_2. The CO_2-rich solvent is then circulated to a stripper where heating with steam is required to regenerate the CO_2-loaded amine at 100-120 ℃ and with the stripped CO_2 for compression, transportation, and storage (Dutcher et al., 2013).

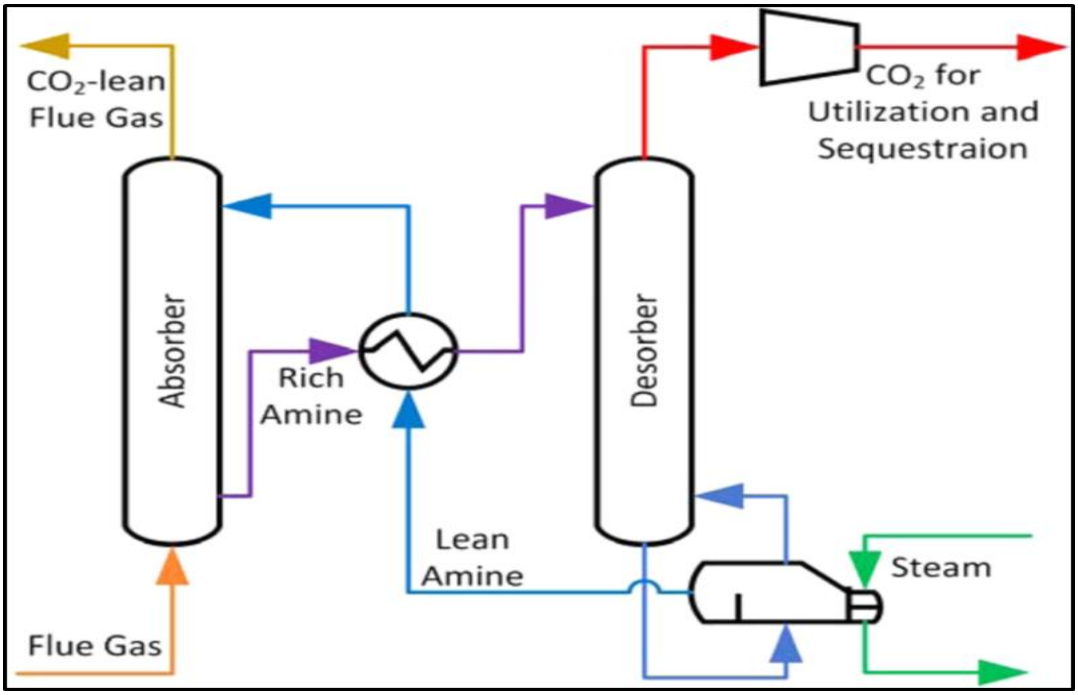

Figure 2.7 Typical amine scrubbing designed for a power plant (Dutcher et al., 2015).

CO_2 scrubbing with MEA has been used in the oil and gas industry for more than 60 years, being the chemical icon for easy handling and fast CO_2 adsorption. However, for CO_2 capture from power plants, the method suffers from major shortcomings, such as prohibitively high energy cost which can reduce power plant efficiency by a factor of 30 %, thermal degradation of amines due to the presence of NO_x and SO_x in the flue gas, production of volatile compounds that are highly corrosive and toxic (Spigarelli and Kawatra, 2013; Zhao and Luo, 2018).

2.5.2 Solid adsorbents for post-combustion CO_2 capture

In adsorption-based CO_2 capture, CO_2 (adsorbate) is preferentially captured on the surface of a porous solid adsorbent via various mechanisms varying from physisorption to chemisorption or their combinations (Patel et al., 2016). In physisorption, the adsorbate interacts on any adsorbent surface having a high surface

area and pore structure through intermolecular forces such as van der Waals. In the case of chemisorption, however, the adsorbent undergoes chemical reactions on the active sites present on the surface of the solid adsorbent. Microporous carbons, metal-organic frameworks (MOFs), zeolites, and amine-functionalized porous materials can all be used as solid adsorbents.

Regeneration of the adsorbent after CO_2 adsorption from the flue gas can be accomplished through either a temperature-swing process (TSA) or pressure-swing adsorption (PSA) process (Wu et al., 2018). TSA is considered promising for post-combustion CO_2 capture and is of particular interest when compared to PSA, due to the avoidance of either flue gas compression and/or decompression in a PSA process. In a typical TSA cycle, as illustrated in Figure 2.8, the saturated adsorbent is transferred from an adsorber to a desorber where the sorbent is heated up to a selected suitable desorption temperature to desorb the adsorbed CO2 and regenerate the sorbent for recirculation. In general, the time required to regenerate the adsorbent in a TSA process is longer than in the PSA process, but high CO_2 purity and recovery rate of greater than 95 % and 85 % respectively can be achieved (Clausse et al., 2011).

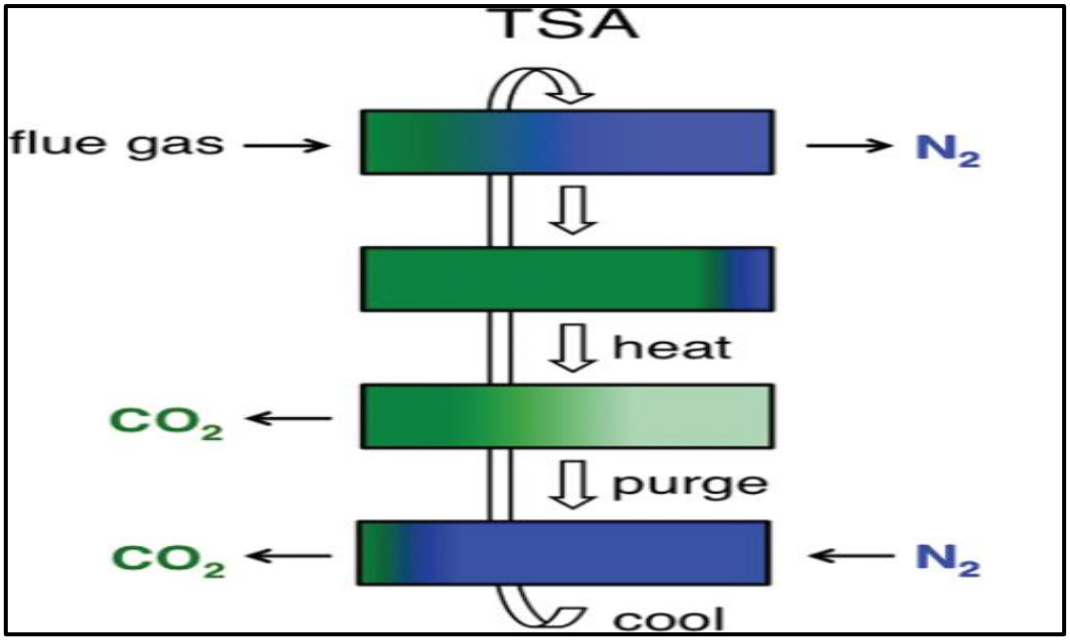

Figure 2.8 Temperature swing adsorption for post-combustion capture (Sumida et al., 2012).

PSA is a commercially available CO_2 separation technique that can have efficiencies of higher than 85 % (Takamura et al., 2001). For a PSA adsorption/desorption process, the column is filled with flue gas in which CO_2 is selectively adsorbed onto the surface of a solid adsorbent at high pressure and then desorbed at low pressure (usually atmospheric pressure) (Riboldi and Bolland, 2017). From a practical perspective, PSA is expected to be most appropriate for pre-combustion capture since the flue gases are immanently pressurized after the conversion reactions (Herm et al., 2011), lower energy demand, and shorter time for adsorbent regeneration. However, there are technical difficulties with flue gas compression, and regular PSA process costs might be prohibitively high for the post-combustion capture of CO_2 (Theo et al., 2016).

The two types of solid adsorbents commonly used for CO_2 capture include physical and chemical adsorbents. Physical adsorbents include zeolites, activated carbon

materials, and metal-organic frameworks (MOFs). Chemical adsorbents typically include various amine-functionalized mesoporous silica materials.

Zeolites. Zeolites are ordered microporous crystalline framework materials that are widely used as adsorbents for the separation of CO_2. Zeolites are based on the Si/Al ratio, which leads to negative framework charges with exchangeable cations (usually Na^+, Ca^{2+}, Li^+) within the pore structure. The CO_2 capture capability of zeolites largely depends on their pore size (between 0.5 to 1.2 nm), charge density, and distribution of exchangeable cations in the porous structure (Zhao et al., 1998; Yazaydin et al., 2009). These cations can generate solid electrostatic interaction with CO_2 possessing a high dipole or quadruple of -14.29×10^{-40} C m^2 (Coriani et al., 2000). The CO_2 is adsorbed within the framework sites, and strong bound carbonate species are observed, which are associated with bi-coordination. Therefore, zeolites have shown promising results in separating CO_2 from the gas streams. For instance, Siriwardane et al. (2001) reported that zeolites 13X and 4A exhibited high CO_2 adsorption capacities of 3.64 and 3.07 mmol/g, respectively, at 25 °C and 1 atm. In terms of practical application, the presence of water vapor is the major challenge for zeolite-based adsorbents because water molecules can be preferentially adsorbed onto the porous surface compared to CO_2 molecules, thereby decreasing the adsorption capacity.

Metal-Organic Frameworks (MOFs). MOFs are porous solid materials composed of metal species linked by organic spacers (Venna and Carreon, 2015), as shown in Figure 2.9. Their pore size, pore shape, and surface chemistry can easily be tuned by varying the organic linkers. Much attention has been paid to a wide range of MOFs such as HKUST-1, MIL-100/101, Zeolitic imidazolate frameworks, and the MOF-74

family due to their high surface area and controlled pore size, particularly in their separation of CO_2 (Plant et al., 2007; Llewellyn et al., 2008; Caskey et al., 2008). Although most investigations showed that MOFs performed well at high pressure and room temperature. For example, Millward and Yaghi (2005) reported that MOF-117 with a BET surface of 4508 m^2/g exhibits a high CO_2 adsorption capacity of 150 wt% at 40 bar. It is essential to mention that at low partial pressure (~0.1 atm), the CO_2 adsorption in MOFs is influenced by the heat of adsorption of CO_2 rather than surface area or pore volume (Yazaydin et al., 2009). Heats of adsorption ranging from 90 kJ/mol would favor CO_2 uptake at lower pressures in MOFs (Demessence et al., 2009).

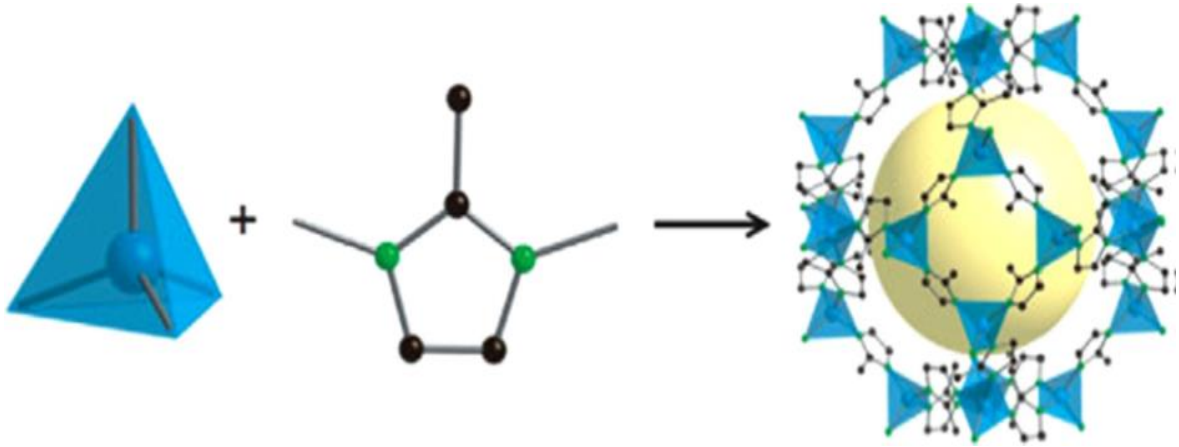

Metal-based cluster (ZnN4) Organic linker MOF

Figure 2.9 A typical MOF structure formed by a metal-based cluster and an organic linker (Venna and Carreon, 2015).

However, there are some limitations with MOFs-based CO_2 adsorbents. One of the issues is that most MOFs exhibit unfavorably CO_2 adsorption capacities at low partial pressure, particularly below 0.15 bar (Wang et al., 2014). A promising solution to this issue is modifying amine or carboxyl groups, creating active sites on the adsorbents

by eliminating bound solvent molecules. Lin et al. (2013) reported that polyethyleneimine-incorporated metal-organic frameworks showed a high CO_2 adsorption capacity of 4.2 mmol/g at 25 °C, and 3.4 mmol/g at 50 °C, with a high CO_2/N_2 selectivity up to 770 at 25 °C, and 1200 at 50 °C, at 0.15 bar and 100 wt% PEI loading. Another practical issue for MOFs is the effect of moisture. Yu and Balbuena (2013) reported that the CO_2 adsorption capacity and selectivity of Mg-MOF-74 were reduced in the presence of water molecules linked to coordinatively unsaturated metal sites instead of CO_2.

Activated-Carbon-Based Solid Sorbents. Activated carbons (ACs) are among the most promising materials used as CO_2 adsorbents because of their easy and wide availability, low cost, and high surface areas. Regarding adsorption capacity, ACs derived from different raw materials such as coal, wood, or biomass have performed well, particularly at high pressure. For instance, Himeno et al. (2005) reported the synthesis of Maxsorb-activated carbons with BET surface areas of up to 3250 m^2/g and a high adsorption capacity of 113 wt% at 30 bar and room temperature. However, due to the microporous structure of ACs that fails to offset the limitation of the physical adsorption processes, such as poor selectivity and temperature sensitivity, their CO_2 adsorption capacity drops in the typical flue gas temperature range between 50 to 120 ℃ (Arenillas et al., 2005). Therefore, strategies to increase the strength of CO_2 interactions with ACs at a low partial pressure have been considered promising; 1). Improving the porous structural properties (BET surface area, pore volume, and pore size). For instance, Sevilla et al. (2011) and Lee and Park. (2013) reported that the development of AC adsorbents, with a large volume of small micropores at 25 ℃ and 1 bar, can influence their CO_2 adsorption capacity. 2) many studies have shown that surface modifications can enhance the CO2 capture capacity of AC materials through

N-doping and amine impregnation. Various nitrogen-containing ACs have been prepared from chitosan (Fan et al., 2013) and polyamine (Wang et al., 2013b) with CO_2 uptakes being as high as 3.86 mmol/g at 25 °C and 5.3 mmol/g at 0 °C and 1 bar CO_2, respectively.

Most physical adsorbents, such as activated carbons, zeolites, and metal-organic frameworks, have shown promising CO_2 adsorption capacities. However, they suffer from low CO_2 adsorption capacities at relatively low CO_2 partial pressure, low tolerance to moisture in the flue gas streams, and lower selectivity towards CO_2 (Samanta et al., 2012).

Amine-functionalized adsorbents. Recently, significant research interest has been focused on amine-functionalized solid adsorbents because of their high adsorption capacity and selectivity for CO_2 from the flue gas streams, and also the regeneration heat of amine-functionalized adsorbents is lower than aqueous amines solution (Khatri et al., 2006; Hou et al., 2018). There are two ways to prepare amine-functionalized solid adsorbents: chemical grafting and physical impregnation. Amine-containing silane is covalently bonded to the mesoporous carbon or silica support in the chemical grafting route. The grafted amine adsorbents have high thermal and chemical stability due to the strong bond between the amino silanes and hydroxyl groups on the porous silica surface (Pirngruber et al., 2009; Unveren et al., 2017). Various chemical grafting methods have been used to prepare grafted amine adsorbents, such as direct synthesis via co-condensation, anionic template method, and Impregnation (Chew et al., 2010). In direct co-condensation synthesis, the aminosilanes in the presence of silica templates, employing acid or base catalyst surfactant, are mixed and allowed to age for complete hydrolysis and condensation of silica to occur. Finally, the amine-functionalized adsorbent can be obtained (Huh et

al., 2003). It was reported by Wen et al. (2010) that amine-modified mesostructured silica monolith is prepared via a one-pot synthesis procedure, and the adsorbent showed a high capacity of 171 mg/g in CO_2 adsorption. The anionic template synthesis method involves the addition of the anionic surfactant, aminosilane, and tetraethyl orthosilicate to a solvent with continuous stirring, and the mixture is kept at the selected time and temperature. Removal of the surfactant by extraction using a combination of HCl and ethanol led to an amine-functionalized adsorbent. In the chemical grafting method, the conventional approach synthesizes a grafted adsorbent via a condensation reaction between the hydroxyl groups on the silica surface and the aminosilanes or polymer-containing amino group. Typically, silica is dissolved in anhydrous toluene followed by the addition of aminosilanes. The resultant mixture is heated under reflux, and the unreacted aminosilanes are removed by washing the solid materials (Huang et al., 2003). Harlick and Sayari (2007) reported the grafting of MCM-41 mesoporous silica with 3-[2-(2-aminoethylamino)ethylamino] propyltrimethoxysilane to produce an amine adsorbent with a high amine content of 6.11 mmol N/g, and CO_2 adsorption capacity of 117 mg/g at 25 °C and 0.05 atm for a dry 5% CO_2 in N_2.

Physical impregnation is an effective method of dispersion of amine compounds onto the pores of mesoporous solid supports. Compared to the chemical grafting method, the apparent advantages of physical impregnation lie in its simple synthesis procedure, higher amine loading due to the large pore volume of the supports, and a lower rate of corrosion (Peng et al., 2019). Among the various polymeric amines, polyethyleneimine (PEI) has been the most studied polyamine for the preparation of solid CO_2 adsorbents due to its high amine content, widespread availability, favorable adsorption temperature from 20 to 90 ℃, good cycling stability, and potential for high

adsorption capacity (Zhang et al., 2017; Zhao et al., 2012; Subagyono et al., 2011). In 2001, Satyapal reported the first use of PEI for regeneratively removing CO2 in space aircraft applications. To further enhance the adsorption capacity of this PEI, Ma et al. (2009) synthesized a “molecular basket” sorbent exhibiting a high sorption capacity of 140 mg/g at 75 °C under 15 kPa CO2 partial pressure. In addition, important parameters such as the PEI type (linear or branched), molecular weight, and loading can play a vital role in optimizing mesoporous support materials. Figure 2.10 exhibits the structure of linear and branched PEI. Compared to the linear PEI, the use of branched-chain PEI with numerous amino groups was found to offer the advantages of lower heat of adsorption, good thermal stability, enhanced adsorption/desorption of CO_2, and requires less energy (Xu et al., 2002; Subagyono et al., 2011; Li et al., 2015). Therefore, physical impregnation with branched PEI has been widely studied to produce highly effective CO_2 sorbents from mesoporous carbons (Wang et al., 2015; Wang et al., 2011b) and silica adsorbents (Niu et al., 2016; Yan et al., 2011).

Furthermore, PEI-mesoporous carbon adsorbents with high molecular weight have shown higher thermal stability and good cyclic CO_2 adsorption capacity than small-molecule PEI-mesoporous carbon adsorbents (Li et al., 2014). Interestingly, increasing the amount of PEI in the adsorbent offers more amine groups to react with CO_2, which enhances CO_2 capture (Peng et al., 2019). However, the increase in PEI loading amount could lead to pore blockage and aggregation of PEI, suggesting the restricted diffusion of CO_2 into deep layers, and reducing CO_2 adsorption capacity (Kong and Liu, 2019).

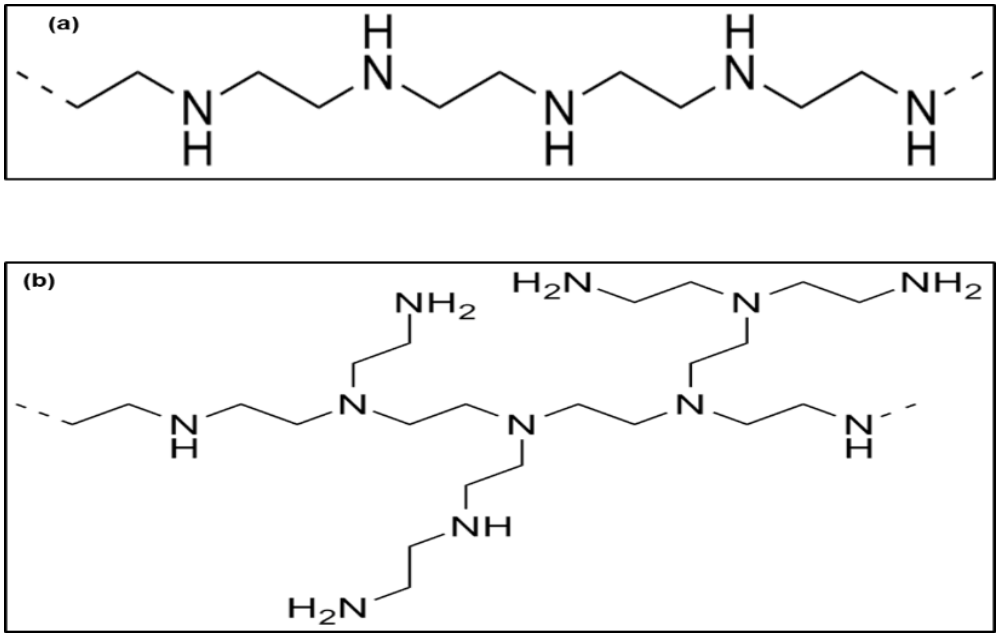

Figure 2.10 The fragment of linear PEI (a) and branched PEI (b) (Prud'homme and Nabki, 2020)

2.5.3 Amine functionalized OMCs for CO_2 adsorption

Mesoporous carbons are particularly attractive as support for preparing PEI-functionalized adsorbents due to their many advantages, including high surface area, large pore volume, ordered and uniform pore size, and ease of surface functionalization (Wang et al., 2011c; Chen et al., 2020). In general, the large pore volume is useful for high loading of amine compounds, which maximizes the densities of the amine in the mesoporous carbon materials, while the ordered and large mesopore size are beneficial for homogenous dispersion of amine on the carbon framework, leading to a high CO_2/amine interfacial area (Kong and Liu 2019). Various mesoporous carbons prepared via templating methods have been employed to fabricate PEI/mesoporous carbon sorbents for CO_2 adsorption with the hard templating method using different porous materials such as zeolites, opals, and mesoporous silicas as template-leading the way because of their tunable textural

properties widely available carbon sources (Cho and Ryoo, 2012; Wang et al., 2016; Park et al., 2017; Lakhi et al., 2016. Previous investigations have shown that mesoporous carbons with large pore volume and controlled pore size are preferable candidates to prepare PEI functionalized CO_2 sorbents (Wang et al., 2012; Wang et al., 2013; Chen et al., 2021; Peng et al., 2019). Wang et al. (2012) studied the CO_2 adsorption performance of mesoporous carbons with different pore volumes (0.64-2.69 cm^3/g) and pore sizes (2.2- 7.26 nm) at a PEI loading level of 50 wt%. They found that the adsorption capacity increased with total pore volume and pore size. Chen et al. (2021) synthesized a series of mesoporous carbon spheres with a controlled pore size (7.6-10.8 nm) and pore volume (1.25 to 2.68 cm^3/g) via a hard template reverse emulsion method. It was found that the increase in pore volume and pore size could effectively improve the PEI loading level and amine accessibility. Therefore, a high CO_2 capture capacity of 3.22 mmol/g and a fast adsorption rate was achieved at a partial pressure of 0.05 bar and a temperature of 75 ^oC. Xie et al. (2017) also found a similar trend for PEI-modified resorcinol-based mesoporous carbon aerogels. Compared to pore volume, pore size plays a critical role in determining CO_2 diffusion and amine accessibility in sorbents. Kong and Liu (2019) prepared ordered mesoporous carbon with a large pore volume of 3.40 cm^3 /g and pore size 2.2 to 8.2 nm via self-assembly phloroglucinol-formaldehyde and triblock copolymer template (Pluronic F-123). The PEI-impregnated sorbents yielded adsorption capacities of 2.58 and 1.84 mmol/g in pure CO2 at 30 ^oC and 75 ^oC, respectively. However, the adsorption capacity of PEI/mesoporous carbon sorbents was slightly lower than that of PEI-impregnated mesoporous carbon nanospheres (MCNs) with a pore size of 9 nm and pore volume of 0.52 cm^3/g at 75 °C and pure CO_2. By using colloidal silica as a template, Wang et al. (2016) synthesized mesoporous carbon spheres (MCSs) with

a large pore size of 16.6 nm and pore volume of 2.87 cm^3/g and a high CO_2 adsorption capacity of 3.71 mmol/g at 15% CO_2, and 75 ^oC was achieved by PEI modified mesoporous carbon spheres.

In addition, the performance of amine-functionalized OMC for CO_2 capture also depends on adsorption temperature and PEI loading. The PEI loading is an important parameter that has a complex influence on CO_2 capacity; for one reason, increasing the amount of PEI loading offers more amine groups to interact with CO_2, which is favorable for CO_2 adsorption. For another reason, the increase in the amount of PEI loading blocks the diffusion of CO_2 into the deep layers, which is not beneficial for CO_2 adsorption (Peng et al., 2019). For example, Wang et al. (2013a) investigated the CO_2 adsorption performance of PEI/mesoporous carbon sorbent with different PEI loadings. It was found that the increase in PEI loading from 15 to 65 wt% led to a rise in CO_2 capacities, and the optimal PEI loading was achieved at 65 wt% with a capture capacity of 4.82 mmol CO_2/g in 15% CO_2 at 75 °C. With a further increase in PEI loading to 80 wt%, the CO_2 capacity dropped to 2.83 mmol CO_2/g. Kong and Liu (2019) reported a similar variation in CO_2 capture uptake with different amounts of PEI loading could be obtained for PEI@AOMC. The CO_2 capture uptakes increased from 0.48 to 1.84 mmol CO_2/g as the amount of PEI loading increased from 25.7 to 51.6 wt% in 15% CO_2 at 75 °C. As the PEI loading was dispersed to 60.2 wt%, there was no apparent rise in CO_2 uptake of PEI@AOMC (1.84 mmol CO_2/g).

The adsorption temperature also affects the CO_2 capture capacity in the following ways; (a) promotion effect- a rise in adsorption temperature could promote the diffusion of CO_2 from the surface of PEI into the deep PEI layers, which benefits the CO_2 capture process, (b) suppression effect- the increased adsorption temperature

suppresses the exothermic reaction between amine groups and CO_2, which is unfavorable for CO_2 adsorption (Peng et al., 2019; Bezerra et al., 2014; Li et al., 2014).

One significant advantage of mesoporous carbon supports over silica materials is their excellent thermal and electrical conductivity, making them potential candidates for the electric swing adsorption (ESA) process. Being different from the conventional temperature swing adsorption process (TSA), the electrical current could be directly passed through the adsorbents to regenerate the adsorbents via “in-situ” heating by the Joule effect, which could potentially reduce the regeneration energy consumption (Wang et al., 2016; Gibson et al., 2015).

Chapter 3 Experimental Methodologies

This chapter presents the experimental methodologies used in this PhD project, which includes the chemicals/materials involved and the preparation of ordered mesoporous materials, such as mesoporous carbon and silica materials including mesocellular silica foam (MCF) and SBA-15. The two most abundant biomass precursors, lignin and chitosan, were selected to prepare the ordered mesoporous carbon materials via hard template methods. The experimental parameters like carbonization temperature and mass ratio were designed based on the references (Kumar et al., 2020; An et al., 2012). Although mesoporous carbon materials have a wide range of advanced energy-related applications, the as-prepared mesoporous carbon materials were used in this research as the support for preparing PEI-functionalized adsorbents for CO_2 capture, using a well-established wet impregnation method.

3.1 Preparation of ordered mesoporous carbons using different mesoporous silica templates.

A wide range of ordered mesoporous carbon materials with controllable pore size distributions was successfully synthesized using lignin and chitosan as carbon precursors and mesocellular silica foam (MCF) and SBA-15 as silica templates.

3.1.1 Chemicals

Two kinds of easily accessible precursors lignin (Mw = ~10,000, pH = 10.5), and chitosan (high molecular weight = 50000-190000 Da based on viscosity, degree of deacetylation 75-85 %) were used to prepare the mesoporous carbon materials in this

project. Other chemicals used in the preparation of the comprehensive material include; acetic acid, pluronic P123 (poly (ethylene oxide)-block-poly (propylene oxide)-block-poly (ethylene oxide), EO20-PO70-EO20 (MW = 5800), 1,3,5-trimethylbenzene (99.0%, TMB), sodium hydroxide (NaOH), tetraethyl orthosilicate (98%, TEOS), hydrochloric acid (37%, HCl), ammonium fluoride (99.99%, NH_4F), polyethyleneimine (Mw = 600, branched, liquid), tetrahydrofuran (THF). All chemicals were purchased from Sigma-Aldrich, while a commercial PQ silica used in the preparation was obtained from PQ Corporation.

3.1.2 Preparation of mesostructured cellular foam (MCF) and SBA-15 templates.

The mesocellular siliceous foam templates were prepared using the micro-emulsion approach (Schmidt-Winkel et al., 2000), which used Pluronic P123 as a template, TEOS as a silica source, and TMB as the pore-expanding agent. In this procedure, 8 g of Pluronic P123 was dissolved in 130 ml deionized water and 20 ml HCl under constant stirring conditions at 40 ˚C. Then, 16 g of TMB was added, and the solution was stirred continuously for 2 h before 17.3 g of TEOS was added. The new mixture was first kept at 40 ˚C for 20 h for complete hydrolysis, followed by the addition of 10 ml of 0.25M NH_4F solution. The resulting milky solution was then transferred to an autoclave and aged at different temperatures (100 or 120 ˚C) for 24 h under static conditions. The solution was then allowed to cool to room temperature, and the white solid was first separated by vacuum filtration and then washed with deionized water. The white precipitate was dried overnight at room temperature and finally calcined at 550 ˚C for 8 h in airflow of 5 ˚C /min to obtain the MCF template. The mesocellular

foam silica templates were denoted as MCF1 and MCF2 aged at 100 ˚C and 120 ˚C, respectively. Each sample was prepared in triplicate.

The preparation of the SBA-15 silica template was similar to that of MCF silica, except there was no addition of trimethyl benzene (TMB), and the milky solution was aged at 100 ˚C.

3.1.3 General carbon sample preparation conditions.

Carbonization temperature. The temperature was designed referring to the references (Chu et al. 2020; Pastor-Villegas et al. 1998; Ji et al. 2010, Lu et al. 2005). According to conventional thermal heating, low carbonization temperature (typically < 600 ℃) leads to mesoporous carbons with ill-defined mesostructured and cannot form enough mechanical strength due to incomplete carbonization (Shon et al., 2016; Lee et al., 2007). The carbonization temperature in the range of 700 to 800 °C ensures the full development of porosity and surface area. While temperatures that are too high, like above 900 °C, are time and energy-consuming processes that can result in a decrease in surface area and pore volume with a large amount of ash content and eventually lead to the blockage of the pores due to structural shrinkage (Hendrawan, 2019; Zhou et al., 2021).

Template-to-carbon ratio by mass. The mass ratio was selected based on the theoretical maximum loading of lignin, which has a density of 1.35 g/cm^3 (Gregorova et al., 2006), and the total pore volume of the MCF templates (2.53 and 3.58 cm^3/g), which was estimated at 3-4 g of lignin per gram of the templating silicas used, and the total pore volume of SBA-15 (1.13 cm^3/g), which was found to be 1.5 g.

3.1.4 Preparation of lignin-based mesoporous carbons using MCF as the hard template.

The lignin-based ordered mesoporous carbons were prepared via a solvothermal method using the prepared MCF silicas and the commercially available mesoporous silica purchased from PQ Corporation as the hard templates. In a typical synthesis, 2.4 g of lignin was first dissolved in 15 mL of tetrahydrofuran (THF), and 1.2 g of each selected mesoporous hard template was then added into the mixture under vigorously stirred conditions for 2 h. A carbon-silica composite was then obtained following the removal of THF solvent via evaporation at 50 ˚C for 24 h. After the impregnation process, carbonization was carried out in a horizontal tube furnace (Figure 3.1). The composite was then carbonized at selected temperatures (700, 800, and 900 ˚C) for 1 h in a flow of N_2 at 1 L/min. Once cooled to ambient temperature, the carbonized product was treated with 1 M NaOH for 24 h under continuously stirred conditions at ambient temperature to remove the hard silica template. After that, the carbon product was separated via filtration, washed with deionized water until the pH become neutral, and finally dried in the oven at 100 ˚C to obtain the lignin-derived carbon materials. Thermogravimetric analysis (TGA) of the mesoporous carbon materials under oxygen flow showed only a residue of less than 3 wt %, indicating that the template was successfully removed. The ordered mesoporous carbons prepared using the MCF template under various conditions were denoted MCx-y-z and those prepared from the PQ silica template as MCPQ x-y-z, where x, y, and z represent the type of template, carbonization temperature, and the silica template/lignin ratio by mass, respectively. Table 3.1 summarises the variation in preparation conditions examined.

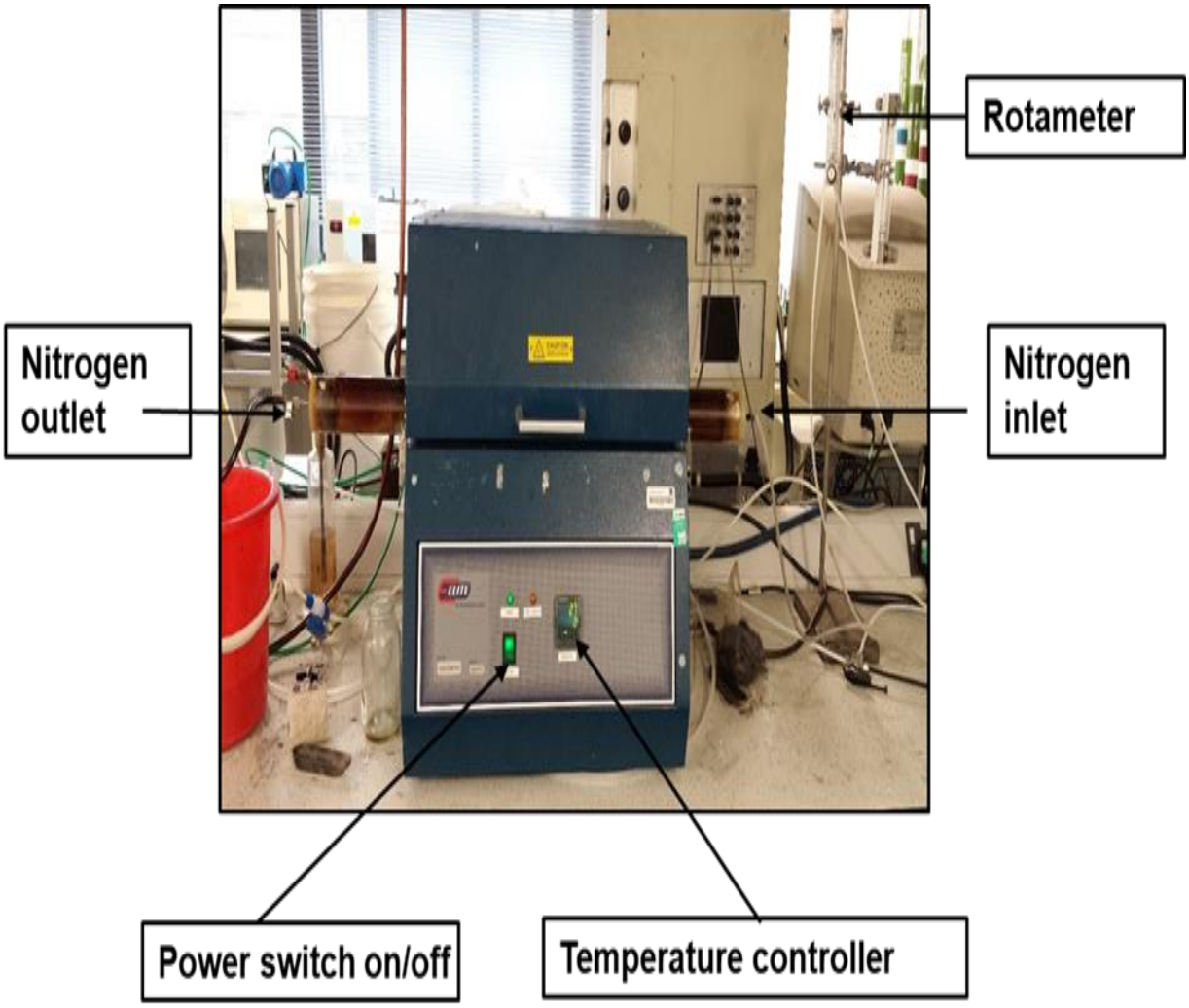

Figure 3.1 Horizontal Tube Furnace

Table 3.1 Synthesis conditions used for different lignin-derived mesoporous carbon materials using MCF and PQ silica templates

Sample	Mesoporous Silica	Carbonization temperature, ˚C	Mesoporous silica: lignin mass ratio
MC1-700-2	MCF1	700	1:2
MC1-800-2	MCF1	800	1:2
MC1-900-2	MCF1	900	1:2
MC1-800-1	MCF1	800	1:1
MC1-800-3	MCF1	800	1:3
MC2-800-0.5	MCF2	800	1:0.5
MC2-800-1	MCF2	800	1:1
MC2-700-2	MCF2	700	1:2
MC2-800-2	MCF2	800	1:2
MC2-900-2	MCF2	900	1:2
MC2-800-3	MCF2	800	1:3
MCPQ-700-2	PQ silica	700	1:2
MCPQ-800-2	PQ silica	800	1:2
MCPQ-900-2	PQ silica	900	1:2

3.1.5 Preparation of lignin-based mesoporous carbons using SBA-15 as the hard template.

The overall synthesis procedure is very similar to that applied for the preparation of ordered mesoporous carbons using lignin as the carbon source and MCF silica as a template (section 3.1.3). The ordered mesoporous carbons prepared under different conditions were denoted C/SBA-15-a-b-c, where a, b, and c represent the mesoporous silica, carbonization temperature, and mesoporous silica to lignin mass ratio, respectively. The variation in preparation conditions is shown in Table 3.2.

Table 3.2 Synthesis conditions used for lignin-derived mesoporous carbons using SBA-15 silica template

Sample	Carbonization temperature, (˚C)	Mesoporous silica: lignin mass ratio
CSBA-15-700-0.5	700	1:0.5
CSBA-15-700-1	700	1:1
CSBA-15-700-2	700	1:2
CSBA-15-700-2.5	700	1:2.5
CSBA-15-700-3	700	1:3
CSBA-15-800-1	800	1:1
CSBA-15-900-1	900	1:1

3.1.6 Preparation of chitosan-derived mesoporous carbons

The chitosan-derived mesoporous carbons (CMC1 and CMC2 samples) were synthesized by a hard-template approach based on the method reported by Kumar and co-workers (Kumar et al., 2020). In a typical procedure, 2.0 g of chitosan was dissolved in 1 wt% of acetic acid solution (80 mL) with continuous stirring for 24 h at room temperature. 1.0 g of mesoporous silica (MCF1 and MCF2) was dispersed into 20 mL of distilled water with vigorous stirring using a magnetic stirrer to create a homogenous dispersion. The mesoporous silica dispersion was added to the chitosan solution with stirring, and then the mixture was further stirred for 6h and allowed to dry at a temperature of 50 ˚C to form a semi-transparent film. The films were carbonized at different temperatures (700 ˚C, 800 ˚C, and 900 ˚C) for 1 h in Nitrogen at 1 L/min. Then the carbonized product was treated with 1 M NaOH aqueous solution for 24 h at room temperature to etch the silica template. Afterward, the carbon product was filtered, washed with distilled water until the pH was neutral, and dried overnight in an oven at 100 ˚C. Finally, the black carbon powders were obtained. Thus, the effect of

preparation parameters on the surface textural properties of the mesoporous carbon materials was investigated, including the mesoporous silica template/chitosan ratio and carbonization temperature. The chitosan-derived mesoporous carbons prepared under different conditions were denoted CMC-x-y-z, where x, y, and z represent the mesoporous silica template, carbonization temperature, and silica-to-chitosan mass ratio, respectively. The variation in preparation conditions is shown in Table 3.3.

Table 3.3 Synthesis conditions used for different chitosan-derived mesoporous carbon materials.

Sample	Mesoporous Silica	Carbonization temperature (˚C)	Mesoporous silica:lignin mass ratio
CMC1-700-1	MCF1	700	1:1
CMC1-800-1	MCF1	800	1:1
CMC1-900-1	MCF1	900	1:1
CMC2-700-0.5	MCF2	700	1:0.5
CMC2-700-1	MCF2	700	1:1
CMC2-700-1.5	MCF2	700	1:1.5
CMC2-700-2	MCF2	700	1:2
CMC2-700-3	MCF2	700	1:3
CMC2-800-0.5	MCF2	800	1:0.5
CMC2-800-1	MCF2	800	1:1
CMC2-800-1:5	MCF2	800	1:5
CMC2-800-2	MCF2	800	1:2
CMC2-800-2.5	MCF2	800	1:2.5
CMC2-800-3	MCF2	800	1:3
CMC2-900-1	MCF2	900	1:1

3.2 Preparation of Mesoporous Carbons and their supported polyethylenimine (PEI) sorbent materials for CO_2 capture

The overall synthesis procedure is very similar to that of preparing ordered mesoporous carbons using lignin as the carbon source and MCF and PQ silica as the templates (section 3.1.3). The MCs produced from the various MCF2 were denoted as MC-n-m, where n represents the carbonization temperature, and m is the mass ratio. In contrast, the mesoporous carbon prepared from PQ-silica was denoted MCPQ-n-m respectively. The variation in preparation conditions is shown in Table 3.4.

Table 3.4 Summary of synthesis conditions used for different ordered mesoporous carbon materials

Sample	Mesoporous Silica	Carbonization temperature, (˚C)	Mesoporous silica:lignin mass ratio
MC2-700-1	MCF2	700	1:1
MC2-800-1	MCF2	800	1:1
MC2-700-2	MCF2	700	1:2
MC2-800-2	MCF2	800	1:2
MC2-900-2	MCF2	900	1:2
MCPQ-700-1	PQ-Silica	700	1:1
MCPQ-800-1	PQ-Silica	800	1:1
MCPQ-700-2	PQ-Silica	700	1:2
MCPQ-800-2	PQ-Silica	800	1:2
MCPQ-900-2	PQ-Silica	900	1:2

The mesoporous carbon-supported polyamine adsorbents for CO adsorption were prepared using a wet impregnation method according to the procedure reported by Sun and co-workers (Sun et al., 2018). In a typical preparation, a calculated amount

of polyethyleneimine (PEI) was dissolved in 10 mL of water with continuous stirring, and 0.2 g of the prepared lignin mesoporous carbon was gradually added to the aqueous amine solution. After being stirred overnight, the resultant slurry was dried at 40 ˚C in a vacuum oven for 24 h to produce the mesoporous carbon-supported PEI sorbent. The various PEI-impregnated mesoporous carbon materials were designated as MC-x or MCPQ-x, where x denotes the weight percentage of the PEI in the adsorbent.

3.3 Characterization of samples

3.3.1 BET measurements and surface textural properties

Gas adsorption measurement is a well-established technique used to characterize the textural properties of porous materials. The measurement of reversible physisorption of gas molecules on the solid surface is essential in determining the adsorption of gas as a function of pressure. Then, the textural properties such as BET surface area, pore volume, and pore size distribution can be calculated using different models.

3.3.1.1 General experimental information

The textural properties of all the samples were characterized using a Micrometrics ASAP 2420 apparatus. Prior to the analysis, the samples were degassed at 120 °C for 16 h. The specific surface area was calculated using the Brunauer-Emmette-Teller (BET) equation from the linear part of the BET plot (P/Po = 0.05 - 0.2). The pore size distributions (PSDs) are calculated using the Density Functional Theory (DFT) model. The pore size was determined from the adsorption branch, while the window size was calculated from the desorption branch using Barrett-Joyner-Halenda (BJH) method.

The total pore volume was determined at P/Po = 0.99 using the Density Functional Theory (DFT) model.

3.3.1.2 BET measurement and types of adsorption isotherms/ mechanisms

The pore size has a major effect on the interactions that occur during adsorption because the adsorption mechanism in different pores varies. For micropores (< 2 nm), the adsorption behavior is almost entirely controlled by the interactions between the gas molecules and the surface due to the presence of a very small pore width that restricts multiple gas particle's interactions with the pore walls. The filling of micropores is a continuous process and shows no phase transition. Narrow micropores of width < 0.7 nm fill at a low relative pressure ($p/p_o < 0.01$), with wider micropores fill at a higher relative pressure (p/p_o = 0.01-0.15) (Thommes and Cychosz, 2014). Adsorption in mesopores (2-50 nm) depends on both gas-gas interactions and gas-surface interactions. Mesopores have a significant influence that multilayer adsorption can occur on the surface, where the pore wall is covered by the multilayer adsorbed substance. The strength of the adsorbed multilayer depends not only on van der Waals interactions but also on the surface tension of the gas-surface interface (Thommes, 2004). For small mesopores, the adsorption behavior is similar to micropores, which are dominated by gas-surface interaction. However, as the mesopores thicken and widen, the adsorption potential becomes less significant, whereas the effect of surface tension plays a major role. Eventually, the adsorbed multilayer builds up to a certain critical thickness denoted as t_c and remains unstable. At this point, the gas condenses into a liquid-like phase in the core of the pore at a pressure (p) less than the saturation pressure (p_o) of the gas. This phenomenon is known as capillary (pore) condensation, and it is controlled by intermolecular forces in the gas molecules (Thommes, 2010).

As for macropores (> 50nm), they are large enough to be considered transportation paths. Capillary condensation does not occur due to the abundance of space between the pore walls and the adsorbate that limits their interaction.

The adsorption isotherm of a porous material is expressed as the adsorbed amount as a function of the equilibrium gas pressure at a constant pressure. The adsorption isotherms produced from materials with different porous structures exhibit different shapes, and six general types have been defined, as shown in Figure 3.2 (Sing *et al.* 1985). Type I isotherms are observed by materials such as activated carbon and zeolites with small external surfaces. A steep uptake occurs at low relative pressure (p/p_0 ~ 0.1) due to filling the micropore quickly, followed by a plateau at high relative pressures. Narrow micropores with a width < 1 nm lead to Type I(a), with broader micropores and possibly small mesopores (< 2.5 nm) lead to Type I(b). Type II isotherms are found in nonporous or macroporous materials, where N_2 molecules are adsorbed in unrestricted mono/multilayer. The transition point, marked as point B in Type II isotherms indicates the completion of monolayer coverage and the beginning of multilayer adsorption at high relative pressure. Type III isotherms are not very common and only occur when the adsorbent-adsorbate interaction is relatively weaker than the intermolecular forces of the adsorbate. In this case, there is no Point B, therefore no definitive point of monolayer formation. Type IV isotherms are commonly exhibited by porous materials with mesoporous and macroporous structures. In the case of Type IVa isotherm, the initial monolayer-multilayer adsorption on the sample has similar features to Type II isotherms. They are characterized by a hysteresis loop at a high relative pressure of about 0.4, which is associated with capillary condensation in large mesopores. Type IVb isotherms are found in conical and cynical mesopores, with the isotherm completely reversible (Ball and Evans, 1989). Type V isotherms are

similar to Type III, and this also corresponds to cases of weak adsorbent-adsorbate interactions. Type VI isotherms represent the stepwise layer-by-layer adsorption on a highly uniform nonporous surface, for example, the adsorption of krypton on carbon black (graphitized at 2727 ℃).

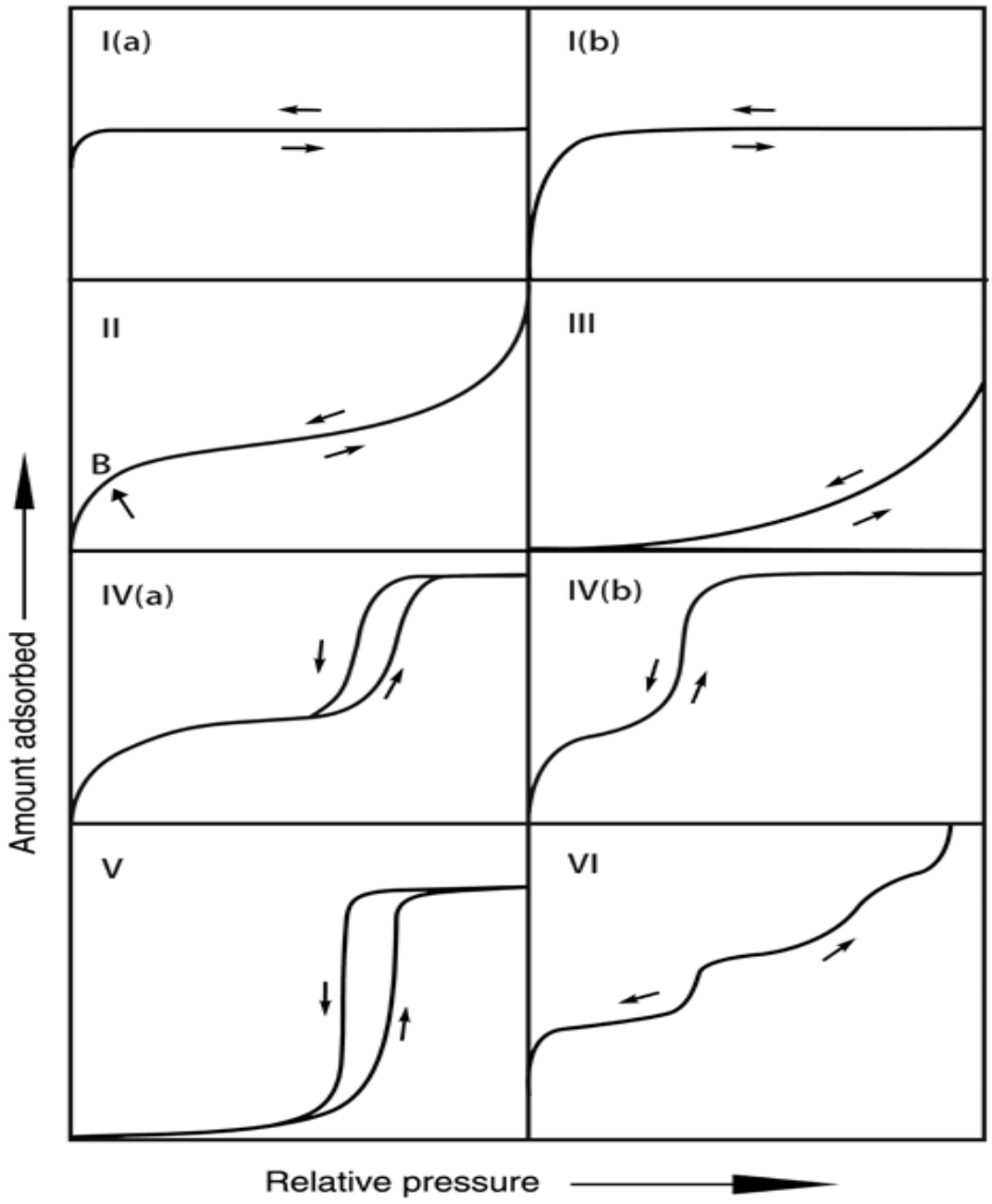

Figure 3.2 Six types of adsorption isotherms (Thommes et al., 2015)

Considering the occurrence of the capillary (pore) condensation in mesopores, the desorption branch will be entirely different from the adsorption path, leading to the formation of a hysteresis loop as seen in type IV and V isotherms. An empirical classification of the hysteresis loop into four groups (types H1-H4) was given by Sing et al. (1985), as illustrated in Figure 3.3. Type H1 loop is found in porous materials exhibiting a uniform distribution of cylindrical and spherical narrow mesopores, for instance, ordered mesoporous silicas (MCF, SBA-15), pore glasses, and mesoporous carbons. The steep, narrow shape of the adsorption branch indicates delayed condensation. The hysteresis loop of Type H2 represents materials (ink-bootle pores) containing more complex pore networks with interconnected narrow pores. The steep desorption step in the isotherm represents Type H2a, which can be attributed to factors such as pore blocking or percolation in a narrow neck size distribution versus the pore size distribution. It is associated with ordered mesoporous materials and silica gels. Type H2b occurs when the neck size distribution is wider than the pore cavity size distribution. Materials that exhibit the H3 hysteresis are observed in slit-shaped porous materials, giving rise to slit shape pores. These materials do not have an adsorption limit at high relative pressure. Loop of Type H4 exhibits the characteristic features of microporous materials associated with narrow slit-like pores. The type H5 hysteresis loop is very rare and has a unique form that makes it peculiar to certain pore structures containing opened and partly blocked mesopores (e.g Hexagonal silica).

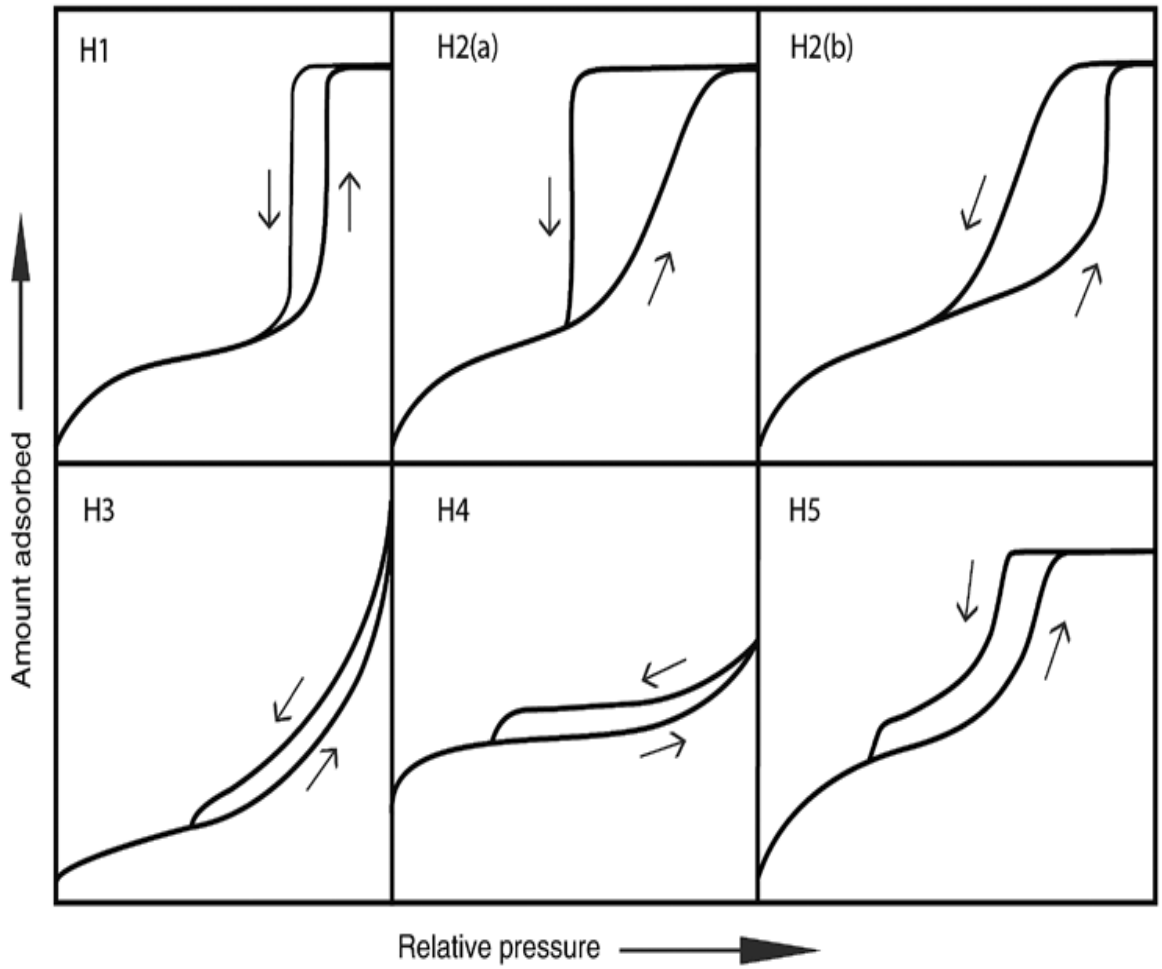

Figure 3.3 The hysteresis loops of adsorption isotherms (Thommes et al., 2015)

3.3.1.3 Determination of BET surface area

The Brunauer-Emmett- Teller (BET) method is the most widely used to determine the specific surface area of solid materials (Brunauer et al. 1938). The BET model extends to the possibility of multilayer adsorption (Type Ⅱ, Ⅳ, and VI isotherms) compared to the Langmuir model, which is limited to monolayer adsorption (Type Ⅰ isotherm). The BET theory assumes the following:

1. The adsorption sites are homogenous and independent of adsorption energy.

2. Gas molecules are not limited to monolayer adsorption but lead to multilayer formation, interacting only in the vertical direction.

3. Lateral interaction between adsorbate molecules is negligible.

4. The equilibrium with the vapor phase occurs in the uppermost layer, and at saturation pressure of 1, the layer number becomes infinite.

5. The heat of adsorption of each layer is equal to the liquefaction energy of the materials except for the first layer.

Thus the BET equation is described as, Equation 3.1

$$\frac{p/p_0}{n_a(1-\frac{p}{p_0})} = \frac{1}{n_m C} + \frac{C-1}{n_m C}\frac{p}{p_0} \qquad 3.1$$

Where p/p_o = (p and p_o are the actual and saturated vapor pressure of the adsorbate, respectively), n_a is the amount of gas adsorbed by unit mass of adsorbent, c is an empirical constant, and n_m is the monolayer capacity. Using the multipoint method, a plot of p/p_0 / $n_a(1 – p/p_0)$ on the x-axis versus p/p_0 on the y-axis produces a straight line in the partial pressure range of 0.05 to 0.35. The BET surface area is then determined by using Equation 3.2

$$S_{BET} = \frac{n_m}{M} N_A б \qquad 3.2$$

Where S_{BET} is the specific surface area, M is the nitrogen molar mass, N_A is the Avogadro number (6.02×10^{23}), and б is the cross-sectional area occupied by each molecule.

3.3.1.4 Total pore volume

The total pore volume (V_p) can be calculated from the amount of gas adsorbed at a relative pressure of 1, where the pores are then fully occupied with a liquid adsorbate. So the total pore volume could be determined:

$$V_p = \frac{P_a V_{ads} V_m}{RT} \qquad 3.3$$

In Equation 3.3, P_a is the ambient pressure, Vads is the volume of N_2 adsorbed, Vm is the molar volume of the liquid nitrogen (34.7 cm^3/mol), R is the universal gas constant, and T is the ambient temperature.

3.3.1.5 Pore size and pore size distribution

The pore size distribution can be determined on the physisorption equilibrium isotherms by using the appropriate model applicable to the shape and structure of the pores. Among the commonly used methods are the Barrett-Joyner-Halenda (BJH) and density functional theory (DFT). The Barrett-Joyner-Halenda (BJH) method can be used to calculate the mesopore size. It is based on the Kelvin equation, which considers the relationship between the pressure of when the gas will condense or evaporate in a cylindrical pore geometry with its radius. It is given as follows;

$$r_k = \frac{-2\gamma V_m}{RT} \, In \, \frac{P}{Po} \qquad 3.4$$

Where r_k is the kelvin radius of the pore, Υ is the surface tension, Vm is the molar volume of the liquid nitrogen (34.7 cm^3/mol), R is the universal gas constant (8.314 × 10^7 ergs/deg/mol), and T is the temperature. p/p_o is the relative pressure.

BJH, thus, is based on the assumption that the shape of the pore is cylindrical and that the adsorbed amount of gas and adsorbed phases occur via both physical adsorptions on the pore walls and capillary condensation in mesopores (Barrette et

al., 1951). The BJH method calculates the change in the thickness of the physically adsorbed layer of N_2 molecules from the decrease of p/po in the desorption curve. It can be expressed in Equation 3.5;

$$V_{pm} = \frac{r_{pm}^2}{(r_{km} + \Delta t_n)^2} * \Delta V_n - \frac{r_{pm}^2}{(r_{km} + \Delta t_n)^2} * \Delta t_n * \sum_{j-1}^{n-1} \frac{r_{pj} - t_j}{r_{pj}} A_{pj} \qquad 3.5$$

Where V_{pm} is the pore volume, r_{pm} is the radius of the pore, r_{km} is the inner capillary radius, Δt_n is the reduction in thickness of the adsorbed layer of nitrogen in the desorption branch, ΔV_n is the desorption volume of the adsorbed layer of nitrogen, t_j is the thickness of the adsorbed layer of nitrogen, A_p is the area of the pore.

The BJH method fails to describe the micropore diameter because the multilayer thickness correction on the Kelvin equation depends largely on pore diameter, temperature, and pressure (Sing, 2001) and the related kelvin equation. In addition, it was found that due to the hypothesis of BJH, the method could underestimate the pore size of narrow mesopores by 20-30% (Ojeda et al., 2003; Lowell et al., 2004).

Compared to BJH, the density functional theory (DFT) is based on the principles of statistical mechanics, which yield the thermodynamics and density properties of confined fluids and describe details on the distribution of adsorbed molecules on a molecular level. The DFT method captures the essential characteristics of both micropore filling and the mechanism of capillary condensation and hysteresis, and so provides a more accurate assessment of pore size distribution in the complete range from micropores to mesopores. The calculation of the pore size distribution function f(W) is based on the generalized adsorption isotherm (GAI) equation (Bardestani et al., 2019) and is expressed as follows;

$$N_{exp}\left(\frac{P}{P_o}\right) = \int_{W_{min}}^{W_{max}} N\left(\frac{P}{P_o}, W\right) f(W) dW \qquad 3.6$$

Where $N_{exp}\left(\frac{P}{P_o}\right)$ is the experimental adsorption isotherm, $N_{exp}\left(\frac{P}{P_o}, W\right)$ is the kernel of the theoretical adsorption or desorption isotherms, W_{max} and W_{min} are the maximum and minimum pore width, respectively.

3.3.2 Thermogravimetric Analysis (TGA)

Thermogravimetric analysis is a method of thermal analysis that measures the amount of change in the weight of a sample as a function of temperature or time in a specified atmosphere. Other characteristics of samples that can be examined using the TGA include thermal stability, CO_2 adsorption-desorption behavior, moisture, and volatile content. A well-equipped thermogravimetric analyzer (Q500 TGA) with an operating temperature in the range from ambient to 1000 ℃ and isothermal temperature accuracy of ±1 ℃, as shown in Figure 3.4, was used to determine the CO_2 adsorption performance of the samples.

3.3.2.1 CO_2 adsorption

The CO_2 adsorption performance of all the samples under anhydrous conditions was determined using a thermogravimetric analyzer (TGA Q500 instrument) in a gas mixture consisting of 15 % CO_2 in N_2. In a typical adsorption procedure, about 25 mg of the sample was placed in a small platinum sample pan, heated to 110 ˚C in the N_2 atmosphere at a flow rate of 100 mL $min^{-1,}$ and held at 110 ˚C for about 30 min to remove any moisture and pre-adsorbed gases. The sample was then allowed to cool down, the temperature was lowered to the adsorption temperature of 75, 80, 85, and 90 ˚C, and the gas was switched to 15 % CO_2 in N_2 at a flow rate of 100 mL min^{-1} and held for 60 min to carry out adsorption. The CO_2 adsorption capacity of the sample in mmol g^{-1} was determined from the weight gain by the sample during the adsorption

process. An empty platinum pan was used as a blank correction under identical conditions.

Cyclic adsorption-desorption testing was also performed. In each cyclic test, the sample was first allowed to reach adsorption temperature at 75 ˚C in the simulated flue gas (15% CO_2/85% N_2) for 10 min for the adsorption test, and then the temperature of the sample was heated up to 110 ˚C and kept at this temperature for 10 min to desorb the adsorbed CO_2, with the gas switched to N_2. The sample temperature is then allowed to cool down to 75 ˚C to begin another cyclic test. The CO_2 adsorption/desorption test was repeated for 50 cycles.

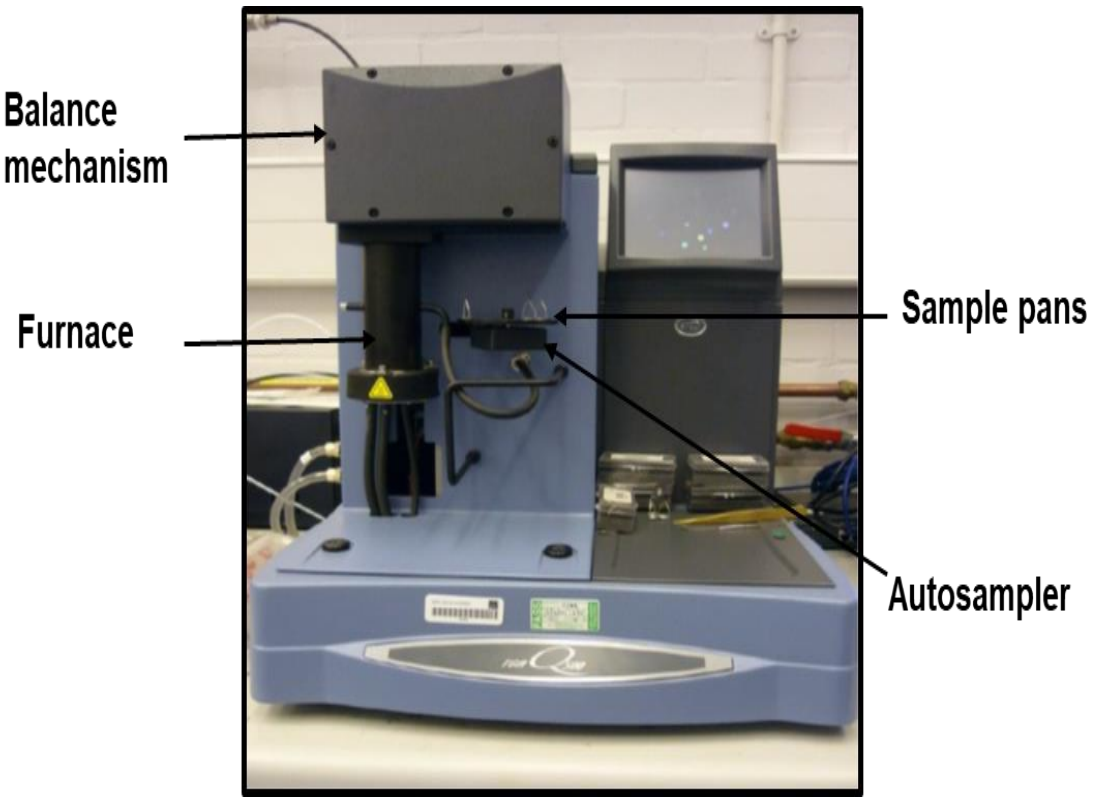

Figure 3.4 Thermogravimetric analyser (TGA Q-500)

3.3.2.2 Experimental error analysis

To ensure the accuracy and reliability of the results, some selected sample measurements were repeated three times, and the standard deviation of the results was evaluated using equation 3.7.

$$s = \sqrt{\frac{1}{n-1}} \sum_{i=1}^{n} (x_i + \dot{x})^2 \qquad 3.7$$

Where s is the standard deviation, n is the number of measurements for a given sample, xi is the result for a specific measurement and $\dot{x}$ is the mean of the results from different tests for a sample.

Repeatability of measurements

The repeatability of the prepared samples is a very important parameter to show the reliability of the measurement methods and the preparation methods. Considering the limited time on facilities, only selected were repeated for error analysis. In this PhD project, several types of instrument were used to characterize the prepared samples. Before use, all the instruments were calibrated following the standard procedure to avoid any systematic error. The textural properties of MCF1, MCF2, and PQ-silica were repeated three times, MC2-800-1 was repeated twice and CO_2 adsorption capacities of MC2-800-1-60-75 and MC2-800-1-60-85 were repeated three times, and the elemental analysis of all CMC1 and CMC2 samples were all repeated three times.

3.3.3 Morphology

Scanning electron microscopy (SEM) is a kind of electron microscope designed primarily to scan material surfaces. SEM works at very high magnification, typically in the range of 10-500,000x. This enables the characterization of organic and inorganic

materials at various length scales, from micro to nanoscale (Inkson, 2016). In SEM, a beam of electrons of high energy (1-30 keV) is emitted at the top of the microscope by an electron gun fitted with a tungsten filament cathode. The electron beam travels through the electromagnetic lenses and focuses highly on the samples. At each location, signals such as backscattered electrons and secondary electrons are emitted due to the interaction between the electron beam and the sample surface. Detectors collect these signals in series, which combine to form an SEM image. The secondary electrons are abundant with relatively low energy (10-50 keV). They can be used to show the morphology of the samples. In contrast, backscattered electrons are less abundant compared to secondary electrons but have higher energy and can be used for illustrating the difference between areas with different chemical compositions in multiphase samples (Goldstein et al., 2003).

Before the tests, the samples were coated with iridium coated to avoid electron charging, and blurred images and also to improve conductivity, and then fixed to conductive carbon tabs onto SEM sample holders for analysis to begin. The accelerating voltage for all images was operated at 15 kV. The morphology of the samples in this project was identified using a JEOL 7100F Field Emission Gun Scanning Electron Microscope (FEG-SEM) (JEOL USA, Inc).

A transmission electron microscope (TEM) was used to examine the internal structure of the mesoporous carbon samples. In TEM, high energy (typically 80-300keV) beam of electrons is transmitted via a thin sample of the specimen to form an image. Condenser lenses focus the electrons transmitted through the specimen in the column of the microscope into a beam of controlled convergence depending upon its thickness and electron transparency. The objective lens focuses on the transmitted part of the electrons to create an image. The magnified image can then be viewed through a

projector lens on a fluorescence screen coated with phosphor. The resolution of TEM may be limited by spherical aberration. However, modern TEMs fitted with additional lenses for an extra scan have been developed to correct spherical aberration and improve the spatial resolution of TEM down to < 0.05 nm (Brysdson, 2011; Emi, 2015). Prior to analysis, the samples were dry-deposited onto holey carbon film supports. The samples were analyzed using a JEOL 2100F FEGTEM operating at 200kV, equipped with a Gatan Orius camera and Gatan Digital Micrograph software. (EM Resolutions Ltd).

3.3.4 Elemental analysis

The chemical contents of the mesoporous carbon materials were determined by using the LECO CHN 628 series elemental analyzer to detect elements such as N, C, H, and S, as shown in Figure 3.5. The equipment utilizes a combustion procedure that results in a rapid analysis time of 5 to 6 minutes for all the elements obtained.

Figure 3.5 LECO CHN628 series elemental analyser.

Prior to the analysis, calibration tests were first conducted on the analyzer by carrying out several blanks and then followed by weighing approximately 75 mg of 2,5-(Bis(5-tert-buttyl-2-benzo-oxazol-2-yl) thiophene (BBOT). In a typical analysis, about 100 mg of each sample was weighed and encapsulated, then placed in the equipment's holder, and transferred to the purge chamber at the top of the furnace, removing all unwanted gases during the process. The sample is then introduced to the furnace under a pure oxygen atmosphere, resulting in rapid and complete combustion at a temperature of 1050 ℃. The three major elements C, N, and H present in the mesoporous carbon samples were completely oxidized to carbon dioxide (CO_2), NOx, and water (H_2O), respectively. Each sample was determined in triplicate with the average values reported in weight percentage.

3.3.5 X-ray photoelectron spectroscopy (XPS)

X-ray photoelectron spectroscopy (XPS) has been used extensively for the surface (1 nm to 10 nm) elemental composition analysis of materials, as well as the chemical state of the elements present (Van der Heide, 2014). Typically, in a vacuum, an X-ray having constant energy, Ehv, is irradiated to the sample's surface because of the photoelectric interaction between the highly energized X-rays and the solid sample. Photoelectrons with discrete kinetic energies will be ejected from the surface. Due to the balance between the kinetic energy of the photoelectrons and the constant energy, the binding energy of the electron could be calculated by the following equation (Konno, 2016; Hollander and Jolly, 1970)

$$Ehv = Ek + E\phi + EB \qquad 3.8$$

Where Ek represents the photoelectron kinetic energy, $E\phi$ is a small correction for solid effects (work function, etc.), and EB is the electron binding energy to the nucleus relative to the Fermi level. Identifying atoms/ions of a specific element in a sample (except for H_2 and He) is easy since the binding energies of the electrons in various electron orbitals are known. The photoelectron spectrum plots the number of electrons detected vs. binding energy (Van der Heide, 2011). The set of characteristic peaks in the XPS spectrum is utilized to identify chemical elements on the surface and their composition. In addition, since the same atom/ion can exist in a different chemical functional group with different binding energy, then the peaks of some elements, such as carbon and nitrogen, need to be deconvoluted into sub-peaks.

The as-prepared samples were analyzed using the Kratos AXIS ULTRA with a monochromatic Al kα X-ray source (1486.6eV) operated at 10 mA emission current and 12 kV anode potential (120 W.) Spectra were acquired with the Kratos VISION II software. A charge neutralizer filament was used to prevent surface charging. Hybrid–slot mode was used to measure a sample area of approximately 300 x 700 μm. The analysis chamber pressure was better than 5 x 10^{-9} mbar. Three areas per sample were analyzed. A wide scan was performed at low resolution (Binding energy range 1400 eV to -5 eV, with pass energy 80 eV, step 0.5 eV, sweep time 20 minutes). High-resolution spectra at pass energy 20 eV, a step of 0.1 eV, and sweep times of 10 minutes each was also acquired for photoelectron peaks from the detected elements, and these were used to model the chemical composition. The spectra were charge corrected to the C 1s peak set to 284.5 eV.

3.3.6 Fourier Transform Infrared (FTIR) Spectroscopy

Fourier Transform Infrared (FTIR) Spectroscopy is a technique used in determining an infrared spectrum of material, including their functional group, as well as possible molecular bonds between chemical compounds. The IR spectroscopy is applicable for collecting high-resolution data over a wide range. The FTIR spectrometer creates a beam of infrared radiation over a range of wavenumbers (4000-400 cm^{-1}) emitted from the blackbody source (Mohamed et al., 2017). The IR beam passes via an interferometer where the spectral coding occurs. The beam recombines in various path lengths in the interferometer to produce an interferogram. The resulting interferogram is then transferred from the sample surface, where specific energy frequencies are absorbed (Undavalli et al., 2021). Then the detector records the interferogram signal in energy as a function of time.

In this study, Fourier Transform Infrared (FT-IR) spectra of the samples were generated by a Bruker IFS66 with a Specac "Golden Gate" ATR attachment. The as-prepared sample of about 0.0015g was transferred to the FTIR analyzer to detect the presence and changes of specific functional groups of the samples. The FT-IR spectra were recorded by accumulating 8 scans per sample within the range of 5000 – 400 cm^{-1} at a spectral resolution of 8 cm^{-1}.

3.3.7 X-ray Diffraction (XRD)

The XRD is based on the interference of monochromatic X-rays produced by a cathode x-ray tube and a crystalline sample. The interference can be generated according to Bragg's law and expressed as;

$$n\lambda = 2d \sin \theta \qquad 3.9$$

Where n is an integer, λ is the wavelength of radiation (0.154 nm for Cu $K\alpha$), θ is

the angle between the incident radiation and the surface of the solid and *d* is the spacing between the layer of atoms.

In this work, a small angle X-ray diffraction pattern was recorded on a Bruker D8 Advance instrument, 0.5 g of the sample was placed into the holders and created a flat surface that does not rise above the level of the sample holder, and then placed into the machine. The sample was scanned in Bragg Brantano mode with dynamic beam optimization with a 10mm illumination length, and data were collected in the range of 2θ between 0.5 and 5 with the scan rate at 0.1 s.

Chapter 4 Synthesis and characterization of three-dimensional interconnected large-pore mesoporous cellular lignin carbon materials.

4.1 Introduction

Lignin is the third most abundant natural organic polymer next to cellulose and chitin, and isolated, lignin is readily available but underutilized as a significant by-product of chemical pulping and biofuel production (Zakzeski et al., 2010). The three phenylpropanoid monomers that combine to make up the structure of lignin polymers are coumaryl, coniferyl and sinapyl alcohol, as presented in Figure 4.1 (Harmsen et al., 2010).

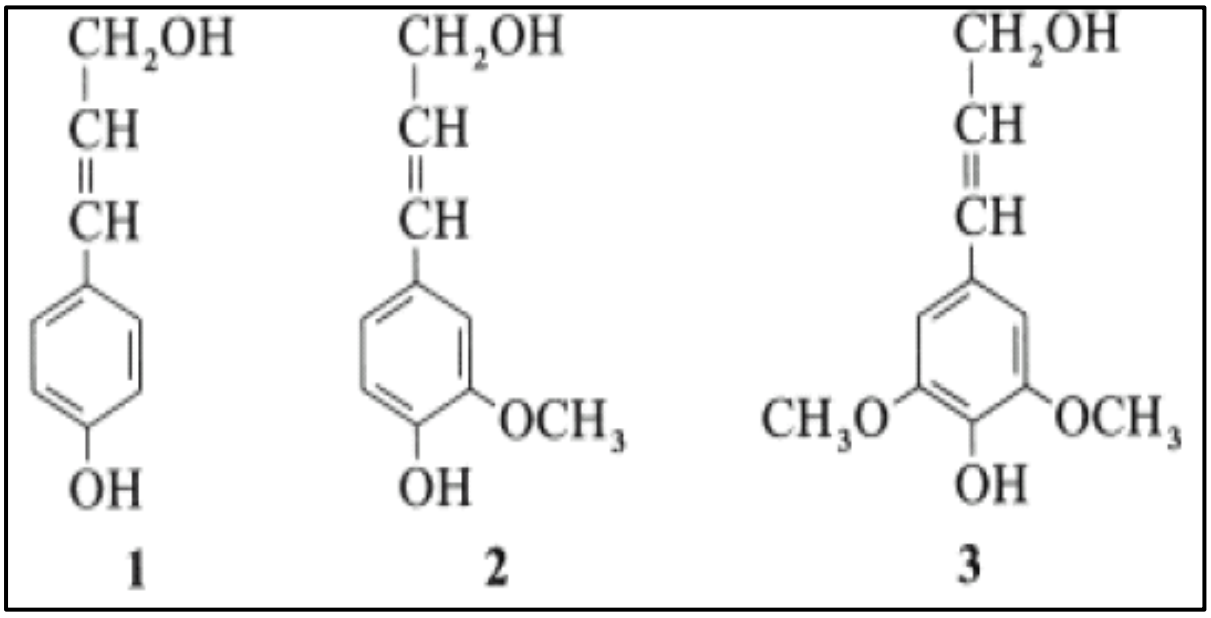

Figure 4.1 P-coumaryl, coniferyl and sinapyl alcohol major building blocks of lignin polymer (Harmsen *et al*., 2010).

Due to its heterogeneous aromatic structure, lignin has been successfully employed to prepare activated carbons (Chatterjee et al., 2014; Carrott et al., 2008, Carrott et al., 2007; Hayashi et al., 2002) and carbon fibers (Luo et al., 2011; Baker et al., 2012). However, the use of lignin as a low-cost renewable carbon precursor for preparing advanced spherical mesoporous carbon materials remained underdeveloped, perhaps due to its heterogeneous molecular structure, functionality, and hyperbranched structure (Fierro et al., 2013, Zhou et al., 2021a). There are a few studies so far on using lignin as raw material for preparing ordered mesoporous carbons, with both hard and soft templates having been examined. Wang et al. (2020) prepared OMCs from alkali lignin using both evaporation-induced and salt-induced self-assembly approaches, and the prepared carbons exhibited an ordered 2D hexagonal mesoporous structure, which had surface areas in the range of 345 – 598 m^2/g with an average pore size of 3.4 nm and mesopore volume of 0.025 – 0.140 cm^3/g. Song et al. (2017) synthesized lignin-based mesostructured carbons using nano-sized MgO and Pluronic F123 as the templates. The prepared mesoporous carbons had a large average pore size of 9 nm with mesopore volumes of up to 0.71 cm^3/g depending on the preparation conditions. Besides, formaldehyde was usually needed to prepare lignin-derived mesoporous carbons as a cross-linking agent. Saha et al. (2013 and 2014) reported the synthesis of lignin-derived mesoporous carbon materials by using formaldehyde as a cross-linking agent and F127 as a sacrificial template in a surfactant-templated approach. The prepared activated carbons using physical and chemical activation methods and their combinations were found to have mesopore volumes of 0.11-0.34 cm^3/g and pore sizes in the range of 2.5-12 nm. It appears that despite the success of the preparation of lignin-based microporous carbon materials with surface areas of up to 3000 m^2/g (Hayashi et al., 2000; Correa

et al., 2017), the preparation of lignin-derived large-pore mesoporous carbon materials still remains a challenge, and the mesostructured lignin carbons reported so far usually had wide pore size distributions, with mesopore volumes being rarely higher than 1.0 cm^3/g, which are much lower than those prepared using synthetic polymeric precursors (Wang et al., 2016; Lu et al., 2003; Szewczyk et al., 2020). Saha et al. (2013 and 2014) reported the synthesis of lignin-derived mesoporous carbon by using formaldehyde as a cross-linking agent and F127 as a sacrificial template. The prepared carbons exhibit a mesopore volume of 0.11-0.34 cm^3/g and a pore size of 2.5-12 nm.

4.2 Results and discussion

4.2.1 Structural characterization and morphology of mesoporous silica templates.

Three mesoporous silica materials were examined as the hard templates for preparing the mesoporous lignin carbon materials, including two 3D interconnected mesocellular foam silicas (MCF1, MCF2) and one commercially available 2D mesoporous silica (PQ silica). The Nitrogen adsorption-desorption isotherms and the pore size distributions of all the mesoporous silica templates are shown in Figures 4.2a and b. Obviously, all the mesoporous silica templates represented type IV(a) isotherm with hysteresis loop of type H1 at high relative pressures (> 0.8), indicating relatively high pore size uniformity and mesoporous characteristics with large pore size existing in the silica templates. It can be found that the hysteresis of the MCF silica templates is much larger than that of the PD silica, which is consistent with the features of the 3D porous

network of an MCF material that comprises large pore cages interconnected by small

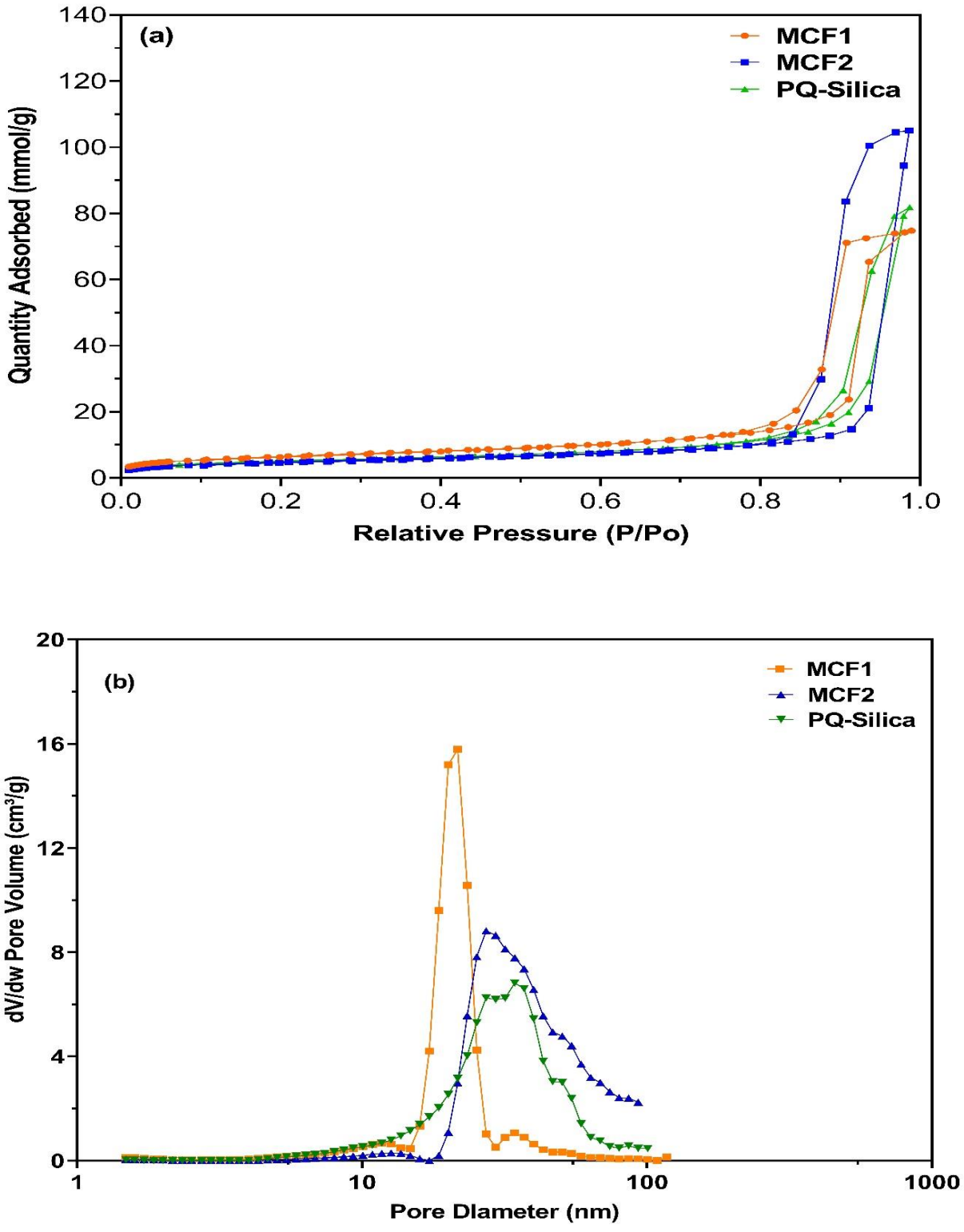

Figure 4.2 Nitrogen adsorption/desorption isotherms (a) and pore size distributions of silica templates (b).

windows. As shown in Figure 4.2b, the pore size distribution becomes narrow for MCF1, which gives better control in the mesoporous region. A sharp rise at the end of the nitrogen adsorption for MCF2 was observed, suggesting the presence of macropores in the sample. These macropores might be developed between numerous-sized particles of the sample (Kim et al., 2001a). However, the pore size distribution curve becomes wider for MCF-2, which appears to be dominantly macro-structured. This may be due to aging treatment at relatively high temperatures (120 ˚C), which partly breaks down the structure of the silica template. Moreover, it can be seen that MCF1 has a sharp peak with narrow pore size distribution centered at 20 nm, while commercial mesoporous PQ-silica and MCF-2 have broad pore size distributions with a peak centered at about 30 nm.

Table 4.1 summarizes the surface textural properties of different silica templates. The textural properties of the silica templates were repeated three times. For example, MCF1 gave the maximum and minimum difference of BET surface area of 9.5 m^2/g and total pore volume of 0.25 cm^3/g. MCF2 and PQ-silica had a difference of 5 m^2/g, 0.17 cm^3/g, and 12 m^2/g, 0.22 cm^3/g, respectively. The aging step appears to be essential for forming MCF materials with well-defined pores. It is apparent that the total pore volume, pore size, and window size increased significantly with increasing aging temperature. With aging at 100-120 ˚C, the pore size increases from 23.31 to 38.64 nm (~66 %), while the window size increases from 16.80 to 18.99 nm (~13 %). This implies that the degree of silica condensation that formed TMB/P123 droplets was remarkably enhanced due to the hydrolysis of TEOS at high aging temperatures and TMB concentrations, thus leading to the development of larger pores (Sun et al., 2018).

Table 4.1 Textural properties of the mesoporous silica templates

Hard templates	S_{BET} (m^2/g)	V_{total} (cm^3/g)	V_{meso} (cm^3/g)	V_{micro} (cm^3/g)	Pore size (nm)	Window size (nm)
MCF1	530±9.5	2.53±0.25	2.49±0.19	0.04±0.06	23.31±0.28	16.80±0.70
MCF2	387±5.0	3.58±0.17	2.76±0.23	0.04±0.08	38.64±0.22	18.99±0.24
PQ-silica	413±12.0	2.79±0.22	2.49±0.08	0.03±0.04	31.32±0.24	23.82±0.17

Values are presented as the means of triplicates with standard deviation (SD) of the mean.

The surface area of the MCF materials was found to depend upon the aging temperature, varying from 530 m^2/g for MCF-1 to 387 m^2/g for MCF-2 prepared with a TMB/P123 ratio of 2 at 100 ˚C and 120 ˚C respectively. As shown in Table 4.1, by increasing the aging temperature from 100 to 120 ˚C, the surface area of MCF1 and MCF2 was found to decrease as the pore volume increased. The reduced surface areas in these MCF materials were due to the enlarged window sizes. As the window sizes become larger, they take away a larger fraction of the cell's surface area (Schmidt-Winkel et al., 2000; Sridhar et al., 2014). In particular, MCF-2 aged at 120 ˚C with a TMB/P123 ratio of 2 was found to have the highest window size of 18.99 nm but with the lowest surface area of 387.45 m^2/g. Among all the mesoporous silica templates, MCF2 was found to have the highest pore volume of 3.58 cm^3/g and the largest average mesopore size of (38.64 nm), accordingly giving rise to the smallest surface area (387 m^2/g). In comparison, the MCF-1 and the 2D commercial PQ silica have the same mesopore volume (2.49 cm^3/g), but the commercial PQ silica has a larger average pore size and broader pore size distribution centered at 30 nm in contrast to the narrower pore size distribution of MCF1 centered at 20 nm.

The morphological features of MCF1 and MCF2 are shown in Figure 4.3. Generally, the MCF silica exhibits spherical morphology with 3D-interconnected open polygonal

networks framed by silica struts. A slight morphological transformation can be detected for the MCF materials prepared at different aging temperatures. SEM images of MCF-1 prepared at an aging temperature of 100 ˚C displayed large, uniformed, and packed spherical particles, as seen in Figures 4.3a and b, whereas MCF-2 synthesized at an aging temperature of 120 ˚C transformed into larger and less packed spherical particles (Figure 4.3c and d).

MCF1 (a and b)

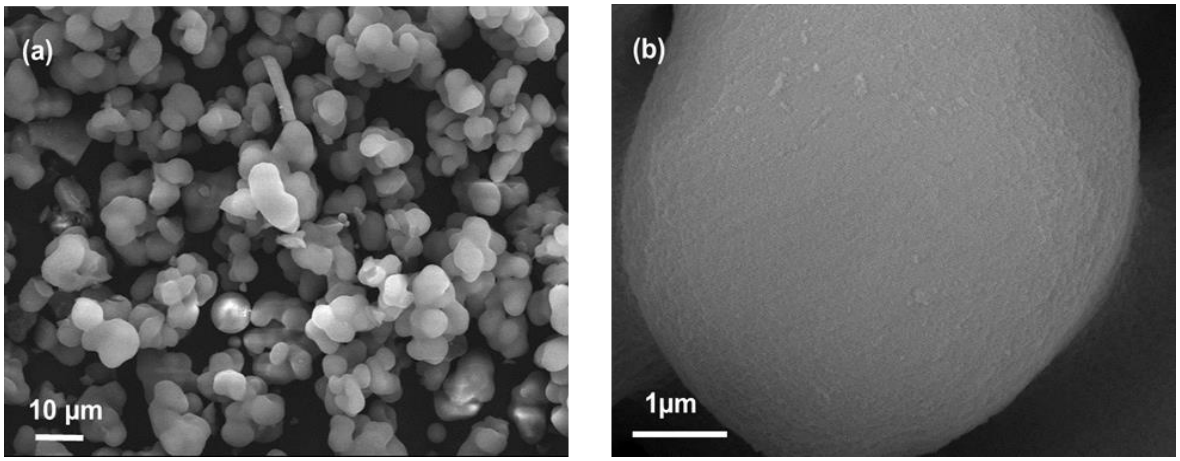

MCF2 (c and d)

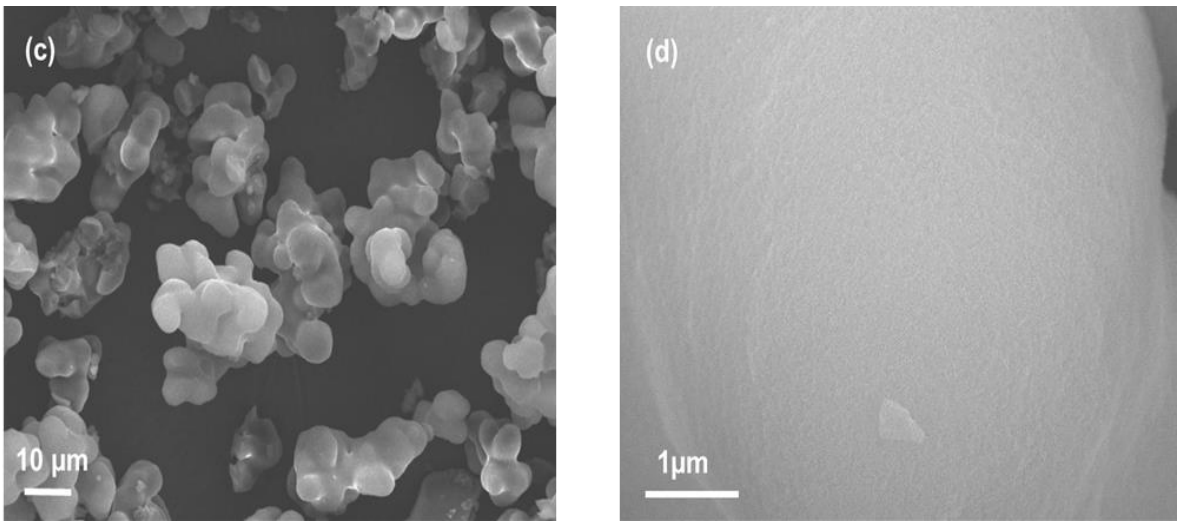

Figure 4.3 SEM images of MCF1 and MCF2 silica templates.

4.2.2 Surface textural property and morphology of lignin-derived mesoporous carbons

4.2.2.1 Effect of carbonization temperature

Figure 4.4 shows the nitrogen adsorption-desorption isotherms of the mesoporous carbons synthesized using MCF silica templates at carbonization temperatures varying from 700 to 900 ˚C at a selected silica-to-lignin ratio of 2 by mass. Both carbonization temperature and silica template played an important role in determining the porous structure of the final carbon products. It can be seen that all the synthesized hard-templated lignin-derived mesoporous carbon materials showed a typical type IV isotherm according to IUPAC classification (Thommes et al., 2015), with a sharp capillary condensation step at P/Po > 0.8. In addition, all the isotherms are highly characterized by the broad and relatively symmetrical large hysteresis loop of H2b type across the relative pressure range of 0.45-1.0. This is indicative of the uniformity of the mesocellular pore network that is composed of ink-bottle-shaped mesopores interconnected by smaller pores or pore windows, which gives rise to kinetic restrictions of N_2 flow within a porous network. Desorption occurs via pore-blocking controlled evaporation, indicating the neck size of the mesoporous carbons synthesized in this research was larger than the critical neck width of 5-6 nm (Sotomayor and Thommes, 2018). The presence of micropores in the mesostructured lignin carbons is negligible, given the relatively very small amount of N_2 adsorbed at low relative pressures. The results also suggest that the effect of carbonization temperature varied for the two MCF templates. For the MC1 series (Figure 4.4a), an increase in the carbonization temperature from 700 to 900 °C led to a steady decrease in the amount of N_2 adsorbed with the hysteresis loop becoming narrower and shifted towards higher relative pressures, indicating a reduction in pore volume but with an

increase in pore size. However, carbonization temperature appears to have a negligible effect on the overall porosity of the MC2 carbons prepared using the MCF2 template with a much larger mesopore volume (Table 4.1), although the hysteresis loop also became narrower with increasing temperature. Nevertheless, a small amount of microporosity in both the MC1 and MC2 carbons was found to further decrease with increasing carbonization temperature, as shown by the decreased amount of N_2 adsorbed at low relative pressures. The evolution of the isotherms with carbonization temperature suggests that the pore constriction diameter or window size of the three-dimensional interconnected mesoporous carbons increased disproportionately as the hard-templated carbon skeletal matrix became densified with increasing carbonization temperature due to shrinkage, which agrees well in general with previous findings (Pastor-Villegas et al., 1998; Fu et al., 2009, Chu et al., 2020; Lu et al., 2005).

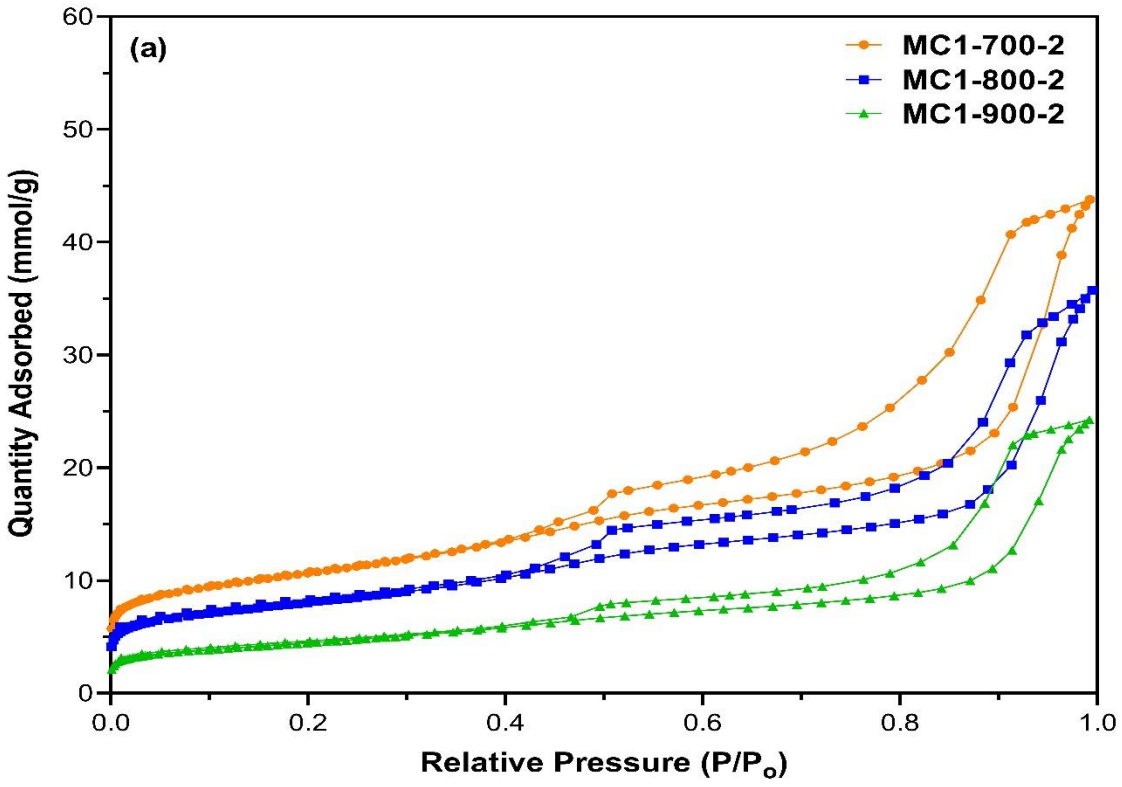

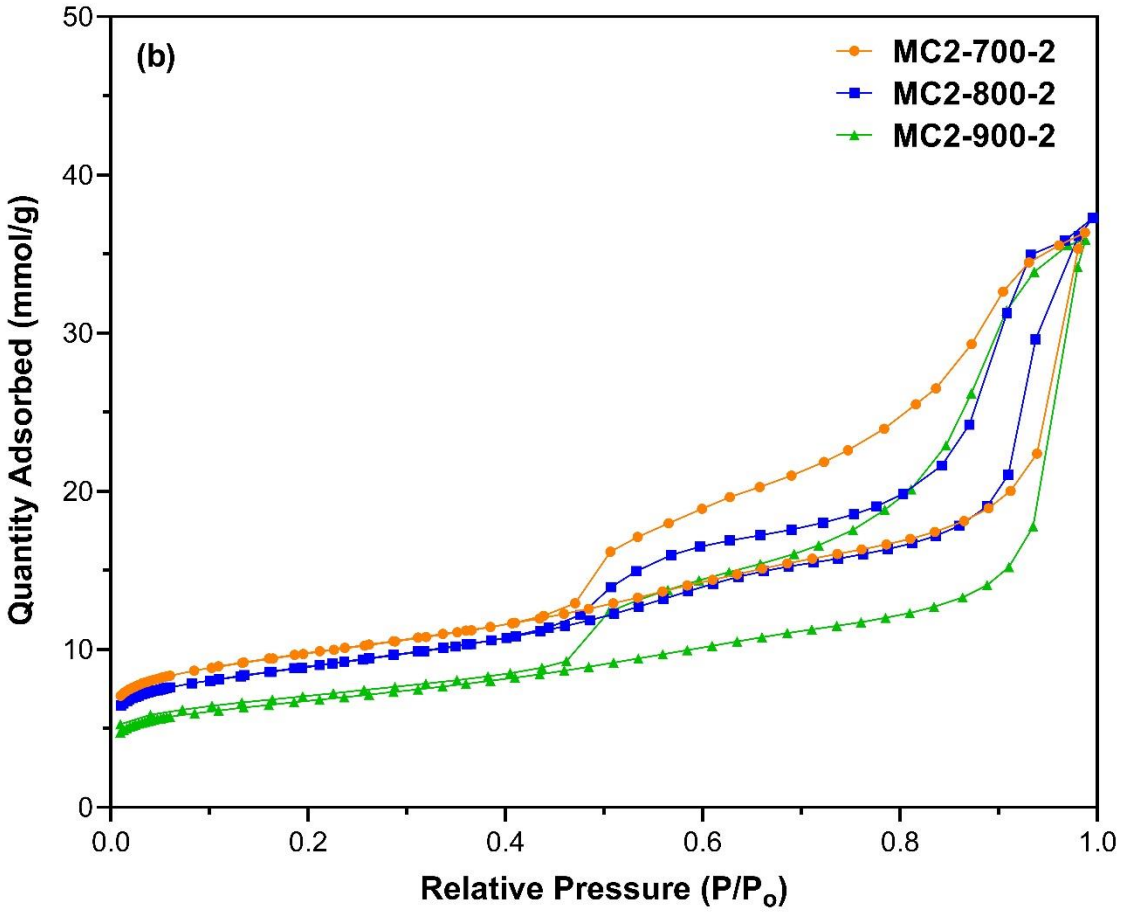

Figure 4.4 N_2 adsorption-desorption isotherms of (a) MC1 and (b) MC2 synthesized at different carbonization temperatures.

Table 4.2 shows the surface textural properties of the mesoporous carbon samples prepared at different temperatures. It is evident that both MC1 and MC2 carbon series prepared at different temperatures carbons are extremely mesoporous, with mesoporosity accounting for up to 90% of the total pore volume. The fabrication of ordered mesoporous carbons MC1 and MC2 based on silica templates MCF1 and MCF2, respectively, provides a series of samples with well-developed BET surface area (353-849 m^2/g), total pore volume (0.68-1.23 cm^3/g), and average pore size (9.59-14.14 nm), which outperforms many 'designer' mesoporous carbons prepared from using synthetic polymers with hard templates. In general, it was found that an

increase in carbonization temperature led to increased mesopore size but at the cost of surface area and pore volume, particularly the microporosity. The carbon MC2-900-2 prepared at 900 °C was found to have the largest average mesopore size of 14.1 nm with a surface area of 543 m^2/g, followed by MC1-900 with an average pore size of 11.2 nm and surface area of 353 m^2/g, respectively. In contrast, the carbons prepared at the lowest temperature of 700 ^oC were found to have the highest surface area but the smallest average pore size (9.6 ~ 10.4 nm). In general, all mesoporous carbons prepared using the MCF2 hard template, which had a larger mesopore size and pore volume, were found to have larger average pore sizes and mesopore volumes than the MCF1-templated carbons prepared in similar conditions. The increase in carbonization temperature may be attributed to the structural shrinkage of the residual carbon in the pores due to the breakdown of interlayer carbon-oxygen bonds (Pastor-Villegas et al., 1998; Fu et al., 2009) and the increasing weight loss of carbon residue, which might lead to the reduction of pore volume and surface area but the increase of pore size (Chu et al., 2020; Lu et al., 2005).

Table 4.2: Surface textural properties of MC1 and MC2 mesoporous carbons synthesized at different carbonization temperatures

Sample	S_{BET} (m^2/g)	V_{total} (cm^3/g)	V_{meso} (cm^3/g)	V_{micro} (cm^3/g)	Average pore size, (nm)
MC1-700-2	849	1.23	1.06	0.17	9.6
MC1-800-2	638	1.07	0.88	0.12	9.8
MC1-900-2	353	0.68	0.61	0.66	11.2
MC2-700-2	788	0.80	0.60	0.16	10.4
MC2-800-2	716	1.15	0.96	0.15	10.6
MC2-900-2	543	0.89	0.72	0.10	14.1

Figure 4.5 displays the pore size distribution (PSDs) of MC1 and MC2 carbons. All the carbon samples showed a bimodal mesoporous structure heavily dominated by the large mesopores centered at 20-25 nm, followed by those with pore diameters in the range of 4-5 nm. The mesopores were believed to originate mainly from the removal of silica walls and the coalescence of the silica pores partially filled with the precursor when the silica walls were removed, respectively (Bohme et al., 2005; Lu et al., 2003, Fuertes and Nevskaia, 2003). Although the carbonization of precursors could usually generate a significant amount of microporosity in the mesoporous carbons synthesized with hard template methods (Janus et al., 2020; Klinthongchai et al., 2020; Vinu et al., 2007), the presence of microporosity is generally very negligible in the hard-templated lignin carbons, with the diameter of a detectable minor amount of micropores being centered at about 1.2 nm. With the increasing carbonization temperature from 700 to 900 °C, the pore shape in MC1 carbons (Figure 4.5a) remains the same, whereas the intensity of all pores, especially micropores and small mesopores decrease gradually. However, in the case of MC2 carbons prepared using MCF2 as a template (Figure 4.5b), at a carbonization temperature of 800 °C, the sample MC2-800-2 presents a sharp peak centered at 21 nm, indicating the existence of highly ordered mesoporosity with large pore size. In comparison to the MC1 series, at carbonization temperatures of 700 and 900 °C, the peak of the large mesopore shifted to a larger pore size region, and a relatively wider PSD was obtained for MC2-700-2 and MC2-900-2. Therefore, 800 °C was selected as the optimal temperature which ensures carbonization of the precursors and developed mesoporosity.

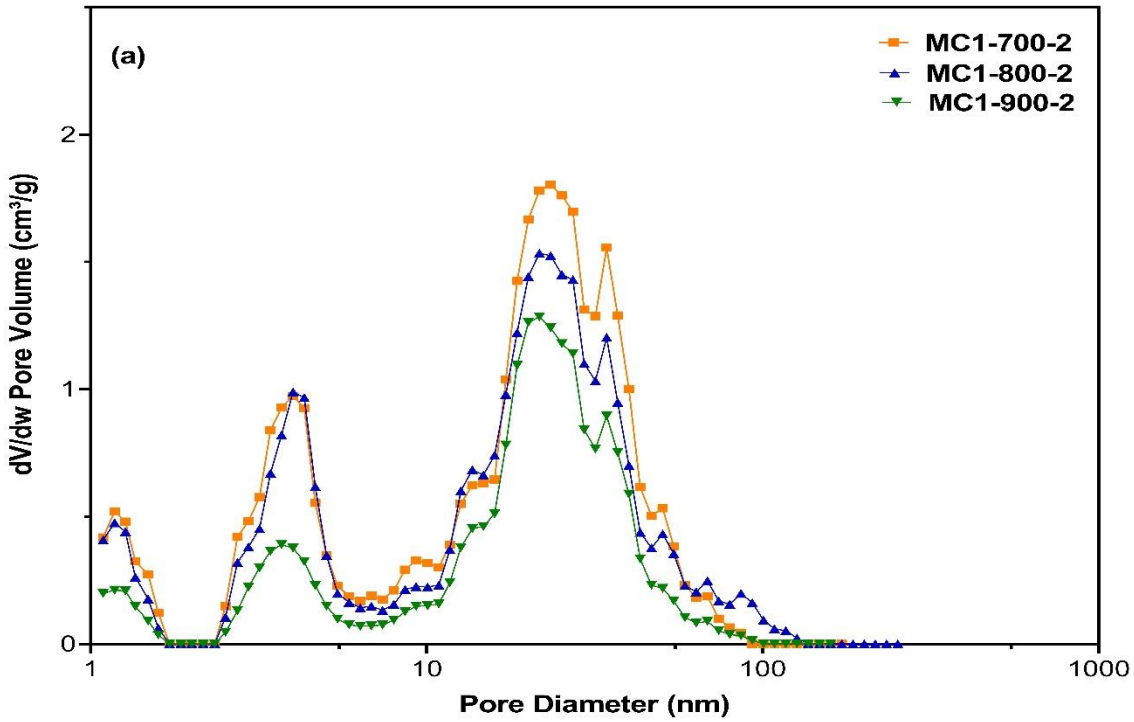

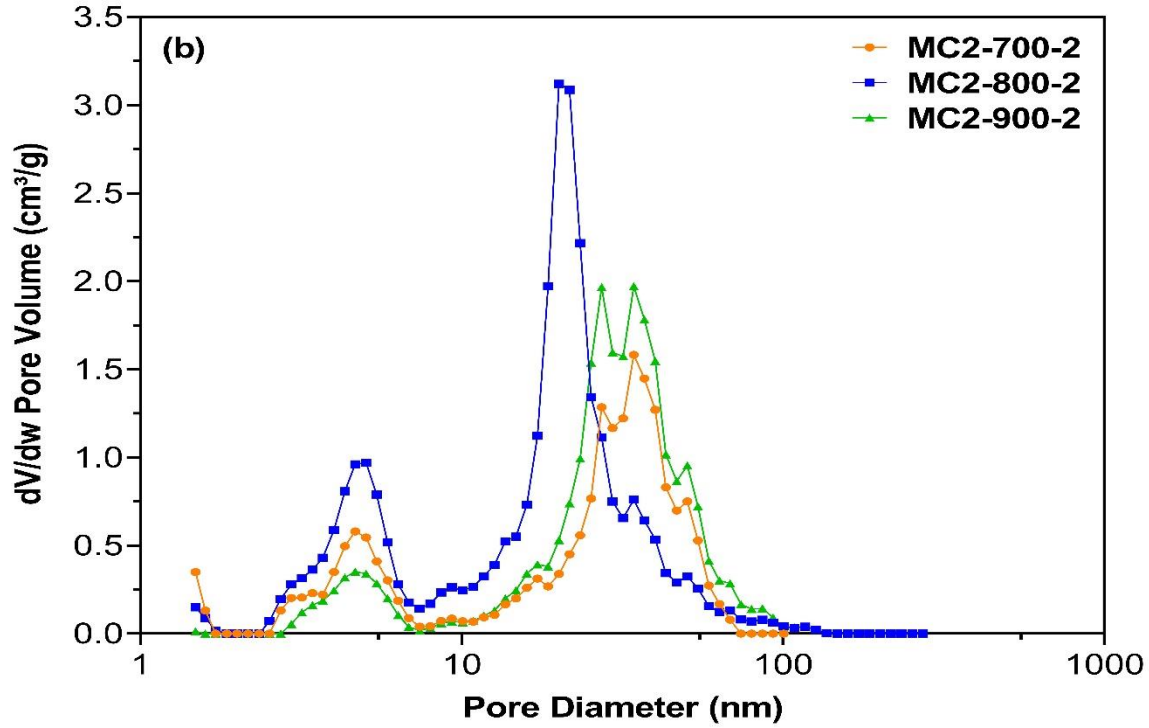

Figure 4.5 Pore size distributions of (a) MC1 and (b) MC2 carbon series synthesized at different carbonization temperatures.

4.2.2.2 Effect of lignin to silica mass ratio

The theoretical maximum loading of lignin, which has a density of 1.3 g/cm^3 (Gregorova et al., 2006), was determined by the pore volume of the templates, which were estimated at 3-4g of lignin per gram of the templating silicas used. To investigate the effect of various silica-to-lignin ratios on the final structure of the carbon samples, mesoporous carbons were prepared by varying silica-to-lignin ratios from as low as 0.5 to a maximum of 3 at a carbonization temperature of 800 °C. All the samples showed similar type IV(a) isotherms with the H2(b) hysteresis loops, as shown in Figure 4.6. As the lignin-to-silica ratio increased from 1 to 3, the amount of N_2 adsorbed decreased steadily due to the increased wall thickness of the resultant carbon networks with an increasing amount of lignin loaded into the templating silica pores.

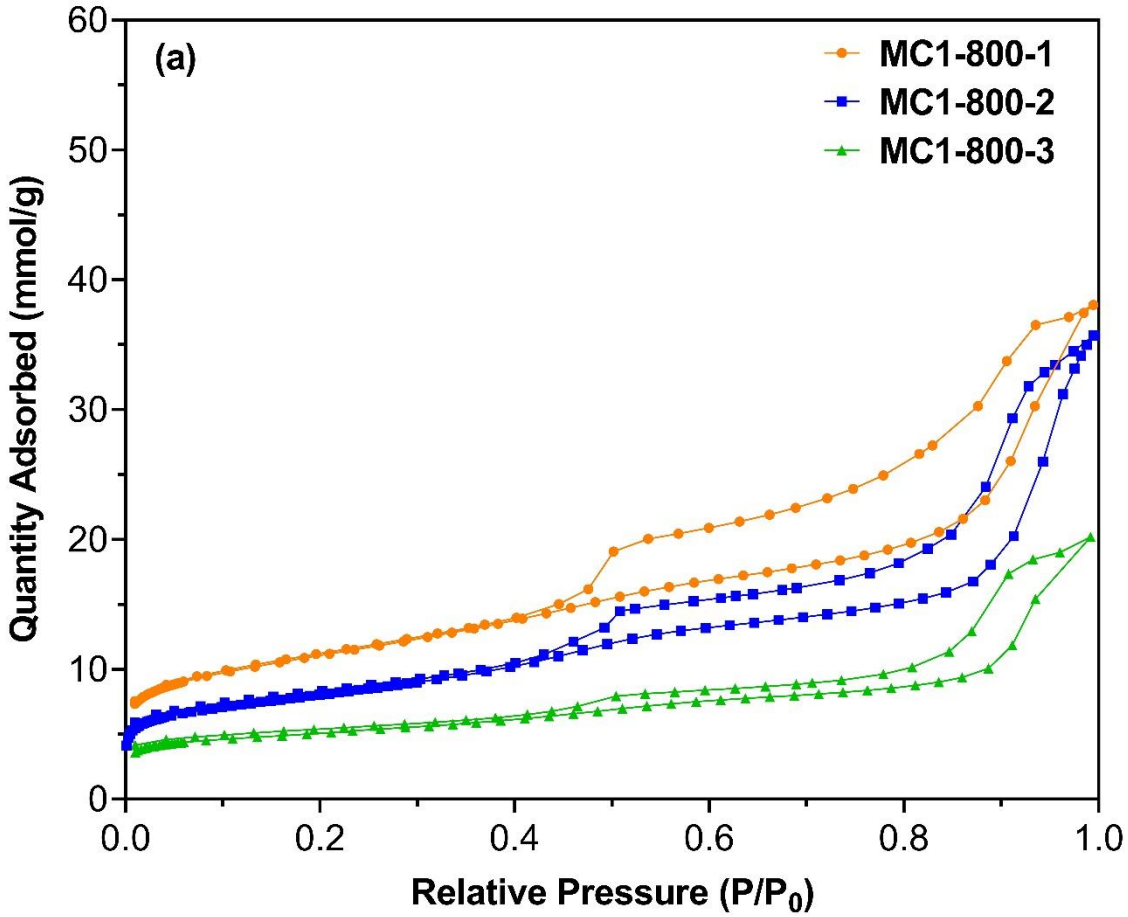

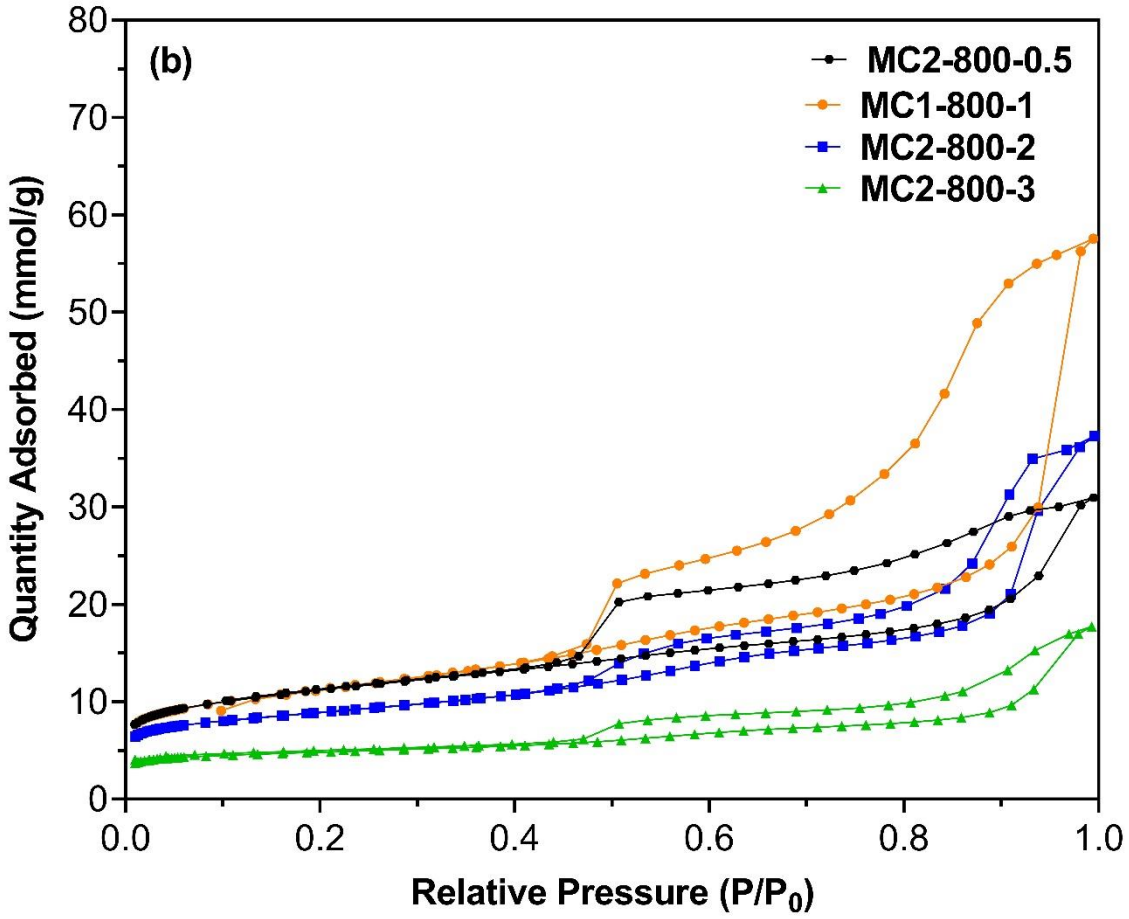

Figure 4.6 N_2 adsorption-desorption isotherms of MC1 (a) and MC2 (b) samples prepared using different lignin/template ratios by mass at a carbonization temperature of 800 ℃.

Table 4.3 indicates that the surface area and pore volume decreased significantly with increasing lignin/template mass ratio. For instance, as the lignin-to-silica ratio increased from 1 to 3, the surface area of the MCF2-templated mesoporous lignin carbons decreased by over 50% from 960 to 413 m^2/g while the pore volume decreased by 70% from 1.80 cm^3/g (MC2-800-1) to 0.50 cm^3/g, respectively. This is presumably due to the higher degree of pore filling of the hard templates with lignin at higher lignin-to-template ratios, which leads to increasingly tighter packing of lignin inside the porous networks of the templates and hence a lower amount of empty or

porosity produced upon the removal of the hard template. Meanwhile, the increased pore filling also produces higher compressive forces resulting from volatile release during carbonization, which may suppress the porosity development of the resultant carbons, particularly the micropores, due to secondary carbon formation from the volatiles ((Vinu et al., 2007). Similarly, when MCF1 and MCF2 were compared as the hard templates at the same lignin-to-silica ratio, it was found that the mesoporous lignin carbons (MC2 series) prepared from using MCF2, which has larger pore volume and diameter, were always found to have higher pore volumes and larger mesopore diameters than the MCF1-templated carbons, due to the lower degree of pore filling at the same lignin-to-template mass ratio. Amongst all the carbons prepared with different lignin/template ratios, the mesoporous carbon prepared from MCF2 with a lignin/silica ratio of 1:1 (MC2-800-1) exhibited the highest total pore volume (1.80 cm^3/g) and mesopore volume (1.50 cm^3/g) with most ordered mesoporous structure with large mesopore diameters of up to 50nm, which are twice as high as those of other lignin-derived mesoporous carbons with mesopore volume of up to 0.71 cm^3/g (Herou et al., 2019; Saha et al., 2014; Wang et al., 2020; Song et al., 2017, and Chen et al., 2013) and comparable or even higher than some mesoporous carbon prepared by using synthetic polymers (Han et al., 2003; Sudhagar et al., 2011 and Ignat et al., 2010).

Table 4.3: Surface textural properties of hard-templated mesoporous lignin carbons prepared using different lignin/template ratios by mass.

Sample	S_{BET} (m^2/g)	V_{total} (cm^3/g)	V_{meso} (cm^3/g)	V_{micro} (cm^3/g)	Average pore size, (nm)
MC1-800-1	885	1.16	0.94	0.19	8.1
MC1-800-2	638	1.07	0.88	0.12	9.8
MC1-800-3	415	0.53	0.42	0.09	10.5
MC2-800-0.5	902	0.92	0.66	0.22	8.3
MC2-800-1	960	1.80	1.50	0.17	12.4
MC2-800-2	716	1.15	0.96	0.15	10.6
MC2-800-3	413	0.50	0.38	0.10	12.4

Figures 4.6(c, d) show that the carbon samples prepared with different silica-to-lignin ratios maintained the bimodal mesopore size distribution with minor quantities of micropores. The carbons prepared with lignin/MCF ratios in the range of 1-2 were generally found to have the most ordered mesopore structures with the narrowest pore size distributions (Fig. 4.6d). The carbon MC2-800-1 exhibited the largest pore volume with the largest mesopore sizes centered at 35 nm.

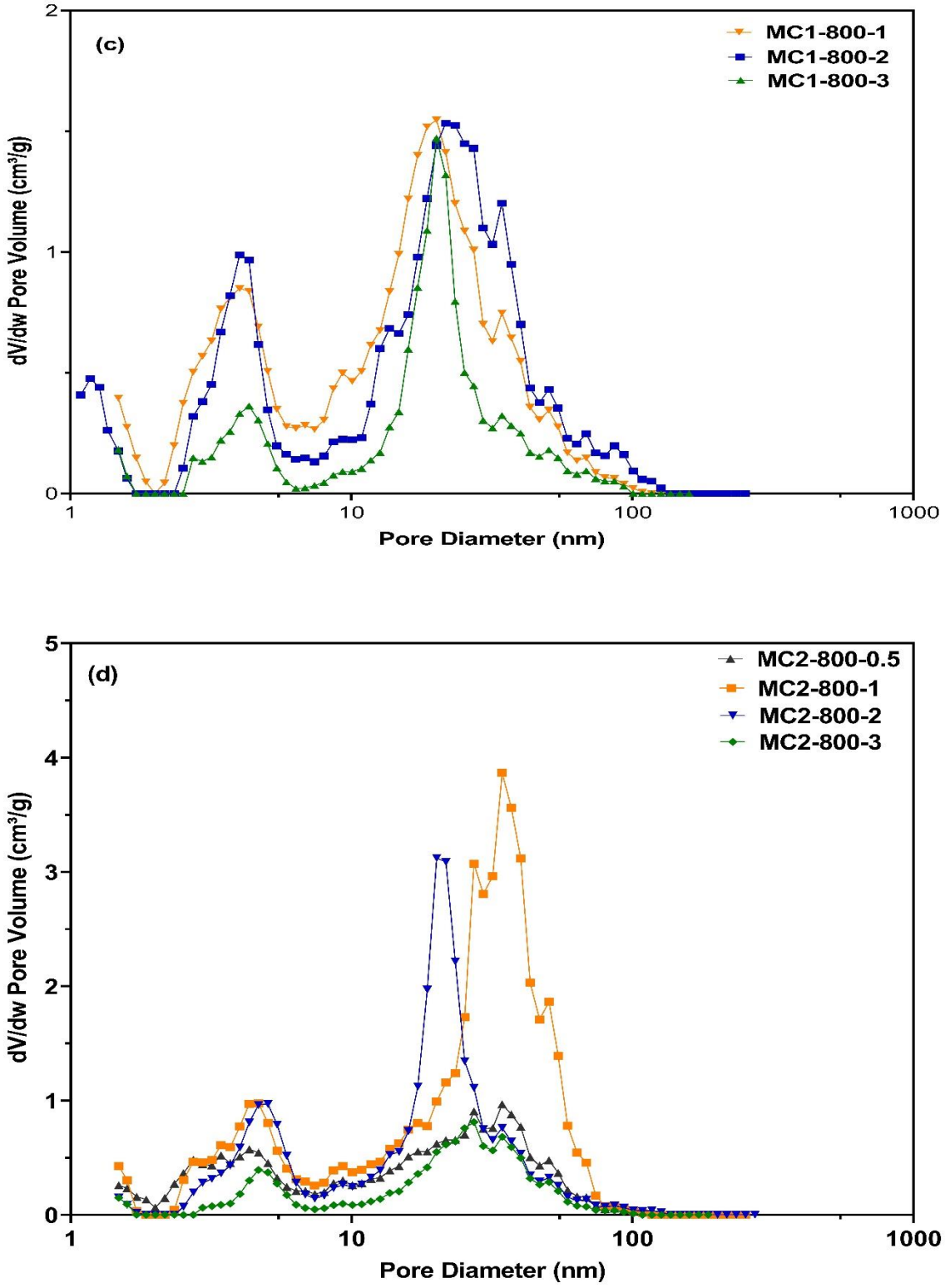

Figure 4.6 Pore size distributions of MC1 (c) and MC2 (d) prepared using different lignin/template ratios by mass at a carbonization temperature of 800 ℃.

4.2.2.3 Effect of the template: 3D vs. 2D hard silica template

To investigate the effect of 3D interconnecting structure on the porosity development of mesoporous carbons, mesoporous silica with 2D connected porous structure (PQ silica) and large pore size was also used as a hard template. Figure 4.7a shows the N_2 adsorption-desorption isotherms of mesoporous carbon materials prepared using PQ silica with a 2D porous structure. Differing from the isotherms obtained by MC carbons using the 3D MCF hard template, the isotherms of PQ-templated carbon samples showed two major capillary condensation steps at the P/Po range of 0.6 to 1.0, corresponding to the presence of the bimodal mesoporous networks. As presented in Figure 4.7b, the smaller mesopores with pore diameter centered at 6.4 nm were believed to originate predominantly from the dissolution/removal of the silica where the filling of lignin is hindered because of non or micro-porosty, so they mostly represent the wall thickness of the 2D PQ template, which were thicker than that of the 3D MCF silica that has a wall thickness of about 4 nm. In contrast, the larger mesopores centered at ~19 nm were formed from the lignin-filled mesopores of PQ silica with the contribution of the porosity from the removal of the silica walls. Compared to the PQ-templated carbons, the MCF-templated mesoporous carbon was found to have much higher nitrogen adsorption capacity with a more ordered and better-connected mesostructure, with a much greater distribution of large-pore mesoporosity as shown in Figure 4.7 b.

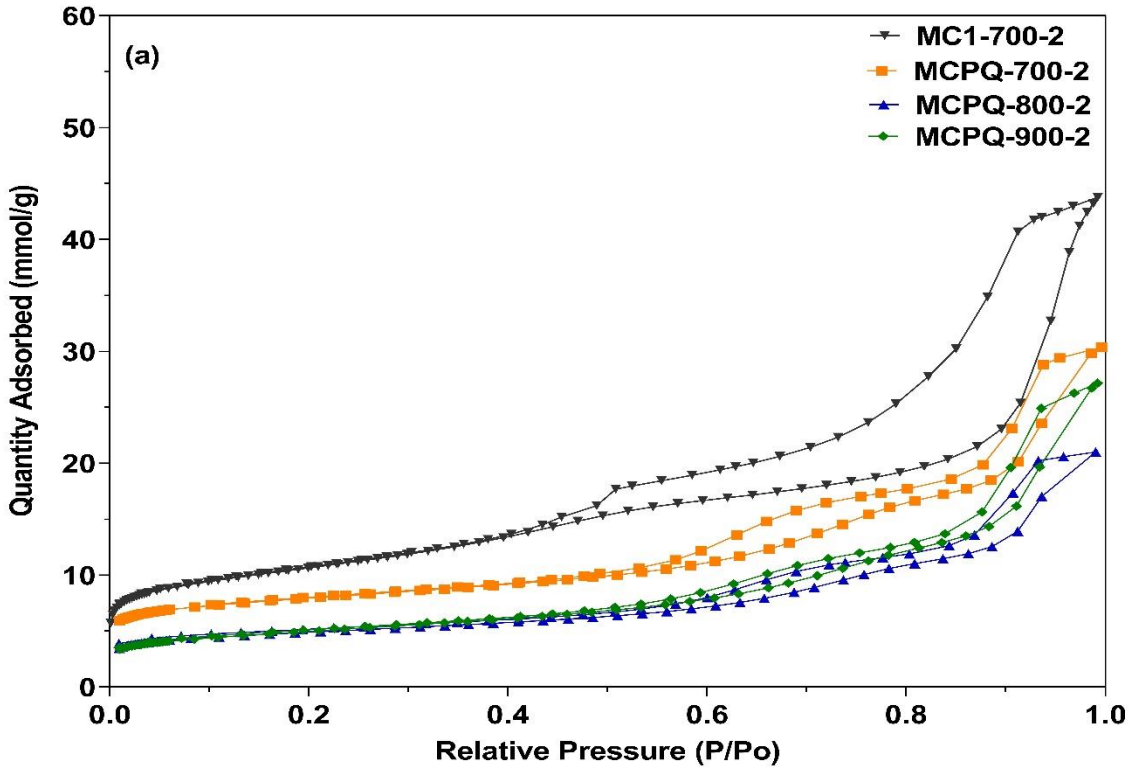
(a)
MC1-700-2
MCPQ-700-2
MCPQ-800-2
MCPQ-900-2
Quantity Adsorbed (mmol/g)
Relative Pressure (P/Po)
0
10
20
30
40
50
60
0.0
0.2
0.4
0.6
0.8
1.0

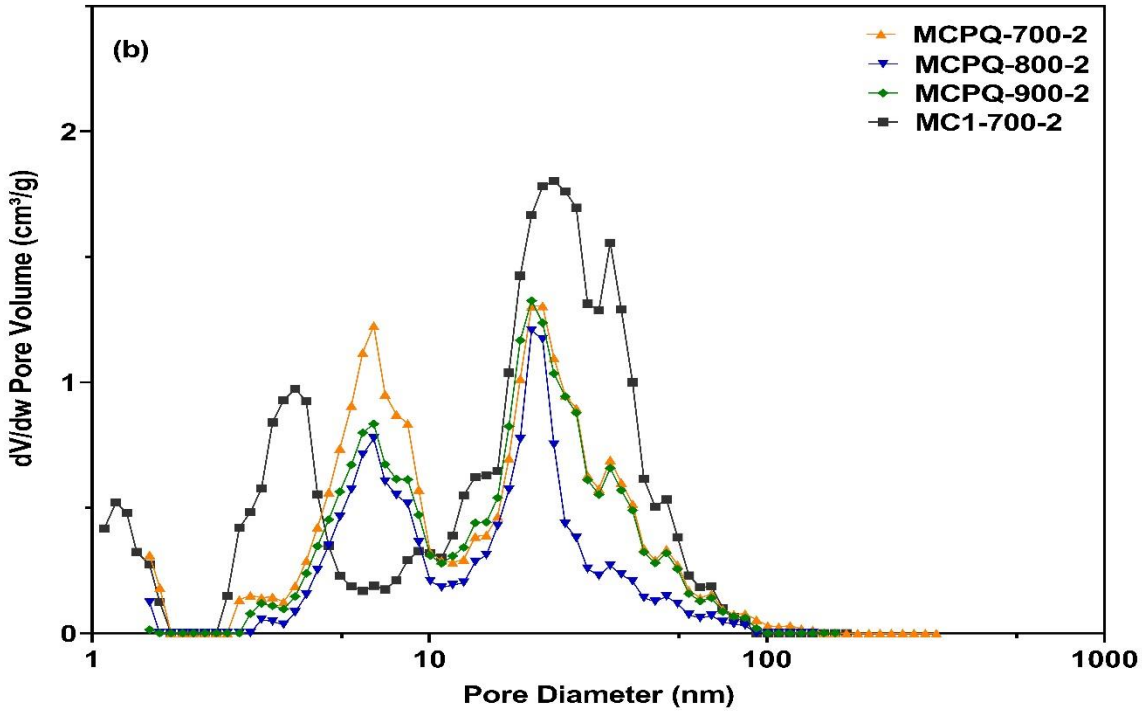
(b)
MCPQ-700-2
MCPQ-800-2
MCPQ-900-2
MC1-700-2
dV/dw Pore Volume (cm³/g)
Pore Diameter (nm)
0
1
2
1
10
100
1000

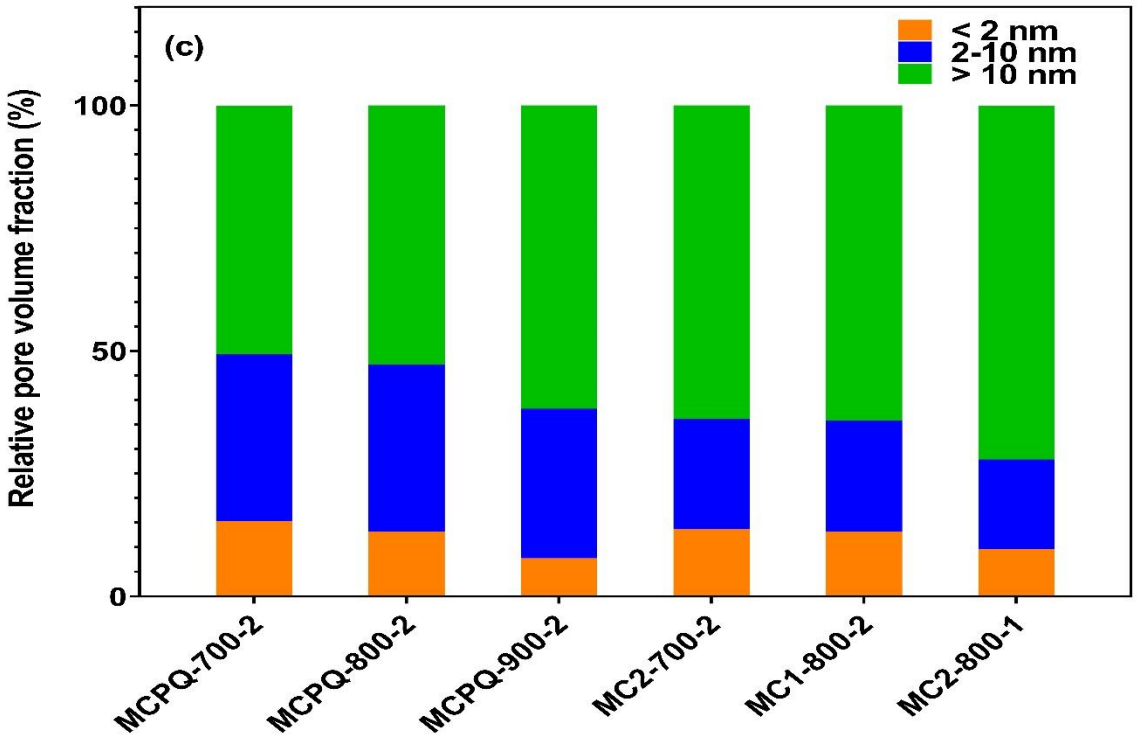

Figure 4.7: N_2 adsorption-desorption isotherms and pore size distributions (a and b) of MCPQ samples synthesized at different carbonization temperatures, and MC1-700-2 (c) contributions of Relative Pore Volume Fractions of Mesoporous Carbon Materials.

The detailed textural properties of the MCPQ carbons are summarised in Table 4.4. Compared to the MCF-templated carbons, the PQ-templated mesoporous carbons displayed significantly lower BET surface areas and pore volumes. For instance, the largest pore volume of 0.95 cm^3/g with a surface area of 650 m^2/g was obtained for MCPQ-700-2 prepared at 700 °C, compared to the pore volume of 1.23 cm^3/g with a surface area of 849 m^2/g obtained for the MCF-templated carbon (MC1-700-2) prepared in the same conditions. As the carbonization temperature increased to 800 °C, the pore volume (MCPQ-800-2) was further reduced to only half of the MCF-templated carbons (Table 4.3). Meanwhile, the fraction of large mesopores (> 10 nm) in the PQ-templated carbons are generally well below 60% of the total pore volume, compared to 80% achieved by MCF-templated carbons (Figure 4.7c, Table 4.3).

Table 4.4: Surface textural properties of MCPQ carbons, MC1-700-2, and MC1-800-2

Samples	S_{BET} (m^2/g)	V_{total} (cm^3/g)	V_{meso} (cm^3/g)	V_{micro} (cm^3/g)	Pore size (nm)	Window size (nm)
MCPQ-700-2	650	0.95	0.77	0.15	11.07	9.79
MCPQ-800-2	400	0.56	0.47	0.07	11.17	10.00
MCPQ-900-2	394	0.78	0.69	0.06	12.00	11.12
MC1-700-2	849	1.23	1.06	0.17	9.59	7.91
MC2-800-2	716	1.15	0.96	0.15	10.62	8.13

4.3 Morphology

Figure 4.8 shows the SEM images of selected mesoporous carbon prepared using different silica templates It is evident that the original morphology and hexagonal structure of the 3D silicious cellular foams, as shown in Figure 4.3a-d, were well preserved in the hard-templated mesoporous carbons (Figure 4.8a-d). In addition, the desirable spherical or quasi-spherical structure of the MCF-templated mesoporous carbons can be easily distinguished from the irregular granular morphology of the PQ-templated carbons (e.g., MCPQ-700-2).

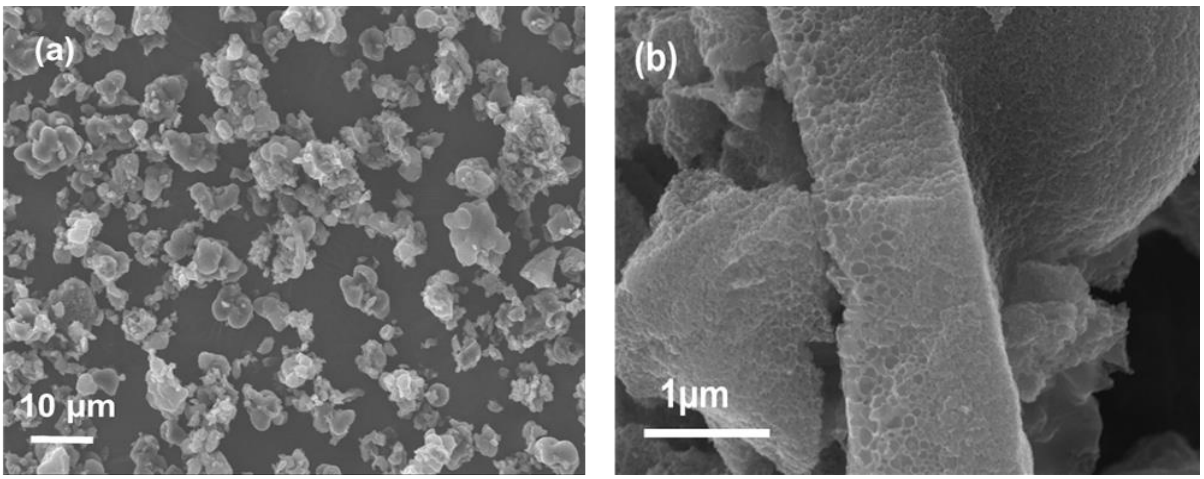

MC1-700-2 (a and b)

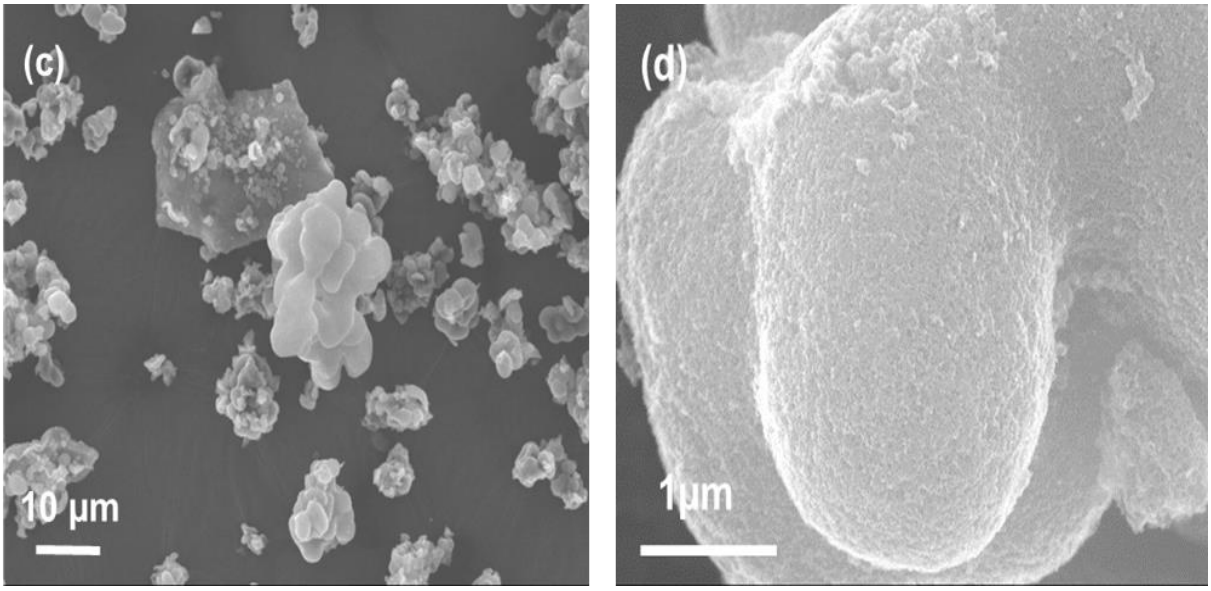

MC2-700-2 (c and d)

Figure 4.8 SEM images of mesoporous carbons using silica templates.

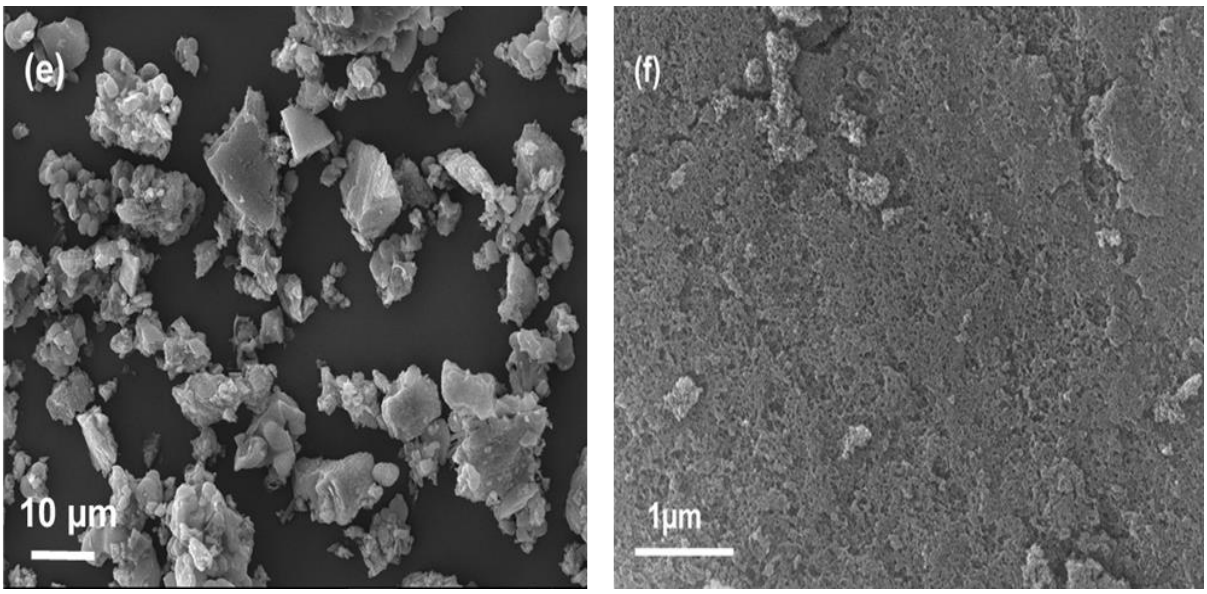

MCPQ-700-2 (e and f)

Figure 4.8 SEM images of mesoporous carbons using silica templates.

Figure 4.9 presents TEM images obtained for selected MCF and PQ silica templated mesoporous carbons. The MCF-templated carbon (MC1-700-2) exhibited well-

ordered and highly interconnected mesostructures with polydispersed spherical pore cages varying in size from 5 to 50 nm, compared to the PQ-templated carbon showing no clearly defined domain, as shown in Figures 4.7a and c. No significant difference was observed in texture between the MCF and PQ-templated carbons (Figures 4.7b and d), although the MCF-templated carbon appeared to have a denser texture due to the smaller micropores generated during the pyrolysis/carbonization of the lignin.

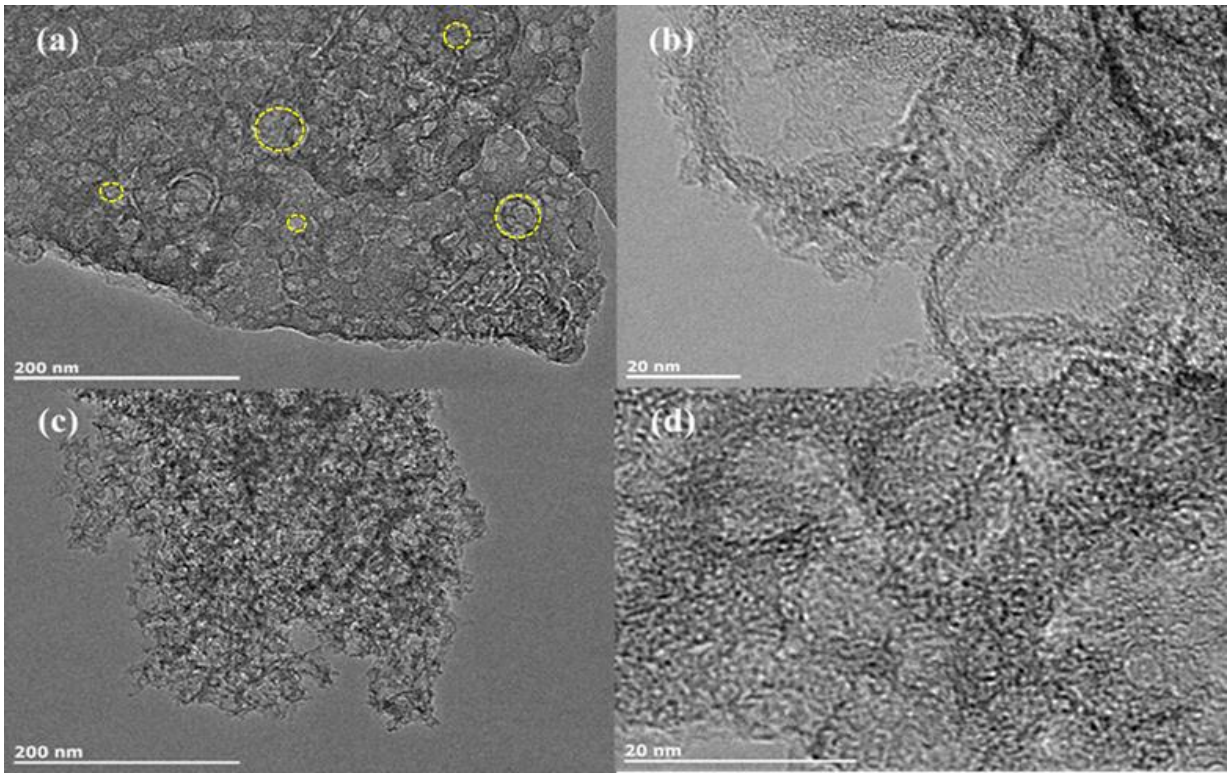

Figure 4.9 TEM images of mesoporous carbons prepared by using MCF (a,b) and PQ silica (c,d) as the template

4.4 Conclusions

Ordered Three-dimensional spherical mesoporous carbons with large pore size and mesopore volume have been successfully synthesized through a hard-templating route using mesostructured cellular foam (MCFs) as templates and lignin as the

carbon source. Depending on the preparation conditions (e.g., carbonization temperature, lignin-to-template ratio), the hard-templated mesoporous lignin carbons exhibited high BET surface areas of up to 960 m^2/g and mesopore volumes of 1.50 cm^3/g, which are significantly higher than those of other mesoporous carbons (MCPQ carbons) obtained from 2D commercial silica, that shows bimodal pore size distributions. The results showed that by varying both the carbonization temperature from 700 to 900 ℃ and the silica-to-lignin mass ratio ranging from 0.5-3, the textural and structural parameters of the final mesoporous carbon materials can be easily controlled. An increase in carbonization temperature shows a continuous evolution in the pore size but impedes the BET surface area and pore volume of the OMCs. Characterizations demonstrated that the ordered mesoporous lignin carbon is present in arrays of microspheres with dense texture and highly developed, three-dimensional connected mesopores. Finally, this work paves the way toward successfully utilizing lignin to synthesize highly ordered mesoporous carbon materials.

Chapter 5 Synthesis of ordered mesoporous carbons with SBA-15 as the hard template

5.1 Introduction

In recent years, there has been a growing interest in the synthesis of mesoporous carbons because of their use in a wide field of advanced energy-related applications like adsorption, catalysis, energy storage, and water purification (Tan et al., 2010; Komanoya et al., 2011; Bohme et al., 2005). These mesoporous carbons are novel 2-dimensional (2D) and 3-dimensional nanostructured materials with a highly ordered adjustable pore size (2-50 nm), large pore volume, high surface area as well as high mechanical and chemical stability (Walcarius, 2017; Ryoo et al., 1999). Generally, ordered mesoporous silicas such as SBA-1, SBA-15, KIT-6, MCM-48, and HMS have been widely used as hard templates to prepare mesoporous carbon materials (Parmentier et al., 2003; Kim et al., 2005; Sevilla et al., 2004). Among these templates, Santa Barbara Amorphous (SBA-15) possesses a well-ordered 2-dimensional hexagonal structure (Fuertes, 2003), with a large surface area and uniform pore size, which can be achieved in the presence of amphiphilic poly(alkylene oxide)-type triblock copolymers (Momcilovic et al., 2013). The synthesis procedure of ordered mesoporous carbon is through nanocasting method, which involves filling the pores of the template with an appropriate carbon precursor, its subsequent carbonization, and the template removal (Ryoo et al., 2001; Jun et al., 2000).

It should be noted that previous studies have already reported the synthesis of mesoporous carbons exhibiting high surface area, large pore volume, and pore size using SBA-15 as a template and various carbon precursors. For instance, Jun et al. (2000) reported the synthesis of ordered CMK-3 by wet impregnating an SBA-15 silica template with an acidified sucrose solution as a carbon source. The carbon was characterized by a BET surface area of 1520 m^2/g, a total pore volume of 1.3 cm^3/g, and a pore size of 3.5 nm. Fuertes (2004) synthesized a series of CMK-3 carbons using mesostructured SBA-15 silica samples as templates and furfuryl alcohol as carbon precursors. The resultant carbons exhibit a high surface area, pore volume, and pore size in the range of 900-1790 m^2/g, 0.81-1.47 cm^3/g, and 3.0-4.9 nm, respectively. Liu et al. (2020) synthesized ordered mesoporous carbon (SOMC), exhibiting a surface area of 882 m^2/g with an average pore diameter of 3.5 nm using SBA-15 as a hard template and soybean oil as a carbon precursor. Wang et al. (2015a) prepared OMC materials using SBA-15 as a hard template, sucrose as a carbon precursor, and boric acid as a pore-expanding agent. The synthesized OMCs had surface areas in the range of 640-1100 m^2/g and pore sizes of 3.4-7.7, which allowed them to be used as adsorbents for benzene removal.

In the previous chapter, the author demonstrated that mesocellular siliceous foams (MCFs), which are composed of large pore size and spherical shape with a 3D interconnected structure, are a potential template candidate for preparing bio-based lignin mesoporous carbon materials. The promising results inspired the author to study further the formation of mesoporous carbons inside the pore structure of a 2D silica template.

5.2 Results and discussion

5.2.1 Structural characterization and morphology of SBA-15 silica template.

The SBA-15 silica was synthesized in our lab using triblock copolymer Pluronic P123 $(EO)_{20}(PO)_{70}(EO)_{20}$ as the structure-directing agent. In addition, the silica template was aged at 100 ˚C as described in section 3.1.2. The N_2 adsorption-desorption isotherm and the pore size distribution curve are shown in Figure 5.1. The SBA-15 sample exhibits a typical type Ⅳ isotherm as classified by the IUPAC (Thommes et al., 2015). The isotherm also featured the well-distinguished H1 hysteresis loop at a relative pressure of 0.6-0.8, which indicates the delayed condensation of nitrogen in the well-defined cylindrical mesopores (Figure 5.1a). The steepness of the capillary condensation results in a narrow pore size distribution centered at 8 nm (Figure 5.1b).

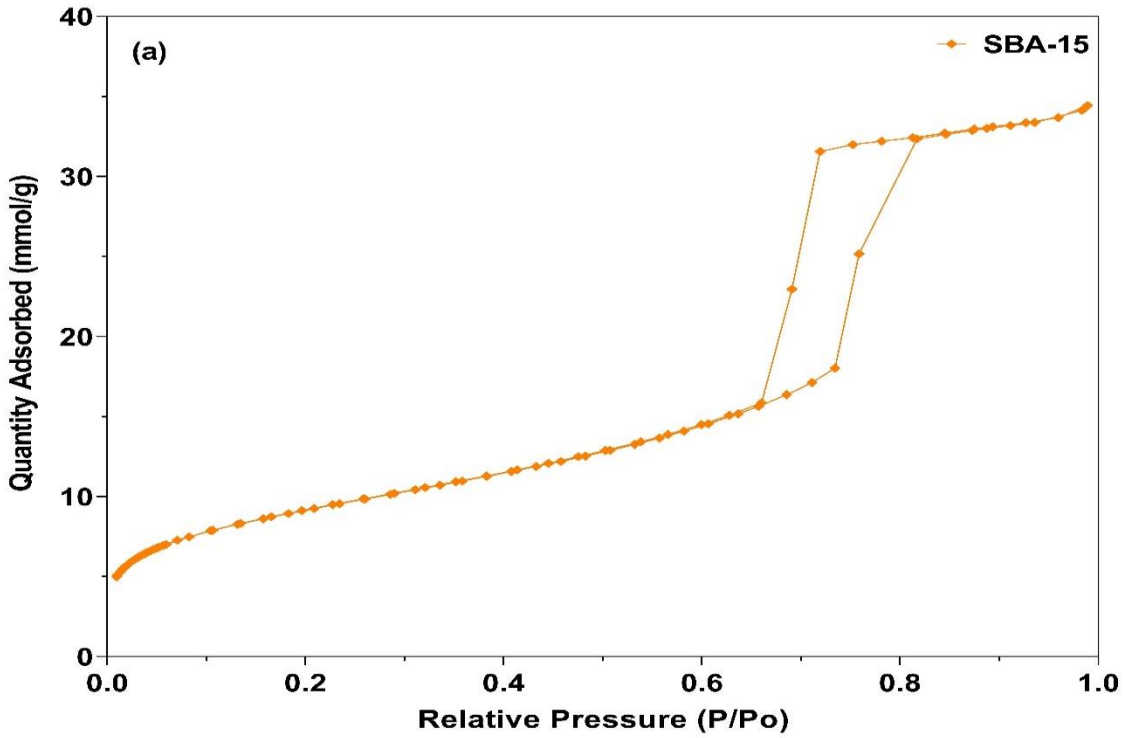

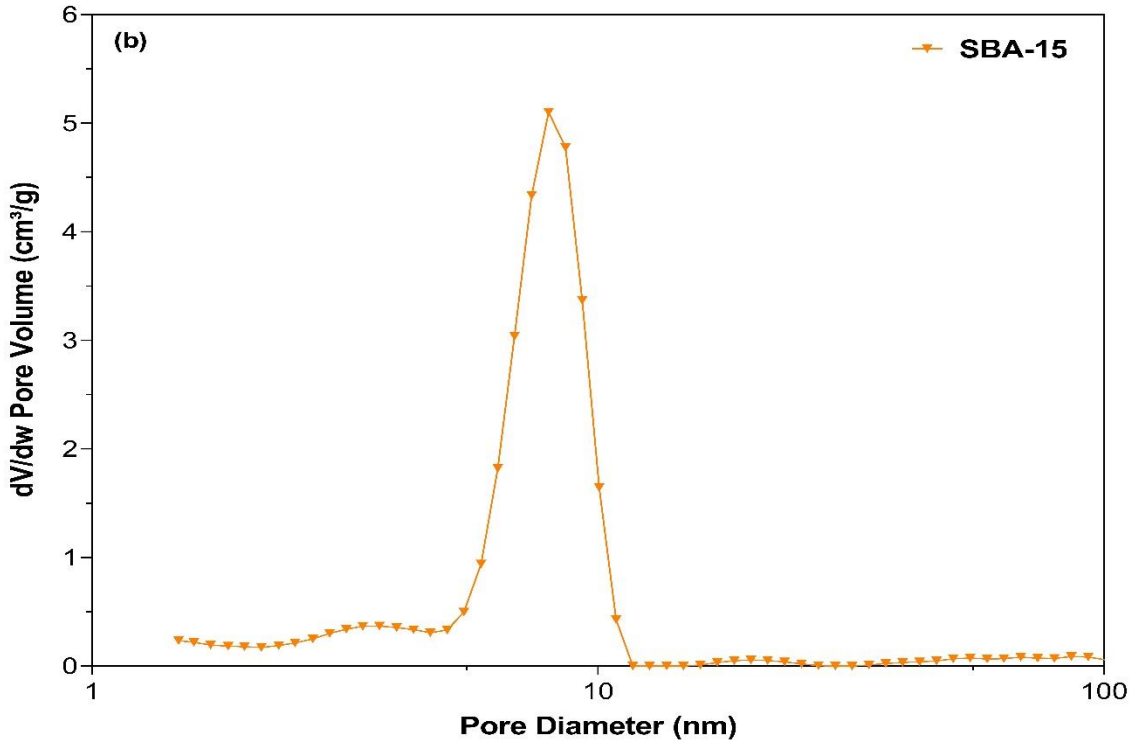

Figure 5.1 Nitrogen adsorption isotherm (a) and (b) pore size distributions of SBA-15 silica template.

The XRD pattern of SBA-15 in the small-angle range (Figure 5.2) exhibits three well-resolved peaks at 2θ of 0.92˚, 1.52˚, and 1.81˚ which are assigned to (100), (110) and (120) reflections of the 2D hexagonal (p6mm) symmetry, respectively (Janus et al., 2020; Wang et al., 2016b).

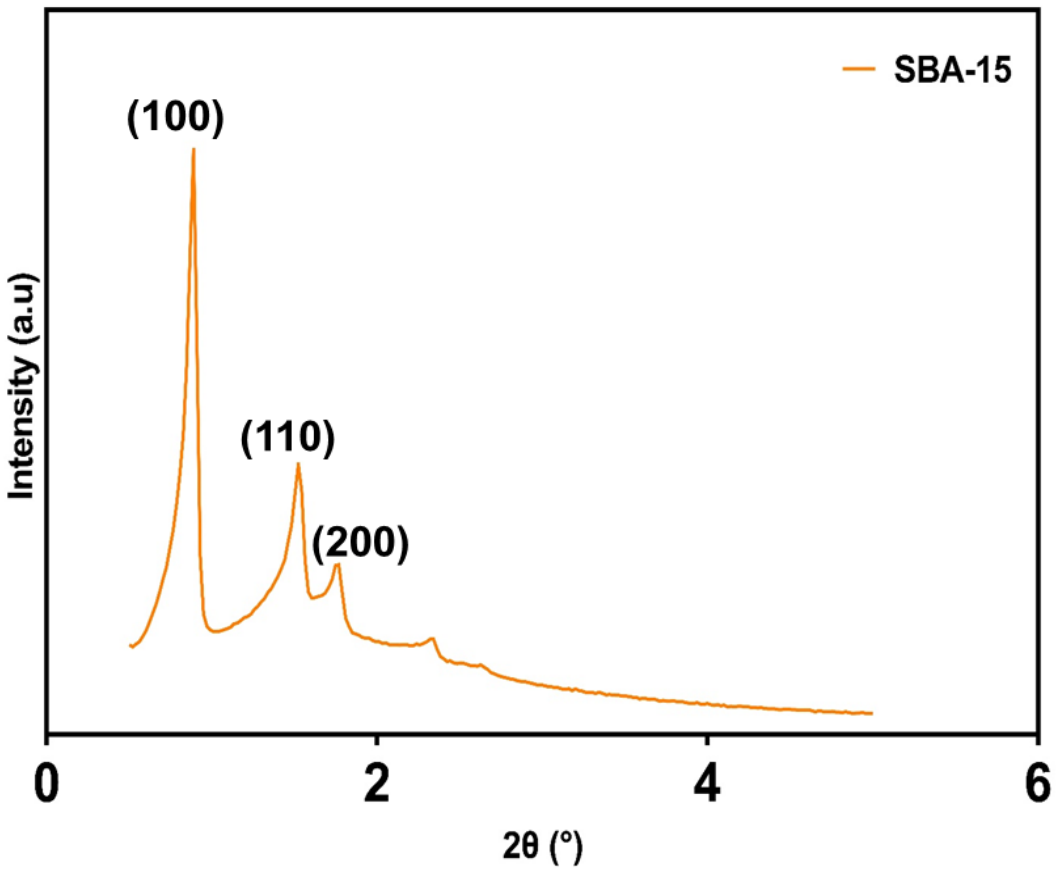

Figure 5.2 Small-angle XRD pattern of SBA-15.

5.2.2 Morphology of SBA-15 silica template

The morphological structure of the SBA-15 silica template is displayed in Figure 5.3. The silica template's low magnified high-resolution SEM images showed a uniform and linear rod-like morphology of a relatively uniform size of 10 µm and 1µm, bundled together as shown in Figures 5.3 a and b. The HR-SEM image of SBA-15 exhibits rods of larger width (Figure 5.3c).

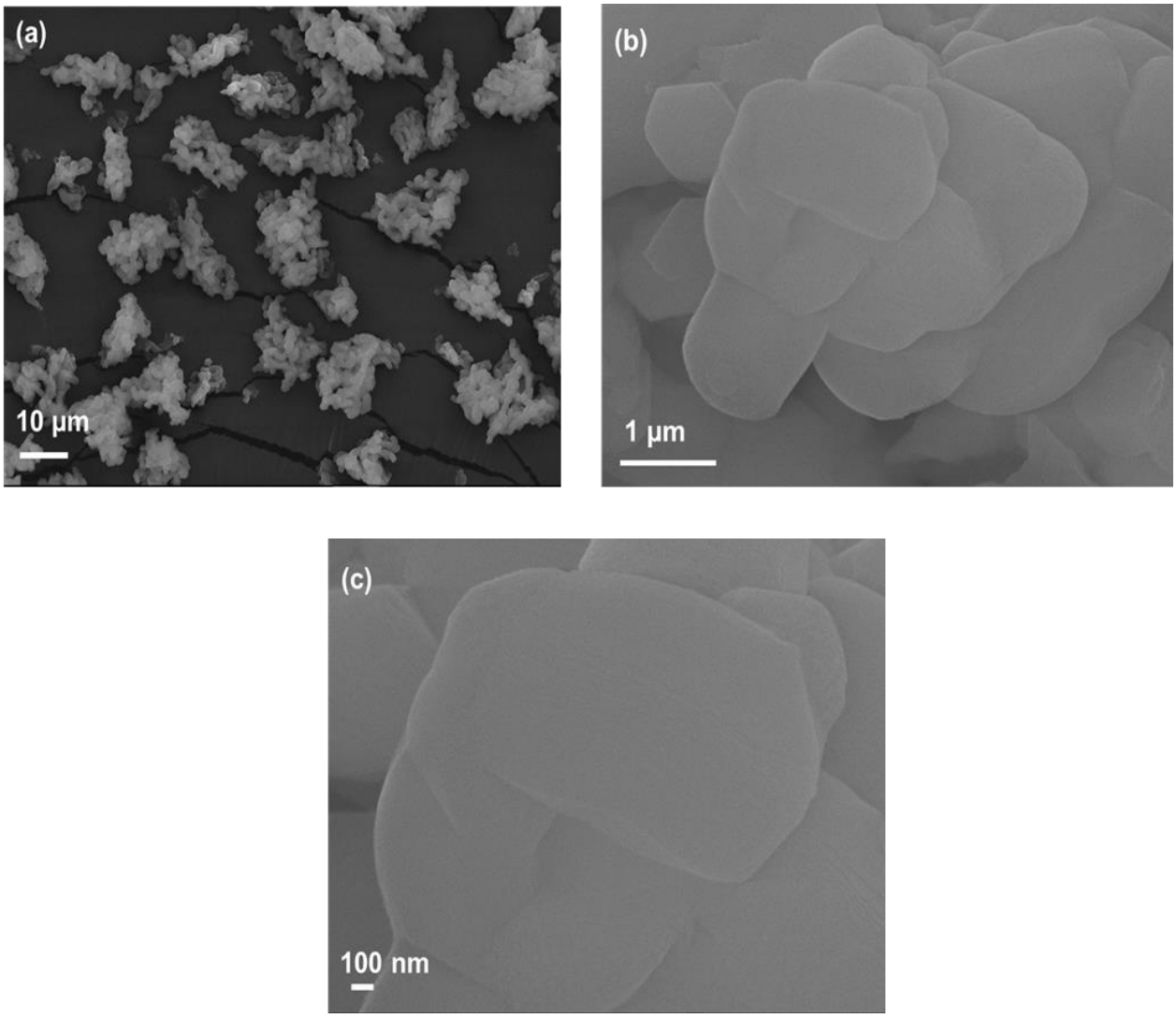

Figure 5.3 SEM images of SBA-15 silica template.

5.2.3 Surface textural property and morphology of SBA-15 mesoporous carbons

5.2.3.1 Effect of carbonization temperature

The nitrogen adsorption-desorption isotherms of the mesoporous carbons prepared using the SBA-15 silica template at carbonization temperatures of 700, 800, and 900 ℃ with a selected silica-to-lignin ratio of 1 by mass are shown in Figure 5.4. All the synthesized mesoporous carbons showed type IV (a) isotherm according to the IUPAC classification, featuring a clear H2(a) hysteresis loops, which is a typical

characteristic of mesoporous material exhibiting a pore network with limited restrictions to the pore (Thommes et al., 2015; Gor et al., 2012). It can be observed that the nitrogen adsorption capacity of the SBA-15-derived carbons in the low-pressure region is high, indicating the presence of micropores. With the increase of carbonization temperature from 700 to 900 °C, the nitrogen uptake decreased steadily, suggesting a decrease in the total pore volume of the carbons.

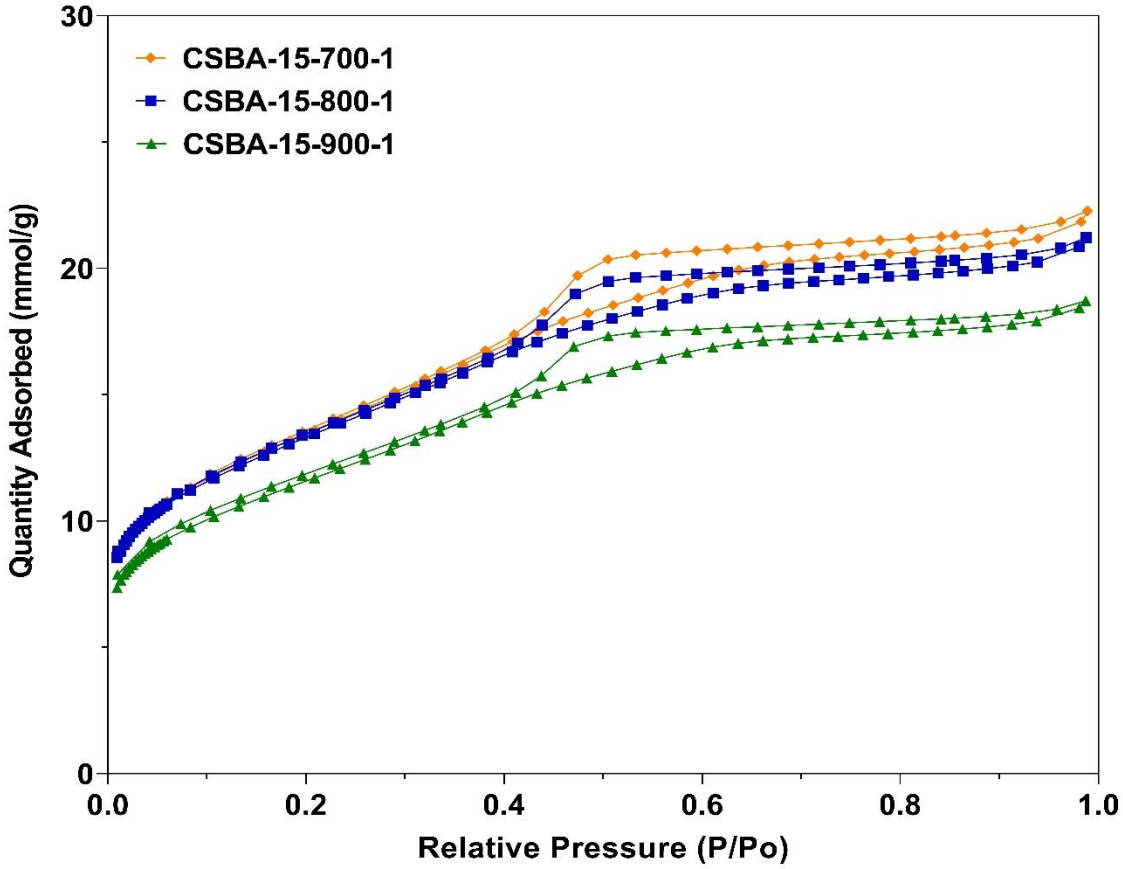

Figure 5.4 N_2 adsorption-desorption isotherms of CSBA-15 samples prepared at different carbonization with a silica-to-lignin mass ratio of 1.

The detailed textural properties of the SBA-15 silica template and CSBA-15 carbon samples prepared at different carbonization temperatures with the silica-to-lignin ratio of 1 are also shown in Table 5.1. The SBA-15 possesses a high surface area of 740

m^2/g, a total pore volume of 1.13 cm^3/g, and a pore size of 7.41 nm. The average pore size of the CSBA-15 carbons was in the range of 3.34-3.87 nm. The BET surface areas and pore volumes of the present CSBA-15 carbons were in the range of 926-1076 m^2/g and 0.54-0.66 cm^3/g, respectively. The samples prepared have pore size and surface area similar to that of ordered mesoporous carbon (3.7 nm and 1016 m^2/g) (Chang et al. 2013), CMK-3 (3.3 nm and 986 m^2/g) (Kiomarsipour et al., 2021) and OMC (3.2 nm and 351 m^2/g) (Ding et al. 2011). With the increase in carbonization temperature from 700 to 900 °C, a slight decrease in the BET surface area, pore volume, and pore size was observed for all the CSA-15 carbons. The increased temperature could lead to the thermal shrinkage of the carbon walls, as revealed by the decreased surface area and total pore volume (Lee et al., 2014; Shao et al., 2022).

Table 5.1: Surface textural properties of SBA-15 and CSBA-15 carbon samples prepared at different carbonization temperatures

Sample	S_{BET} (m^2/g)	V_{total} (cm^3/g)	V_{meso} (cm^3/g)	V_{micro} (cm^3/g)	Average pore size (nm)
SBA-15	740	1.13	1.00	0.13	7.41
CSBA-15-700-1	1076	0.66	0.38	0.28	3.87
CSBA-15-800-1	1064	0.61	0.35	0.26	3.36
CSBA-15-900-1	926	0.54	0.31	0.23	3.34

Figure 5.5 shows the pore size distributions (PSDs) of the CSBA-15 samples. All the PSDs of CSBA-15 carbon samples have bimodal mesoporous structures, with small mesopores size peaks centered at 2.7-2.9 nm formed from the removal of the silica template and large mesopores size peaks centered at 3.4 nm originating from the

coalescence of SBA-15 pores, that was partially filled with a carbon precursor. With the increase in carbonization temperature from 700 to 900 °C, the CSBA-15 carbons maintained a similar pore shape, whereas the intensity of large mesopores was slightly reduced.

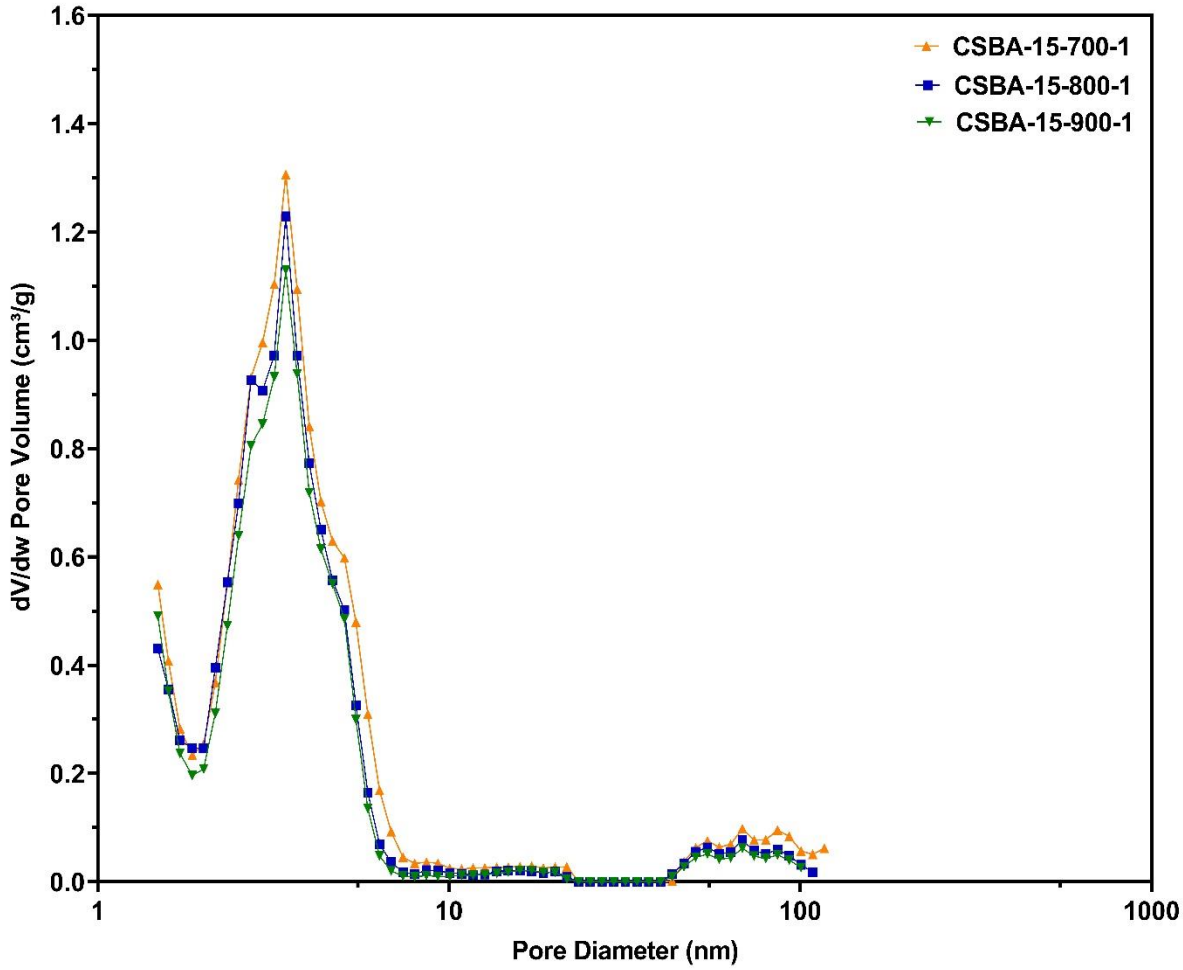

Figure 5.5 Pore size distributions of CSBA-15 samples prepared at different carbonization with a silica-to-lignin mass ratio of 1.

5.2.3.2 Effect of lignin to silica mass ratio on the mesoporous carbon materials

The maximum loading of lignin to silica mass was found to be 1.5, and it was estimated based on the density of the lignin (1.35 g/cm^3) and the total pore volume of SBA-15

(1.13 cm^3/g). Therefore, the effect of various lignin-to-silica mass ratios was investigated by synthesizing mesoporous carbons at 700 ℃ with varying lignin-to-silica mass ratios from 0.5 to 3. The nitrogen adsorption-desorption isotherms for the CSBA-15 carbon replicas are displayed in Figure 5.6. All the carbon samples also presented the type IV (a) isotherm with a well-distinguished H2(a) hysteresis loop, which is similar to that of CSBA-15 carbons prepared with lignin to silica of 1 (Figure 5.3). As the silica-to-lignin ratio was increased from 0.5 to 1, it was noticed that the nitrogen adsorption capacity increased, being indicative of an increase in the total pore volume for CSBA-15-700-1. However, increasing the lignin-to-silica mass ratio from 1 to 3, the amount of nitrogen adsorbed steadily decreased for the CSBA-15-700-2, CSBA-15-700-2.5, and CSBA-15-700-3, indicating a decrease in the total pore volume.

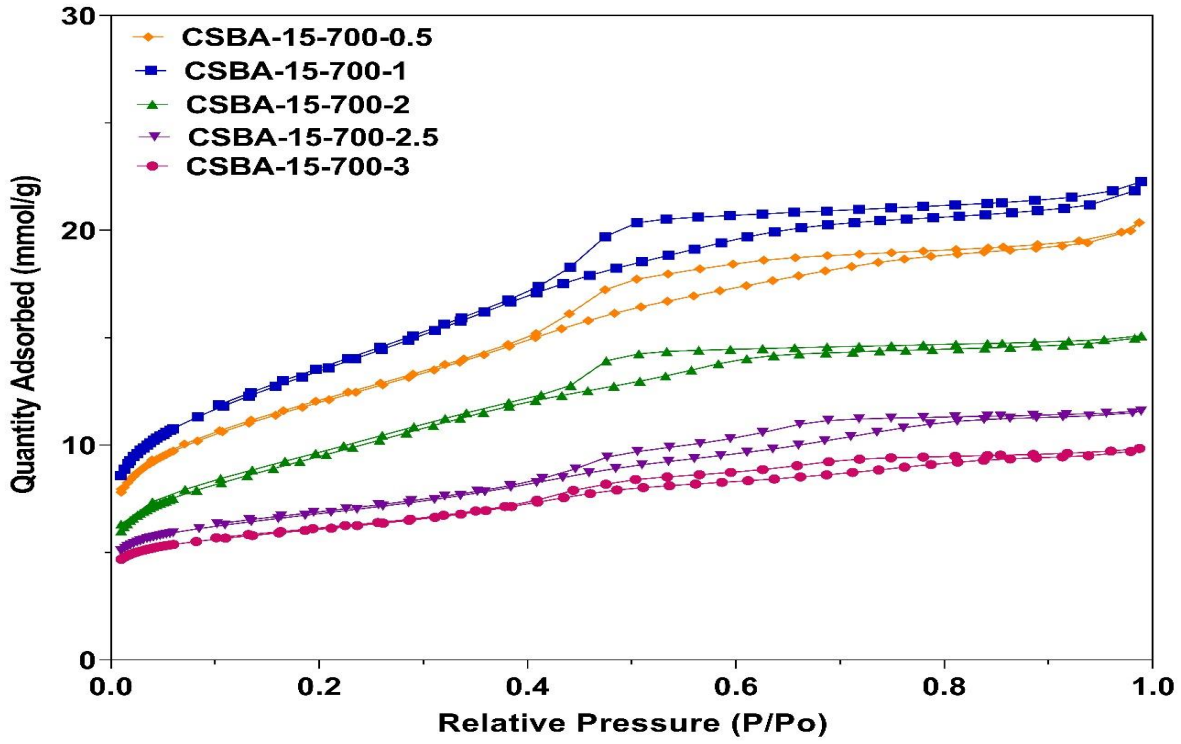

Figure 5.6 N_2 adsorption-desorption isotherms of CSBA-15 carbon samples prepared at a carbonization temperature of 700 ℃ with different mass ratios.

The textural properties of the CSBA-15 carbon samples are listed in Table 5.2. The sample obtained at a low lignin-to-silica ratio of 0.5-1 shows an increased surface area from 958 m^2/g to 1076 m^2/g and total pore volume from 0.58 cm^3/g to 0.66 cm^3/g. It is apparent that with increasing lignin to silica ratio from 1 to 3, there is a gradual decrease in both BET surface area and pore volume from 1076 m^2/g and 0.66 cm^3/g (CSBA-15-700-1) to only 505 m^2/g and 0.29 cm^3/g (CSBA-15-700-3). Interestingly, both the mesopore and micropore volumes also decrease with the mass ratio increase. This clearly evidences that a well-defined structure and less disordered pore voids can be achieved by increasing the mass ratio. The increase in the lignin-to-silica ratio could lead to the deposition of extra carbon at the external surface of the SBA-15 template, causing the carbon's reduced BET surface area and pore volume (Shao et al., 2022). In addition, the increase in carbon residue in the pores with silica to lignin mass ratio might also cause a reduced pore volume (Vinu et al., 2007). Slight growth in the average pore size of the resulting CSBA-15 carbon samples with an increase in the lignin-to-silica ratio from 0.5 to 3, with sample CSBA-15-700-3 exhibiting the largest pore size of 4.01 nm. Amongst all the CSBA-15 carbons, the sample CSBA-15-700-1 showed the highest total pore volume of 0.66 cm^3/g with an average pore size of 3.87 nm and surface area of 1076 m^2/g which is higher than the SBA-15 mesoporous carbon with a pore volume of 0.37 cm^3/g and surface area of 570 m^2/g (Lazaro et al., 2007), ordered mesoporous carbons (SOMC) exhibiting surface areas (783-882 cm^3/g), and average pore sizes (3.5-3.9 nm) (Liu et al., 2020), or OMCs synthesized by Duraisamy et al. (2019) with a BET surface area in the range of 224 m^2/g to 643 m^2/g, and total pore volume of 0.26 cm^3/g to 0.11 cm^3/g).

Table 5.2: Textural properties of CSBA-15 carbon samples with different mass ratios.

Sample	S_{BET} (m^2/g)	V_{total} (cm^3/g)	V_{meso} (cm^3/g)	V_{micro} (cm^3/g)	Pore size (nm)
CSBA-15-700-0.5	958	0.58	0.34	0.23	3.80
CSBA-15-700-1	1076	0.66	0.38	0.28	3.87
CSBA-15-700-2	756	0.44	0.26	0.17	3.89
CSBA-15-700-2.5	560	0.34	0.20	0.14	4.00
CSBA-15-700-3	505	0.29	0.15	0.14	4.01

It is worth mentioning that the porosity development of the CSBA-15 carbons prepared from 2-dimension SBA-15 and MCF-derived carbons obtained from a 3D network structured MCF template was affected by the role of the porous structure of the silica template. It seems that the porous structure of the templates plays a vital role in determining the final structure of the carbon. For instance, when compared to a similar synthesis condition, MC-800-1 obtained from MCF2 (Table 4.3) had a 3D interconnected network with values that were four times as high as those of CSBA-15-800-1 in mesopore volume (1.50 cm^3/g vs. 0.35 cm^3/g).

Figure 5.7 shows that the samples CSBA-15-700-0.5, CSBA-15-700-1, CSBA-15-700-2, CSBA-15-700-2.5, and CSBA-15-700-3 preserved the bimodal pore size distributions with a peak centered at about 2.7-3.7 nm and 3.7-6.8 nm. With an increasing amount of lignin from 0.5 to 3, the intensity of small mesopores reduces, while the pore size distribution shifts toward the large mesopore region. This could be attributed to the increase in the average pore size of the CSBA-15 carbon samples.

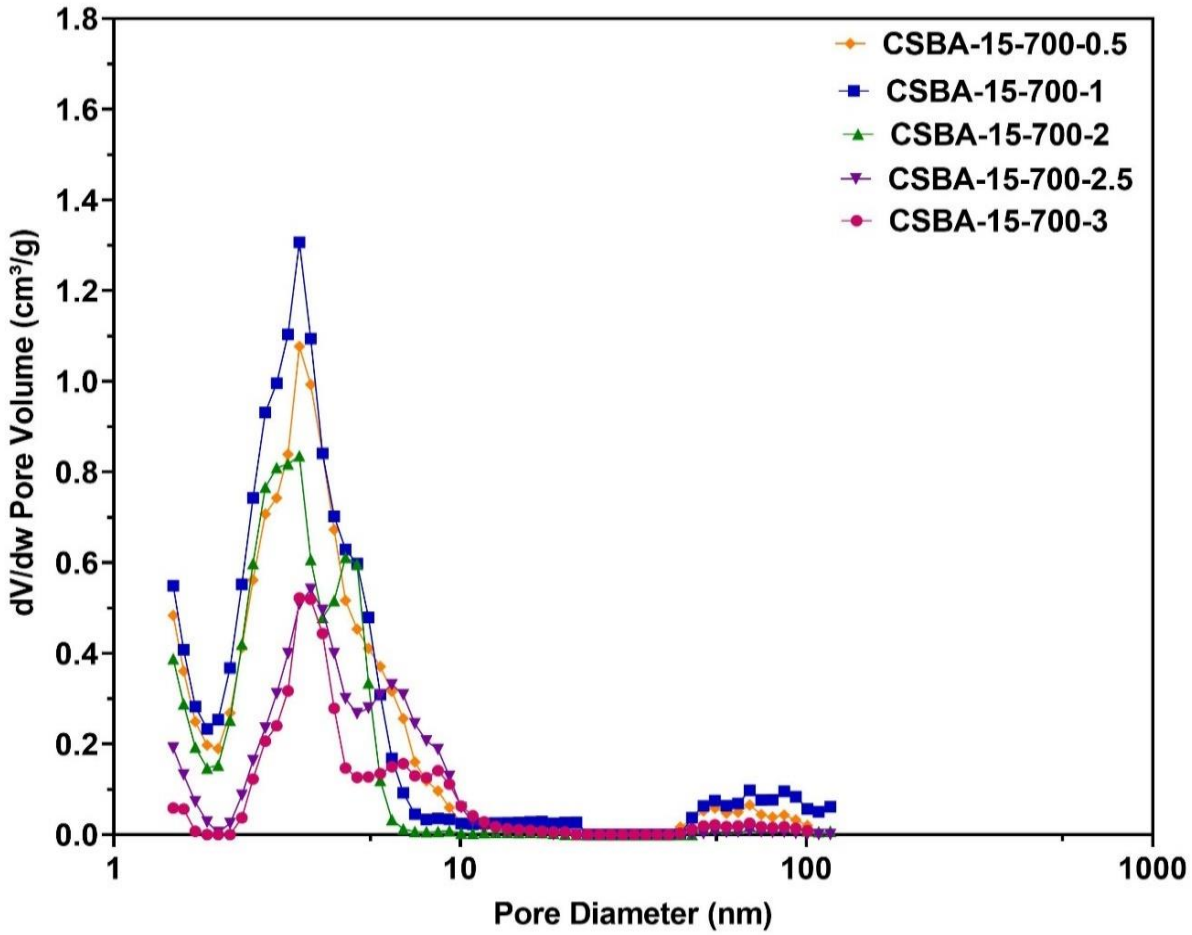

Figure 5.7 Pore size distribution curves of CSBA-15 carbon samples prepared at a carbonization temperature of 700 ℃ with different mass ratios.

5.3 Morphology

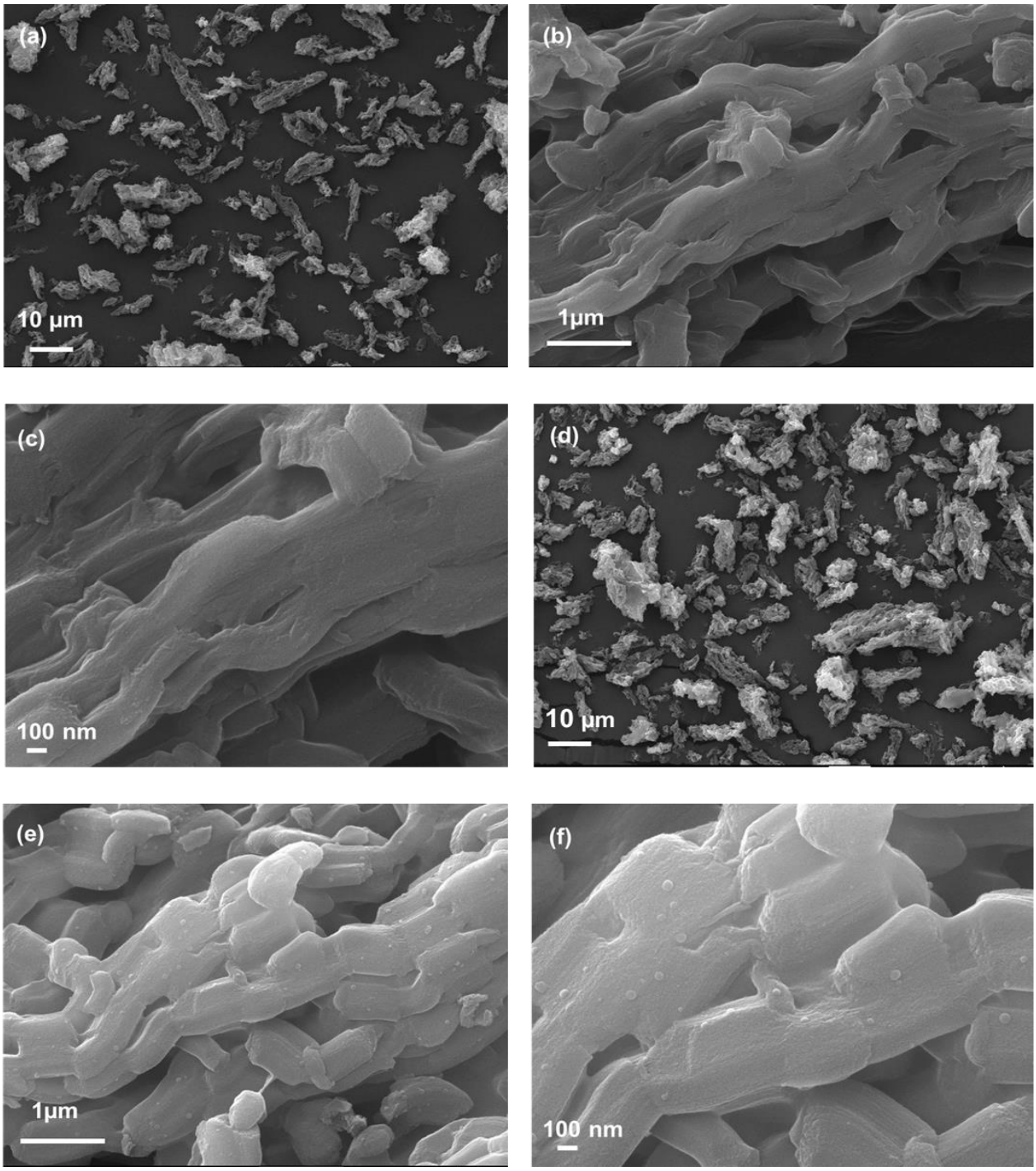

Figure 5.8 Low and high magnification SEM images of the CSBA-15 carbon materials obtained at 700 °C (a, b, c) and 800 °C (d, e, f).

The scanning electron microscopy (SEM) images of the mesoporous carbon materials prepared at carbonization temperatures of 700 and 800 °C with a silica-to-lignin mass

ratio of 1 are presented in Figure 5.7. Similarly, all the CSBA-15 carbon samples obtained from the SBA-15 silica template preserved the long rod-like morphology as shown in Figures 5.7a, b, d, and e. Obviously, these images reveal the successful replication process of SBA-15. from the parent SBA-15 silica template. In the high-magnification images of the CSBA-15 samples, it is observed that the width of the rods decreased (Figure 5.7 c and f). This may be due to heat treatment at a high temperature that leads to shrinkage. Similar structures of SBA-15 and CSBA-15 are in good agreement with the reports (Shao et al., 2022).

5.4 Conclusions

A series of highly ordered mesoporous carbons termed “CSBA-15” were successfully synthesized using SBA-15 as a hard template and lignin as the carbon precursor at carbonization temperatures of 700, 800, and 900 °C under a nitrogen atmosphere, with lignin to silica ratio varying from 0.5 to 3. The results showed that the BET surface area of the samples was in the range of 505-1076 m^2/g, and the maximum achievable average pore size can be controlled by varying the silica-to-lignin mass ratio. The average pore diameter shows a continuous evolution with the increase in silica to lignin mass ratio from 0.5 to 3. The SEM images showed that the CSBA-15 carbon samples had a 2D hexagonal symmetry, with a rod-like form of particles.

Chapter 6
Chitosan-derived mesoporous carbons with high nitrogen content.

6.1 Introduction

Chitosan is a linear polysaccharide biopolymer with major structural units of 2-amino-2-deoxy-D-glucopyranose and β-(1-4)-linked 2-acetamido-2-deoxy- β-D-glucopyranose (Ou et al., 2016). It is derived from chitin via partial deacetylation and depolymerization with an aqueous alkaline solution at 100-160 ˚C for 1-3 h, as shown in Figure 6.1 (Ababneh and Hameed, 2021). As reported in other literature, chitosan is the second most abundant biomass in nature after cellulose, with high nitrogen content between 7 and 11 wt% (Olejniczak et al., 2013). This allows the preparation of nitrogen-containing carbon materials (Khan et al., 2020; Wang et al., 2016a) in the absence of exogenous nitrogen sources such as urea, ammonia, and protein, which are expensive and may add cost, complicate the procedure and as well as alter the good biocompatibility of the final carbon materials (Hammi et al., 2020).

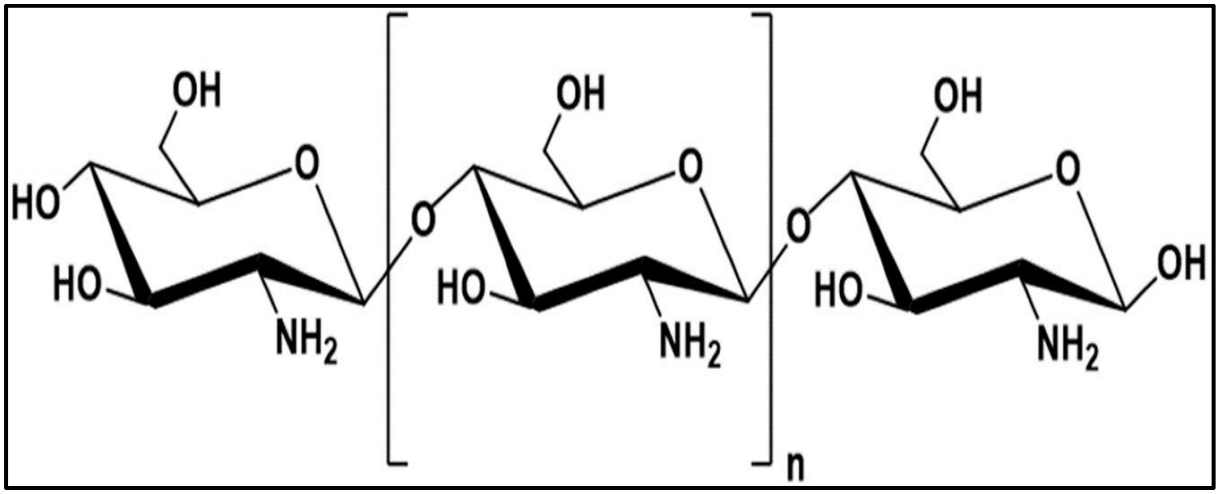

Figure 6.1 Chemical structure of chitosan (El-banna et al., 2019).

Chitosan has been reported as a carbon precursor for the preparation of carbon materials using several approaches, including heat treatment, hydrothermal carbonization, and templating methods (Kucinska et al., 2012; Zhao et al., 2010; Ji et al., 2010; He et al., 2010). The pyrolysis of chitosan in an inert gas environment is a sustainable, convenient, and cost-effective approach to prepare carbons with a nitrogen content of about 6 at.% (Kucinska et al., 2012). However, the derived carbon materials were characterized by their low BET surface areas of rarely higher than 400 m^2/g. The hydrothermal carbonization of nitrogen-doped carbons under mild temperatures of 180 ˚C resulted in materials with significant nitrogen content. Still, the resulting materials had a BET surface area lower than 10 m^2/g. Even upon a further increase in carbonization temperature, only a slight increase in surface area (up to 30-50 m^2/g) was obtained (Zhao et al., 2010).

The use of the hard template method (Ryoo et al., 1999; Joo et al., 2001) and the soft template method (Nelson et al., 2016) were alternatives, versatile, and commonly applied for the preparation of mesoporous carbon materials. The successful transformation of chitosan as a carbon source into mesoporous carbons using the soft template approach has been documented. For example, Sun et al. (2019) synthesized mesoporous carbons using chitosan-protic salt as a carbon source and F127 as a template. The carbons featured a surface area, pore volume, and nitrogen content up to 927 m^2/g, 0.47 cm^3/g, and 5.13 at%, respectively. Wang et al. (2020a) prepared mesoporous carbon materials with a BET surface area of 804 m^2/g, pore volume of 0.87 cm^3/g, and nitrogen content of 4.59 at. %. However, these prepared mesoporous carbons exhibited a low BET surface area, total pore volume, wide pore size distribution, and low nitrogen content. Compared to the soft template method, the hard template method has been extensively and widely used in preparing chitosan-derived

mesoporous carbons. For instance, Olejniczak et al. 2013, synthesized mesoporous carbon that featured a BET surface area of 1337 m^2/g, pore volume of 4.31 cm^3/g, and nitrogen content of 5.83 at. %, using chitosan as a carbon precursor and colloidal silica as a template. Peng et al., 2019, prepared mesoporous carbons with a surface area of 871 m^2/g, pore volume of 3.04 cm^3/g, and nitrogen content of 7.0 at. %. However, these chitosan-derived mesopores featured low nitrogen content and irregular morphology.

6.2 Results and discussion

6.2.1 Pore textural properties of chitosan-derived mesoporous carbons prepared from MCF silica template.

6.2.1.1 Effect of carbonization temperature.

To elucidate the role of textural properties of silica template on the porosity development of chitosan-derived mesoporous carbons, two mesostructured cellular foam silica (MCF-1 and MCF-2) having different pore volumes and pore sizes were chosen to prepare the mesoporous carbons. The structural characterization and morphology of the mesostructured cellular foams, MCF-1 (aged at 100 ˚C) and MCF-2 (aged at 120 ˚C), were discussed in Chapter 4, section 4.2.1. The silica template's textural properties (BET surface area, pore volume, and pore size) were also discussed and presented in Table 4.1.

Figure 6.2 shows the nitrogen adsorption-desorption isotherms of CMC1 and CMC2 carbons prepared using MCF1 and MCF2 as silica templates at carbonization temperatures of 700, 800, and 900 ˚C at selected silica-to-lignin ratio of 1 by mass. Both the carbonization temperature and silica template had a synergistic effect and played a critical role in determining the pore structure of the resulting mesoporous

carbons. Generally, as shown in Figure 6.2, all the CMC1 and CMC2 carbons exhibit a type IV isotherm, indicating the mesopore-dominant structure (Sing et al., 1985; Thommes et al., 2015). Besides the mesopores, the considerable adsorption of N_2 at low relative pressure (P/Po < 0.1) suggests the presence of micropores in all the carbon samples. For CMC1 samples (Figure 6.2a), with the increase in carbonization temperature from 700 to 900 ˚C, the amount of N_2 adsorbed decreased steadily, indicating a decrease in pore volume. It can also be seen that both CMC1-700-1 and CMC1-800-1 featured the well-distinguished H2(b) hysteresis loop, which is typical of ink-bottle mesopores (Klinthongchai et al., 2020, Daniel et al*.,* 2021), while the shape of the loop for CMCF1-900-1 changes into a complex mixture of H2-H4 type, which indicates bottle-shaped pores and/or slit-shaped pores (Olejniczak et al., 2013). In the case of CMC2 carbons (Figure 6.2b), all the samples exhibit the H2(b) hysteresis loop in the relative pressure range of 0.45-1, indicating the existence of a large quantity of mesopores (Wu and Liu, 2016). Amongst all the CMC2 carbons, the sample CMC2-800-1 manifested the highest N_2 uptake, exhibiting the highest pore volume. Compared to the CMC1 samples, at similar carbonization temperatures, the CMC2 samples prepared using the MCF2 template with a much larger mesopore volume exhibited higher nitrogen uptake.

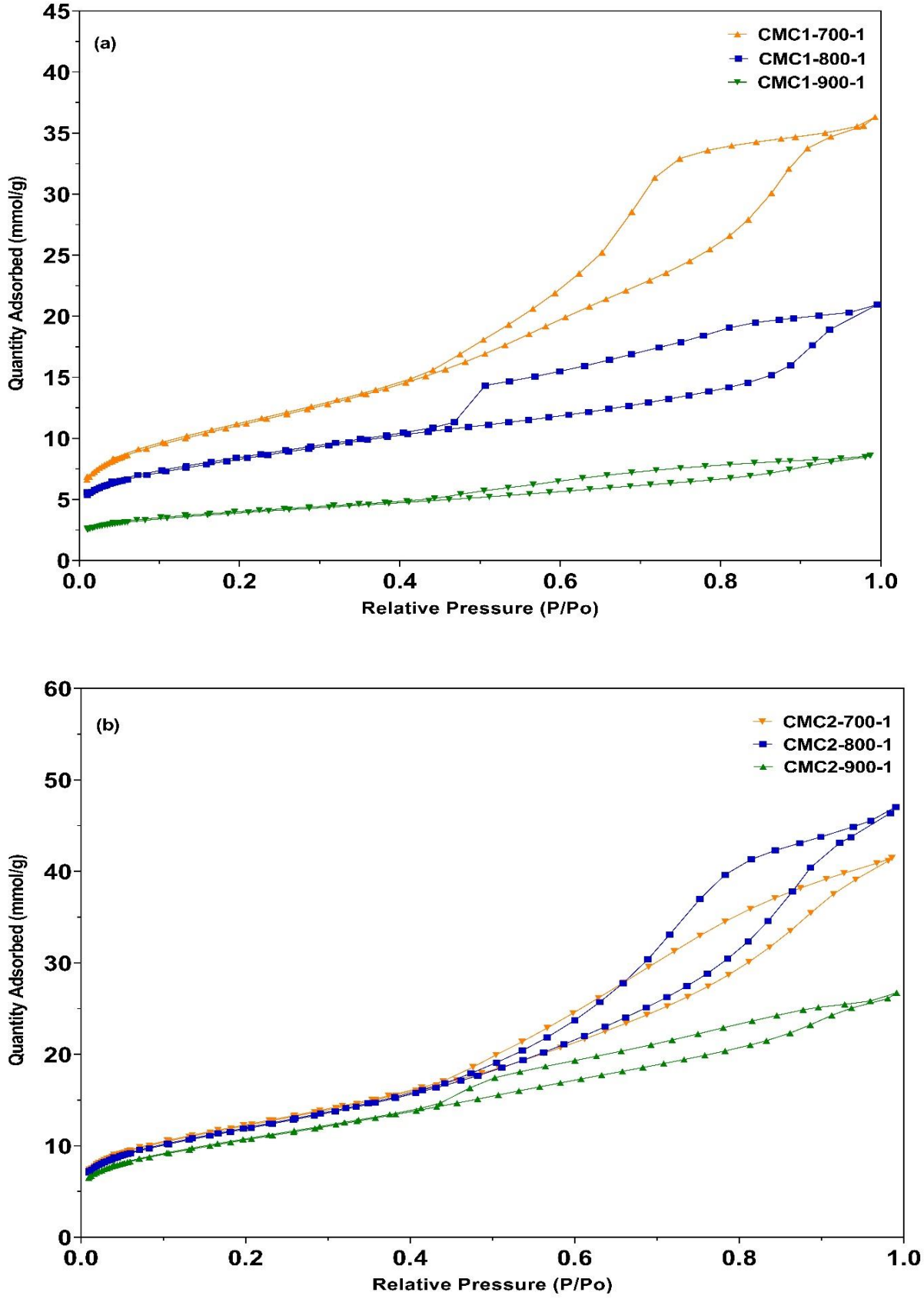

Figure 6.2 Nitrogen adsorption-desorption isotherms of (a) CMC1 and (b) CMC2 synthesized at different carbonization temperatures.

Table 6.1 shows the textural properties of mesoporous carbon materials. It can be found that the total pore volume of the nitrogen-rich carbons ranged from 0.22-1.32 cm^3/g with a high surface area of up to 983 m^2/g. In general, it is visible that with the increase in carbonization temperature from 700 to 900 ˚C, noticeable decreases in both BET surface area and pore volume were observed. However, at 800 ˚C, the carbon CMC2-800 was found to have the highest pore volume of 1.32 cm^3/g with a BET surface area of 953 m^2/g. It can be deduced that the chitosan-derived mesoporous carbons underwent a structural shrinkage upon treatment at elevated temperature, thereby accompanying a decrease in pore volume (Qian et al., 2010), while the reduction in BET surface area may be related to the collapse of porous (meso and micropores) structure at high temperature (Lian et al., 2014). In addition, by elevating the carbonization temperature, more energy is available to break up the intermolecular bonds and release more volatile materials in the chitosan (Heidari et al., 2019). When the textural properties of CMC1 and CMC2 carbons were compared, the CMC2 samples produced using MCF2 with large pore size and pore volume as a template exhibited a larger BET surface area and pore volume at similar synthesis conditions. The largest proportion of mesopore volume increased to 87.61, 90.91, and 78.38% for the CMC2 samples prepared at 700, 800, and 900 ˚C, which is higher than the 87.16, 74.60, and 68.18 % obtained by CMC1-700, CMC1-800, and CMC1-900, respectively. Furthermore, all the CMC1 and CMC2 carbon materials prepared from MCF1 and MCF2 silica supports are composed of a similar well-defined interconnected three-dimensional mesoporous structure, exhibiting reasonable BET surface areas and pore volumes, indicating that the properties of all these carbons materials are clearly related to the structural and textural properties of the silica

templates. These results revealed that CMC2 samples have better structural ordering and developed mesoporosity than CMC1 samples.

Table 6.1 Surface textural properties of chitosan-derived mesoporous carbons at different carbonization temperatures.

Sample	S_{BET} (m^2g^{-1})	V_{total} (cm^3g^{-1})	V_{meso} (cm^3g^{-1})	V_{micro} (cm^3g^{-1})	Average pore size, (nm)
CMC1-700-1	888	1.09	0.95	0.19	6.1
CMC1-800-1	663	0.63	0.47	0.15	6.3
CMC1-900-1	312	0.22	0.15	0.07	5.4
CMC2-700-1	983	1.13	0.99	0.14	6.5
CMC2-800-1	953	1.32	1.20	0.12	7.1
CMC2-900-1	857	0.74	0.58	0.16	5.2

The pore size distributions of CMC1 and CMC2 carbons are depicted in Figure 6.3. The pore size distributions of CMC carbons (Figure 6.3a) showed a bimodal mesoporous structure in the pore size region between 2 to 30 nm. with average pore sizes in the range of 5.4-6.3 nm (Table 6.1). The small mesopores in the pore size distributions ranging from 2 to 9 nm, with pores centered at 3-5 nm, are formed by the removal of the silica walls, and large mesopores mainly in the pore size distributions region of 10-30 nm, with pores centered at 13-18 nm, which originates from unfilled silica pores with the carbon (Bohme et al., 2005; Janus et al., 2020). An essential microporosity of the carbonized chitosan was observed at a pore diameter of less than 1.4 nm. With the increase in carbonization temperature from 700 to 900 ˚C, the intensity of both the small and large mesopores steadily reduced, with the large pore size region becoming slightly narrower and most of the pores shifting to the small pore size region. When MCF2 was used as the template, a similar pore size distribution was obtained in the small and large mesopore regions (Figure 6.3b), indicating the

change in pore volume and pore size of silica template has a limited impact on pore size distribution. However, the peak intensity in CMC2 carbons is much higher than in CMC1 samples. This suggests that the larger pore volume of MCF benefits the development of mesoporosity as the total pore volume of CMC2 carbons is much higher than that of CMC1 under similar conditions. At a carbonization temperature of 800 ˚C, the sample CMC2-800-1 showed a pronounced peak at about 10-20 nm, indicating the presence of well-developed mesoporosity and considerably higher pore volume and pore size. With a further increase in carbonization temperature to 900 ˚C, the peak intensity of both small and large mesopores sharply dropped, especially those of large mesopores, probably due to the collapse of the sample pores.

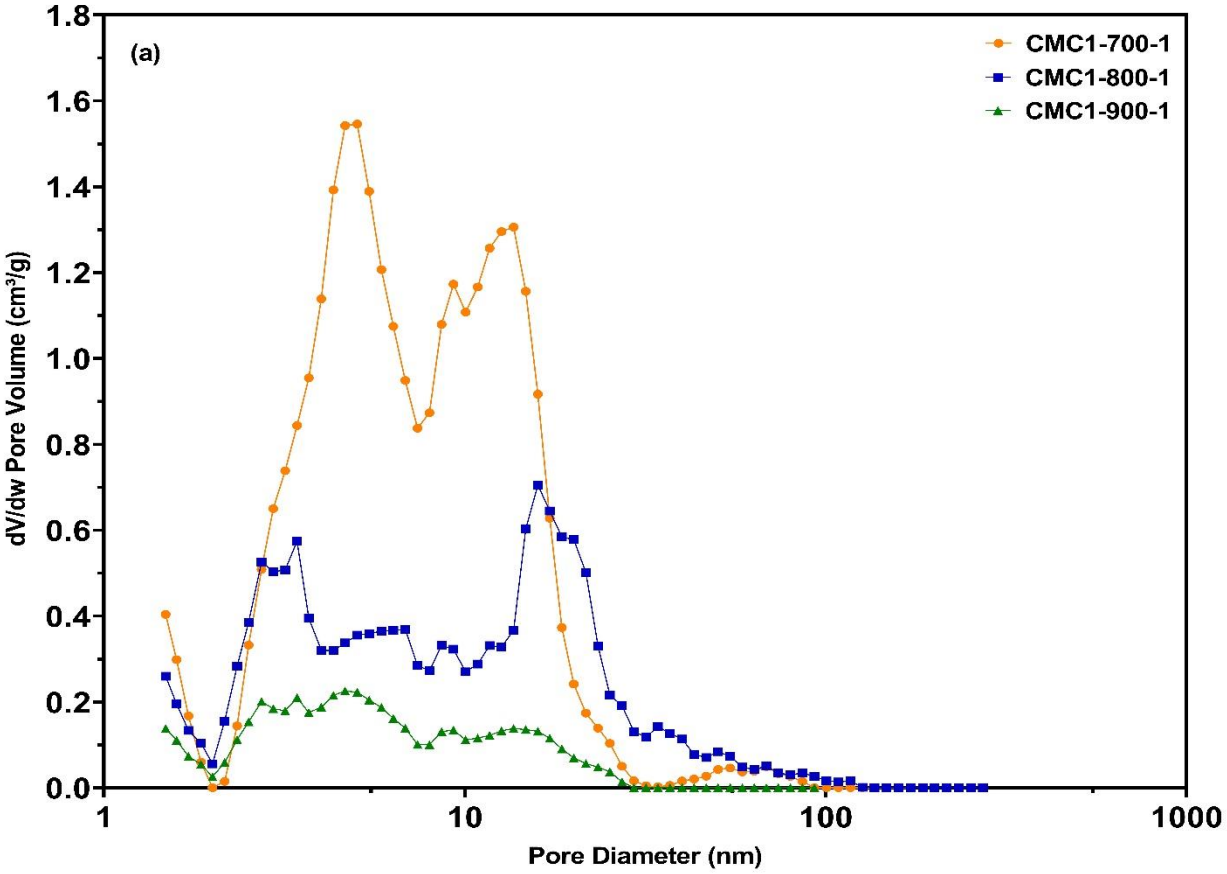

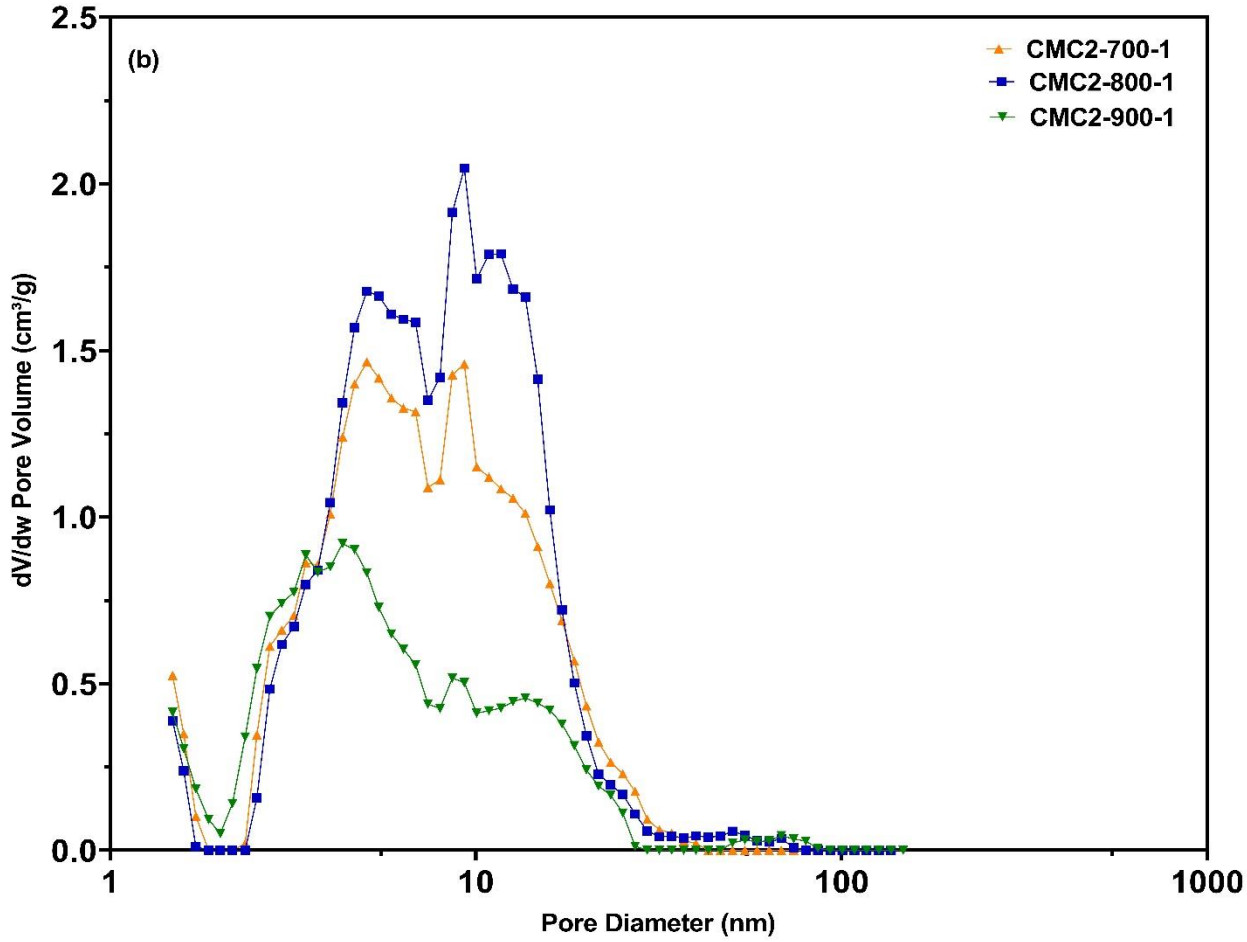

Figure 6.3 Pore size distributions of (a) CMC1 and (b) CMC2 carbons synthesized at different carbonization temperatures.

6.2.1.2 Effect of chitosan to silica mass ratio

The effectiveness of various chitosan-to-silica ratios on the final structure of the carbon materials was as well studied by using MCF2 as the silica template to prepare mesoporous carbons with different chitosan-to-silica ratios, ranging from 0.5 to 3 at carbonization temperature of 700 and 800 ˚C, and the results are presented in Figure 6.4. All the nitrogen adsorption-desorption isotherms collected for CMC2-700 and CMC2-800 samples (Figures 6.4a and b) demonstrated similar behavior to that of the

carbon materials obtained at a chitosan-to-silica ratio of 1 presented in Figure 6.2, which is characteristics of type IV(a) according to IUPAC classification, with H2(b) hysteresis loop, indicating the existence of large quantity of mesopores (Thommes et al., 2015). At 700 ˚C (Figure 6.4a), the CMC2 samples obtained at a low mass ratio of 0.5-1 exhibited a pronounced condensation step by a rapid increase in nitrogen uptake at high relative pressure, indicating an increase in pore volume.

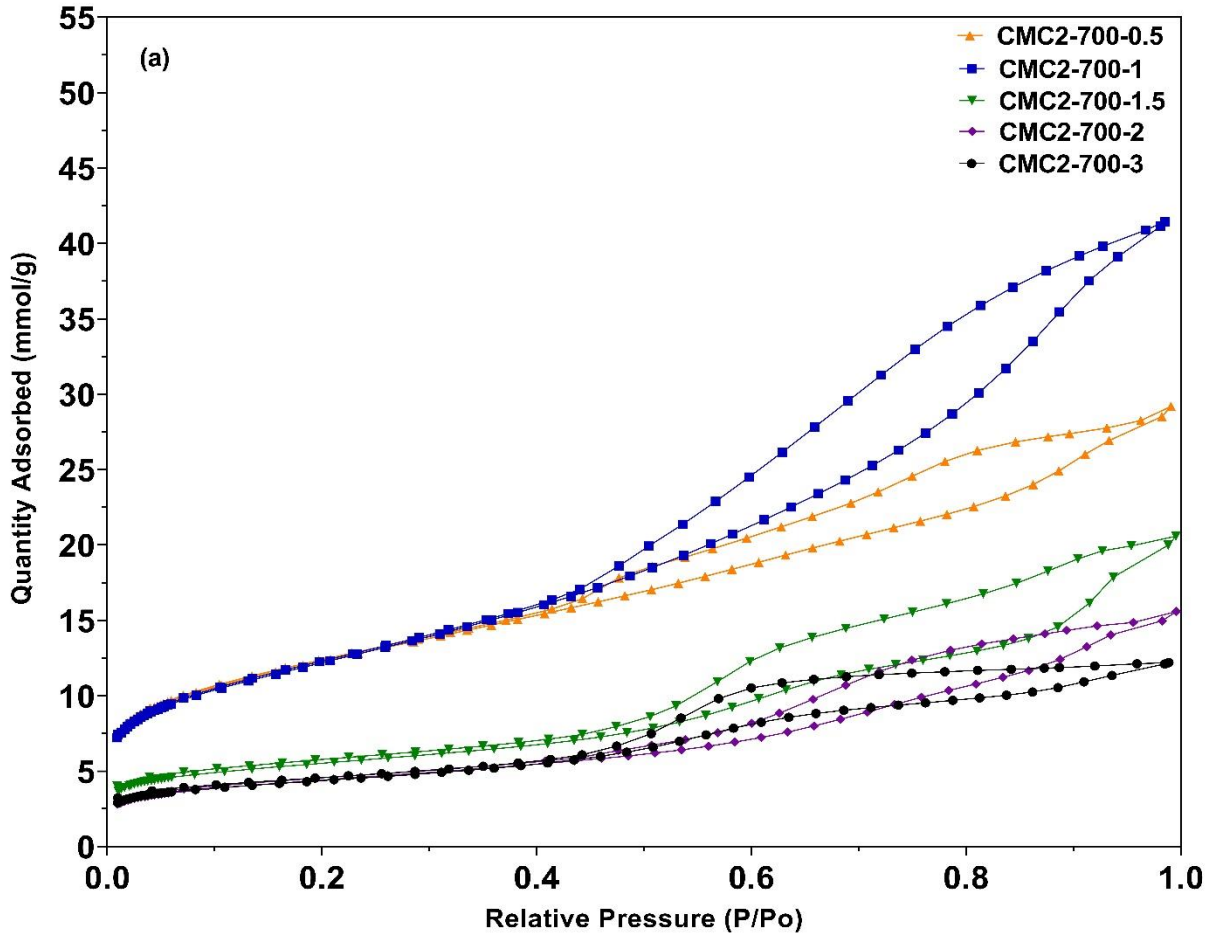

Figure 6.4 Nitrogen adsorption-desorption isotherms of CMC2-700 (a) and CMC2-800 (b) prepared from MCF2 silica template using different chitosan/template ratios by mass

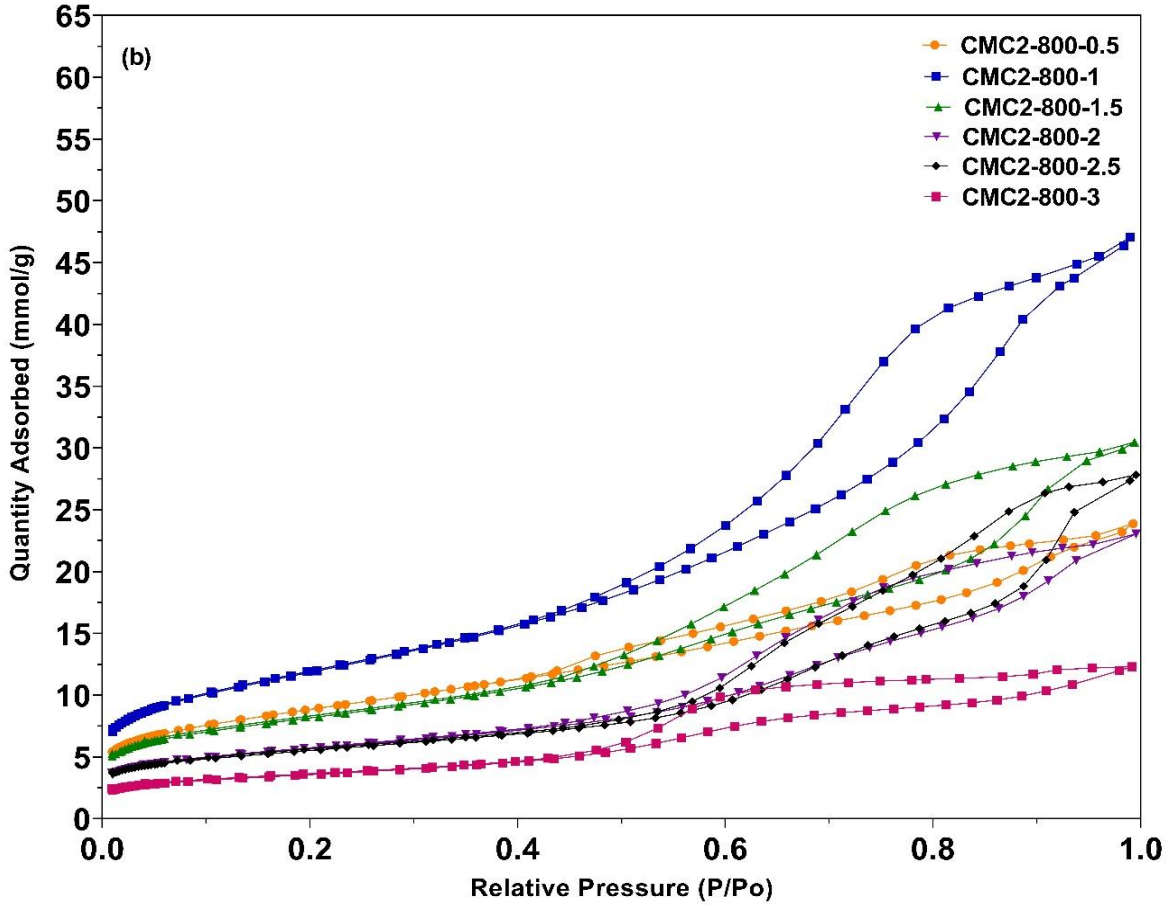

Figure 6.4 Nitrogen adsorption-desorption isotherms of CMC2-700 (a) and CMC2-800 (b) prepared from MCF2 silica template using different chitosan/template ratios by mass

As the chitosan to silica ratio increased to a higher mass ratio from 1.5 to 3, the shape of the hysteresis loop for CMC2-700-1.5, CMC2-700-2, and CMC2-700-3 became gradually narrowed, and the amount of N_2 adsorbed decreased steadily, being indicative of the decrease in the total pore volume of the final carbons. When the carbonization was increased to 800 ˚C, the CMC2-800 carbons (Figure 6.4b) showed a similar behavior of increment in N_2 adsorption capacity for carbons with a low chitosan-to-silica ratio (CMC2-800-0.5 and CMC2-800-1). A gradual drop in N_2 uptake as the chitosan-to-silica ratio increases from 1 to 3 was observed. Compared to the N_2 adsorption-desorption isotherms of CMC2-700 carbon materials, at similar

chitosan-to-silica ratios, the CMC2-800 carbons showed a higher N_2 uptake, indicating a higher pore volume in these carbons.

The detailed textural properties of CMC2-700 and CMC2-800 carbon samples are summarized in Table 6.2. All chitosan carbons prepared showed high surface areas (285-983 m^2/g) and large pore volumes (0.39-1.32 cm^3/g). It can be found that at 700 ˚C, the CMC2 series samples obtained at a low chitosan-to-silica ratio of 0.5 to 1 showed an increasing BET surface area and total pore volume from 981 m^2/g, 0.78 cm^3/g to 983 m^2/g, and 1.13 cm^3/g. However, when the chitosan-to-silica was increased to a higher mass ratio of 3, the resulting carbon materials showed a decreasing trend in both BET surface area and pore volume to only 351 m^2/g and 0.34 cm^3/g (CMC2-700-3). The decreased BET surface area and total pore volume of the samples with increasing silica-to-carbon ratio were due to the additional amount of carbon (chitosan) deposited at the external surface of the MCF silica template that occupied the pore space and therefore reduced the pore volume (Shao et al., 2022). This can be further verified by the average pore size, which decreases with increasing the chitosan-to-silica ratio from 1 to 3. A similar evolution trend of porosities was observed in the CMC2-800 samples at a low mass ratio of 0.5 to 1 and a decreasing trend of both surface area and pore volume at high chitosan to silica ratio of 3. Among all the CMC2-700 and CMC2-800 carbons, the sample (CMC2-800-1) prepared with a low chitosan-to-silica ratio of 1 by using MCF2 as a template showed the highest mesopore volumes of 1.20 cm^3/g, which is higher than those of mesoporous carbons with mesopore volume up to 0.77 cm^3/g (Wang et al., 2019) or mesoporous carbons with mesopore volume of 0.81 cm^3/g (Wang et al., 2020a). This suggests that the large mesopore volume of the silica hard template benefits the development of mesoporosity of the derived mesoporous carbons.

Table 6.2 Surface textural properties of chitosan-derived mesoporous carbons (CMC2-700 and CMC2-800) prepared using different chitosan-to-silica mole ratios.

Sample	S_{BET} (m^2/g)	V_{total} (cm^3/g)	V_{meso} (cm^3/g)	V_{micro} (cm^3/g)	Average pore size (nm)
CMC2-700-0.5	981	0.78	0.57	0.20	5.2
CMC2-700-1	983	1.13	0.99	0.14	6.5
CMC2-700-1.5	443	0.60	0.50	0.08	8.0
CMC2-700-2	353	0.46	0.39	0.06	7.5
CMC2-700-3	351	0.34	0.27	0.07	5.6
CMC2-800-0.5	710	0.66	0.52	0.13	5.6
CMC2-800-1	953	1.32	1.20	0.12	7.1
CMC2-800-1.5	653	0.92	0.82	0.10	6.9
CMC2-800-2	444	0.72	0.64	0.07	7.8
CMC2-800-2.5	439	0.91	0.81	0.06	9.7
CMC2-800-3	285	0.39	0.33	0.04	6.1

Figures 6.5 (a, b) shows the pore size distributions of CMC2-700 and CMC2-800 samples synthesized with chitosan-to-silica ratios from 0.5 to 3. As can be seen, both CMC2-700 and CMC2-800 carbon materials preserved the bimodal pore size distributions with micropores centered at less than 1.4 nm, small mesopores centered at 5-6.3 nm, and large mesopores centered at 10-21.6 nm. For the CMC2-700 samples (Figure 6.5a) with the intended chitosan-to-silica ratio of 0.5 to 3, the pore size of the small mesopores transformed gradually into a narrower pore size distribution with a decrease in peak intensity, indicating the mesopore becomes more uniform while the pore volume reduces as the chitosan-to-silica ratio increases. The PSDs of the large mesopores of CMC2-700-0.5, CMC2-700-1, CMC2-700-1.5, and CMC2-700-2 gradually broadened, and the intensity of the pore peaks sharply dropped, especially for CMC2-700-3. This suggests that the increase in chitosan loading level leads to the

blockage of pore space of MCF after carbonization, resulting in the reduction of large mesopores, while the small mesopores originated from the removal of silica pore walls were well preserved. A similar trend was also exhibited by the pore size distributions of CMC2-800 carbon materials (Figure 6.5b).

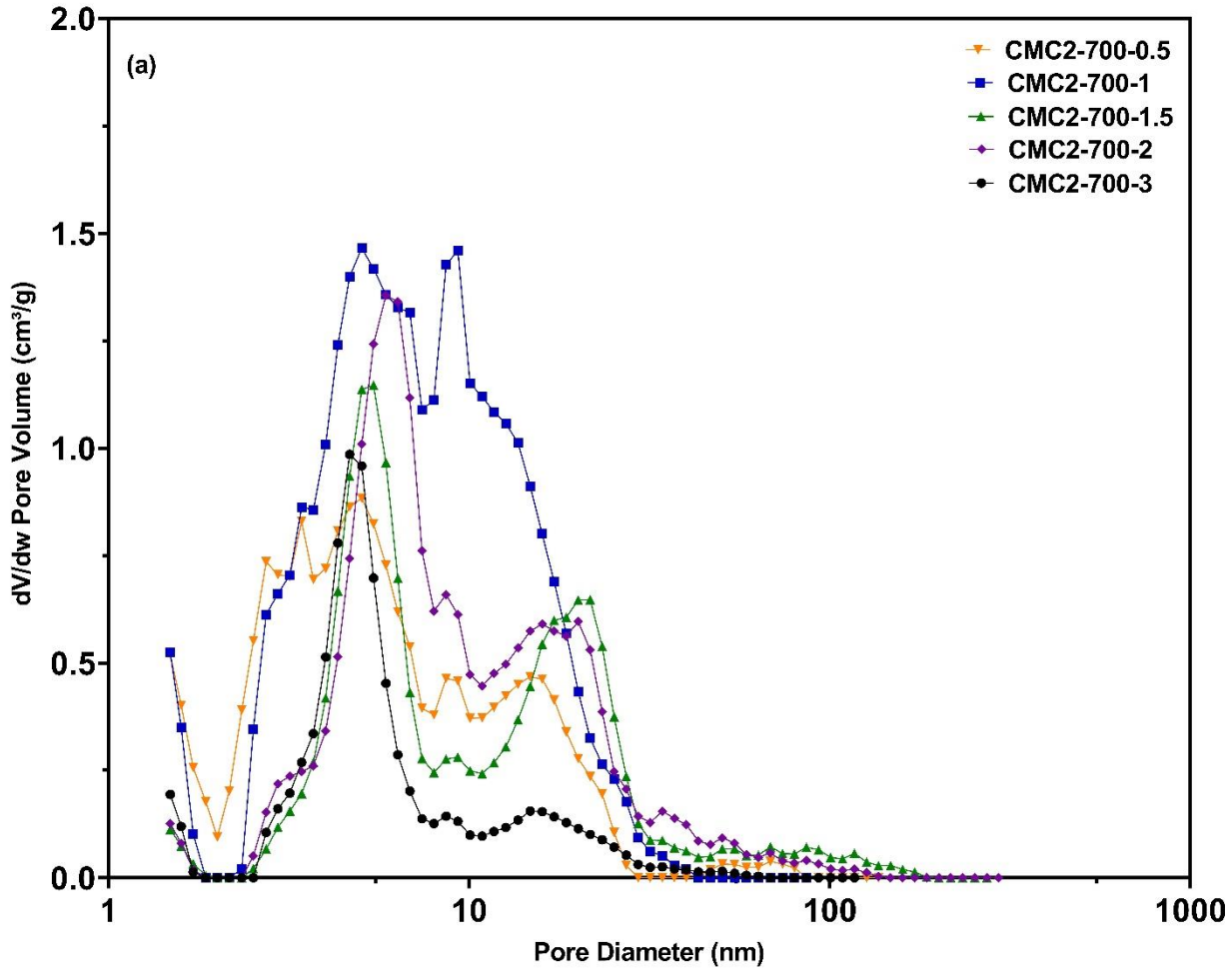

Figure 6.5 Pore size distributions of CMC2-700 (a) and CMC2-800 (b) prepared from MCF2 silica template using different chitosan/template ratios by mass.

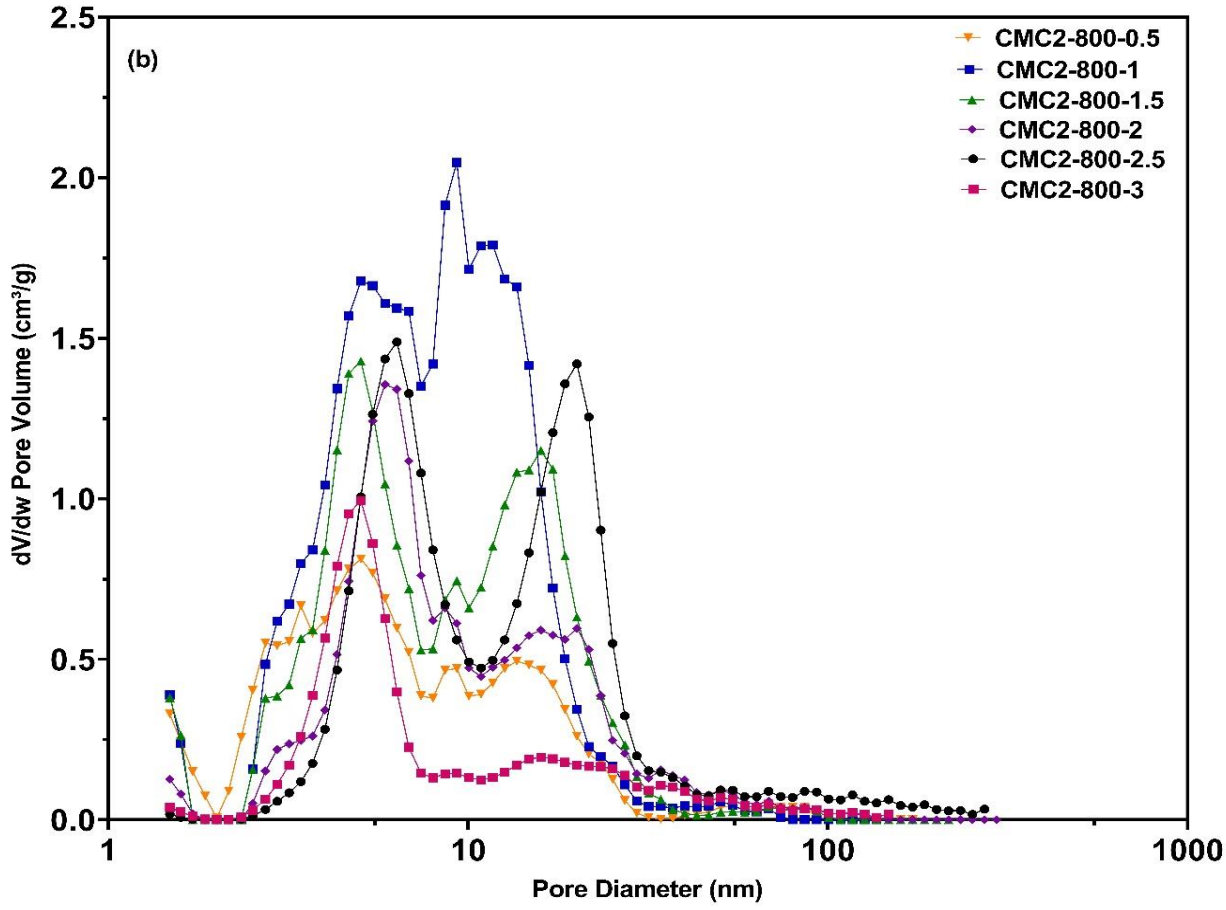

Figure 6.5 Pore size distributions of CMC2-700 (a) and CMC2-800 (b) prepared from MCF2 silica template using different chitosan/template ratios by mass.

6.3 Morphology

Figure 6.6 shows the morphological features of CMC2-800 produced by varying the silica-to-chitosan ratio from 1 to 3, examined using the SEM at low and high magnifications. All the CMC2-800 carbons are in the granular form, and the hexagonal structure of the 3D silicious cellular foams was well preserved in the mesoporous carbons. For the CMC2-800 produced with a chitosan-to-silica mass ratio of 1, the sample is composed of disconnected particles with a high degree of uniformity (Figure

6.6a-c). For the CMC2-800 carbons obtained with the chitosan-to-silica mass ratios of 2-3 (Figure 6.6d-i), the high-resolution images showed that the surface morphologies transformed into densely large mesopore and less sharp aggregates (Figure 6.6d-i). This is because a high amount of chitosan loading leads to the coating of chitosan on the external surface of the MCF template, which can cause carbon deposition on the external surface of the carbons.

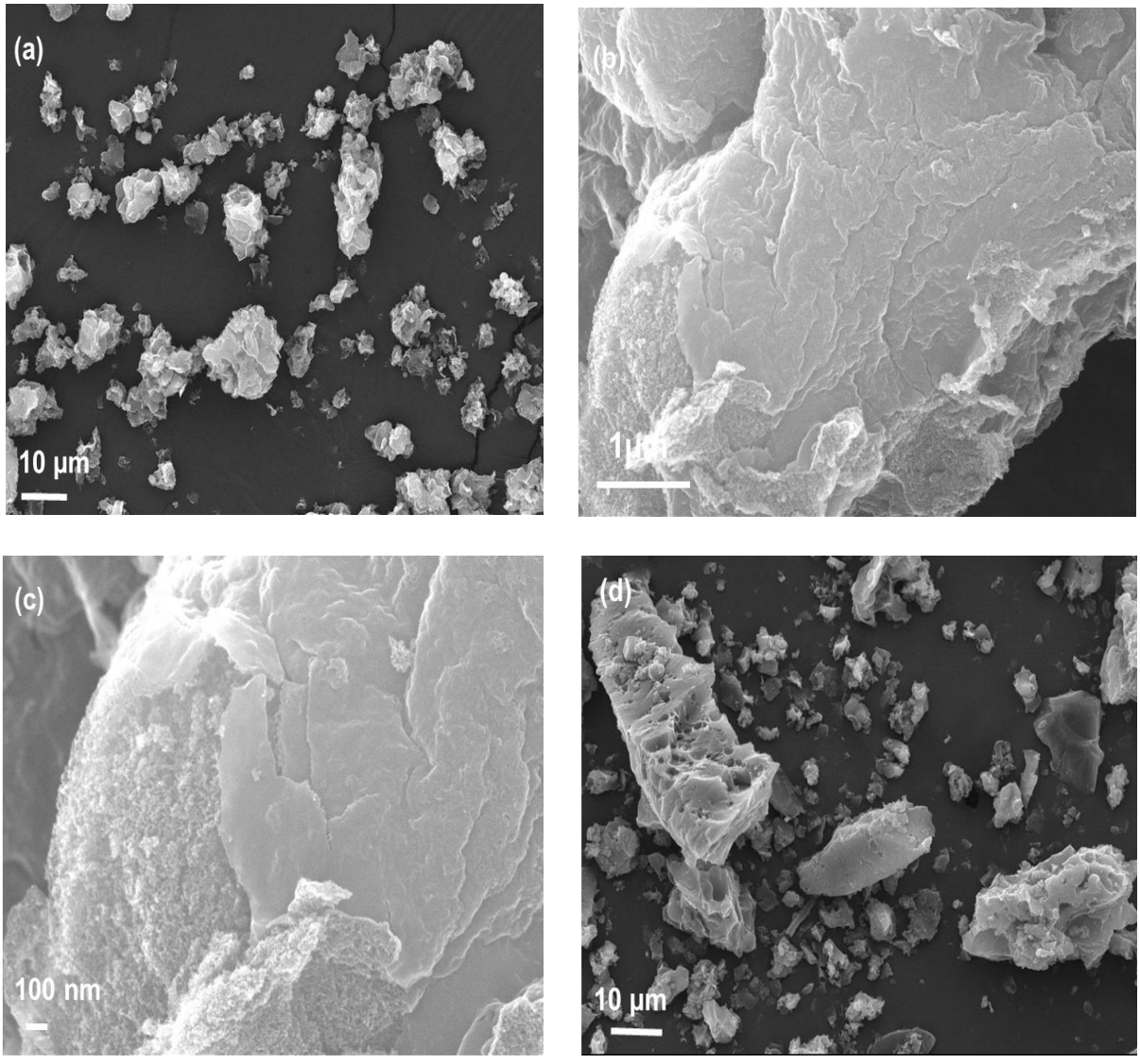

Figure 6.6 SEM images of CMC2 obtained at 800 ˚C with a silica-to-chitosan mass ratio of 1 (a-c), 2 (d-f), and 3 (g-i)

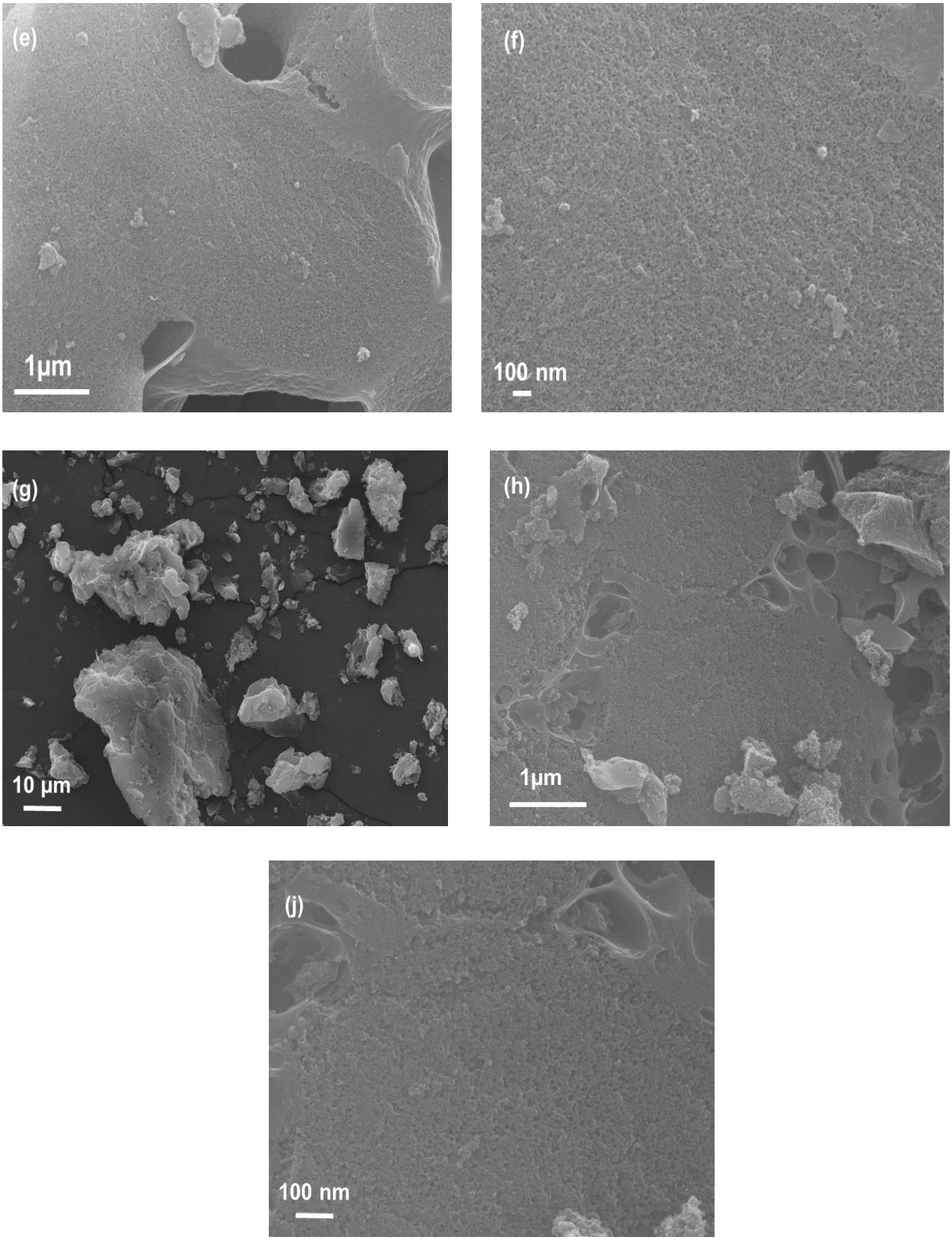

Figure 6.6 SEM images of CMC2 obtained at 800 ˚C with a silica-to-chitosan mass ratio of 1 (a-c), 2 (d-f), and 3 (g-i)

The TEM images of CMC2-800-1 are shown in Figure 6.7a-c. These images revealed the ordered characteristic of mesopores, and the 3D interconnectivity of MCF is well maintained in the hard-templated mesoporous carbons. The MCF-templated carbon CMC2-800-1 exhibited ordered, spherical mesopores with a 3-dimensional interconnected porous structure varying in size from 5 to 50 nm. Moreover, micropores (< 2 nm) were also observed.

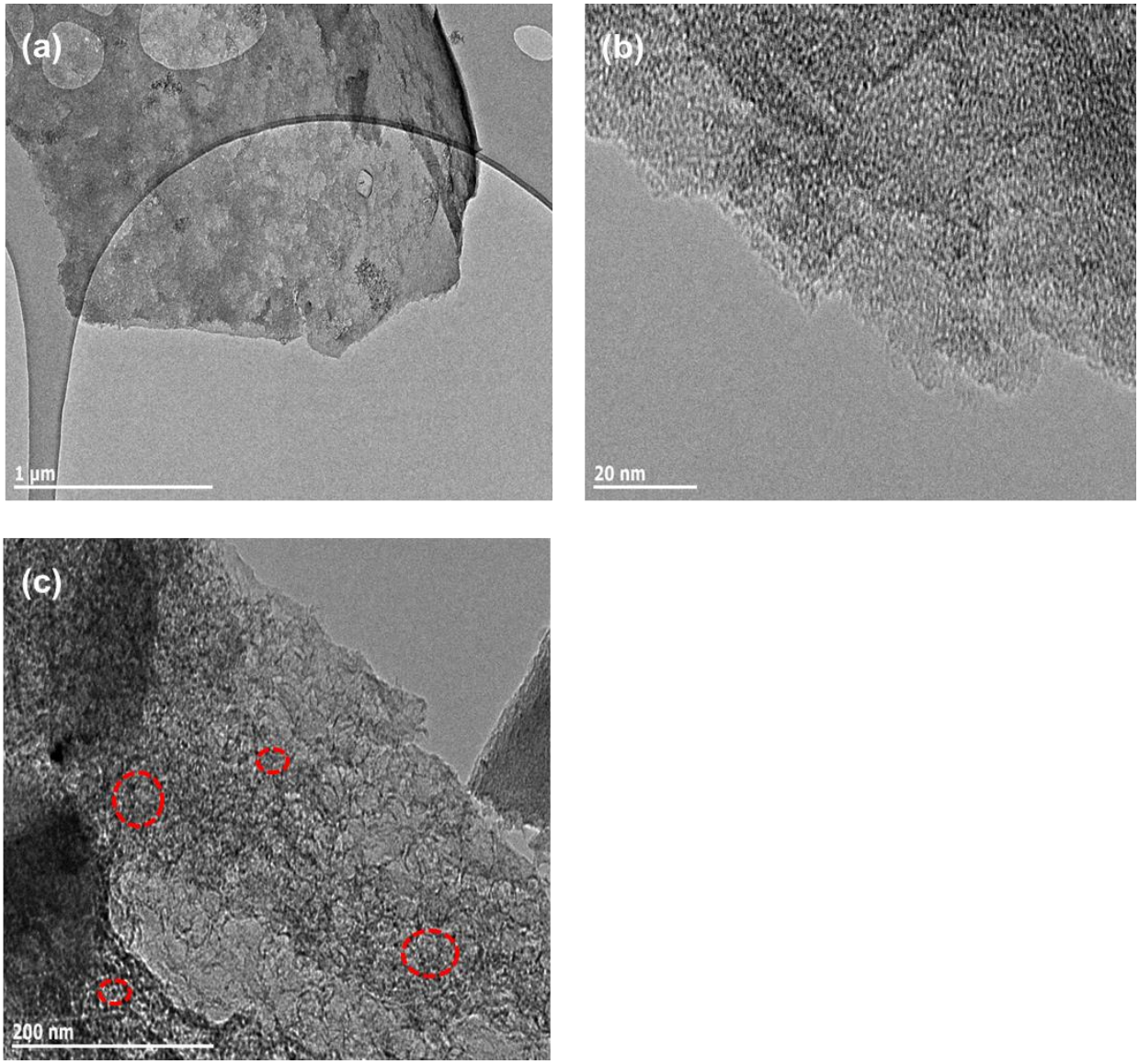

Figure 6.7 TEM images of CMC2-800-1 (a-c)

6.4 Characterisation of chitosan-derived mesoporous carbons

6.4.1 Fourier transform infrared spectroscopy (FTIR) analysis.

Figure 6.8a shows the FTIR spectra of pure chitosan and chitosan-derived mesoporous carbons prepared at carbonization temperatures of 700, 800, and 900 ˚C. The FTIR spectrum for pure chitosan (CS) is characterized by vibration absorption of peaks at approximately 3355 and 3290 cm^{-1} assigned to the R-NH and R-OH groups (Sneddon et al., 2015). The strong C-H vibration is shown at 2900 cm^{-1} (Bibi et al., 2015). The absorption peak belonging to the C=O of amide Ⅰ shows at 1646 cm^{-1}, whereas the NH_2 bending vibration of the primary amine group appears at 1590 cm^{-1} (Lezanska et al., 2018; Ou et al., 2016). The absorption band at 1456 cm^{-1} can be attributed to the hydroxyl group of chitosan. The band at 1374 cm^{-1} represents the stretching vibrations of the C-O group (Drabczyk et al., 2020). The C-O-C stretches, which are characteristics of the saccharine structure, can be seen at 1025 and 885 cm^{-1} (Sneddon et al., 2015; Bibi et al., 2015), while the peak at 522 cm^{-1} is assigned to the bending of NH (Drabczyk et al., 2020). For the CMC2 samples carbonized at various temperatures, as shown in Figure 6.8a, the peak intensities of CMC2-700-1, CMC2-800-1, and CMC2-900-1 at 1590 cm^{-1} and 1025 cm^{-1} sharply decreased with the increase in carbonization temperature from 700 to 900 ˚C. This is possibly attributable to the increased amount of heat treatment, especially at high temperatures. Figure 6.8b shows the FTIR spectra of CMC2 samples prepared at 800 ˚C with silica-to-chitosan mass ratios varying from 0.5 to 3. It can be found that all the samples preserved the FTIR spectra, which is similar to that of the carbon samples prepared at chitosan to silica ratio of 1, shown in Figure 6.8 a. However, the absorption

peak intensities of all the CMC2 carbons are almost undetectable with the increase in a silica-to-chitosan mass ratio from 0.5 to 3. It is worth noting that most of the peaks of CMC-800 were reduced or eliminated with the silica-to-chitosan mass ratio increased to 3.

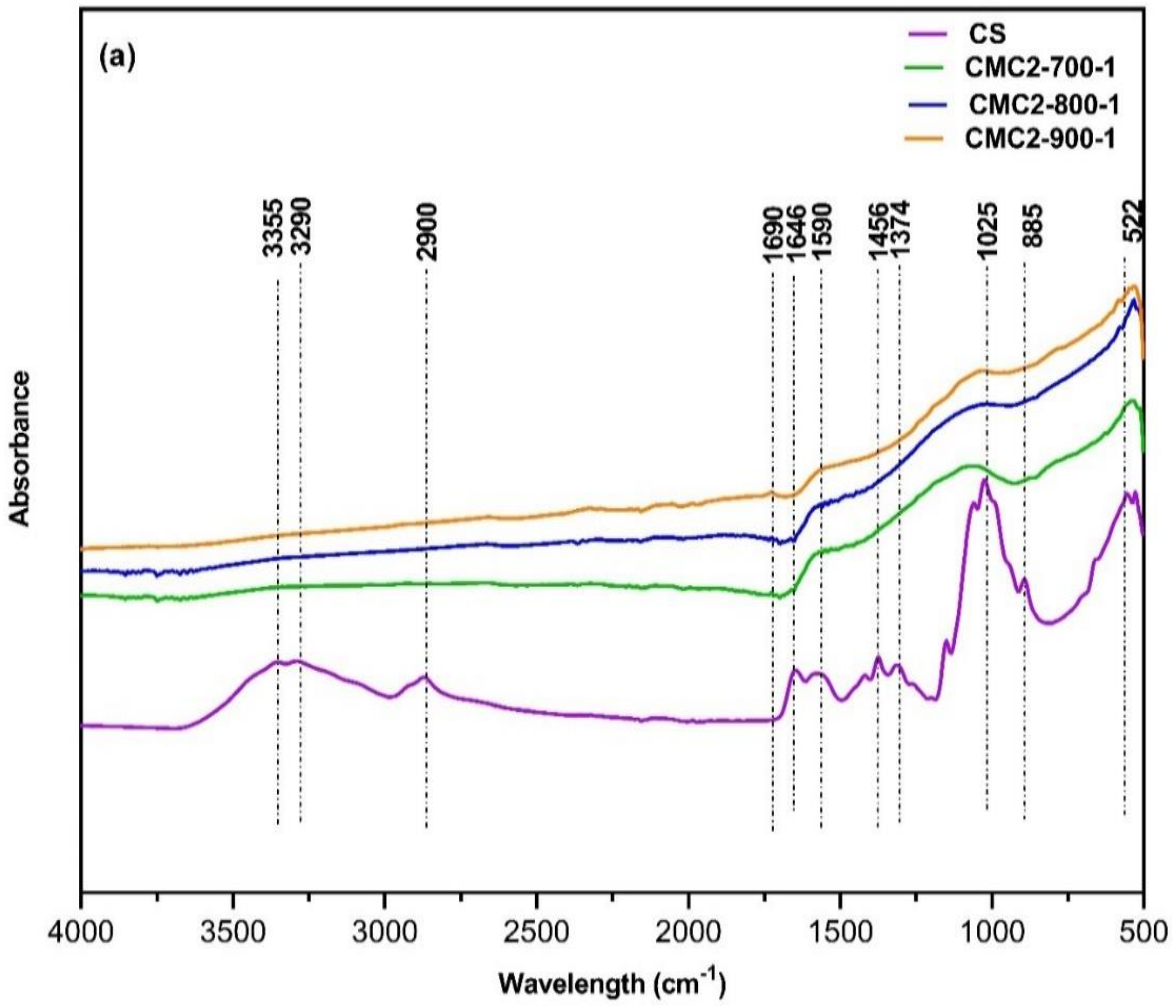

Figure 6.8 FTIR spectra of chitosan (CS), CMC2 carbons prepared at various carbonization temperatures (a), and CMC2-800 carbons prepared at different chitosan-to-silica mass ratios (b).

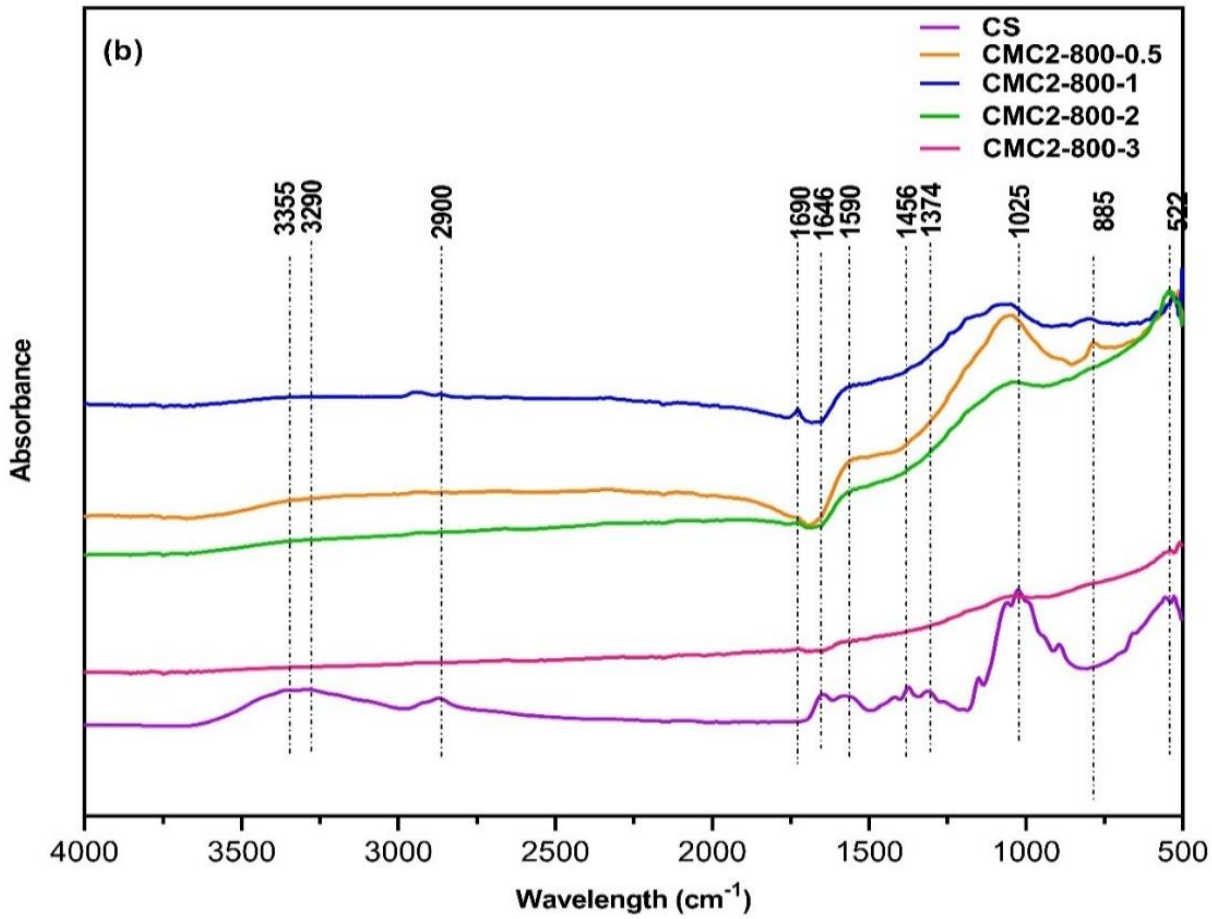

Figure 6.8 FTIR spectra of chitosan (CS), CMC2 carbons prepared at various carbonization temperatures (a), and CMC2-800 carbons prepared at different chitosan-to-silica mass ratios (b).

6.4.2 Elemental analysis (EA)

The elemental analysis of the chitosan-derived mesoporous carbon materials is shown in Table 6.3.

Table 6.3 Chemical composition from elemental analysis of CMC1 and CMC2 obtained at different carbonization temperatures, and CMC2-700-1 prepared with different silica-to-chitosan mole ratios.

Sample	C (wt%)	N (wt%)	N/C ratio	H (wt%)	O* (difference) (wt%)	Ash (wt%)
CMC1-700-1	81.75±0.07	10.00±0.03	0.105	0.80 ±0.11	3.57 ± 0.09	3.73 ±0.01
CMC1-800-1	79.61±0.09	8.57 ±0.05	0.092	0.85 ±0.12	3.31 ± 0.06	7.66 ±0.08
CMC1-900-1	77.67±0.07	7.95 ± 0.13	0.088	0.98 ±0.08	2.90 ± 0.16	10.19±0.11
CMC2-700-1	83.73±0.09	9.57 ± 0.13	0.098	0.77 ±0.09	2.95 ± 0.13	2.99 ± 0.12
CMC2-800-1	82.48±0.08	8.79 ± 0.05	0.091	0.71 ±0.07	2.52 ± 0.13	5.49 ± 0.03
CMC2-900-1	82.70±0.04	7.98 ± 0.06	0.083	0.76 ±0.02	3.06 ± 0.04	5.40 ± 0.08
CMC2-700-0.5	76.26±0.06	8.20 ± 0.05	0.092	1.06 ±0.13	7.97 ± 0.12	6.51 ± 0.08
CMC2-700-2	76.99±0.05	9.23 ±0.02	0.103	0.88 ±0.06	3.94 ± 0.11	8.95 ± 0.20
CMC2-700-3	73.49±0.16	9.03 ± 0.03	0.105	0.83 ±0.14	4.73 ± 0.02	11.88±0.03

O* = 100 – (C + N + H +Ash), Values presented as the means of triplicates with standard deviation (SD) of the mean.

Table 6.3 shows the C, N, H, and O contents on the surface of the CMC1 and CMC2 carbon materials obtained from elemental analysis. Generally, the EA results revealed that all the CMC1 and CMC2 samples mainly contained carbon (74-84 wt%), followed by nitrogen (8-10 wt%), oxygen (2.5-3.5 wt%), and hydrogen (0.7-0.9 wt%). Clearly, the chitosan-derived mesoporous carbons exhibit high nitrogen content of up to 10 wt%. It can be found that a certain amount of ash is present in the final carbons, which can be attributable to the silica residue remaining in the final carbon after NaOH washing. The ash content increased with increasing carbonization temperature or chitosan-to-silica ratio due to the reduced pore volume that makes the silica template

trapped in the carbon matrix and challenging to be washed out. This also explains the lower ash content of CMC2 carbons than CMC1 carbons prepared under the same condition. For the CMC1 carbons, at a fixed chitosan-to-silica mass ratio of 1, the carbon, nitrogen, and oxygen contents decreased gradually from 82.00 wt%, 10.00 wt%, and 3.57 wt% at a carbonization temperature of 700 ℃ to 77.67 wt%, 7.95 wt%, and 2.90 wt% at 900 ℃, respectively. An increase in the carbonization temperature from 700 to 900 ℃ led to a steady decrease in the N/C atomic ratio from 0.105 to 0.088, indicating the extensive removal of nitrogen in the form of gas at high temperatures due to its low thermal stability (Shao et al., 2020; Xu et al., 2020). Interestingly, a similar trend was observed for the carbon, nitrogen, and hydrogen contents in the CMC2 carbons when MCF2 was used as a template. Among all the carbon materials synthesized, the sample prepared using MCF1 at 700 ℃ with a chitosan/MCF ratio of 1:1 (CMC1-700-1) shows the highest N content of 10.00 wt% with an N/C atomic ratio of 0.105. The data reported in the literature for the chitosan-derived carbons exhibit a good agreement with the level of nitrogen content. For example, Titrici et al. (2012) found a nitrogen content of 9.1 wt% for hydrothermal carbons and 7-11 wt% for aerogel-derived carbons.

On the other hand, at a fixed temperature of 700 ℃, with the increase in chitosan-to-silica mass ratio from 0.5 to 1, there was an increase in nitrogen content from 8.20 wt% to 9.57 wt%. However, a further rise in chitosan-to-silica mass ratio to 3 decreased nitrogen content to 9.03 wt.%. This might be attributed to the fact that at a low chitosan-to-silica mass ratio, there is a high amount of Si-OH in the system with low amounts of OH and NH_2 groups on the chitosan available for hydrogen bonding. Therefore, there is a high tendency of contact between NH_2 with Si-OH coupled with a strong binding force and 3D structure, leading to a larger amount of N in the carbon

during the calcination process. However, the OH and NH_2 groups on chitosan barely produce a 3D porous structure at a high chitosan-to-silica ratio. Therefore, a small amount of N is produced following the carbonization process due to evaporation into the N atmosphere (Wang et al., 2019).

6.4.3 X-ray photoelectron spectroscopy (XPS)

The atomic composition and electronic state of nitrogen and carbon of the CMC2 samples at different carbonization temperatures were determined by the XPS measurements.

Table 6.4 Elemental composition of chitosan-derived mesoporous carbons as determined by XPS.

Samples	Elemental composition (at.%)		
	C	N	O
CMC2-700-1	88.89	6.78	4.51
CMC2-800-1	89.16	4.56	5.47
CMC2-900-1	89.41	3.83	7.10

As expected, the XPS scan spectra of CMC2-700-1, CMC2-800-1, and CMC2-900-1 mainly consist of spectral peaks for carbon, nitrogen, and oxygen. The derived elemental composition of all the carbon samples is provided in Table 6.4. It was observed that the amount of carbon element in the chitosan-derived mesoporous carbon materials slightly increased from 88.89 to 89.41 at%, and the amount of nitrogen element reduced from 6.78 to 3.83 at% upon increasing the carbonization temperature from 700 to 900 ˚C. The results also indicate that the measured surface carbon content by XPS was considerably higher than the bulk carbon content

measured by EA analysis, suggesting that some of the silica hard templates are intercalated into the bulk phase of the carbon matrix and are hard to be removed.

The C1s XPS spectra of the chitosan-derived mesoporous carbons are shown in Figure 6.8a-c. The peak centered at 284.6 eV, representing the sp2-bonded (C=C) carbon atom, is the most intense peak of the C1s peak (Wang et al., 2020a). The successive tail of asymmetric C1s sub-peaks at binding energies of 285.7 eV and 287.2 eV, and 289.3 eV originated from the presence of carbon atoms bonded to nitrogen (C=N) and different oxygen functional groups (C=O) and (O-C=N), respectively (Song et al., 2015).

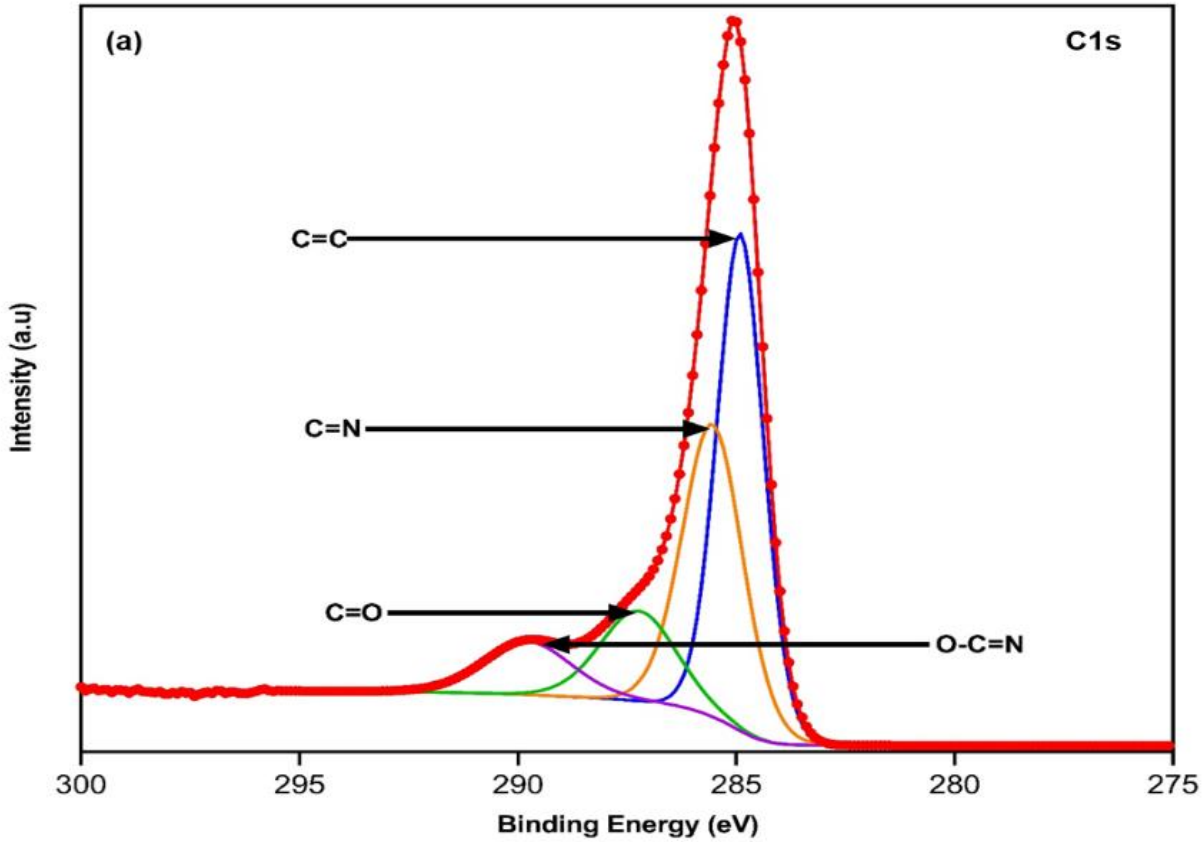

Figure 6.9 XPS high-resolution spectra C1s of CMC2-700-1 (a), CMC2-800-1 (b), and CMC2-900-1 (c).

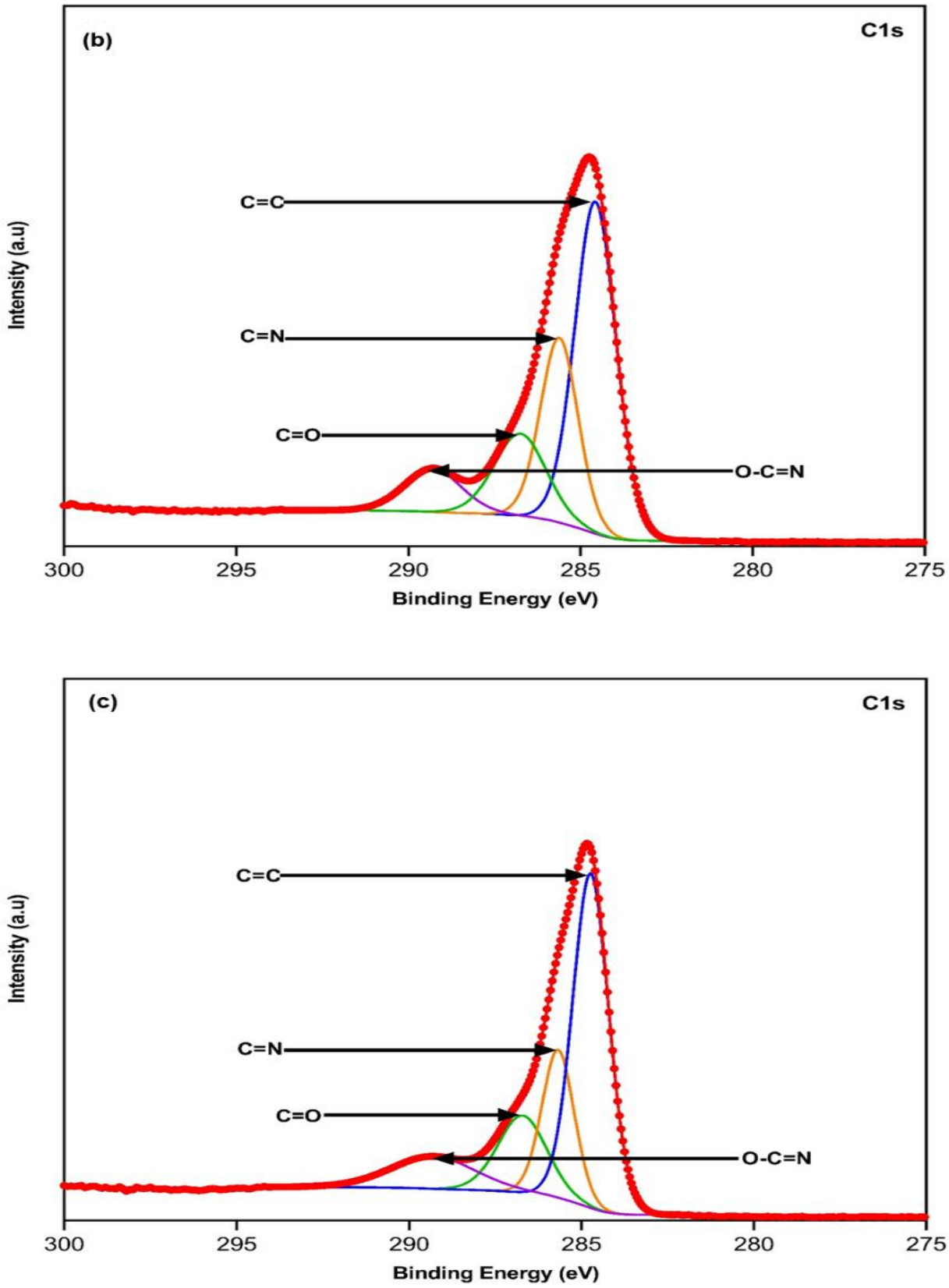

Figure 6.9 XPS high-resolution spectra C1s of CMC2-700-1 (a), CMC2-800-1 (b), and CMC2-900-1 (c).

The high-resolution N1s XPS spectra of CMC2-700-1, CMC2-800-1, and CMC2-900-1 are shown in Figure 6.9d-f. Generally, it can be observed that the spectra of all the carbon materials are similar to each other, which indicates that the carbonization temperature had a negligible impact on the chemical bonding state of nitrogen. A peak differentiation and fitting were applied to deconstruct the N1s XPS spectrum into four peaks with corresponding binding energies centered at 398.5 eV (N-6), 400.7 eV (N-5), 402.8 eV (N-Q), and 404.2 eV (N-X). The N-6 peak is ascribed to pyridinic nitrogen, which is the most stable form of nitrogen at high temperatures (Pels et al., 1995; Olejniczak et al., 2013). The N-5 peak is attributed to pyrrolic nitrogen. The N-Q and N-X peaks represent quaternary nitrogen and pyridine N-oxide, respectively (Ghimbeu and Luchnikov 2018). Increasing the carbonization temperature from 700 to 900 ˚C resulted in a decrease in the relative peak intensities for the pyridinic and pyrrolic nitrogen components.

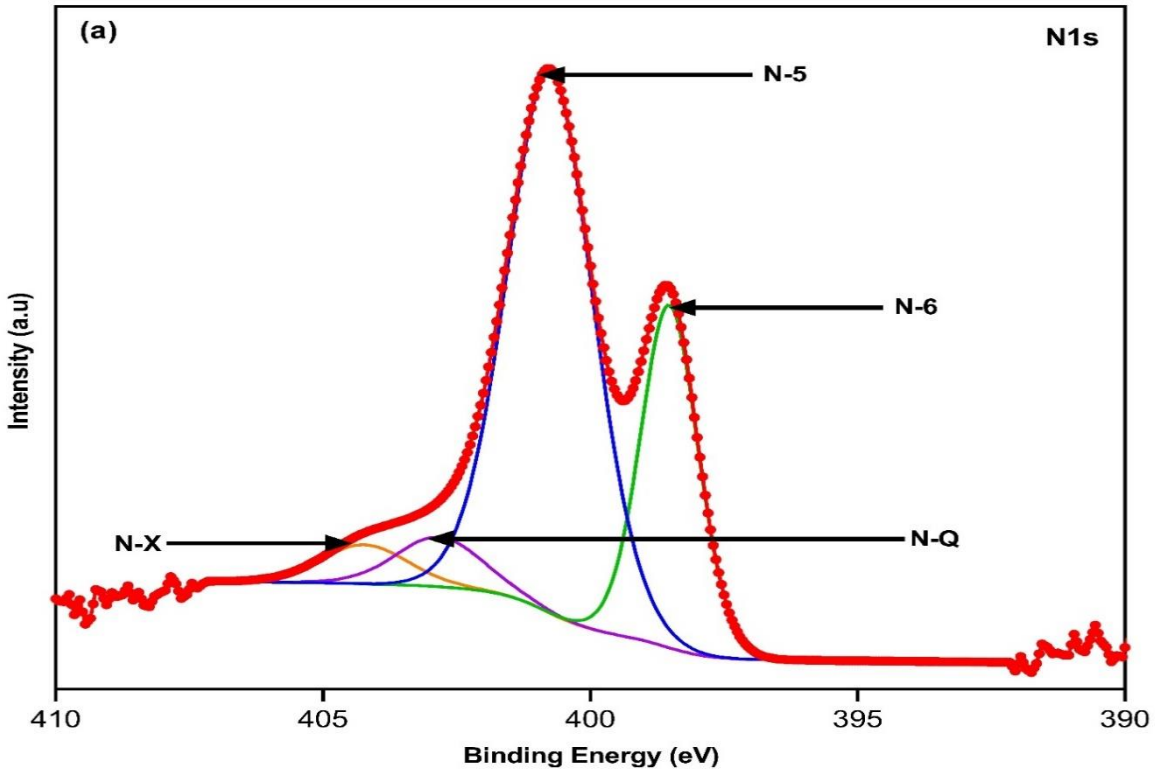

Figure 6.10 XPS high-resolution spectra N1s of CMC2-700-1 (a), CMC2-800-1 (b), and CMC2-900-1 (c).

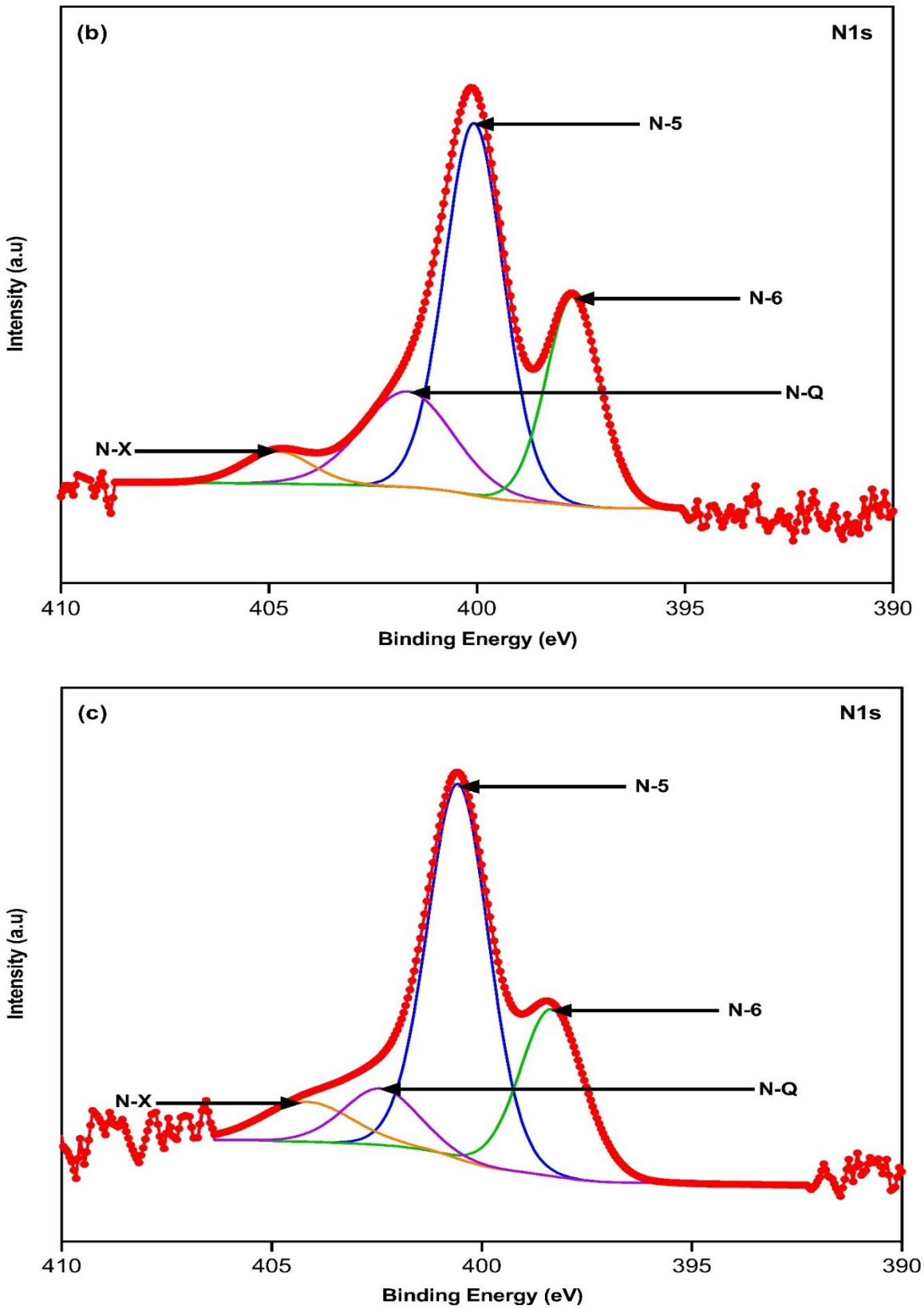

Figure 6.10 XPS high-resolution spectra N1s of CMC2-700-1 (a), CMC2-800-1 (b), and CMC2-900-1 (c).

The values of binding energy distributions and relative contributions of CMC2 carbons are summarized in Appendix 1. The pyridinic and pyrrolic nitrogen contents are the dominant components in all the carbon samples. Thus, the sample CMC2-700-1 showed the highest relative contributions of N-6 and N-5 (26.6 at% and 62.6 at%, respectively).

The pyridinic and pyrrolic nitrogen are known to enhance the pseudo-capacitance performance of mesoporous carbons (Guo et al., 2019; Shen and Fan, 2013; Kichambare et al., 2011). Thus, their relative contributions in this work could probably make them suitable electrode materials for energy storage. Other potential applications for such nitrogen-rich mesoporous carbons include CO_2 capture, adsorption of heavy metals, and catalysis (Valle-Vigon et al., 2013; Shen and Fan, 2013; Chen et al., 2013).

6.5 Conclusions.

In summary, a nanocasting method has been used successfully as a facile route to synthesize a wide range of nitrogen-rich ordered mesoporous carbons with high pore volume and large surface area, using 3D mesostructured cellular foam (MCF) as a template and readily available biopolymer “chitosan” as the carbon and nitrogen precursor. The present results demonstrated that the textural properties and the nitrogen content in the obtained chitosan-derived mesoporous carbons could be determined by synthesis conditions such as carbonization temperature, chitosan-to-silica ratio, and textural properties of the hard template (MCF1 and MCF2). The maximum achievable surface area, total pore volume, and mesopore size of CMC2 carbon materials prepared using the MCF2 template were much larger than CMC1

carbons obtained from the MCF1 silica template under similar synthesis conditions. The carbon CMC2-800-1 exhibited the highest mesopore volume of 1.20 cm^3/g with a BET surface area of 953 m^2/g. These chitosan-derived mesoporous carbons are essentially mesoporous and showed high nitrogen content of up to 10 wt%. The availability of a simple synthetic route for these novel nitrogen-rich mesoporous carbons can open new exciting opportunities for various applications such as energy storage, drug delivery, and CO_2 adsorption.

Chapter 7 Amine functionalized sustainable lignin-derived mesoporous carbons for CO_2 adsorption.

7.1 Introduction

Carbon dioxide (CO_2) is a significant greenhouse gas. It is mainly produced from industrial activities such as coal and biomass gasification under inert gas conditions and the combustion product of fossil fuels – coal, petroleum, and natural gas. According to the data reported by the Emissions Database for Global Atmospheric Research, fossil fuels contributed to approximately 35.76 Gt of global CO_2 emissions in 2016 (Janssens-Maenhout et al., 2017). Atmospheric CO_2 concentration has reached more than 25% over the past century due to the continuous use of fossil fuels in industrial and anthropogenic activities, which has a severe potentials threat as it creates environmental damage (Sriram et al., 2020; Cox et al., 2000; Plaza et al., 2008). The carbon capture and storage (CCS) techniques have the potential to reduce global CO_2 emissions and combat climate change (Metz et al., 2005).

The literature review discussed in Chapter 2, section 2.6.3, shows the great potential of mesoporous carbons as supports to prepare PEI-modified sorbents for CO_2 adsorption. However, most mesoporous carbons are synthesized via a complicated synthetic protocol and expensive and/or toxic precursors (Gadipelli et al., 2015; Tang et al., 2013; Wang et al., 2012a; Wang et al., 2013a; Wang et al., 2015). Meanwhile, the pore size of most mesoporous carbon, mainly determined by the template, was usually small (< 10 nm), which limited their potential application as support for

preparing PEI-based sorbents for CO_2 adsorption. Modern industry prefers renewable materials, specifically those obtained from low-cost, abundant, environmentally benign biomass (Titrici and Antonietti, 2010; Titrici et al., 2015).

7.2 Results and discussion

7.2.1 Pore structure of mesoporous carbons and PEI-impregnated adsorbents.

Lignin-derived mesoporous carbons with ordered 3D-interconnected porous structure, large pore size, and pore volume via a facile hard-templating approach using 3D spherical mesocellular foam silica (MCF) have been proposed and successfully developed, as shown in Chapter 4. The pore volume and pore size could be regulated by varying the preparation parameters, including the lignin-to-silica ratio and carbonization temperature. Given the most developed mesoporous structure of mesocellular foam silica (MCF2), with a large window size of 18.99 nm and pore volume of 3.58 cm^3/g, it was selected as a template and used to prepare lignin-derived mesoporous carbons. As a comparison, mesoporous carbons were also synthesized using mesoporous silica with a 2D porous structure with a smaller pore volume of 2.79 cm^3/g but a larger window size of 23.82 nm as a template. Both were used as support to prepare PEI-based sorbents. Figure 7.1 shows the N_2 adsorption-desorption isotherms of MC2-800-1 together with its PEI-loaded samples. As can be seen, the pristine MC2-800-1 (Figure 7.1a) exhibited a type IV isotherm with H2b hysteresis loop at medium and high relative pressure (P/Po), indicating the pore networks with ink-bottle shape mesopores (Donohue and Aranovich, 1999; Saikia et al., 2015). The pore size distribution is shown in Figure 7.1b. The carbon, MC2-800-1 presented a bimodal

mesoporous structure, with the mesopore diameters mainly centered at 20-27 nm and the small mesopore centered at about 4-10 nm. Figure 7.1a also shows the nitrogen adsorption isotherms of MC2-800-1 sorbents with different PEI loadings. As expected, the nitrogen adsorption capacity decreased with the increasing PEI loading level from 40 to 60 wt. %, indicating that amine molecules occupied the mesopores of the adsorbents. A hysteresis loop with reduced nitrogen adsorption capacity was observed for all PEI-based sorbents, suggesting preserving the pristine porous structure of mesoporous carbons. As shown in Figure 7.1b, the intensity of all peaks reduced drastically with increasing PEI loading from 40 to 60 wt%. More importantly, both micropores and small mesopores (4-10 nm) were reduced to nearly zero with different levels of PEI impregnation, indicating that all those small pores were occupied by the PEI impregnated.

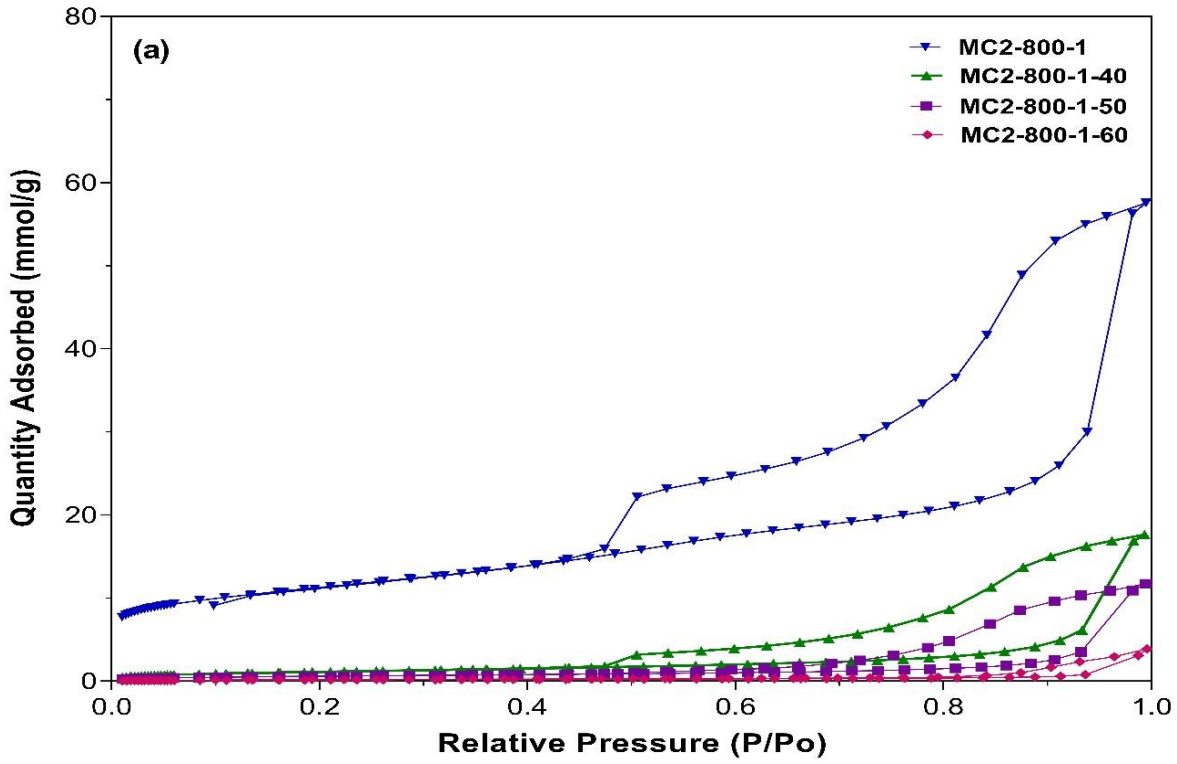

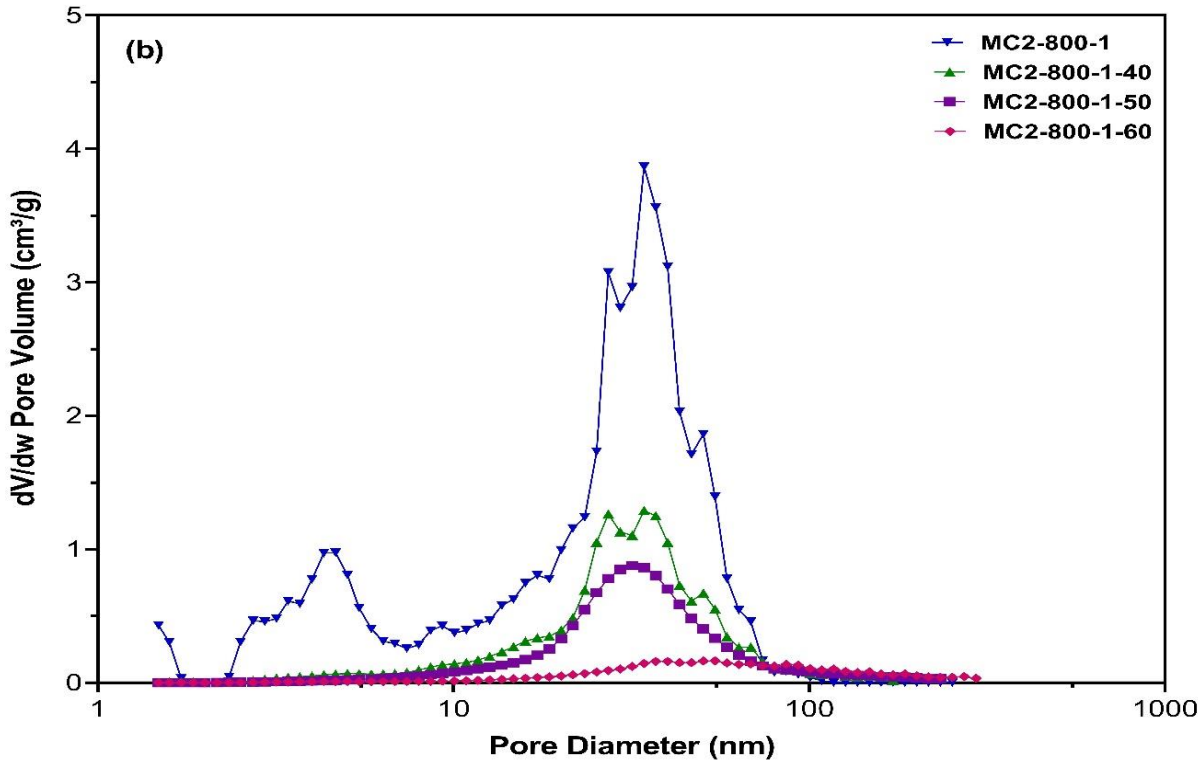

Figure 7.1 Nitrogen adsorption-desorption isotherms (a) and pore size distributions (b) of MC2-800-1 and different PEI/MC2-800-1 sorbents.

Table 7.1 summarizes the textural properties of all the samples. The pristine MC2 carbons possessed BET surface area in the range of 543-900 m^2/g, a total pore volume of 0.80-1.80 cm^3/g. In comparison, the BET surface area of the mesoporous carbons prepared using mesoporous silica with a 2D porous structure is similar (394-900 m^2/g). In contrast, the total pore volume of MCPQ carbons is much smaller than the MC2 samples prepared under similar conditions. More importantly, MCF-derived mesoporous carbons showed a much higher pore volume of large mesopores than the samples prepared using mesoporous silica with a 2D porous structure as a template. The large mesopores allow a high amount of PEI loading with good dispersion and could effectively improve amine accessibility and reduce the diffusion resistance of CO_2 molecules (Chen et al., 2021; Peng et al., 2019). After PEI loading, a sharp

decrease in BET surface area and mesopore volume of MC2-800-1 was observed with an increase in PEI loading level from 40 to 60 wt. %, confirming that PEI has been successfully impregnated into the mesopores of MC2-800-1. It is also notable that the adsorbent MC2-800-1-60 still had a surface area of 12 m^2/g and pore volume of 0.13 cm^3/g, indicating that there are still available porous spaces for CO_2 diffusion in the pores at such a high PEI loading level of 60 wt%.

Table 7.1 Surface textural properties of mesoporous carbon support before and after PEI loadings.

Sample	S_{BET}[a] (m^2/g)	V_{total}[b] (cm^3/g)	$V_{meso < 10 nm}$[c] (cm^3/g)	$V_{meso\ 10\text{-}100nm}$[d] ($cm^3/g$)
MC2-700-1	735	1.12	0.2297	0.7156
MC2-800-1	900	1.80	0.3260	1.2848
MC2-800-1-40	91	0.58	0.0417	0.5241
MC2-800-1-50	48	0.40	0.0184	0.3674
MC2-800-1-60	12	0.13	0.0054	0.0982
MC2-700-2	788	0.80	0.1421	0.4968
MC2-800-2	716	1.15	0.2602	0.7355
MC2-900-2	543	0.89	0.0884	0.7082
MCPQ-700-1	971	1.12	0.5150	0.4264
MCPQ-800-1	719	1.30	0.5081	0.6964
MCPQ-700-2	650	0.95	0.3237	0.4806
MCPQ-800-2	400	0.56	0.1913	0.2973
MCPQ-900-2	394	0.78	0.2380	0.4826

Note: a BET-specific surface area, b Total pore volume calculated at a relative pressure of 0.99, c Mesopore volume of pores smaller than 10 nm, d Mesopore volume of pores between 10-100 nm calculated by the DFT method.

7.3 Morphology

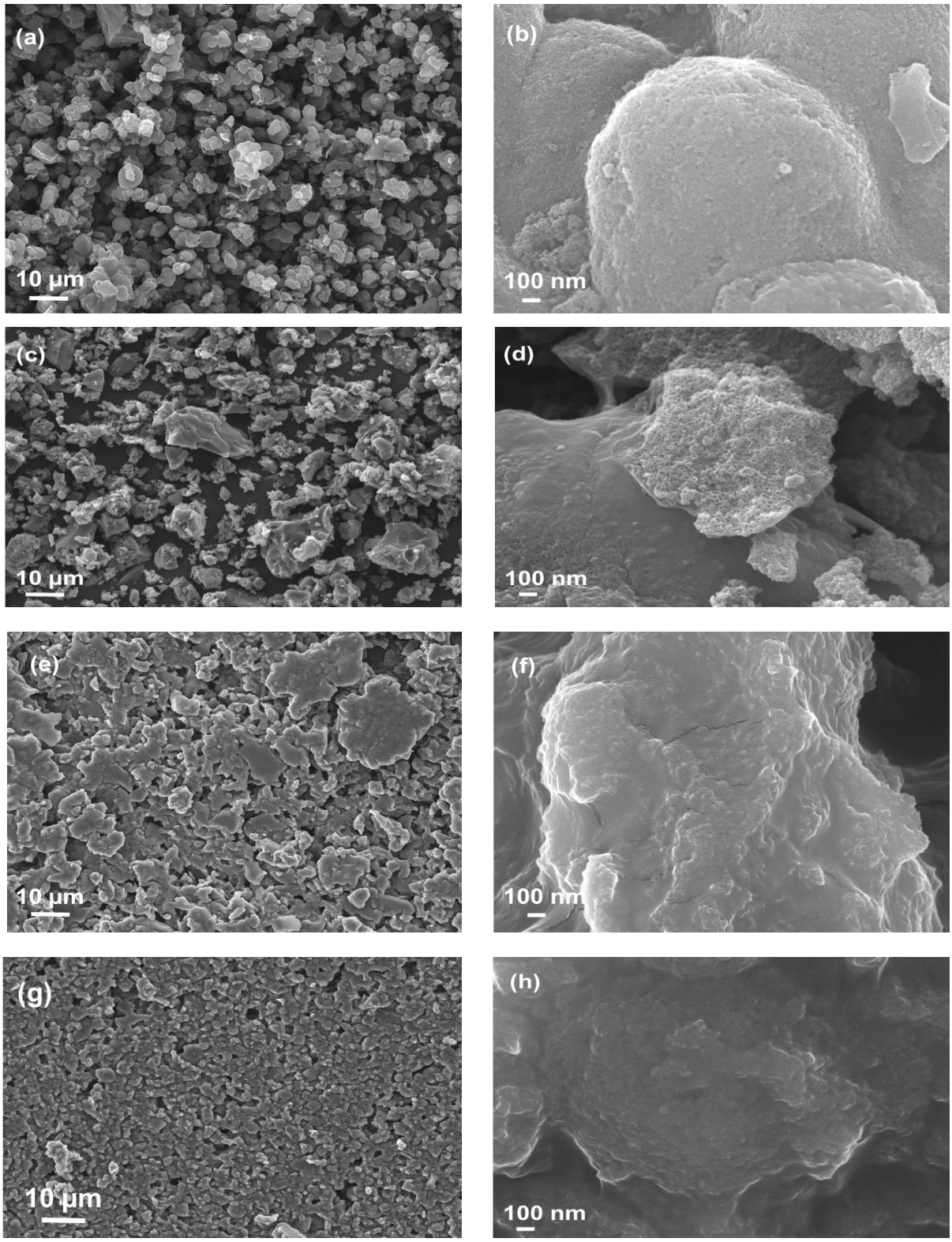

Figure 7.2 Low and high magnification SEM images of MC2-800-1 (a, b), MC2-800-1(40) (c, d), MC2-800-1(50) (e, f), and MC2-800-1(60) (g, h)

Figure 7.2 shows the SEM images of MC2-800-1 and the resultant adsorbents with different PEI loading levels. It can be found that the morphology of the obtained mesoporous carbons is similar to those of the molecular geometry of the template, MCF, which is in the form of large aggregates assembled by small spheres. A high-resolution image reveals the open polygonal networks framed by carbon struts (Figure 7.2a-b). For PEI immobilized mesoporous carbon shown in Figure 7.2c-d, the mesopores are gradually occupied by PEI molecules which still showed a distinct spherical framework feature of MC2-800-1. With the increase in PEI loading level to 60 wt% (Figure 7.2g-h), the open polygonal networks could barely be seen, and the clean spherical morphology that was obtained by MC2-800-1(40) was destroyed. These findings are inconsistent with the BET results shown in Figure 7.1 and Table 7.1. In addition, it can be seen that the small particles of mesoporous carbon tend to assemble into larger particles with the increasing PEI loading level. This indicates that PEI molecules presumably acted as a binder in the wet impregnation process, leading to the formation of large particles.

7.4 Fourier Transform Infrared Spectroscopy (FT-IR) Analysis

FT-IR spectra of selected mesoporous carbon, MC2-800-1, and its derived PEI sorbents are shown in Figure 7.3. It can be found that MC2-800-1 displayed a band at 800 cm^{-1} for a benzene ring (Nabavinia et al., 2021; Klinthongchai et al., 2020). The peak of Si-O-Si bonds at 1060 cm^{-1} was also observed in MC-800-1 (Klinthonggchai et al., 2020), suggesting that silica residue remains in mesoporous carbon after NaOH washing. Furthermore, the TGA test showed that the ash content of MC2-800-1 is less

than 3 wt%, indicating that most of the silica has been washed out. After PEI impregnation, new peaks at around 1550 and 1450 cm^{-1} were observed, which correspond to the asymmetric and symmetric bending vibration peaks related to NH_2 and the N-H bending vibration in PEI (Wang et al., 2013a, Wang et al., 2009). Moreover, the C-N stretching vibration could also be found at 1250 cm^{-1} (Faisal et al., 2021). The peaks for NH_2, N-H, and C-N increased with the increase in PEI loading level. All the above results confirm that PEI/mesoporous carbons were successfully developed by the wet impregnation process.

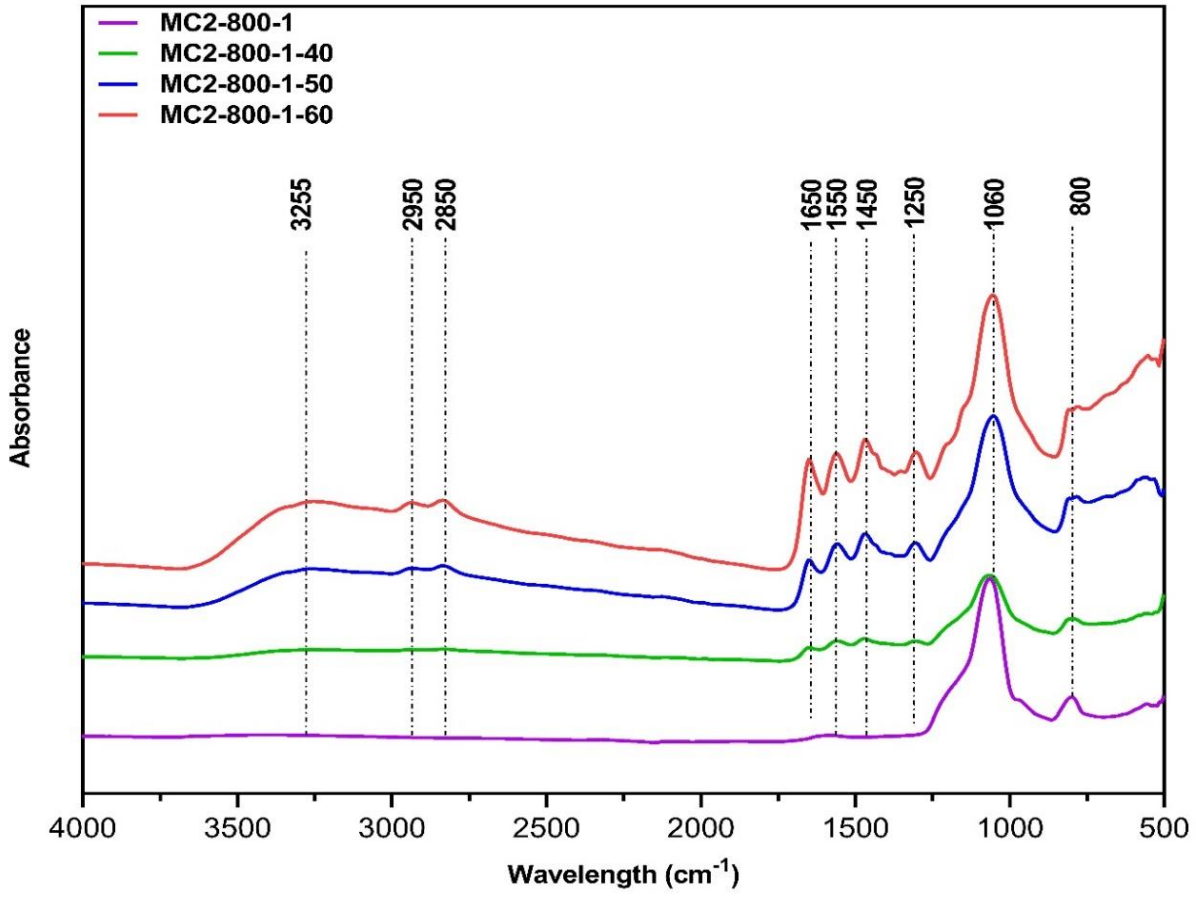

Figure 7.3 FT-IR Spectra of MC2-800-1 and PEI/MC2-800-1 adsorbents.

7.5 CO_2 adsorption performance of the PEI-impregnated Mesoporous Carbon Adsorbents

The CO_2 adsorption performance of PEI-functionalized mesoporous carbon sorbents with different PEI loading levels was first evaluated at an adsorption temperature of 75 °C and CO_2 partial pressure of 0.15 bar, and the results are shown in Figure 7.4. As expected, the pristine MC2 carbons showed limited CO_2 uptakes within the range of 8.5 to 11 mg-CO_2/g-adsorbent (0.17-0.25 mmol-CO_2/g-adsorbent) because of their mesoporosity and non-existence of CO_2-active functionalities. After PEI impregnation, it can be seen that all the PEI-functionalized sorbents showed increased CO_2 adsorption capacity with increasing amine loading levels while the sorption capacity varied with the textural properties of the mesoporous carbons. The PEI-modified sorbents prepared using MC-800-1 with the largest mesopore volume exhibited much higher adsorption capacity at different PEI loading levels between 40-60 wt% than other mesoporous carbon-based sorbents. The significantly enhanced CO_2 adsorption capacities of the PEI/mesoporous carbon adsorbents may be attributed to the strong chemical reaction between CO_2 and the amine groups (Peng et al., 2019). Among different samples, MC2-800-1-60 with a PEI loading level of 60 wt% gave rise to the highest adsorption capacity of 129.9 mg-CO_2/g-adsorbent (2.94 mmol-CO_2/g), followed by MC-800-1-50, MC-900-2-60, and MC-800-2-60. To investigate the relationship between the CO_2 adsorption capacity and the textural property of the mesoporous carbon supports, the CO_2 adsorption capacity of MC2 samples as a function of the pore volume is presented in Figure 7.5. It can be seen that an excellent linear relationship between total pore volume and CO_2 adsorption capacity at different amine loading levels was observed. At PEI impregnation of 40 wt%, a weak correlation (R^2 = 0.53) between the CO_2 adsorption uptake of the supported PEI mesoporous

carbons with the pore volume was observed due to the existence of a large pore volume. It is obvious that at a PEI loading of 50 and 60 wt%, straight lines were found, suggesting a strong and linear correlation (R^2 = 0.78 and R^2 = 0.81), respectively, exist between the CO_2 adsorption uptake and the carbon supports, which agrees well with previous investigations (Lakhi et al., 2016; Montiel-Centeno et al., 2019). At a similar amine loading level, the larger pore volume of porous support could effectively improve the surface dispersion of PEI on pore walls; hence, a higher CO_2 adsorption capacity can be achieved.

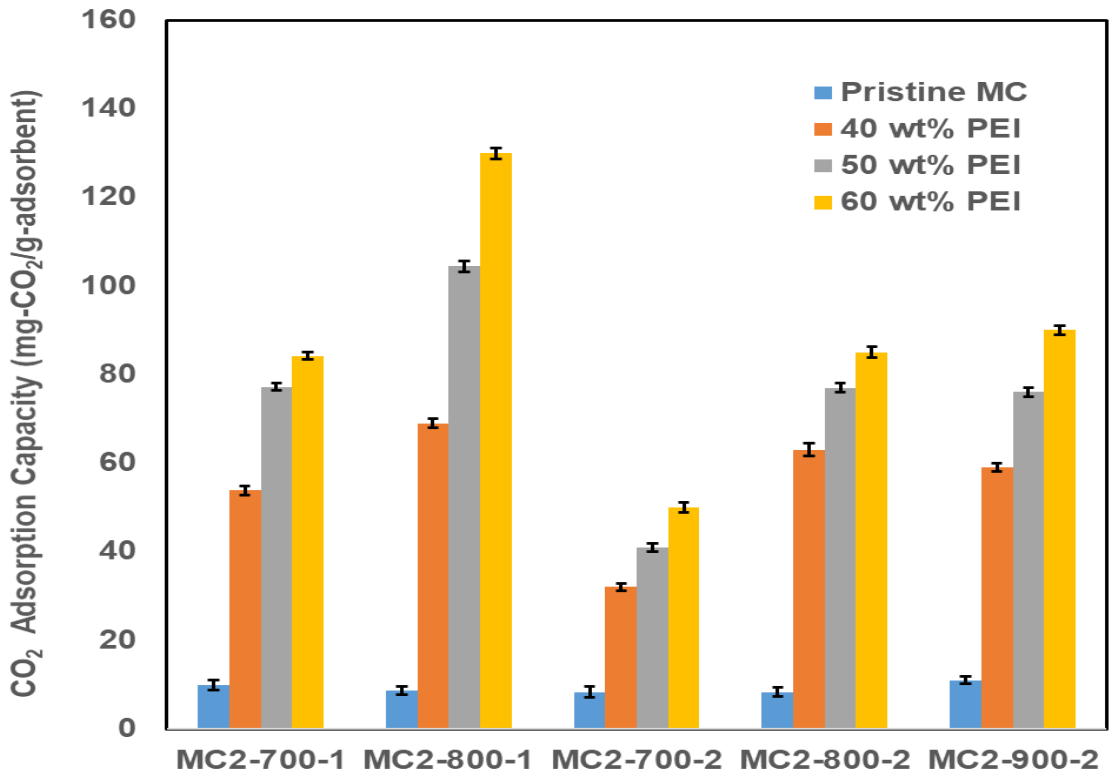

Figure 7.4 CO_2 adsorption performance of mesoporous carbons and PEI-impregnated adsorbents.

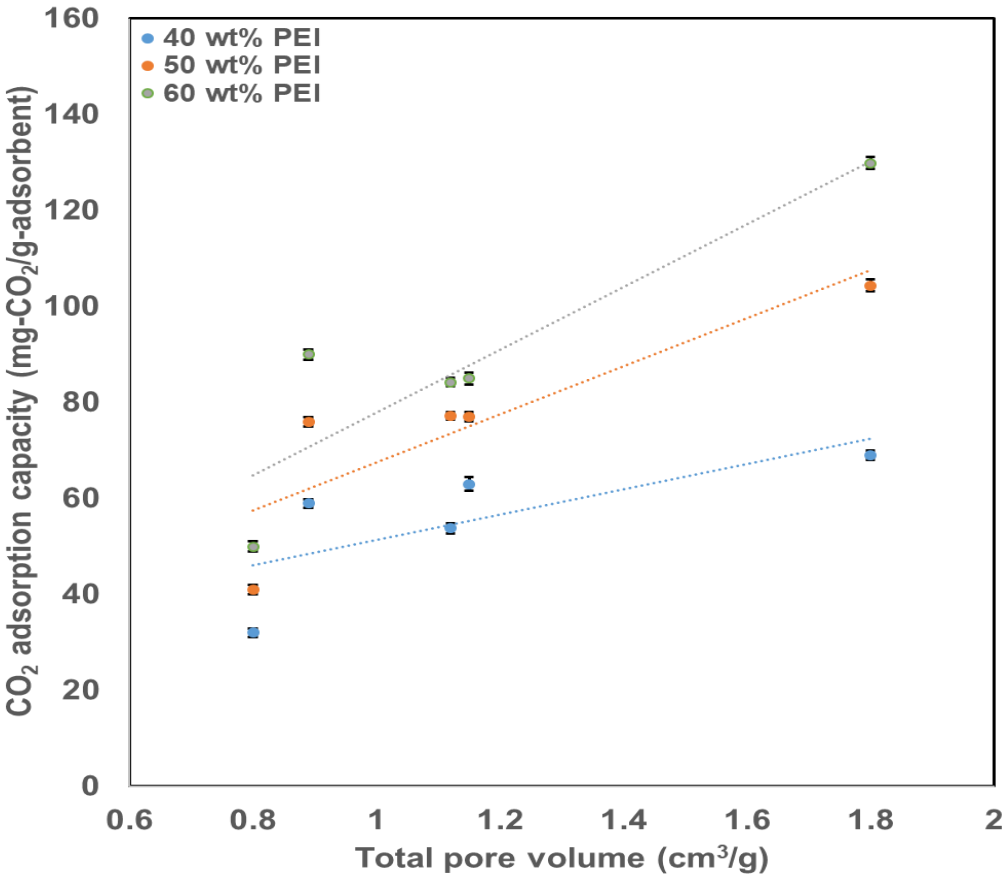

Figure 7.5 Adsorption performance of PEI-impregnated MC2 adsorbents, and their relationship with the total pore volume of the mesoporous carbon support.

To investigate the impact of porous structure on the performance of PEI-modified mesoporous carbon sorbents, the CO_2 adsorption performance of PEI-modified MCPQ adsorbents was also tested, and the results are shown in Figure 7.6. Similar to PEI-modified MC sorbents, the CO_2 adsorption capacities increased with increasing PEI loading from 40 to 60 wt%. Compared to PEI-modified MC carbons, the adsorption capacity of MCPQ-based sorbents exhibited a much lower adsorption capacity. Among these adsorbents, MCPQ-800-1-60, with a PEI loading level of 60 wt%, demonstrates the highest capacity of only 85.6 mg- CO_2/g-adsorbent, which was about 50% lower than MC-800-1-60. Moreover, it seems that using MC carbon support with 3D interconnected porous structures could effectively improve the accessibility of PEI

into the pores, and therefore higher adsorption capacity was achieved compared to mesoporous carbons with 2D porous structures. For instance, the pore volume of MC-900-2 was much smaller than that of MCPQ-800-1 while the adsorption capacity of MC-900-2-60 at a PEI loading level of 60 wt% was even higher than that of MCPQ-800-1-60. The over results suggest the critical role of the 3D-interconnected porous structure by enhancing the accessible sorption sites of the sorbents. A summary of PEI-modified mesoporous carbon and silica sorbents reported by previous studies is shown in Table 7.2. At an operating temperature of 75 °C and high PEI loading of 60 wt.%, the adsorption capacity of MC2-800-1 is higher than some PEI-impregnated silica sorbents (Ma et al., 2009; Zhang et al., 2020a; Zhang et al., 2014) or most of the amine-modified mesoporous carbons reported in previous studies shown in Table 7.2. Meanwhile, it is also notable that the adsorption capacity of MC2-800-1-60 was higher than that of sorbents prepared by using mesoporous carbons with much larger pore volume but much smaller pore size (Kong and Liu, 2019; Chen et al., 2021), indicating that the large pore size could effectively improve the CO_2 adsorption capacity of PEI/mesoporous carbon sorbents.

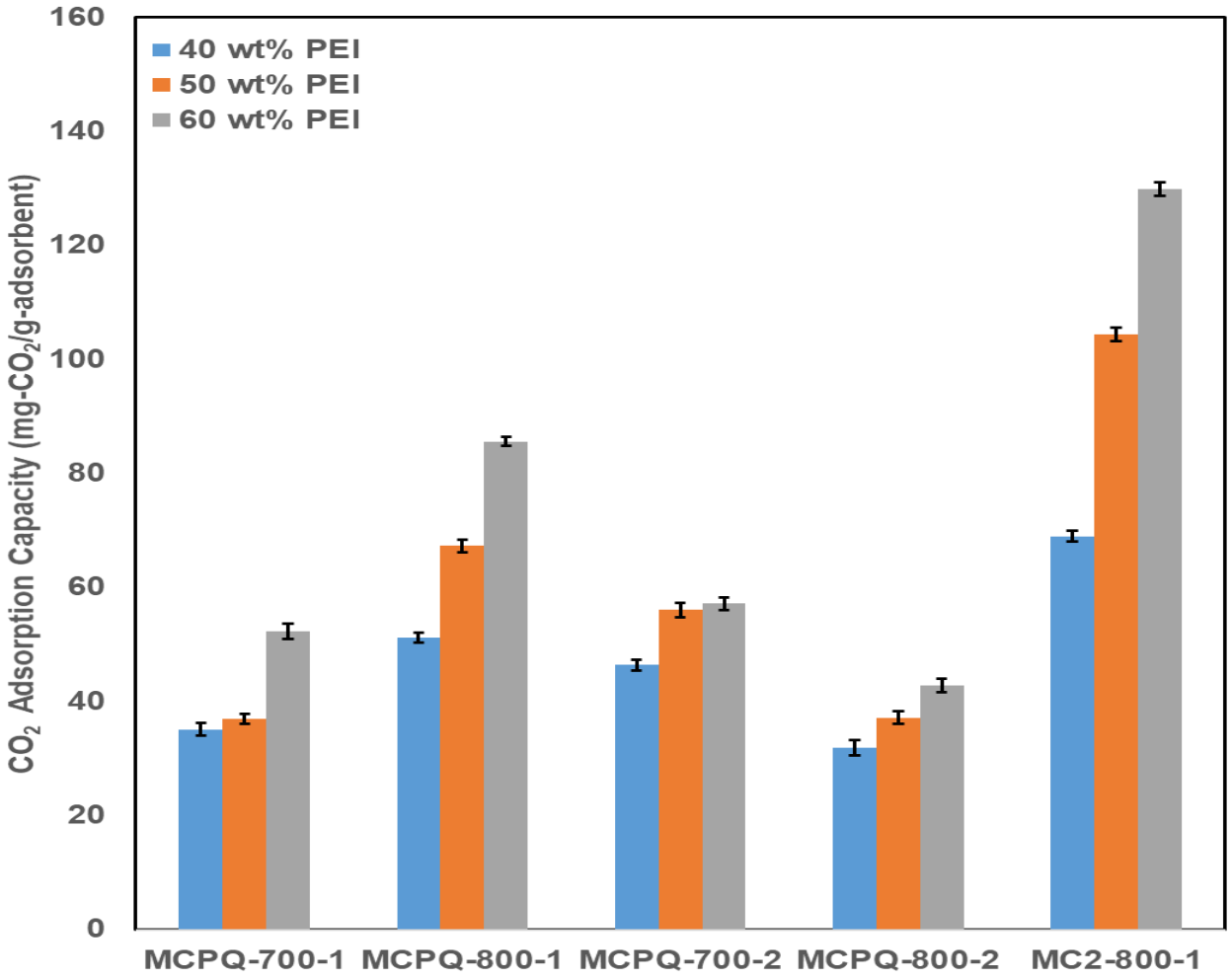

Figure 7.6 CO_2 adsorption performance of PEI-impregnated MCPQ adsorbents

Table 7.2 CO_2 adsorption capacities of various amine-modified adsorbents reported in the literature and this work.

Samples	Adsorption temperature (°C)	Pressure (bar)	Adsorption capacity (mmol g^{-1})	Reference
MC2-800-1-60	75	0.15	2.95	This work
MCNs	75	1	1.97	Chai et al., 2016
Mesoporous carbon spheres	75	0.05	3.22	Chen et al., 2021
Activated ordered mesoporous carbon	75	0.15	1.84	Kong et al., 2019
POP	75	1	1.0	Mane et al., 2018.
MCM-41	75	0.15	2.03	Ma et al., 2009
SBA-15	75	0.15	3.18	Ma et al., 2009
MC-PEI(65)	75	1	4.82	Wang et al., 2013a
MCM-41	75	1	2.95	Panek et al., 2017
PEI-STPR-3	75	0.3	1.09	Tang et al., 2013
MC(PEI 50)	75	0.1	1.30	Gibson et al., 2015
MC(TETA 43)	75	0.1	1.85	Gibson et al., 2015
ZSM-5(PEI 33..3)	40	0.1	2.63	Lee et al., 2015
Meso-13X (PEI 33)	100	0.1	1.82	Chen et al., 2015
CA-K-1 (PEI 55)	75	0.05	2.06	Xie et al., 2017
CA-K-1 (PEI 60)	75	0.05	2.03	Xie et al., 2017

According to the PEI loading level and CO_2 capacity, the amine efficiencies could be estimated as the molar ratio of CO_2 adsorbed to the amine groups in the amine-based sorbents, as displayed in Figure 7.7. Under dry conditions, the mechanism for the reaction of amine groups with CO_2 was known that the primary and secondary amines could react strongly with CO_2 by forming zwitterionic intermediates to produce carbamate salts (equations 1 and 2) (Fujiki and Yogo, 2014). The formations are as follows;

$$2RNH_2 + CO_2 \leftrightarrow RNH_3 + RNHCOO \quad (1)$$

$$2R_2NH + CO_2 \leftrightarrow RNH_2 + R_2NCOO \quad (2)$$

The amine efficiency was found to increase linearly with the increasing amine loading level from 40 to 60 wt.% for all the adsorbents. MC2-800-1-60 exhibited the maximum amine efficiency of 0.30 mol CO_2/mol-PEI with a PEI loading level of 60 wt%. Notably, the PEI-modified sorbents prepared by using MC-800-1 with the largest pore volume had higher amine efficiency (0.21-0.30 mol CO_2/mol-PEI) than other samples with different amine loading levels (0.09-0.20 mol CO_2/mol-PEI).

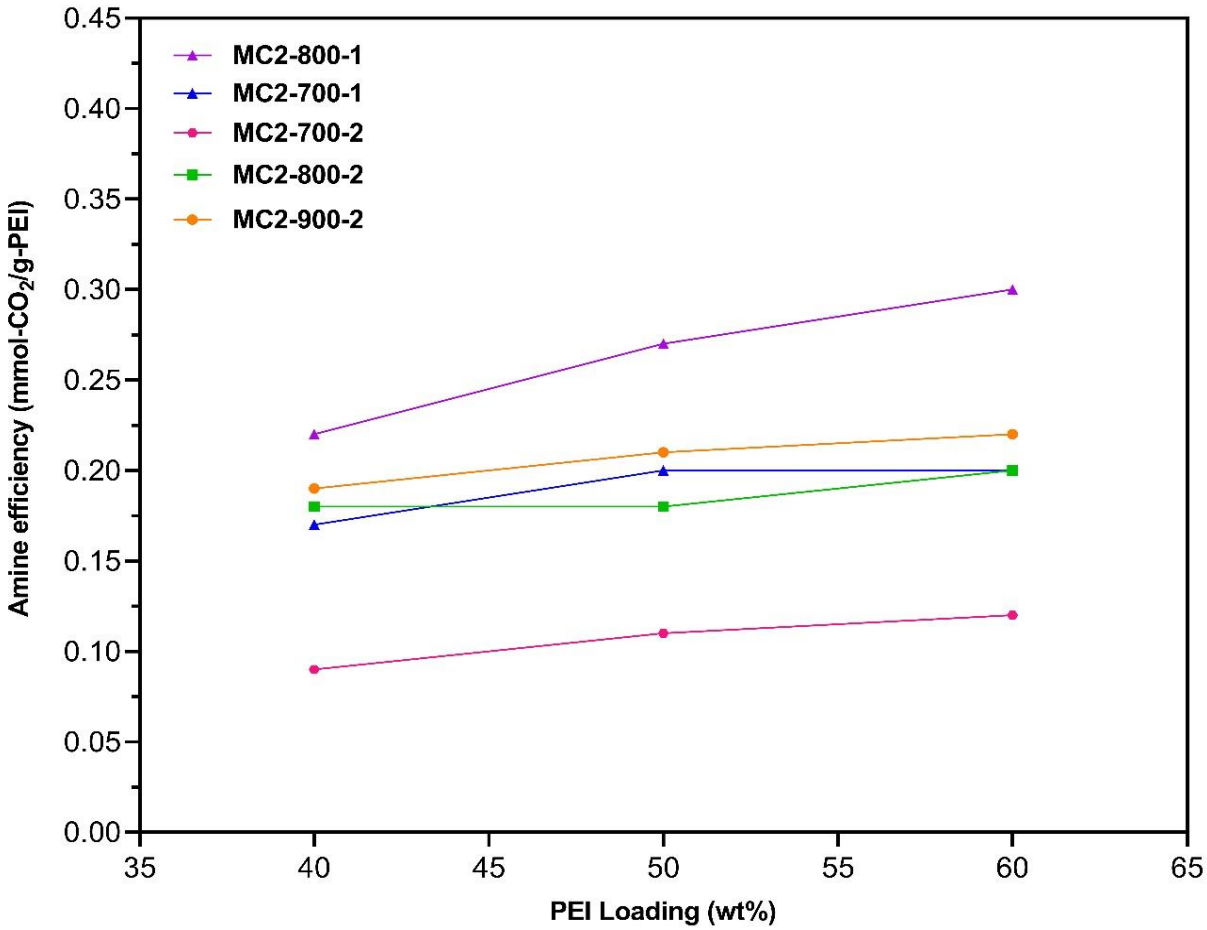

Figure 7.7 Effect of PEI loadings on CO_2 amine efficiencies of mesoporous carbon adsorbents.

Figure 7.8 shows the CO_2 adsorption kinetics at 75 ℃ for the PEI/impregnated mesoporous carbon adsorbents. As can be seen, the CO_2 adsorption on PEI-functionalized mesoporous carbon materials follows a two-stage process; a rapid CO_2 uptake within the first few minutes of adsorption, which is due to the surface chemical reaction between CO_2 and PEI (Niu et al., 2016 and Liu et al., 2019); followed a comparatively slow CO_2 adsorption process controlled by CO_2 diffusion within the phase of supported amine.

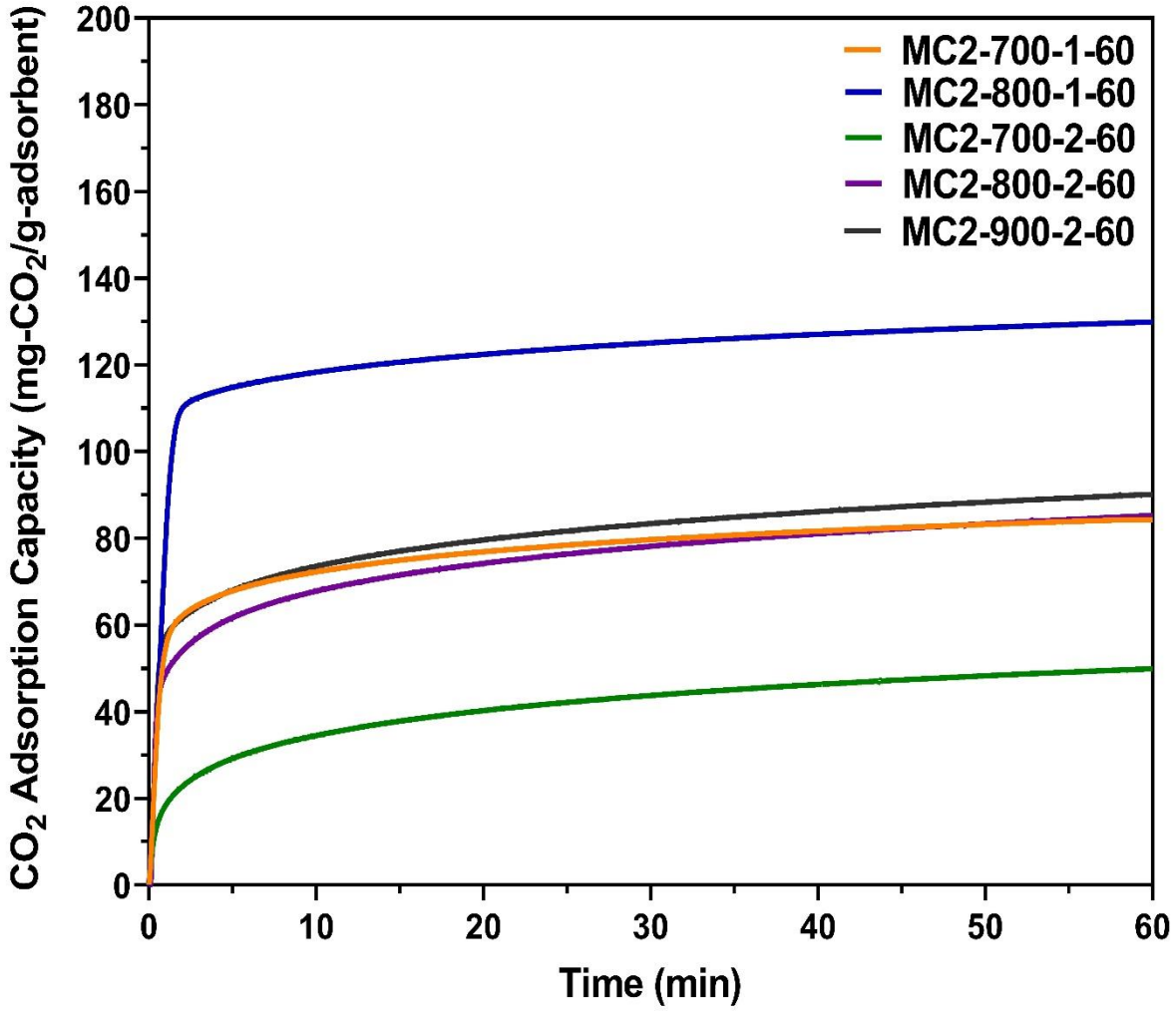

Figure 7.8 CO_2 adsorption kinetics profiles at 75 ℃ and 15% CO_2 in N_2 of PEI-impregnated mesoporous carbon adsorbents (b and c).

The adsorption kinetics of the PEI/impregnated mesoporous carbon adsorbents were evaluated by comparing the times taken to attain 70% (t_{70}) and 90% (t_{90}) of the adsorption capacity for the PEI/impregnated mesoporous carbon adsorbents, as exhibited in Figure 7.9a and b. Generally, it can be seen that the 70% (t_{70}) and 90% (t_{90}) varied with both mesoporous carbon supports and PEI loading amount for impregnation. The PEI-modified sorbents prepared by using MC2-800-1 with the highest pore volume (1.80 cm^3/g) exhibited the fastest adsorption rate, with a much

shorter time being required to achieve 70% and 90% of the adsorption capacity than other samples. For instance, MC2-800-1-60 attained 70% and 90% CO_2 adsorption capacity in less than 2 min and within 7 min, respectively. In comparison, PEI-modified sorbents prepared with MC2-700-2, which had the smallest pore volume (0.80 cm^3/g) showed the longest t_{70} of 11 min and t_{90} of 34 min, suggesting that the low adsorption rate originated from the greatly increased thickness or reduced CO_2 accessibility of the amine layer on pore walls as a result of the small pore volume.

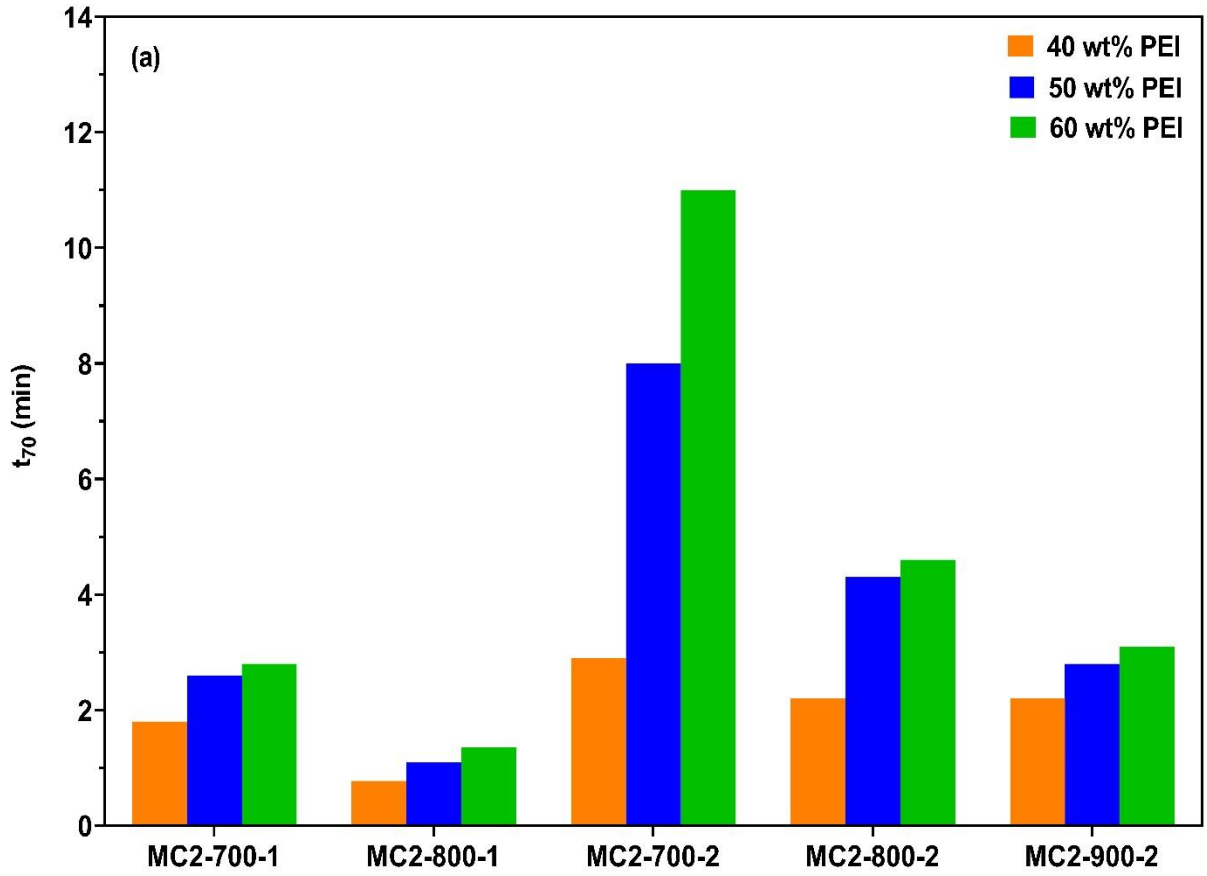

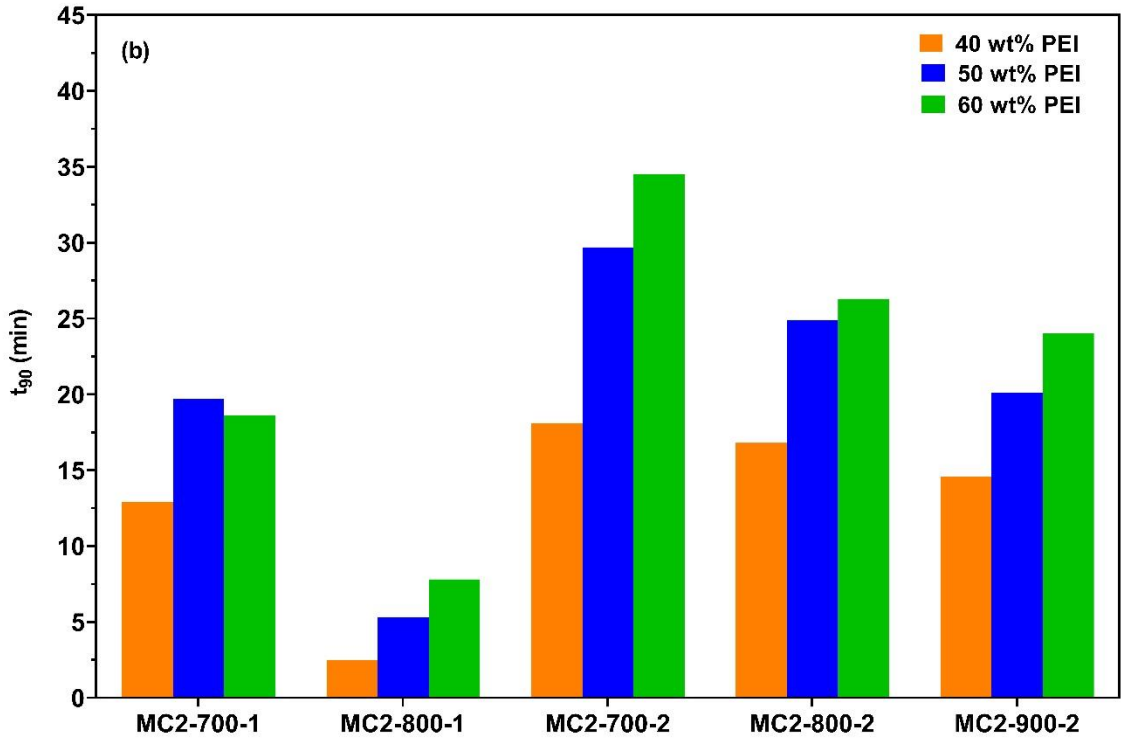

Figure 7.9 Time taken to achieve 70% and 90% of the adsorption capacity of PEI-impregnated mesoporous carbon adsorbents (a and b).

The CO_2 adsorption on the PEI-functionalized mesoporous carbons with 2D porous structures follows a similar two-stage process, as shown in Figure 7.10a. In comparison, the CO_2 adsorption of MC carbons was overall much faster than MCPQ carbons. For instance, the t_{70} and t_{90} of MC2-800-1-60 were just 1.35 and 7.81 min, respectively, which is 2 and 3 times faster than the 2.9 and 22.9 min achieved for the best MCPQ sorbent, MCPQ-800-1-60. Although the pore volume of MC2-700-1 (1.12 cm^3/g) was smaller than that of MCPQ-800-1 (1.30 cm^3/g), the $t_{70,}$ and t_{90} of MC2-700-1-60 (2 min and 18 min) were shorter than that of MCPQ-800-1-60 (3 min and 23 min). The above results suggest that the 3D interconnected porous structure of MC carbons

could facilitate greater accessibility of amines and reduced CO_2 diffusion resistance, leading to a faster CO_2 adsorption rate and higher CO_2 adsorption capacity.

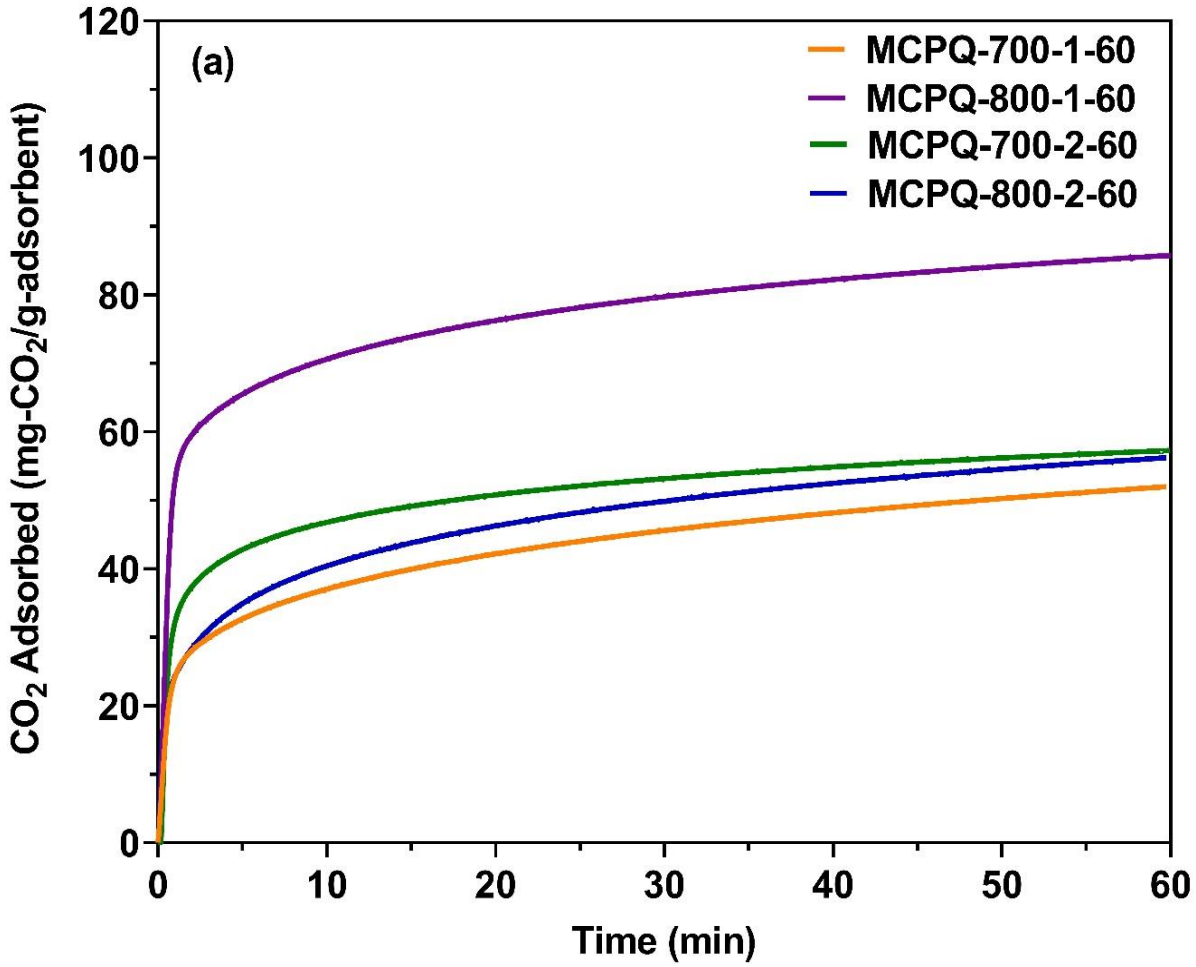

Figure 7.10 CO_2 adsorption kinetics profiles at 75 ℃ and 15% CO_2 in N_2.

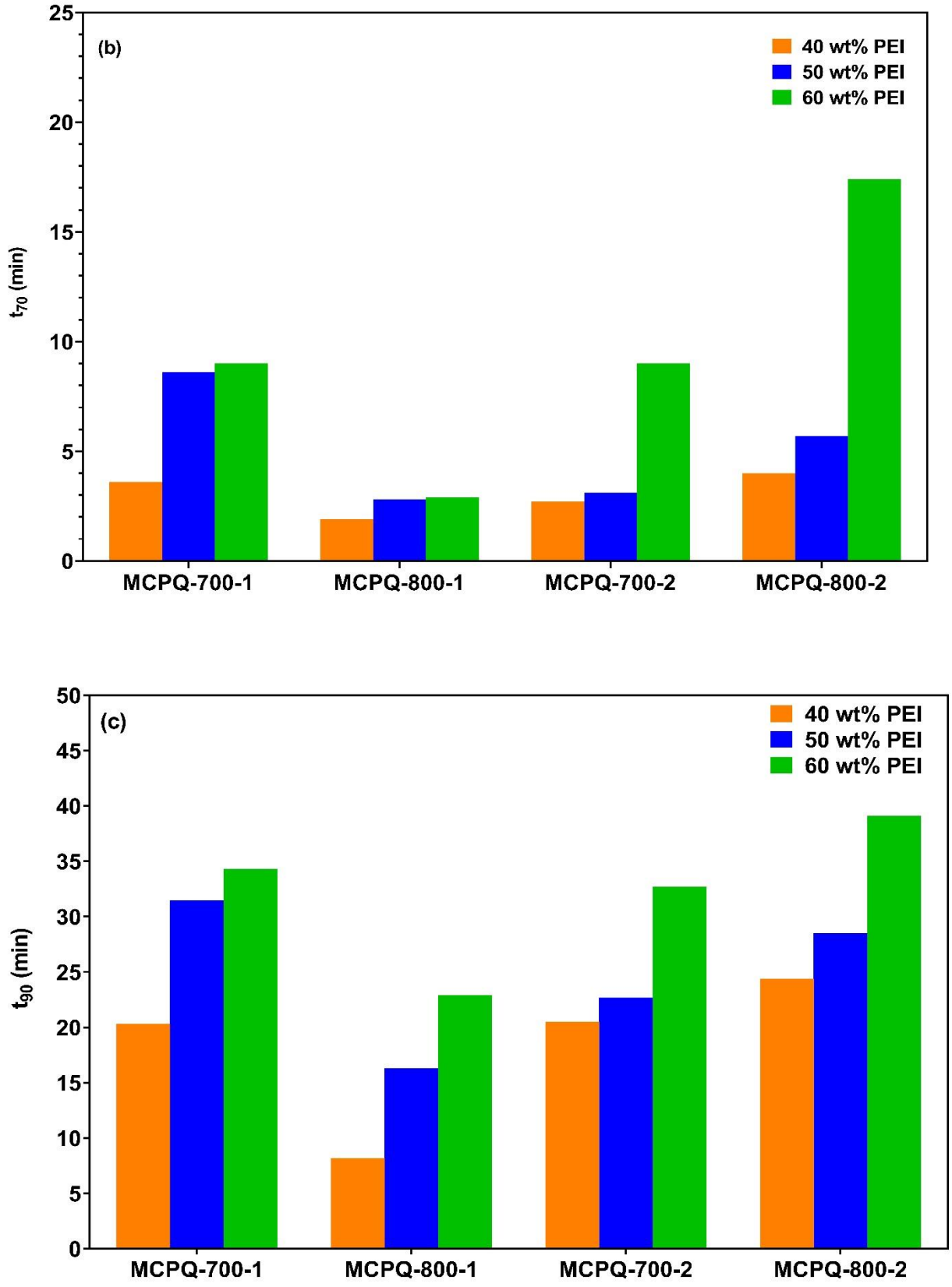

Figure 7.10 Time taken to achieve 70% and 90% of the adsorption capacity (b and c) of PEI-impregnated MCPQ adsorbents.

7.6 Effect of temperature on CO_2 adsorption performance.

To examine the variation of CO_2 adsorption capacity of the best-performing PEI-modified sorbent, MC-800-1-60, along with the adsorption temperature, the adsorption performance of MC2-800-1-60 at a temperature range between 75-90 °C was tested, and the results are shown in Figure 7.11. The adsorption capacity of MC2-800-1-60 first increased and then decreased with adsorption temperature, with the highest adsorption capacity of 137.7 mg-CO_2/g-adsorbent (3.13 mmol/g) being achieved at an adsorption temperature of about 85 °C. Overall, MC-800-1-60 showed a high CO_2 adsorption capacity of 2.90-3.13 mmol/g in the temperature range between 75-90 °C, highlighting the relatively wide operating window of MC-800-1-60 and the potential for reduction of energy required to cool down the flue gas. Figure 7.11b shows the time taken to reach 70% (T_{70}), 80% (T_{80}), and 90% (T_{90}) of equilibrium CO_2 adsorption capacity for MC2-800-1-60 at different adsorption temperatures. It was found that adsorption temperature also had a significant impact on the CO_2 adsorption rate of MC2-800-1-60. T_{90} was sharply reduced with the increase in adsorption temperature. For instance, T_{90} was only about 4 min at an adsorption temperature of 90 °C, which was only half of the T_{90} achieved at an adsorption temperature of 75 °C. This indicates that high adsorption temperature could help overcome the kinetic barrier of CO_2 adsorption by improving the mobility and accessibility of impregnated PEI molecules and reducing the diffusive resistance of CO_2.

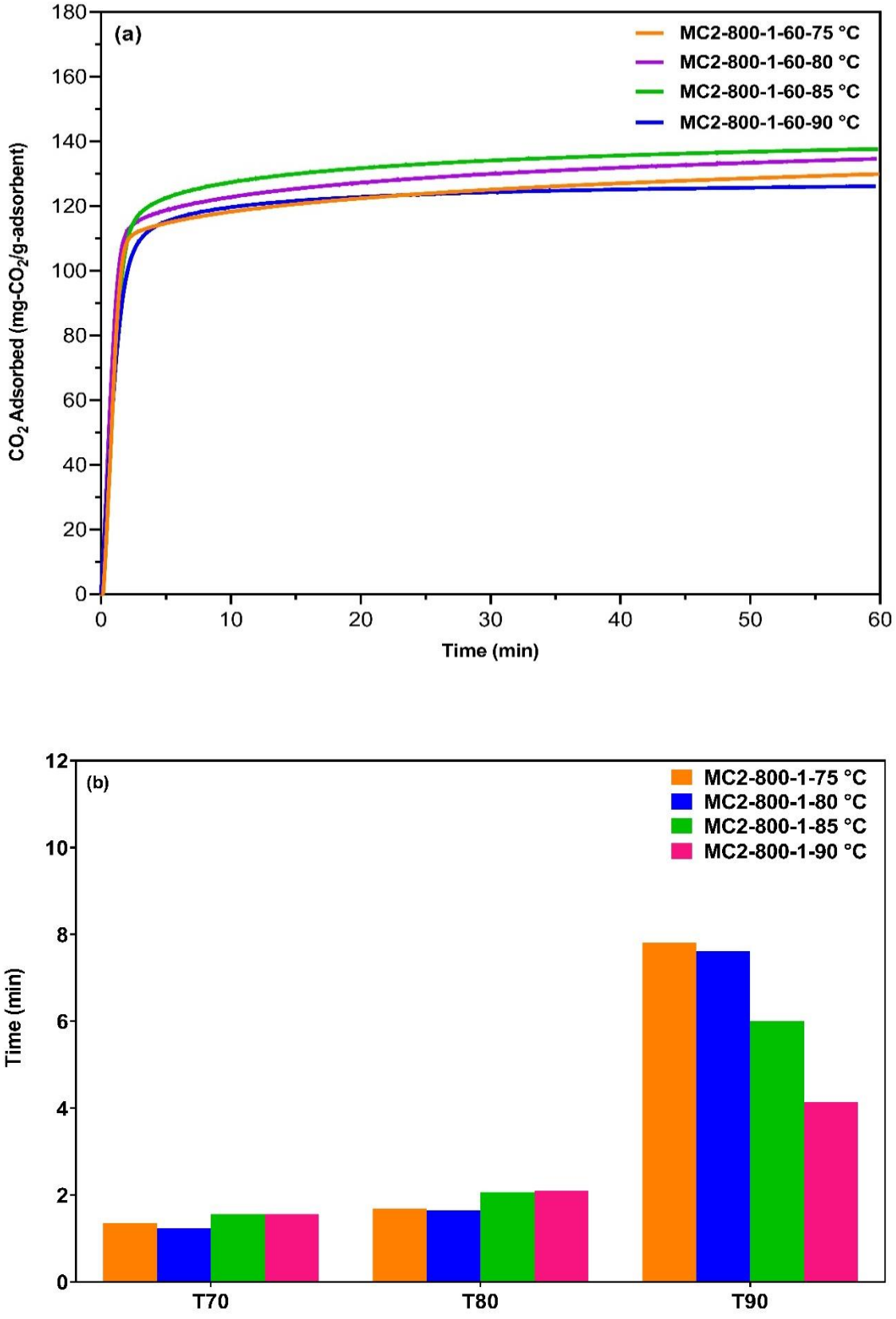

Figure 7.11 Effect of temperature on CO_2 adsorption capacity (a) and adsorption kinetics (b) of MC2-800-1-60 at 15% CO_2 in N_2.

7.7 Regeneration performance of PEI-impregnated mesoporous carbon.

In addition to high CO_2 adsorption capacity and fast adsorption rate, the cyclic adsorption-desorption performance and chemical stability of a solid adsorbent are also critical from a practical application point of view. Therefore, MC2-800-1-60 as the best-performing mesoporous carbon-supported PEI adsorbent was selected to evaluate the cyclic adsorption-desorption characteristics of the mesoporous carbon-supported PEI sorbents under simulated flue gas conditions in a temperature swing process. As shown in Figure 7.12, no appreciable changes in CO_2 adsorption capacity were observed from 50 consecutive adsorption-desorption cycles, highlighting the high cyclic stability of PEI-modified mesoporous carbons for long-term operation. A very small drop (5.42%) in adsorption capacity from 129 mg/g to 122 mg/g, mainly in the first few cycles, is attributable to the evaporation loss of PEI molecules with lower molecular weight present in PEI. The adsorbent MC2-800-1-60 demonstrates comparable high stability for CO_2 capture from the flue gas with the PEI@AOMC composites prepared by Kong and Liu (2019), and MC-PEI(65) obtained by Wang et al. (2013a).

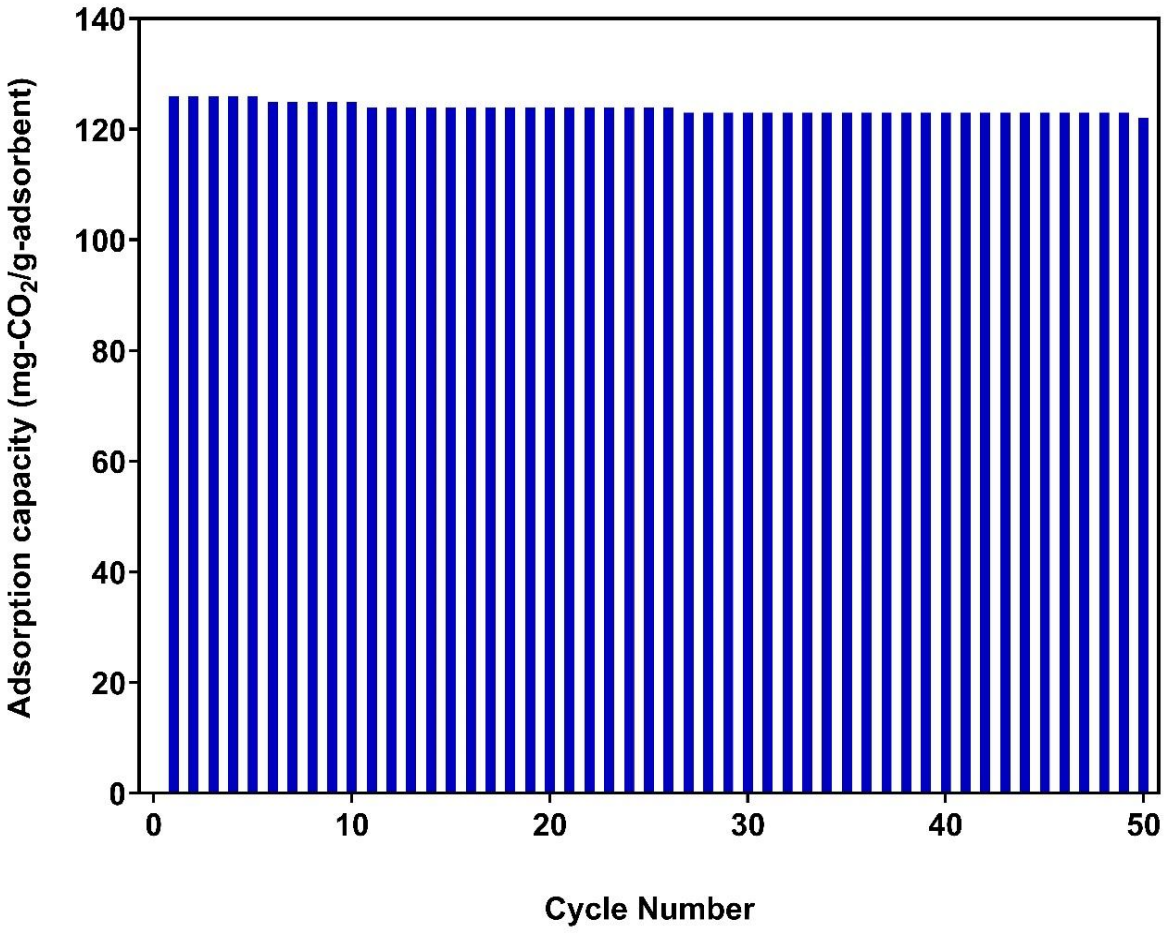

Figure 7.12 Cyclic CO_2 adsorption-desorption profiles of MC2-800-1-60 in simulated flue gas with a CO_2 partial pressure of 0.15 bar in N_2. Conditions: adsorption temperature; 75 °C; desorption temperature: 110 °C

7.8 Conclusions

In summary, a series of polyethyleneimine (PEI)-functionalized sorbents were developed for CO_2 capture using three-dimensional interconnected ordered mesoporous carbon materials with large pore volumes and large pore sizes as porous support. The characterizations carried out in this study demonstrated that PEI-functionalized mesoporous carbon adsorbents exhibit high CO_2 adsorption capacity, fast adsorption kinetics, high amine efficiency, and good regeneration performance.

At the optimal PEI loading of 60 wt%, the CO_2 adsorption capacity of the best-performing PEI mesoporous carbon adsorbent (MC2-800-1) was found to be 129 mg-CO_2/g-adsorbent (2.95 mmol/g) at 75 °C, and 137.7 mg-CO_2/g-adsorbent (3.13 mmol/g) at 85 °C in the simulated flue gas of 15% CO_2 in N_2, which is 52% higher than those of the PEI-functionalized MCPQ with 2D pore networks Furthermore, PEI functionalized mesoporous carbon sorbents showed very good regenerability and stability of CO_2 adsorption, where the adsorption capacity decreased by less than 6% after 50 adsorption cycles. The findings in our work conclude that the lignin-derived mesoporous carbon adsorbents have a good potential as a promising alternative to aqueous amines for large-scale CO_2 capture from industries.

Chapter 8 General Discussions and Conclusions

8.1 General discussions

In this PhD project, two of the most abundant biomass materials, lignin, and chitosan have been successfully applied for the synthesis of a broad range of ordered mesoporous carbons in a solvothermal process, using different mesoporous silica materials as the hard templates, including two 3D interconnected mesocellular foam silicas (MCF1, MCF2), and two 2D mesoporous silicas (SBA-15 and PQ commercial silica). As discussed in Chapters 4-7, the results indicated that the effect of different carbonization temperatures and template-to-precursor mass ratios played an essential role in determining the porous structure of the prepared mesoporous carbons. Owning to their well-developed porous structure and large pore volume, the as-prepared mesoporous carbons had good potential as support for PEI-based adsorbents in carbon capture. This section will discuss the influence of different synthesis conditions and carbon precursors on the mesoporosity development of the final carbons and the effect of template materials.

8.1.1 Impact of preparation conditions on the porosity development of mesoporous carbons.

Table 8.1 presents the surface textural properties of selected hard-templated mesoporous lignin carbons and chitosan-derived mesoporous carbons prepared at different carbonization temperatures using a different template to precursor mass ratios. It can be found that carbonization temperature and template-to-carbon mass ratio significantly affects the textural characteristics of the carbons obtained from both

lignin and chitosan precursors under different synthesis conditions. As shown in Chapter 4, the lignin carbon materials showed a clear trend in the evolution of the mesopore size with an increasing carbonization temperature from 700 to 900 ˚C. However, the surface area and pore volume gradually decreased. The carbon (MC2-900-2) obtained at a high carbonization temperature of 900 ˚C showed the largest mesopore size of 14.1 nm with a surface of 543 m^2/g. It is also evident that the surface area and pore volume of the lignin-derived carbons significantly decreased with an increasing amount of silica-to-lignin mass ratio from 1 to 3. For the chitosan-derived mesoporous carbons, as presented in Chapter 6, a similar BET surface area and pore volume trend were observed when the carbonization temperature was increased from 700 to 900 ˚C and with an increasing amount of silica-to-chitosan ratio from 1 to 3.

8.1.2 Impact of carbon precursor

Based on the results of the nitrogen adsorption-desorption isotherms for MC2-800-1, MC2-800-3, CMC2-800-1, and CMC2-800-3 shown in Chapters 4 and 6, all of these samples were found to have type IV isotherm (Thommes et al., 2015), indicating the pore networks with ink-bottle shaped mesopores. It can be found that the carbon precursor has a significant impact on the textural properties of the resultant carbons prepared under similar conditions using the same silica template. Using a similar template (MCF2), at a carbonization temperature of 800 ˚C and the same mass ratio, the carbon prepared using lignin as carbon precursor had a higher BET surface area, total pore volume, and average pore size than the chitosan-derived mesoporous carbon. For example, the highest pore volume of 1.80 cm^3/g with a BET surface area of 960 m^2/g and average pore size of 12.4 nm was obtained for MC2-800-1 prepared at a temperature of 800 ˚C with a silica-to-lignin ratio of 1, compared to the pore volume

of 1.32 cm^3/g with a BET surface area of 953 m^2/g and average pore size of 7.1 nm obtained for CMC2-800-1 prepared at the same conditions.

8.1.3 Impact of different silica templates.

The surface textural property of mesoporous carbons greatly depends on the template type and carbonization temperature. As shown in Chapters 4, 5, and 7, a series of ordered mesoporous carbon materials with high surface areas and large pore volumes were synthesized using 3D interconnected mesocellular foam silicas (MCF1 and MCF2), a commercial 2D mesoporous silica (PQ silica) and 2D hexagonal SBA-15. Compared to the MCF-templated carbon materials, the PQ-templated carbons and SBA-15 mesoporous carbons showed lower textural properties. This might be attributed to the MCF silica template's 3D-connected porous structure, leading to more ordered and large mesoporosity. In particular, MC2-800-1 (prepared using MCF2) displays a higher pore volume of 1.80 cm^3/g with an average pore size of 12.4 nm compared to the pore volume of 1.30 cm^3/g and 0.61 cm^3/g with an average pore size of 8.1 nm and 3.3 nm obtained for MCPQ-800-1 and CSBA-15-800-1 prepared using PQ silica and SBA-15, respectively.

Table 8.1 Surface textural properties of selected hard-templated mesoporous carbons derived from lignin and chitosan using different mass ratios and temperatures.

Sample	S_{BET} (m^2/g)	V_{total} (cm^3/g)	V_{meso} (cm^3/g)	V_{micro} (cm^3/g)	Average pore size (nm)
MC1-700-2	849	1.23	1.06	0.17	9.6
MC1-900-2	353	0.68	0.61	0.66	11.2
MC2-700-2	788	0.80	0.60	0.16	10.4
MC2-900-2	543	0.89	0.72	0.10	14.1
CMC1-700-1	888	1.09	0.95	0.19	6.1
CMC1-900-1	312	0.22	0.15	0.07	5.4
CMC2-700-1	983	1.32	1.20	0.12	7.1
CMC2-900-1	857	0.74	0.58	0.16	5.2
MC2-800-1	960	1.80	1.50	0.17	12.4
MC2-800-3	413	0.50	0.38	0.10	12.4
CMC2-800-1	953	1.32	1.20	0.12	7.1
CMC2-800-3	285	0.39	0.33	0.04	6.1
SBA-15-800-1	1064	0.61	0.35	0.26	3.36
MCPQ-800-1	719	1.30	1.16	0.09	8.1

8.2 General Conclusions

This PhD project aimed to develop novel technology strategies to prepare bio-carbon materials with regulatable 3-dimensional (3D) interconnected mesoporous structures and evaluate their performance in CO_2 capture. The main conclusions can be summarized as follows;

1) A series of highly ordered mesoporous carbons were synthesized using 3D mesocellular foam silica (MCF1 and MCF2), commercial PQ silica as templates, and lignin as carbon precursors. The mesocellular foam silicas (MCF1 and MCF1) were obtained at aging temperatures of 100 and 120 ˚C, respectively, with meaningful

differences in their textural properties, which were convenient to use as templates for the synthesis of the mesoporous carbon materials. Variations in carbonization temperatures (700-900 ˚C) and silica to lignin mass ratio from 0.5 to 3 allowed the author to obtain the MC1 and MC2 series of carbons. The textural characterization demonstrates that both MC1 and MC2 carbons showed exceedingly high mesoporosity accounting for 90 % of the total pore volume. The mesoporous carbons prepared using MCF silica as a template exhibit the highest BET surface area up to 960 m^2/g and a mesopore volume of 1.50 cm^3/g, which outperforms the mesoporous carbons prepared with PQ commercial silica as a template. Characterizations by SEM and TEM revealed that the obtained MCF-templated carbons exhibited well-ordered and highly interconnected mesopores with spherical cages.

2) As a cheap and environmentally-friendly material, lignin was used again as a carbon precursor and SBA-15 as a hard template to synthesize ordered mesoporous carbon materials at different carbonization temperatures and SBA-15 to lignin mass ratios. The synthesis route was facile and resulted in highly ordered mesoporous carbons exhibiting a 2D hexagonal structure with high surface areas (505-1076 m^2/g). It was also found that by changing the SBA-15 to lignin mass ratio, the pore size of the prepared mesoporous carbons can be tuned.

3) Nitrogen-rich mesoporous carbons materials were successfully prepared using low-cost and naturally abundant chitosan as a carbon precursor through a hard templating technique with mesostructured cellular foam silicas (MCF1 and MCF2) with different pore diameters as the hard templates. The results showed that the mesoporous carbon materials were successfully prepared with a high surface area (up to 983 m^2/g), pore volume (up to 1.32 cm^3/g), and high nitrogen content (up to 10 wt%).

4) Among the numerous applications, the highly mesoporous lignin carbons were evaluated as porous supports for preparing sorbent materials for CO_2 capture. The evaluation demonstrated that the best performing PEI mesoporous carbon adsorbent (MC2-800-1) could effectively accommodate up to 60 wt% polyamine loading, leading to high CO_2 adsorption capacity up to 129.9 mg or 2.95 mmol-CO_2/g-adsorbent at 75 ˚C and 137.7 mg or 3.13 mmol-CO_2/g-adsorbent at 85 ˚C with fast adsorption rate and high amine efficiency in the simulated flue gas of 15% CO_2 in N_2, which is 52% higher than those of the PEI-functionalised MCPQ adsorbents. In addition, MC2-800-1-60 shows excellent stability throughout the 50 consecutive adsorption-desorption cycles.

8.3 Future Work

1) Mesocellular foam silica preparation improvement

This project has focused on developing ordered mesoporous carbons using mesostructured cellular foam silica as a template. As reported in the previous MCF preparation section (Chapter 3), the aging temperature of MCF1 and MCF2 was selected to be 100 and 120 ˚C, respectively, with a Pluronic P123 to TMB mass ratio of 1 to 2. However, aging at 120 ˚C may not be the optimum temperature. For future work, temperatures above 120 ˚C should also be investigated for the formation of MCFs with well-defined pores. The amounts of TMB to Pluronic P123 may also be varied for better control of pore size in the MCFs. In addition, effort should be made to replace the TEOS with a low-cost silica source such as sodium silicate.

2) Mesoporous carbon preparation improvement

The development of mesoporous carbons should be considerably more cost-efficient on an industrial scale. The cost of synthesis of templated mesoporous carbons solely

depends upon the production cost of mesostructured silica templates because silica templates are etched out using NaOH solution in the final step of the preparation of mesoporous carbons. Recycling dissolved silica in these solutions might be an efficient option; however, it has not yet been reported. Most templates require choosing the appropriate carbon precursors from a wide range of raw materials and tailoring the synthesis conditions for producing mesoporous carbons. Thus, in future work, HF or Teflon-assisted could also be used to etch out the silica templates. Other sustainable biomass materials (cellulose and hemicellulose) could be used as carbon precursors due to their renewable nature and abundant resource availability.

3) Potential Applications

CO_2 capture In this project, the mesoporous carbon-supported polyamine adsorbents were prepared via the wet impregnation method using polyethylenimine (PEI) (Mw = 600, branched). Tetraethylenepentamine (TEPA) could be used as an alternative polymer for future work.

Other applications The chitosan-derived mesoporous carbons synthesized using different templates showed high nitrogen contents, which could influence their application. Explorations on the possibility of making the as-prepared chitosan-derived mesoporous carbons promising electrode materials for energy storage in supercapacitors and batteries are strongly recommended.

REFERENCES

ABABNEH, H., & HAMEED, B. H., 2021. Chitosan-derived hydrothermally carbonized materials and its applications: A review of recent literature. *Int. J. Biol. Macromol.*, **186**: 314–327.

AHMED, R., LIU, G., YOUSAF, B., ABBAS, Q., ULLAH, H., & ALI, M. U., 2020. Recent advances in carbon-based renewable adsorbent for selective carbon dioxide capture and separation-A review. *J. Clean. Prod*. **242**: 118409.

AHN, W.S., MIN, K.I., CHUNG, Y.M., RHEE, J.K., JOO, S.H., & RYOO, R., 2001. Environmental Application of Nanotechnology. Stud. Surf. Sci. *Catal*. **135**: 313.

ALKHABBAZ, M. A., KHUNSUPAT, R., & JONES, C. W., 2014. Guanidinylated poly(allylamine) supported on mesoporous silica for CO_2 capture from flue gas, *Fuel*, **121**: 79-85.

ALVAREZ, S., & FUERTES, A.B., 2004. Template synthesis of mesoporous carbons with tailorable pore size and porosity. *Carbon*. **42**: 423–460.

AGBONGHAE, E.O., HUGHES, K.J., INGHAM, D.B., MA, L., & POURKASHANIAN, M., 2014. Optimal process design of commercial-scale amine-based CO_2 capture plants, Ind. Eng. *Chem. Res*. **53**(38):14815–14829.

AHN, W.S., MIN, K.I., CHUNG, Y.M., RHEE, J.K., JOO, S.H., & RYOO, R., 2001. Environmental Application of Nanotechnology. Stud. Surf. Sci. *Cata*l. **135**: 313.

ALKHABBAZ, M. A., KHUNSUPAT, R., & JONES, C. W., 2014. Guanidinylated poly(allylamine) supported on mesoporous silica for CO_2 capture from flue gas, *Fuel*, **121**: 79-85.

ARENILLAS, A., SMITH, K. M., DRAGE, T. C. & SNAPE, C. E. 2005. CO_2 capture using some fly ash-derived carbon materials. *Fuel*, **84:** 2204-2210.

AZMI, A.A & AZIZ, M.A.A, 2019. Mesoporous adsorbent for CO_2 capture application under mild condition: A review. *J. Environ. Chem. Eng.*, **7**: 103022.

BABU, P., LINGA, P., KUMAR, R., & ENGLEZOS, P., 2015. A review of the hydrate based gas separation (HBGS) process for carbon dioxide pre-combustion capture. *Energy*, **85**: 261-279

.

BAE, Y.S., & SNURR, R.Q., 2011. Development and evaluation of porous materials for carbon dioxide separation and capture. *Angew. Chemie Int. Ed*. **50**: 11586–11596.

BAE, T.H., HUDSON, M.R., MASON, J.A., QUEEN, W.L., DUTTON, J.J., SUMIDA, K., MICKLASH, K.J., KAYE, S.S., BROWN, C.M. & LONG, J.R., 2013. Evaluation of cation-exchanged zeolite adsorbents for post-combustion carbon dioxide capture. *Energy Environ. Sci.*, **6**(1), 128-138.

BAE, W., KIM, J., & CHUNG, J., 2014. Production of granular activated carbon from food-processing wastes (walnut shells and jujube seeds) and its adsorptive properties. *J Air Waste Manag Assoc*. **64**(8): 879–886.

BAEK, D.U., LEE, K.L., PARK, J., KIM, J.H., LEE, J., LIM, J.S., LEE, S.Y., SHIN, T.J., JEONG, H.Y., SON, J.S., KANG, S.J., KIM, J.Y., & JOO, S.H., 2021. Ordered Mesoporous Carbons with Graphitic Tubular Frameworks by Dual Templating for Efficient Electrocatalysis and Energy Storage. *Angew. Chem. Int. Ed*. **60**: 1441–1449.

BAHAMON, D., ALKHATIB, I.I.I., ALKHATIB, N., BUILES, S., SINNOKROT, M., VEGA, L.F., 2020. A Comparative Assessment of Emerging Solvents and Adsorbents for Mitigating CO_2 Emissions From the Industrial Sector by Using Molecular Modeling Tools. Front. *Energy Res*. **8**:165.

BAKER, D.A., GALLEGO, N.C., & BAKER, F.S., 2012. On the characterization and spinning of an organic-purified lignin toward the manufacture of low-cost carbon fiber. *J. Appl. Polym. Sci.* **124**: 227–234.

BALL, P.C. & EVANS, R. 1989. Temperature Dependence of Gas Adsorption on a Mesoporous Solid: Capillary Criticality and Hysteresis, *Langmuir*, **5**, 714-723.

BANSAL, R.P. & GOYA, M., 2005. Activated Carbon Adsorption. CRC Press. *Taylor & Francis Group*.

BARDESTANI, R., PATIENCE, G.S., & KALIAGUINE, S., 2019. Experimental methods in chemical engineering: specific surface area and pore size distribution measurements-BET, BJH, and DFT. Can *J Chem Eng*. **97**:2781–2791.

BARRETT, E.P., JOYNER, L.G., & HALENDA, P.P., 1951. The Determination of Pore Volume and Area Distributions in Porous Substances. I. Computations from Nitrogen Isotherms *J. Am. Chem. Soc*. **73**: 373.

BARWE, S., ANDRONESCU, C., MASA, J., VENTOSA, E., KLINK, S., GENC, A., ARBIOL, J., & SCHUHMANN, W. 2017. Polybenzoxazine-derived Ndoped carbon as matrix for powder-based electrocatalysts. *Chem-Sus-Chem*. **10**: 2653−2659.

BAUMANN, T.F., JOE H. & SATCHER, J.H., 2003. Homogeneous Incorporation of Metal Nanoparticles into Ordered Macroporous Carbons. *Chem. Mater*. **15**: 3745-3747.

BENZIGAR, M.R., TALAPANENI, S.N., STALIN JOSEPH, S., RAMADASS, K., SINGHG., SCARANTO, J., RAVON, U., AL-BAHILY, K., & VINU, A., 2018. Recent advances in functionalized micro and mesoporous carbon materials: synthesis and applications. *Chem. Soc. Rev*. **47**: 2680.

BENZIGAR, M. R., JOSEPH, S., ILBEYGI, H., PARK, D.H., SARKAR, S., CHANDRA, G.,UMAPATHY, S., SRINIVASAN, S., TALAPANENI, N., VINU, A., 2018a. Highly Crystalline Mesoporous C60 with Ordered Pores: A Class of Nanomaterials for Energy Applications. *Angew. Chem., Int. Ed*. **57**: 569.

BERT METZ, O. D., HELEEN DE CONINCK, MANUELA LOOS, & LEO MEYER 2005. IPCC Special Report on Carbon Dioxide Capture and Storage. *Cambridge* University Press.

BEZERRA, D.P., SILVA, F.W.MD., MOURA, P.A.SD., SOUSA, A.G.S., VIEIRA, R.S., RODRIGUEZ-CASTELLON, E., & AZEVEDO, D.C.S., 2014. CO_2 Adsorption in Amine-Grafted Zeolite 13X, *Appl. Surf. Sci*. **314**: 314-321.

BISHNOI, S., & ROCHELLE, G.T., (2000). Absorption of carbon dioxide into aqueous piperazine: reaction kinetics, mass transfer and solubility, *Chem. Eng. Sci*. **55**(22): 5531–5543.

BOHME, K., EINICKE, W.F., & KLEPE, O., 2005. Templated synthesis of mesoporous carbon from sucrose—the way from the silica pore filling to the carbon material. *Carbon*. **43**(9): 1918-1925.

BRIAO, G.V., JAHN, S.L., FOLETTO, E.L., & DOTTO, G.L., 2017. Adsorption of crystal violet dye onto a mesoporous ZSM-5 zeolite synthetized using chitin as template, *J. Colloid Interface Sci*. **508**: 313–322.

BROWNSON, D.A., & BANKS, C.E., 2012. Fabricating graphene supercapacitors: highlighting the impact of surfactants and moieties. *Chem. Commun*. **48**(10): 1425–1427.

BRUANER, S., EMMET, P.H. & TELLER, E., 1938. Adsorption of Gases in Multimolecular Layers, *J. Am. Chem*. Soc. **60**: 309-319.

BRYDSON, R., 2001. Electron Energy Loss Spectroscopy. CRC Press, Oxford. **13**: 978-1859961346.

BUI, M., ADJIMAN, CLAIRE, S., BARDOW, A., ANTHONY, EDWARD, J., BOSTON, A., BROWN, S., FENNELL, P., FUSS, S., GALINDO, A., HACKET, LEIGH, A., HERZOG, H. J., JACKSON, G., KEMPER, J., KREVOR, S. C. M., MAITLAND, G. C., MATUSZEWSKI, M., PETIT, C., PUXTY, G., REIMER, J., REINER, D. M., RUBIN, E. S., SCOTT, STEWART, A., SHAH, N., SMIT, B., TRUSLER, J. P. M., WEBLEY, P., WILCOX, J., MACDOWELL, N., 2018. Carbon capture and storage (CCS): the way forward. *Energy Environ. Sci,* **11**: 1062-1176.

BUSETTI, F., HEITZ, A., CUOMO, M., BADOER, S., & TRAVERSO, P., 2006. Determination of sixteen polycyclic aromatic hydrocarbons in aqueous and solid samples from an Italian wastewater treatment plant. *J. Chromatogr. A*, **1102**: 104–115.

CARRASSCO-MALDONADO, F., SPORL, R., FLEIGER, K., HOENIG, V., MAIER, J., & SCHEFFKNECHT, G., 2016. Oxy-fuel combustion technology for cement production - state-of-the-art research and technology development. Int. *J. Greenhouse. Gas Control,* **45**: 189-199.

CARROTT, P., & CARROTT, M.R., 2007.Lignin from Natural Adsorbent to Activated Carbons: *A Review Bioresour.Technol*. **98**(12): 2301-2312.

CARROTT, P.J.M., SUHAS, RIBEIRO CARROTT, M.M.L., GUERRERO, C.I., L.A. & DELGADO, L.A., 2008. Reactivity and porosity development during pyrolysis and physical activation in CO_2 or steam of kraft and hydrolytic lignins. *J. Anal. Appl. Pyrolysis*. **82**(2): 264–271.

CASANOVA, A., JESUS INIESTAB, J., & GOMIS-BERENGUER, A., 2022. Recent progress in the development of porous carbon-based electrodes for sensing applications. *Analyst*, **147**: 767–783.

CASKEY, S. R., WONG-FOY, A. G., & MATZGER, A. J., 2008. Dramatic tuning of carbon dioxide uptake via metal substitution in a coordination polymer with cylindrical pores. *J. Am. Chem. Soc*. **130**: 10870–10871.

CHAI, S.H., LIU, Z.H., HUANG, K., TAN, S., & DAI, S., 2016. Amine Functionalization of Microsized and Nanosized Mesoporous Carbons for Carbon Dioxide Capture. Ind. Eng. *Chem. Res*. **55**: 7355−7361.

CHANG, B., FU, J., TIAN, Y., DONG, X., 2013. Multifunctionalized ordered mesoporous carbon as an efficient and stable solid acid catalyst for biodiesel preparation. *J Phys Chem Lett* **117**(12):6252–6258.

CHATTERJEE, S., CLINGENPEEL, A., MCKENNA, A., RIOS, O., & JOHS, A., 2014. Synthesis and characterization of lignin-based carbon materials with tunable microstructure. *RSC Adv*. **4**(9): 4743–4753.

CHATTERJEE, S., & SAITO, T., 2015. Lignin-derived advanced carbon materials. *ChemSusChem*, **8**: 3941-395.

CHAUHAN, S., 2021. Synthesis of ordered mesoporous carbon by soft template method. *Mater. Today*.

CHEN, F., ZHOU, W., YAO, H., FAN, P., YANG, J., FEI, Z., & ZHONG, M., 2013. Self-assembly of NiO nanoparticles in lignin-derived mesoporous carbons for supercapacitor applications. *Green Chem*. **15**: 3057–3063

CHEN, Y. & SHI, J., 2015. Mesoporous carbon biomaterials. *Sci China Mater.* **58**: 241–257.

CHEN, C., KIM, S-S., CHO, W-S., & AHN, W-S., 2015. Polyethylenimine-incorporated zeolite 13X with mesoporosity for post-combustion CO_2 capture, *Appl. Surf. Sci.* **332**: 167-171.

CHEN, A.B., LI, Y.T., YU, Y.F., LI, Y.Q., XIA, K.C., WANG, Y.Y., & LI, S.H., 2016. Synthesis of mesoporous carbon nanospheres for highly efficient adsorption of bulky dye molecules, *J. Mater. Sci*. **51**: 7016–7028.

CHEN, S., ZHU, M., FU, Y., HUANG, Y., TAO, Z., & LI, W., 2017. 13X. Using, LiX, and LiPdAgX zeolites for CO_2 capture from post-combustion flue gas, *Appl. Energy* **191**: 87 – 98.

CHEN, R., LI, L., LIU, Z., LU, M., WANG, C., LI, H., MA, W., & WANG, S., 2017b. Preparation and characterization of activated carbons from tobacco stem by chemical activation. *J. Air Waste Manag. Assoc*. **67**(6): 713-724.

CHEN, S., CHEN, G., CHEN, H., SUN, Y., YU, X., SU, Y., TANG, S., 2019a. Preparation of porous carbon-based material from corn straw via mixed alkali and its application for removal of dye. *Colloids Surf. A*. **568**: 173–183.

CHEN, Q., WANG, S., ROUT, K.R.,& CHEN, D., 2021. Development of polyethylenimine (PEI)-impregnated mesoporous carbon spheres for low-concentration CO_2 capture. *Catal. Today*, **369**: 69-76.

CHO, S.H., & RYOO, R., 2012. Synthesis of ordered mesoporous MFI zeolite using CMK carbon templates. *Microporous and Mesoporous Materials*. **151**: 107–112.

CHU, N.T.H., NGO, Q.L.D., & LE, H.T.T., 2020. Synthesis of ordered mesoporous carbon from Vietnam natural kaolin clay for supercapacitor application. *Material Science Forum.* **985**:124-136.

CHUENCHOM, L., KRAEHNERT, R., & SMARSLY, B.M., 2012. Recent progress in soft-templating of porous carbon materials. *Soft Matter.* **8**: 10801-10812.

CLAUSSE, M., MEREL, J., & MEUNIER, F., 2011. Numerical parametric study on CO_2 capture by indirect thermal swing adsorption. *Int J Greenhouse Gas Control*, **5**:1206–1213.

CORIANI, S., HALKIER, A., RIZZO, A., & RUUD, K., 2000. On the molecular electric quadrupole moment and the electric-field-gradient induced birefringence of CO_2 and CS_2. *Chem. Phys. Lett*. **326**: 269–276.

CORREA, C.R., STOLLOVSKY, M., HEHR, T., RAUSCHER, Y., ROLLI, B., & KRUSE, A., 2017. Influence of the Carbonization Process on Activated Carbon Properties from Lignin and Lignin-Rich Biomasses. *ACS Sustainable Chem. Eng*. **5**: 8222−8233.

COX, P.M., BETTS, R.A., JONES, C.D., SPALL, S.A., & TOTTERDEL, I.J., 2000. Acceleration of Global Warming Due to Carbon-Cycle Feedbacks in a Coupled Climate Model. *Nature.* **408**: 750-750.

CREPALDI, E.L., DE A., G.J., SOLER-ILLIA, A., GROSSO, D., CAGNOL, F., RIBOT, F., SANCHEZ, C., 2003. Controlled Formation of Highly Organized Mesoporous Titania Thin Films: From Mesostructured Hybrids to Mesoporous Nanoanatase TiO_2. *J Am Chem Soc*, **125**: 9770-9786.

DANG, J. M., & LEONG, K. W., 2006. Natural polymers for gene delivery and tissue engineering*. Advanced Drug Delivery Reviews*. **58**(4): 487–499.

DANISH, M., & AHMAD, T., 2018. A review on utilization of wood biomass as a sustainable precursor for activated carbon production and application. *Renew. Sustain. Energy Rev*. **87**:1–21.

DA SILVA ALVES, D. C., HEALY, B., DE ALMEIDA PINTO, L. A., SANT' ANNA CADAVAL, JR, T. R., CARMEL, B., & BRESLIN, C. B., 2021. Recent Developments in Chitosan-Based Adsorbents for the removal of Pollutants from Aqueous Environments. *Molecules*. **26**: 594.

DAVIS, S.J., CALDEIRA, K., & MATTHEWS, H.D., 2010. Future CO_2 emissions and climate change from existing energy infrastructure, *Science*. **329**: 1330–1333.

DE SOUZA, L.K.C., GONÇALVES, A.A.S., QUEIROZ, L.S., CHAAR, J.S., DA ROCHA FILHO, G.N., DA COSTA, C.E.F., 2020. Utilization of acai stone biomass for the sustainable production of nanoporous carbon for CO_2 capture. SM&T 25.

DEMESSENCE, A., D'ALESSANDRO, D. M., FOO, M. L., & LONG, J. R., 2009. Strong CO_2 binding in a water-stable, triazolate-bridged metal-organic framework functionalized with ethylenediamine. *J. Am. Chem. Soc.***131**: 8784–8786.

DIEZ, N., SEVILLA, M., & FUERTES., A.B., 2021. Synthesis strategies of templated porous carbons beyond the silica nanocasting technique. *Carbon* .**178**: 451-476.

DING, S., ZHENG, S., XIE, M., PENG, L., GUO, X., DING, W., 2011. One-pot synthesis of boron-doped mesoporous carbon with boric acid as a multifunction reagent. *Microporous Mesoporous Mat*er **142**(2–3):609–613.

DONG, C., CHEN, C., CHEN, C., & HUNG, C., 2014. Platinum particles supported on mesoporous carbons: fabrication and electrocatalytic performance in methanol-tolerant oxygen-reduction reactions. *Sci. Rep*. **1:** 1-8.

DONOHUE, M., & ARANOVICH, G., 1999. A new classification of isotherms for Gibbs adsorption of gases on solids. Fluid Phase Equilibria. 557–563.

DURAISAMY, V., SELVAKUMAR, K., KRISHNAN, R., KUMAR, S.M.S., 2019. Investigation on Template Etching Process of SBA-15 Derived Ordered Mesoporous Carbon on Electrocatalytic Oxygen Reduction Reaction. *Chemistry Select*, **4**: 2463 – 2474.

DUTCHER, B., FAN, M., RUSSELL, A. G., 2015. Amine-based CO_2 capture technology development from the beginning of 2013-*A review. ACS Appl. Mater. Interfaces,* **7**: 2137-2148.

DRAGE, T.C., ARENILLAS, A., SMITH, K.M., & SNAPE, C.E., 2008. Thermal stability of polyethylenimine based carbon dioxide adsorbents and its influence on selection of regeneration strategies. *Microporous Mesoporous Mater*., **116**: 504–512.

EL-BANNA, F. S., MAHFOUZ, M. E., S. LEPORATTI, S., EL-KEMARY, M., & HANAFY, N. A. N., 2019. Chitosan as a natural copolymer with unique properties for the development of hydrogels, *Appl. Sci*. **9**: 11.

ERNI, R., 2015. Aberration-corrected Imaging in Transmission Electron Microscopy: *An Introduction, second ed. Imperial College Press*.

ENTERRIA, M., & FIGUEIREDO, J.L., 2016. Nanostructured mesoporous carbons: Tuning texture and surface chemistry. *Carbon*. **108**: 79-102.

FAISAL, M., PAMUNGKAS, A. Z., & KRINANDI, Y. N., 2021. Study of Amine Functionalized Mesoporous Carbons as CO_2 Storage Materials. *Process* **9**: 456.

FAN, X., ZHANG, L., ZHANG, G., SHU Z., SHI, J., 2013. Chitosan derived nitrogen-doped microporous carbons for high performance CO_2 capture *Carbon*, **61**: 423.

FANG, Y., GU, D., ZOU, Y., WU, Z., LI, F., CHE, R., DENG, Y., TU, B., & ZHAO, D., 2010. A Low-Concentration Hydrothermal Synthesis of Biocompatible Ordered Mesoporous Carbon Nanospheres with Tunable and Uniform Size. *Angew. Chem. Int. Ed*. **49**: 7987 –7991.

FANG, Y., DAI, W., CHEN, L., & MA, N., 2016. Facile synthesis of ordered mesoporous carbon with finger citron residue as carbon precursor. *Mater Lett* **174**:246–248.

FAVVAS, E.P., HELIOPOULOS, N.S., KAROUSOS, D.S., DEVLIN, E., PAPAGEORGIOU, S.K., PETRIDIS, D., & KARANIKOLOS, G.N., 2019. Mixed matrix polymeric and carbon hollow fiber membranes with magnetic iron-based nanoparticles and their application in gas mixture separation. *Mater. Chem. Phys*. **223**: 220–229.

FENG, S., LI, W., WANG, J., SONG, Y., ELZATAHRY, A. A., XIA, Y., ZHAO, D., 2014. Hydrothermal synthesis of ordered mesoporous carbons from a biomass-derived precursor for electrochemical capacitors. *Nanoscale*. **6**: 14657−14662.

FIERRO, C. M., GORKA, J., & ZAZO, J. A., 2013. Colloidal templating synthesis and adsorption characteristics of microporous–mesoporous carbons from kraft lignin. *Carbon*. **62**: 233–239.

FU, P., HU, S., SUN, L., XIANG, J., YANG, T., ZHANG, A., & ZHANG, J., 2009. Structural evolution of maize stalk/char particles during pyrolysis. *Bioresource Technology*, **100(**20): 4877-4883.

FUJIKI, J., & YOGO, K., 2014. Carbon Dioxide Adsorption onto Polyethylenimine-Funtionalized Porous Chitosan Beads. *Energy Fuels*. **28**: 6467-6474.

FUERTES, A.B., & NEVSKAIA, D.M., 2003. Control of mesoporous structure of carbons synthesised using a mesostructured silica as template. *Microporous and Mesoporous Materials*. **62**: 177-190.

FUERTES, A.B., 2004. Synthesis of ordered nanoporous carbons of tunable mesopore size by templating SBA–15 silica materials, *Micropor. Mesopor. Mat*. **67**: 273–281.

FURUKAWA, H., KO, N., GO, Y.B., ARATANI, N., CHOI, S.B., CHOI, E., YAZAYDIN, A.Ö., SNURR, R.Q., O'KEEFFE, M., KIM, J. & YAGHI, O.M., 2010. Ultrahigh porosity in metal-organic frameworks. *Science*, **329**(5990), 424-428.

GADIPELLI, S., PATEL, H.A., & GUO, Z., 2015. An ultrahigh pore volume drives up the amine stability and cyclic CO_2 capacity of a solid-amine@carbon sorbent. *Adv. Mater*. **27**: 4903–4909.

GAI, H., GUO, K., XIAO, M., ZHANG, N., LI, Z., LV, Z., & SONG, H., 2018. Ordered mesoporous carbons as highly efficient absorbent for coal gasification wastewater – a real case study based on the Inner Mongolia Autonomous coal gasification wastewater, *Chem. Eng. J*. **341**: 471–482.

GANG, D., AHMAD, Z.U., LIAN, Q., YAO, L., & ZAPPI, M.E., 2021. A review of adsorptive remediation of environmental pollutants from aqueous phase by ordered mesoporous carbon. *Chem. Eng. J.* **403**: 126286.

GARDARSDOTTIR, S. O., NORMANN, F., ANDERSSON, K., PROLß, K., EMILSDOTTIR, S., & JOHNSSON, F., 2015. Post-combustion CO_2 capture applied to a state-of-the-art coal-fired power plant-The influence of dynamic process conditions. Int. *J. Greenhouse. Gas Control*, **33**: 51-62.

GAO, X., CHEN, Z., YAO, Y., ZHOU, M., LIU, Y., WANG, J., WU, W.D., CHEN, X.D., WU, Z., & ZHAO, D., 2016. Direct Heating Amino Acids with Silica: A Universal Solvent-Free Assembly Approach to Highly Nitrogen-Doped Mesoporous Carbon Materials *Adv. Funct. Mater*. **26**: 6649–6661.

GAO, X., YANG, S., HU, L., CAI, S., WU, L., & KAWI, S., 2022. Carbonaceous materials as adsorbents for CO_2 capture: synthesis and modification. *Carbon Capture Sci. Technol.* **3**: 100039.

GHIMBEU, C.M., VIDAL, L., DELMOTTE, L., LE, MEINS, J.M., & VIX-GUTERL, C., 2014. Catalyst-free soft-template synthesis of ordered mesoporous carbon tailored using phloroglucinol/glyoxylic acid environmentally friendly precursors. *Green Chem **16**(6):3079.*

GIBSON, J. A. A., GROMOV, A. V., BRANDANI, S., & CAMPBELL, E. E. B., 2015. The effect of pore structure on the CO_2 adsorption efficiency of polyamine impregnated porous carbons*. Microporous and Mesoporous Materials*, **208**: 129-139.

GIERSZAL, K.P., JARONIEC, M., 2006. Carbons with extremely large volume of uniform mesopores synthesized by carbonization of phenolic resin film formed on colloidal silica template, *J. Am. Chem. Soc*. **128**: 10026-10027.

Global Monitoring Laboratory, 2020. *https://www.esrl.noaa.gov/gmd/ccgg/trends/mlo.html.*

GOKULAKRISHNAN, N., KANIA, N., LEGER, B., LANCELOT, C., GROSSO, D., MONFLIER, E., & PONCHEL, A., 2011. An ordered hydrophobic mesoporous carbon with graphitic pore walls and its application in aqueous catalysis*, Carbon* **49**: 1290–1298.

GOLDSTEIN, J., LYMAN, C.E., NEWBURY, D.E., LIFSHIN, E., ECHLIN, P., SAWYER, L., JOY, D.C., & MICHEAL, J.R., 2003. *Scanning Electron Microscopy and X-Ray Microanalysis*. Kluwer Academic Plenum Publishers, New York.

GONG, J., LIU, J., JIANG, Z., CHEN, X., WEN, X., MIJOWSKA, E., & TANG, T., 2014. Converting mixed plastics into mesoporous hollow carbon spheres with controllable dia GREGOROVA, A., KOSIKOVA, B., & MORAVCIK, R., 2006. Stabilization effect of lignin in natural rubber. *Polym. Degrad. Stab*. **91**: 229-233.

GROSSO, D., DE A. G.J., SOLER-ILLIA, A., BABONNEAU, F., SANCHEZ, C., ALBOUY, P.A, BRUNET-BRUNEAU, A., & BALKENENDE, A.R., 2001. Highly Organized Mesoporous Titania Thin Films Showing Mono-Oriented 2D Hexagonal Channels. *Adv. Mater*.**13**: 14.

GU, J., SU, S., & LI, Y., 2011. Hydrophilic mesoporous carbon nanoparticles as carriers for sustained release of hydrophobic anti-cancer drugs. *Chem Commun*. **47**: 2101-2103.

Hack, J., Maeda, N., & Meier, D.M., 2022. Review on CO_2 Capture Using Amine-Functionalized Materials. *ACS Omega.* **7**: 39520−39530.

HAMMI, N., CHEN, S., DUMEIGNIL, F., ROYER, S., & EL KADIB, A., 2020. Chitosan as a sus- tainable precursor for nitrogen-containing carbon nanomaterials: Synthesis and uses. *Mater. Today Sustain*. **10**: 100053.

HAN, S., LEE, K.T., OH, S.M., & HYEON T., 2003. The effect of silica template structure on the pore mesoporous carbons. *Carbon* **41**: 1049-1056.

HAN, B., CHENG, G., WANG, Y., & WANG, X., 2019. Structure and functionality design of novel carbon and faradaic electrode materials for high-performance capacitive deionization. *Chem. Eng. J*. **360**: 364–384.

HARLICK, P.J.E., & SAYARI, A., 2007. Applications of Pore-Expanded Mesoporous Silica. 5. Triamine Grafted Material with Exceptional CO2 Dynamic and Equilibrium Adsorption Performance. *Ind. Eng. Chem. Res*. **46**: 446-458.

HARMSEN, P.F.H., HUIJGEN, W.J.J., BERMÚDEZ LÓPEZ, L.M., BAKKER, R.R.C., 2010. Literature Review of Physical and Chemical Pretreatment Processes for Lignocellulosic Biomass. *Energy Research Centre of the Netherlands*. 10-013.

HAYASHI, J., KAZEHAYA, A., MUROYAMA, K., & WATKINSON, A.P., 2000. Preparation of activated carbon from lignin by chemical activation. *Carbon* **38**: 1873–1878.

HAYASHI, J.I., MUROYAMA, K., GOMES, V.G., & WATKINSON, A.P., 2002. Fractal dimensions of activated carbons prepared from lignin by chemical activation. *Carbon*. **40**(4): 630-632.

HEIDARINEJAD, Z., DEHGHANI, M.H., HEIDARI, M., JAVEDAN, G., IMRAN ALI, I., SILLANPAA, M., 2020. Methods for preparation and activation of activated carbon: a review. *Environ. Chem. Lett*. **18**:393–415.

HENDRAWAN, Y., NISRINA SAJIDAH, N., CHOIRUL UMAM, C., MUCHAMMAD RIZA FAUZY, M.R., YUSUF WIBISONO, Y., LA CHOVIYA HAWA., L.C., 2019. Effect of Carbonization Temperature Variations and Activator Agent Types on Activated Carbon Characteristics of Sengon Wood Waste (Paraserianthes falcataria (L.) Nielsen. *Earth Environ. Sci*. **239**: 012006.

HERM, Z. R., SWISHER, J. A., SMIT, B., KRISHNA, R., & LONG, J. R., 2011. Metal−Organic Frameworks as Adsorbents for Hydrogen Purification and Precombustion Carbon Dioxide Capture. *J. Am. Chem. Soc,* **133**: 5664.

HEROU, S., RIBADENEYRA, M.C., MADHU, R., ARAULLO-PETERS, V., JENSEN A., SCHLEE, P., & TITIRICI, M., 2019. Ordered mesoporous carbons from lignin: a new class of biobased electrodes for supercapacitors. *Green Chem*. **21**. 550-559.

HIMENO, S., KOMATSU, T., & FUJITA, S., 2005. High-pressure adsorption equilibria of methane and carbon dioxide on several activated carbons, *J. Chem. Eng. Data* **50**: 369–376.

HIROTOMO, N., FUJIMOTO, H., ITOI, H., NOMURA, K., TANAKA, H., MIYAHARA, M.T., BONNAUD, P.A., MIURA, R., SUZUKI, A., MIYAMOTO, N., HATAKEYAMA, N., MIYAMOTO, A., IKEDA, K., OTOMO, T., & TAKASHI, K., 2018. Graphene-based ordered framework with a diverse range of carbon polygons formed in zeolite nanochannels. *Carbon* **129**: 854-862.

HOLLANDER, J. M. & JOLLY, W. L. 1970. X-ray photoelectron spectroscopy. Accounts of Chemical Research, *Accounts Chem. Res*., **3:** 193-200.

HOU, X., ZHUANG, L., MA, B., CHEN, S., HE, H., & YIN, F., 2018. Silanol-rich platelet silica modified with branched amine for efficient CO2 capture*, Chem. Eng. Sci.* **181**: 15-325.

HUANG, H.Y., YANG, R.T., CHINN, D., & MUNSON, C.L., 2003. Amine-Grafted MCM-48 and Silica Xerogel as Superior Sorbents for Acidic Gas Removal from Natural Gas. *Ind. Eng. Chem. Res*. **42**: 2427–2433.

HUH, S., WIENCH, J.W., YOO, J.C., PRUSKI, M., & LIN, V.S.Y., 2003. Organic Functionalization and Morphology Control of Mesoporous Silicas via a Co-Condensation Synthesis Method. *Chem Mater*;**15**:4247.

IGNAT, M., VAN OERS, C.J., VERNIMMEN, J., MERTENS, M., POTGIETER-VERMAAK, S., MEYNEN, V., POPOVICI, E., & COOL, P., 2010. Textural property tuning of ordered mesoporous carbon obtained by glycerol conversion using SBA-15 silica as template. *Carbon* **48**: 1609-1618.

INAGAKI, M., QIU, J., & GUO, Q., 2015. Carbon foam: Preparation and application, *Carbon*, **87**: 128-152.

INAGAKI, M., TOYODA, M., SONEDA, Y., TSUJIMURA, MORISHITA, T., 2016. Templated mesoporous carbons: Synthesis and applications. *Carbon* **107**: 448-473.

INKSON, B.J., 2016. Scanning electron microscopy (SEM) and transmission electron microscopy (TEM) for materials characterization. *Materials Characterization Using Nondestructive Evaluation (NDE) Methods.* 17-43.

International Union of Pure and Applied Chemistry Physical Chemistry Division Commission on Colloid and Surface Chemistry, Subcommittee on Characterization of Porous Solids: 1994. "Recommendations for the characterization of porous solids (Technical Report)". *Pure Appl. Chem*.. **66**(8): 1739–1758.

IQBAL, A.K.M.A., SAKIB, N., IQBAL, A.K.M.P., & NURUZZAMAN, D.M., 2020. Graphene-based nanocomposites and their fabrication, mechanical properties and applications. *Materialia*. **12**: 100815.

JAIN, A., JAYARAMAN, S., BALASUBRAMANIAN, R., & SRINIVASAN, M., 2014. Hydrothermal pre-treatment for mesoporous carbon synthesis: enhancement of chemical activation. *J. Mater. Chem. A*, **2**: 520–528.

JANSEN, D., GAZZANI, M., MANZOLINI, G., DIJK, E. V., & CARBO, M., 2015. Pre-combustion CO_2 capture. *Int. J. Greenhouse. Gas Control*, **40**: 167-187.

JANUS, P., JANUS, R., DUDEK, B., DROZDEK, M., SILVESTRE-ALBERO, A., RODRÍGUEZ-REINOSO, F., & KUSTROWSKI, P., 2020. On mechanism of formation of SBA-15/furfuryl alcohol-derived mesoporous carbon replicas and its relationship with catalytic activity in oxidative dehydrogenation of ethylbenzene. *Microporous and Mesoporous Materials*. **299**: 110118.

JEDRZEJCZYK, M.A., ENGELHARDT, J., DJOKIC, M.R., BLIZNUK, V., VAN GEEM, K.M., VERBERCKMOES, A., DE CLERCQ, J., & BERNAERTS, K.V., 2021. Development of Lignin-Based Mesoporous Carbons for the Adsorption of Humic Acid. *ACS Omega*, **6**: 15222−15235.

JI, Q.Q, GUO, P.Z. & ZHAO, X.S., 2010. Preparation of chitosan-based porous carbons and their application as electrode materials for supercapacitors. *Acta Physico-Chimica Sinica*, **26**(5) 1254-1258.

JIANG, L., SHENG, L., & FAN, Z., 2018. Biomass-derived carbon materials with structural diversities and their applications in energy storage. *Sci. China Mater*. **61**: 133.

JIANG, Y., TAN, P., QI, S.C., LIU, X.Q., YAN, J.H., FAN, F., & SUN, L.B., 2019. Metaleorganic frameworks with target-specific active sites switched by photoresponsive motifs: efficient adsorbents for tailorable CO_2 capture. *In: Chem Int, Angew (Ed.),* **58**: 6600-6604.

JOO, S.H., CHOI, S.J., OH, I., KWAK, J., LIU, Z., TERASAKI, O., & RYOO, R., 2001. Ordered nanoporous arrays of carbon supporting high dispersions of platinum nanoparticles. *Nature*. **412**: 169–172.

JOO, S.H, PAK, C., YOU, D.J, LEE, S.A, LEE, H.I, KIM, J.M, CHANG, H., & SEUNG, D., 2006. Ordered mesoporous carbons (OMC) as supports of electrocatalysts for direct methanol fuel cells (DMFC): effect of carbon precursors of OMC on DMFC performances. *Electrochim Acta*, **52**: 1618.

JUN, S., JOO, S.H., RYOO, R., KRUK, M., JARONIEC, M., LIU, Z., OHSUNA, T., & TERASAKI, O., 2000. Synthesis of New, Nanoporous Carbon with Hexagonally Ordered Mesostructure. *J. Am. Chem. Soc*. **122**(43): 10712-10713.

JUNG, H., LEE, C.H., JEON, S., HUH, D.H. JO, J., KIM, S.H., 2016. Effect of Amine Double Functionalization on CO_2 Adsorption Behaviors of Silica Gel-Supported Adsorbents, *Adsorption*, **22**: 1137–1146.

KAMRAN, U., & PARK, S.J., 2021. Chemically modified carbonaceous adsorbents for enhanced CO2 capture: *A review. J. Clean. Prod.* **290**: 125776.

KHALIL, H.A., SAURABH, C.K., SYAKIR, M.I., FAZITA, M.N., BHAT, A., BANERJEE, A., FIZREE, H.M., RIZAL, S. AND TAHIR, P.M., 2019. Barrier properties of biocomposites/hybrid films. In *Mechanical and physical testing of biocomposites, fibre-reinforced composites and hybrid composites*. 241-258. Woodhead Publishing.

KHALILI, N.R., CAMPBELL, M., SANDI, G., & GOLAS, J. 2000. Production of micro- and mesoporous activated carbon from paper mill sludge I. Effect of zinc chloride activation. *Carbon* **38**: 1905–1915.

KHAN, A., GOEPEL, M., COLMENARES, J. C., & GLÄSER, R., 2020. Chitosan-based N-doped carbon materials for electrocatalytic and photocatalytic applications. *ACS Sustain. Chem. Eng*, **8** (12): 4708–4727.

KHATRI, R. A., STEVEN SC CHUANG, YEE SOONG, AND MCMAHAN GRAY 2006. Thermal and chemical stability of regenerable solid amine sorbent for CO_2 capture*. Energy & Fuels*, **20:** 1514-1520.

KIM, S & PINNAVAIA, T.J., 2001. A low cost route to hexagonal mesostructured carbon molecular sieves. *Chem. Commun*. 2418-2419.

KIM, S.S., KARKAMKAR, A., PINNAVAIA, T.J., KRUK, M., JARONIEC, M., 2001a. Synthesis and Characterization of Ordered, Very Large Pore MSU-H Silicas Assembled from Water-Soluble Silicates. *J. Phys. Chem. B.* **105** (32): 7663-7670.

KIM, J., LEE, J., & HYEON, T., 2004. Direct synthesis of uniform mesoporous carbons from the carbonization of as-synthesized silica/triblock copolymer nanocomposites. *Carbon* **42**: 2711–2719.

KIM, T.W., RYOO, R., GIERSZAL, K.P., JARONIEC, M., SOLOVYOV, L.A., SAKAMOTO, Y., TERASAKI, O., 2005. Characterization of mesoporous carbons synthesized with SBA-16silica template, *J. Mater. Chem*. **15:** 1560–1571.

KIM, Y.S, GUO X.F, & KIM G.J., 2010. Synthesis of carbon monolith with bimodal meso/macroscopic pore structure and its application in asymmetric catalysis. *Catal Today.* **150** (1–2): 91–99.

KIOMARSIPOUR, N., ALIZADEH, M., ALIZADEH, M., & GHANI, K., 2021. Synthesis and surface-functionalizing of ordered mesoporous carbon CMK-3 for removal of nitrate from aqueous solution as an effective adsorbent*. Diamond & Related Materials.***116**: 108419.

KLEITZ, F., CHOI, S.H., & RYOO, R., 2003. Cubic Ia3d large mesoporous silica: synthesis and replication to platinum nanowires, carbon nanorods and carbon nanotubes. *Chem. Commun*. 2136–2137.

KLINTHONGCHAI, Y., PRICHANONT, S., PRASERTHDAM, P., & JONGSOMJIT, B., 2020. Synthesis, characteristics and application of mesocellular foam carbon (MCF-C) as catalyst for dehydrogenation of ethanol to acetaldehyde. *J. Environ. Chem. Eng*.. **8**: 103752.

KNOX, J.H., KAUR, B., & MILLWARD, G.R., 1986. Structure and performance of porous graphitic carbon in liquid chromatography, *J. Chromatogr. A*. **352:** 3–25.

KOMANOYA, T., KOBAYASHI, H., HARA, K., CHUN, W.J., FUKUOKA, A., 2011. Catalysis and characterization of carbon-supported ruthenium for cellulose hydrolysis. *Appl. Catal A: General* **407**: 188–194.

KONG, W., & LIU, J., 2019. Ordered mesoporous carbon with enhanced porosity to support organic amines: efficient nanocomposites for the selective capture of CO2, *New J. Chem*. **43**: 6040–6047.

KONNO, H., 2016. *X-ray Photoelectron Spectroscopy. Materials Science and Engineering of carbon*: Characterizarion. Tsinghua University Press Limited. Published by Elsevier Inc.

KRUK, M., JARONIEC, M., RYOO, R., JOO., S.H., 2000a. Characterization of Ordered Mesoporous Carbons Synthesized Using MCM-48 Silicas as Templates*. J. Phys. Chem. B.* **104**(33): 7960-7968

KRUK, M., DUFOUR, B., CELER, E.B., KOWALEWSKI, T., JARONIEC, M., & MATYJASZEWSKI, K., 2005. Synthesis of Mesoporous Carbons Using Ordered and Disordered Mesoporous Silica Templates and Polyacrylonitrile as Carbon Precursor. *J. Phys. Chem. B*.**109**: 9216-9225.

KUCINSKA, A., CYGANIUK, A. AND LUKASZEWICZ, J.P., 2012. A microporous and high surface area active carbon obtained by the heat-treatment of chitosan. *Carbon*, **50**(8), 3098-3101.

KUMAR, A., & GUPTA, H., 2020. Activated carbon from sawdust for naphthalene removal from contaminated water. *Environ. Technol. Innov*. **20**: 101080.

KUMAR, S., BERA, R., DAS, N., & KOH, J., 2020. Chitosan-based zeolite-Y and ZSM-5 porous biocomposites for H_2 and CO_2 storage. *Carbohydrate Polymers* **232**: 115808.

KYOTANI, T. (2006). Synthesis of Various Types of Nano Carbons Using the Template Technique Bull. *Chem. Soc. Jpn*. **79**(9): 1322–1337.

LABROPOULOS, A., VEZIRI, C., KAPSI, M., PILATOS, G., LIKODIMOS, V., TSAPATSIS, M., KANELLOPOULOS, N.K., ROMANOS, G.E., & KARANIKOLOS, G.N., 2015. Carbon nanotube selective membranes with subnanometer, vertically aligned pores, and enhanced gas transport properties. *Chem. Mater*. **27**: 8198–8210.

LAKHI K. S., CHA, W. S., CHOY, J. H., AL-EJJI, M., ABDULLAH, A. M., AL-ENIZI, A. M., & VINU, A., 2016. Synthesis of mesoporous carbons with controlled morphology and pore diameters from SBA-15 prepared through the microwave-assisted process and their CO2 adsorption capacity. *Microporous and Mesoporous Materials.* **233**: 44-52.

LAZARO, M.J., CALVILLO, L., BORDEJE, E.G., MOLINER, R., JUAN, R., RUIZ, C.R., 2007. Functionalization of ordered mesoporous carbons synthesized with SBA-15 silica as template. *Microporous and Mesoporous Materials* **103**: 158–165.

LEDESMAA, B., MARÍNB, M.O., MURILLOA, A.A., ROMAN, S., & NABAIS, J.M.V., 2018. Method for promoting in-situ hydrochar porosity in hydrothermal carbonization of almond shells with air activation. *J. Supercrit. Fluids*. **138**: 187-192.

LEE, J., YOON, S., HYEON, T., OH, S.M., & KIM, K.B., 1999. Synthesis of a new mesoporous carbon and its application to electrochemical double-layer capacitors. *Chem. Commun*. 2177–2178.

LEE, J., YOON, S., OH, S.M., SHIN, C.H., & HYEON, T., 2000. Development of a New Mesoporous Carbon Using an HMS Aluminosilicate Template. *Adv. Mater*. **12**(5): 359-362

LEE, J., YOON, S., OH, S.M., SHIN, C.H., HYEON, T., 2000. Development of a new mesoporous carbon using an HMS aluminosilicate template. *Adv Mater* **12**(5):359–362.

LEE, J., SOHN, K., & HYEON, T., 2001. Fabrication of Novel Mesocellular Carbon Foams with Uniform Ultralarge Mesopores. *Chem. Soc*. **123**: 5146–5147.

LEE, K.T., & OH, S.M., 2002. Novel synthesis of porous carbons with tunable pore size by surfactant-templated sol–gel process and carbonisation. *Chem. Commun*. 2722-2723.

LEE, J.S., JOO, S.H., & RYOO, R., 2002a. Synthesis of Mesoporous Silicas of Controlled Pore Wall Thickness and Their Replication to Ordered Nanoporous Carbons with Various Pore Diameters. *J. Am. Che*. *Soc*. **124**: 7.

LEE, J., SOHN, K., & HYEON, T., 2002b. Low-cost and facile synthesis of mesocellular carbon foams. *Chem. Comm*. 2674-2675.

LEE, J., HAN, S., & HYEON, T. 2003. Synthesis of new nanoporous carbon materials using nanostructured silica materials as templates. *J. Mater. Chem*. **14**: 478-486.

LEE, J., HAN, S., HYEON, T., 2004a. Synthesis of new nanoporous carbon materials using nanostructured silica materials as templates. *J. Mater. Chem*. 1**4**: 478–486.

LEE, J., KIM, J., KIM, S. W., SHIN, C. H., HYEON, T., 2004b. Mesocellular polymer foams with unprecedented uniform large mesopores and high surface areas. *Chem. Commun*., 2004, 562 – 563.

LEE, H.I., KIM, J.H., JOO, S.H., CHANG, H., SEUNG, D., JOO, O.H., SUH, D.J., AHN, W.S., PAK, C., & KIM, J.M., 2007. Ultrafast production of ordered mesoporous carbons via microwave irradiation. *Letters to the Editor / Carbon* **45**: 2843–2854.

LEE, S.Y., & PARK, S.J., 2012. Influence of oxygen-functional groups on carbon replicas for hydrogen adsorption. *Phys. Status Solidi* (a). **209**(4): 694-697

.

LEE, S.Y., & PARK, S.J., 2013. Determination of the optimal pore size for improved CO2 adsorption in activated carbon fibers. *J. Colloid Interface Sci*., **389**: 230.

LEE, C. H., HYEON, D. H., JUNG, H., CHUNG, W., JO, D. H., SHIN, D. K., & KIM, S. H., 2015. Effects of pore structure and PEI impregnation on carbon dioxide adsorption by ZSM-5 zeolites, *J. Ind. Eng. Chem*. **23**: 251–256.

LEI, Z., CHRISTOV, N., ZHANG, L.L., & ZHAO, X.S., 2011. Mesoporous carbon nanospheres with an excellent electrocapacitive performance. *J. Mater. Chem*., **21**: 2274–2281.

LEUNG, D. Y. C., CARAMANNA, G., MAROTO-VALER, M. M. 2014. An overview of current status of carbon dioxide capture and storage technologies. *Renewable and Sustainable Energy Reviews*, **39**: 426-443.

LEZANSKA, M., OLEJNICZAK, A., & LUKASZEWICZ, J.P., 2018. Hierarchical porous carbon templated with silica spheres of a diameter of 14 nm from pure chitosan or a chitosan/ZnCl2 solution. *J. Porous Mater*. **25**:1633–1648.

LI, F., WU, Z., & ZHAO, D., 2010. A low-concentration hydrothermal synthesis of biocompatible ordered mesoporous carbon nanospheres with tunable and uniform size*. Angew Chemie Int Ed*. **49**:7987–7991.

LI, J., FISET, E., YANG, J., YUAN, P., LING, X., HULICOVA-JURCAKOVA, D., YU, C., & WANG, L., 2012. Formation of graphitic tubules from ordered mesoporous carbon and their effect on supercapacitive energy storage. *J. Mater. Chem*. **22**: 21472–21480.

LI, K., JIANG, J., YAN, F., TIAN, S., & CHEN, X., 2014. The influence of polyethyleneimine type and molecular weight on the CO_2 capture performance of PEI-nano silica adsorbents. *Appl. Energy* **136**: 750–755.

LI, K., JIANG, J., TIAN, S., YAN, F. & CHEN, X. 2015. Polyethyleneimine–nano silica composites: a low-cost and promising adsorbent for CO_2 capture. *J. Mater. Chem. A*, 3, 2166-2175.

LI, Y., LI, D.W., RAO, Y., ZHAO, X.B., WU, M.B., 2016a. Superior CO_2, CH_4, and H_2 uptakes over ultrahigh-surface-area carbon spheres prepared from sustainable biomass-derived char by CO_2 activation. *Carbon* **105**: 454-462.

LI, D., LI, W.B., SHI, J.S., XIN, F.W., 2016b. Influence of doping nitrogen, sulfur, and phosphorus on activated carbons for gas adsorption of H_2, CH_4 and CO_2. *RSC Adv.* **6**: 50138-50143.

LI, W., LIU J., & ZHAO, D.Y., 2016c. Mesoporous materials for energy conversion and storage devices. Nat. Rev. Mater. **1:** 1-17.

LI, K.M., TIAN, S.C. JIANG, J.G., WANG, J.M., CHEN, X.J., & YAN, F., 2016d. Pine cone shell-based activated carbon used for CO2 adsorption. *J. Mater. Chem*. **4**: 5223.

LI, B., XIONG, H., & XIAO, Y., 2020. Progress on Synthesis and Applications of Porous Carbon Materials. *Int. J. Electrochem. Sci.,* **15**: 1363 – 1377.

LIANG, C., HONG, K., GUIOCHON, G.A, MAYS, J.W., & DAI, S., 2004. Synthesis of a large-scale highly ordered porous carbon film by self-assembly of block copolymers. *Angew.Chem.Int.Ed*. **116**(43):5909–5913.

LIANG, C., & DAI, S., 2006. Synthesis of Mesoporous Carbon Materials via Enhanced Hydrogen-Bonding Interaction. *J. Am. Chem. Soc*.,**128**: 5316.

LIANG, C., LI, Z.., & DAI, S., 2008. Mesoporous Carbon Materials: Synthesis and Modification. *Angew. Chem. Int. Ed* **47**: 3696 – 3717.

LIANG, T., CHEN, C., LI, X., & ZHANG, J., 2016. Popcorn-derived porous carbon for energy storage and CO2 capture. *Langmui*r. **32**: 8042–8049.

LIANG, K.H., MA, C., LIU, L., YU, Y.F., LV, H.J., ZHANG, Y., & CHEN, A.B., 2019. Nitrogen and oxygen co-doped ordered dual-mesoporous carbon for supercapacitors. *J. Alloys Compd*., **805**: 859-867.

LILLO-RÓDENAS, M. A., CAZORLA-AMORÓS, D., & LINARES-SOLANO, A. 2003. Understanding chemical reactions between carbons and NaOH and KOH: an insight into the chemical activation mechanism. *Carbon,* **41**(2), 267-275.

LIN, C.F., ZHANG, X., LIN, H., WANG, N., LI, J.B., & YANG, X.Z., 2006. Synthesis of ordered mesoporous carbon using MCM–41 mesoporous silica as template, *Adv. Mater. Res*. **11-12**: 543–546.

LIN, Y., YAN, Q., KONG, C., & CHEN, L., 2013. Polyethyleneimine Incorporated Metal-Organic Frameworks Adsorbent for Highly Selective CO2 Capture. *Sci. Rep*. **3**: 1859.

LIU, R., SHI, Y., & WAN, Y., 2006. Triconstituent co-assembly to ordered mesostructured polymer-silica and carbon-silica nanocomposites and large pore mesoporous carbons with high surface areas. *J. Am Chem Soc*. **128**: 11652–11662.

LIU, L., WANG, F.Y., SHAO, G.S., & YUAN, Z.Y., 2010. A low-temperature autoclaving route to synthesize monolithic carbon materials with an ordered mesostructured*. Carbon*, **48**: 2089.

LIU, N., YIN, L., WANG, C., ZHANG, L., LUN, N., XIANG, D., QI, Y., GAO, R., 2010a. Adjusting the texture and nitrogen content of ordered mesoporous nitrogen-doped carbon materials prepared using SBA-15 silica as a template. *Carbon*. **48**: 3579–3591.

LIU, N., SONG, H., & CHEN, X., 2011. Morphology control of ordered mesoporous carbons by changing HCl concentration, *J. Mater. Chem*. **21**(14): 5345–5351.

LIU, L., DENG, Q.F., AGULA, B., REN, T.Z., LIU, Y.P., ZHAORIGETU, B., & YUAN, Z.Y., 2012. Synthesis of ordered mesoporous carbon materials and their catalytic performance in dehydrogenation of propane to propylene. *Catal. Today*. **186**: 35–41.

LIU, D., LEI, J.H., GUO, L.P., QU, D., LI, Y., & SU, B.L., 2012. One-pot aqueous route to synthesize highly ordered cubic and hexagonal mesoporous carbons from resorcinol and hexamine. *Carbon*, **50**: 476–487.

LIU, Y., FAN, W., WANG, K., WANG, J., 2016. Studies of CO_2 absorption/regeneration performances of novel aqueous monothanlamine (MEA)-based solutions. *J. Clean. Prod*, **112**: 4012-4021.

LIU X, SUN Y, LIU J, SUN C, LIU H, & XUE Q, 2017. Potassium and zeolitic structure modified ultra-microporous adsorbent materials from a renewable feedstock with favorable surface chemistry for CO_2 capture. *ACS Appl Mater Interfaces* **9(**32):26826–26839.

LIU, M., LI, J., CAI, C., ZHOU, Z., LING, Y., & LIU, R., 2017a. A polyacrylonitrile copolymer-silica template for three-dimensional hierarchical porous carbon as a Pt catalyst support for the oxygen reduction reaction. *Dalton Trans*., **46**: 9912–9917.

LIU, X., ZHOU, K., FARNDON, M., MEIER, E., STEVENS, L., LIU, H., & SUN, C., 2019. Mesocellular silica foam supported polyamine adsorbents for dry CO_2 scrubbing: Performance of single versus blended polyamines for impregnation. *Appl. Energy* **255**: 113643.

LIU, S., WANG, Z., HAN, T., FEI, T., ZHANG, T., ZHANG, H., 2019a. Solvent-free synthesis of mesoporous carbon employing KIT-6 as hard template for the removal of aqueous rhodamine B. *J. Porous Mater*. **26**: 941-950.

LIU, W., YUAN, H., & KE, Y., 2020. Preparation and characterization of ordered mesoporous carbon based on soybean oil. *J Mater Sci*. **55**: 6525–6536.

LIU, H., WU, S., TIAN, N., YAN, F., YOU, C., & YANG, Y., 2020a. Carbon foams: 3D porous carbon materials holding immense potential. *J. Mater. Chem. A*, **8**: 23699–23723.

LLEWELLYN, P. L., BOURRELLY, S., SERRE, C., VIMONT, A., DATURI, M., HAMON, L., DE WEIRELD, G., CHANG, J. S., HONG, D. Y., HWANG, Y. K., JHUNG, S. H., & FEREY, G., 2008. High uptakes of CO_2 and CH4 in mesoporous metal orgnanic frameworks MIL-100 and MIL-101. *Langmuir*, **24**: 7245–7250.

LOWELL, S., SHIELDS, J., THOMAS, M.A., & THOMMES, M., 2004. Characterization of Porous Solids and Powders: Surface Area. Porosity and Density, *Springer*.

LOZANO-CASTELLO, D., CALO, J., CAZORLA-AMOROS, D. & LINARES-SOLANO, A. 2007. Carbon activation with KOH as explored by temperature programmed techniques, and the effects of hydrogen. *Carbon,* 45**,** 2529-2536.

LU, A.H., SCHMIDT, W., & SPLIETHOFF, B., 2003. Synthesis of Ordered Mesoporous Carbon with Bimodal Pore System and High Pore Volume. *Adv. Mater*. 1**5**(19): 1602-1606.

LU, G.Q., & ZHAO, X.S., 2004. *Nanoporous Materials, science and engineering, Series of chemical engineering,* Vol.4, Imperial College Press, London.

LU, A.H., LI, W.C., SCHMIDT, W., & SCHUTH, F., 2005. Template synthesis of large pore ordered mesoporous carbon. *Microporous and Mesoporous Materials*. **80**: 117-128.

LU, A.H., SPLIETHOFF, B., SCHUTH, F. 2008. Aqueous synthesis of ordered mesoporous carbon via self-assembly catalyzed by amino acid. *Chem. Mater*. **20**: 5314−5319.

LU, A.H., & SCHUTH, F., 2006. Nanocasting: a versatile strategy for creating nanostructured porous materials, *Adv. Mater*. **18**: 1793–1805.

LUKENS, W. W., STUCKY, G. D., 2002. Synthesis of Mesoporous Carbon Foams Templated by Organic Colloids*. Chem. Mater*. **14**: 1665-1670.

LUO, J., GENCO, J., COLE, B., & FORT, R., 2011. Lignin Recovered from The Near-Neutral Hemicellulose Extraction Process As A Precursor For Carbon-Fiber. *Bio Resources*. **6**: 4566–4605.

MA, X., WANG, X., & SONG, C., 2009. "Molecular Basket" Sorbents for Separation of CO2 and H2S from Various Gas Streams. *American Chemical Society.* **131**(16): 5777-5783.

MA, Z., KYOTANI, T., LIU, Z., TERASAKI, O., & TOMITA, A., 2001. Very High Surface Area Microporous Carbon with a Three-Dimensional Nano-Array Structure: Synthesis and Its Molecular Structure*. Chem. Mater*. **13**: 4413-4415.

MA, Z.X., T. KYOTANI, T., & TOMITA, A., 2002. Synthesis methods for preparing microporous carbons with a structural regularity of zeolite Y. *Chem. Commun*. 2365.

MA, T.Y., LIU, L., & YUAN, Z.Y., 2013. Direct synthesis of ordered mesoporous carbons. *Chem. Soc. Rev*. **42** (9): 3977-4003.

MA, X., YUAN, H., & HU, M., 2019. A simple method for synthesis of ordered mesoporous carbon. *Diam. Relat. Mater*. **98**: 107480.

MAC DOWELL, N., FENNELL, P.S., SHAH, N., & MAITLAND, G.C., 2017. The Role of CO_2 Capture and Utilization in Mitigating Climate Change. *Nature Climate Change,* Volume 7.

MACIA-AGULLO, J.A., MOORE, B.C., CAZORLA-AMOR, D., & LINARES-SOLANO, A. Activation of coal tar pitch carbon fibres: Physical activation vs. chemical activation. *Carbon* **42**:1367–1370.

MCDOUGALL, G. 1991. The physical nature and manufacture of activated carbon. *Journal of the Southern African Institute of Mining and Metallurgy*. **91**:109-120.

MANE, G.P., TALAPANENI, S.N., ANAND, C., VARGHESE, S., IWAI, H., JI, Q., ARIGA, K., MORI, T., & VINU, A., 2012. Preparation of Highly Ordered Nitrogen-Containing Mesoporous Carbon from a Gelatin Biomolecule and its Excellent Sensing of Acetic Acid Adv. *Funct. Mater*., **22**: 3596–3604.

MANE, S., GAO, Z.Y., LI, Y.X., LIU, X.Q., & SUN, L.B., 2018. Rational fabrication of polyethylenimine-linked microbeads for selective CO2 capture, *Ind. Eng. Chem. Res*. **57**:250–258.

MANOCHA, S.M., 2003. Porous carbons. *Sadhana*. **28**:335–348.

MAROTO-VALER, M., LU, Z., ZHANG, Y., & TANG, Z., 2008. Sorbent for CO_2 capture from high carbon fly ashes. *Waste Manag*. **28**: 2320-2328.

MENG, L..Y., & PARK, S.J. 2012. Influence of MgO template on carbon dioxide adsorption of cation exchange resin-based nanoporous carbon. *J. Colloid Interface Sci*. **366**: 125–129.

MENG, Y., JIANG, J., GAO, Y., AIHEMAITI, A., JU, T., XU, Y., & LIU, N., 2019. Biogas upgrading to methane: Application of a regenerable polyethyleneimine-impregnated polymeric resin (NKA-9) via CO2 sorption, *Chem. Eng. J*. **361**: 294–303.

METZ B., DAVIDSON O., DE CONINCK H., LOOS M., & MEYER L., 2005. *IPCC special report on carbon dioxide capture and storage. In: Prepared by Working Group III of the Intergovernmental Panel on Climate Change* (IPCC). Cambridge University Press, New York, UK.

MILLWARD, A.R., & YAGHI, O.M., 2005. Metal-Organic Frameworks with Exceptionally High Capacity for Storage of Carbon Dioxide at Room Temperature. *J. Am. Chem. Soc.* **127**: 17998-17999.

Mishra, A.K., Ramaprabhu, S., 2012. Polyaniline/multiwalled carbon nanotubes nanocomposite-an excellent reversible CO_2 capture candidate, RSC Adv. **2**: 1746–1750.

MOLINA-SABIO, M., GONZALEZ, M.T., RODRIGUEZ-REINOSO, F., & SEPOOJLVEDAESCRIBANO, A. 1996. Effect of steam and Carbon dioxide Activation in the Micropore Size Distribution of Activated Carbon. *Carbon*. **34**(4): 505-509.

MOHAMED, M.A., JAAFAR, J., ISMAIL, A.F., OTHMAN, M.H.D., M.A. & RAHMAN., M.A., 2017. *Fourier Transform Infrared (FTIR) Spectroscopy*. Membrane Characterization.

MOMCILOVIC, M.Z., RANDELOVIC, M.S., ZARUBICA, A.R., ONJIA, A.E., KOKUNESOSKI, M., MATOVIC, B.Z., 2013. SBA-15 templated mesoporous carbons for 2,4-dichlorophenoxyacetic acid removal. *J. Chem. Eng.* **220**: 276–283.

MONTIEL-CENTENO, K., BARRERA, D., VILLARREOEL-ROCHA, J., ARROYO-GOMEZ, J.J., MORENO, M.S., & SAPAG, K., 2019. CMK-3 nanostructured carbon: Effect of temperature and time carbonization on textural properties and H_2 storage. **Chem. Eng. Commun**., **206**(11).

MORENO-CASTILLA, C., MALDONADO-HODAR, F.J., CARRASCO-MARIN, F., & ENRIQUE RODRIGUEZ-CASTELLO, C., 2002.Surface Characteristics of Titania/Carbon Composite Aerogels. *Langmuir*. **18**: 2295-2299.

MORISHITA, T., SUZUKI, T., NISHIKAWA, T., HABAZAKI, H., INAGAKI, M., 2006. Preparation of mesoporous carbons by carbonization of the mixtures of poly(vinyl alcohol) with magnesium salts, *TANSO*. **223**: 220-226.

NABAVINIA, M., KANJILAL, B., FUJINUMA, N., MUGWERU, A., & NOSHADI, I., 2021. Developing Eco-Friendly and Cost-Effective Porous Adsorbent for Carbon Dioxide Capture. *Molecule*s. **26**: 1962.

NALWA, H.S., 2003. *Handbook of Organic-Inorganic Hybryd Materials and Nanocomposites, Vol. 1*, American Scientific Publishers, North Lewis Way.

NAUSHAD, M., AHAMAD, T., AL-MASWARI, B.M., ALQADAMI, A.A., & ALSHEHRI, S.M., 2017. Nickel ferrite bearing nitrogen-doped mesoporous carbon as efficient adsorbent for the removal of highly toxic metal ion from aqueous medium, *Chem. Eng. J.* **330**: 1351–1360.

NISHIHARA, H., & KYOTANI, T., 2018. Zeolite-templated carbons – three-dimensional microporous graphene frameworks. *Chem. Commun*. **54**: 5648—5673.

NIU, M., YANG, H., ZHANG, X., WANG, Y., & TANG, A., 2016. Amine-Impregnated Mesoporous Silica Nanotube as an Emerging Nanocomposite for CO_2 Capture. *ACS Appl. Mater. Interfaces*. **8**: 17312–17320.

NIZAMUDDIN, S., BALOCH, H.A., GRIFFIN, G.J., MUBARAK, ABDUL, N.M., BHUTTO, W., RASHID ABRO, R., MAZARI, S.A., & ALI, B.S ., 2017. An overview of

the effect of process parameters on hydrothermal carbonization of biomass, *Renew. Sustain. Energy Rev*., **73**: 1289–1299.

NOR, N.M., CHUNG, L.L., TEONG, L.K., & MOHAMED, A.R., 2013. Synthesis of activated carbon from lignocellulosic biomass and its applications in air pollution control—a review*. J. Environ. Chem. Eng*. **1**: 658–666.

NOTARIANNI, M., LIU, J., VERNON, K., & MOTTA, N., 2016. Synthesis and applications of carbon nanomaterials for energy generation and storage. Beilstein *J. Nanotechnol*. **7**: 149–196.

NOWICKI, P., PIETRZAK, R., & WACHOWSKA, H., 2010. Sorption properties of active carbons obtained from walnut shells by chemical and physical activation. *Catalysis Today*. **150**:107–114.

OJEDA, M.L., ESPARZA, J.M., CAMPERO, A., CORDERO, S., KORNHAUSER, I., & ROJAS, F., 2003. On comparing BJH and NLDFT pore-size distributions determined from N2 sorption on SBA-15 substrata. *Phys. Chem*. **5**: 1859-1866.

OLAJIRE, A.A., 2010. CO_2 capture and separation technologies for end-of-pipe applications. *A review. Energy*, **35(**6), 2610-2628.

OLEJNICZAK, A., LEZANSKA, M., WLOCH, J., ANNA KUCINSKA, A., JERZY P. & LUKASZEWICZA, J. P., 2013. Novel nitrogen-containing mesoporous carbons prepared from chitosan. *J. Mater. Chem. A*. **1**: 8961-8967.

OLIVIER, J.G., JANSSENS-MAENHOUT, G., MUNTEAN, M., PETERS, J.A., 2016. *Trends in global CO_2 emissions* 2016 report.

OU, C., CHEN, S., LIU, Y., SHAO, J., LI, S., FU, T., FAN, W., ZHENG, H., LU, Q., & BI, X., 2016. Study on the thermal degradation kinetics and pyrolysischaracteristics of chitosan-Zn complex. *J. Anal. Appl. Pyrolysis*, **122**: 268–276.

OZAKI, J., ENDO, N., OHIZUMI, W., IGARASHI, K., NAKAHARA, M., OYA, A., 1997. Novel preparation method for the production of mesoporous carbon fiber from a polymer blend. *Carbon*. **35**:1031–1033

PALLARES, J., GONZALEZ-CENCERRADO, A., & ARAUZO, I., 2018. Production and characterization of activated carbon from barley straw by physical activation with carbon dioxide and steam. *Biomass and Bioenergy*. **115**: 64–73.

PANEK, R., WDOWIN, M., FRANUS, W., CZARNA, D., STEVENS, L.A., DENG, H., LIU, J., SUN, C., LIU, H., & SNAPE, C.E., 2017. Fly ash-derived MCM-41 as a low-cost silica support for polyethyleneimine in post-combustion CO_2 capture. *J. CO_2 Util.* **22**: 81 – 90.

PARK, J., NABAE, Y., HAYAKAWA, T., & KAKIMOTO., M.A., 2014. Highly Selective Two-Electron Oxygen Reduction Catalyzed by Mesoporous Nitrogen-Doped Carbon. *ACS Catal*. **4**: 3749−3754.

PARK, D.H., LAKHI, K.S., RAMADASS, K., KIM, M.K., TALAPANENI, S.N., JOSEPH, S., RAVON, U., AL-BAHILY, K., & VINU, A., 2017. Energy Efficient Synthesis of Ordered Mesoporous Carbon Nitrides with a High Nitrogen Content and Enhanced CO_2 Capture Capacity. *Chem.Eur.J.* **23**:10753–10757.

PARMENTIER, J.,VIX-GUTERL, C., GIBOT, P., REDA, M., ILESCU, M., WERCKMANN, J., PATARIN, J., 2003. Study of the structural evolutions of mesoporous MCM-48 silica infiltrated with carbon by different techniques, *Microporous Mesoporous Mater*. **62**: 87–96.

PASTOR-VILLEGAS, J., DURAN-VALLE, C.J., VALENZUELA-CALAHORRO, C., & GOMEZ-SERRANO, V., 1998. Organic chemical structure and structural shrinkage of chars prepared from rockrose. *Carbon*. **36**(9): 1251-1256.

PATEL, H. A., BYUN, J., YAVUZ, C. T., 2016. Carbon Dioxide Capture Adsorbents: Chemistry and Methods. *ChemSusChem,* 1545.

PEKALA, R.W., ALVISO, C.T., KONG, F.M. & HULSEY, S.S., 1992. Aerogels derived from multifunctional organic monomers. *J Non Cryst Solids .* **145**: 90-98.

PENG, H.L., ZHANG, J.B., ZHANG, J.Y., ZHONG, F.Y., WU, P.K., HUANG, K., FAN, J.P., & LIU, F., 2019. Chitosan-derived mesoporous carbon with ultrahigh pore volume for amine impregnation and highly efficient CO_2 capture. *J. Chem. Eng.* **359**: 1159–1165.

PERDIKAKI, A.V., LABROPOULOS, A.I., SIRANIDI, E., KARATASIOS, I., KANELLOPOULOS, N., BOUKOS, N., FALARAS, P., KARANIKOLOS, G.N., &

ROMANOS, G.E., 2016. Efficient CO oxidation in an ionic liquid-modified, Au nanoparticle-loaded membrane contactor. *Chem. Eng. J*. **305**: 79–91.

PEREGO, C., & MILLINI, R., 2013. Porous materials in catalysis: challenges for mesoporous materials *Chem. Soc. Rev*. **42**: 3956.

PETKOVICH, N.D., STEIN, A., 2013. Controlling macro- and mesostructures with hierarchical porosity through combined hard and soft templating *Chem. Soc. Rev*. 42: 3721.

PETROLEUM, B., 2014. *BP energy outlook* 2035. BP stats.

PFAFF, I., & KATHER, A., 2009. Comparative thermodynamic analysis and integration issues of CCS steam power plants based on oxy-combustion with cryogenic or membrane-based air separation. *Energy* Procedia, **1**(1): 495-502.

PIRES, J.C.M., MARTINS, F.G., & SIMOES, M., 2011. Chemical engineering research and design recent developments on carbon capture and storage: an overview. *Chem. Eng. Res. Des*. **89**: 1446-1460.

PIRNGRUBER, G. D., CASSIANO-GASPAR, S., LOURET, S., CHAUMONNOT, A. & DELFORT, B. 2009. Amines immobilized on a solid support for postcombustion CO_2 capture–A preliminary analysis of the performance in a VSA or TSA process based on the adsorption isotherms and kinetic data*. Energy Procedia*, **1:** 1335-1342.

PLANT, D. F., MAURIN, G., DEROCHE, I., & LLEWELLYN, P. L., 2007. Investigation of CO2 adsorption in Faujasite systems: Grand Canonical Monte Carlo and molecular dynamics simulations based on a new derived Na+-CO2 force field. *Microporous Mesoporous Mater*. **99**: 70–78.

PLAZA M.G, PEVIDA C, ARIAS B, FERMOSO J, ARENILLAS A, & RUBIERA F., 2008. Application of thermogravimetric analysis to the evaluation of aminated solid sorbents for CO2 capture*. J. Therm. Anal. Calorim.*, **92**(2): 601–605.

POOLE, C.F., 2005. Gas Chromatography | Column Technology*. Encyclopedia of Analytical Scienc*. 18-34

PRESSER, V., MCDONOUGH, J., YEON, S.H., GOGOTSI, Y., 2011. Effect of pore size on carbon dioxide sorption by carbide-derived carbon. *Energy Environ. Sci*. **4**: 3059.

PRUD'HOMME, A., & NABKI, F., 2020. Comparison between Linear and Branched Polyethylenimine and Reduced Graphene Oxide Coatings as a Capture Layer for Micro Resonant CO_2 Gas Concentration Sensors. *Sensors*. **20**: 1824.

PUTHIARAJ, P., & AHN, W.S., 2017. Facile synthesis of microporous carbonaceous materials derived from a covalent triazine polymer for CO_2 capture. *J. Energy Chem*. **26**: 965-971.

QIAO, W.M., SONG, Y., HONG, S.H., LIM, S.Y., YOON, S.H., KORAI, Y., & MOCHIDA, I., 2006. Development of Mesophase Pitch Derived Mesoporous Carbons through a Commercially Nanosized Template. *Langmuir*. **22**: 3791-3797.

QIU, Z.P., WANG, Y.S., BI, X., ZHOU, T., ZHOU, J., ZHAO, J.P., MIAO, Z.C., YI, W.M., FU, P., & ZHUO, S.P., 2018. Biochar-based carbons with hierarchical micro-meso-macro porosity for high rate and long cycle life supercapacitors. J*. Power Sources.* **376**: 82-90.

QUAN, C., SU, R., GAO, N., 2020. Preparation of activated biomass carbon from pine sawdust for supercapacitor and CO_2 capture. *Int. J. Energy Res*. **44**: 4335–4351.

RAJ, A.P.A. LEWIS, A. DERBY, B., YOUNG, R.J., KINLOCH, I.A., & ZAN, R., 2014. Wide-area strain sensors based upon graphene-polymer composite coatings probed by Raman spec- troscopy. *Adv. Func. Mater*. **24**(19): 2865–2874.

RANA, M., SUBRAMANI, K., SATHISH, M., & GAUTAM, U.K., 2017. Soya derived heteroatom doped carbon as a promising platform for oxygen reduction, supercapacitor and CO_2 capture. *Carbon* **114**: 679-689.

RIAHI, K., RUBIN, E.S., & SCHRATTENHOLZER, L., 2003. Prospects for carbon capture and sequestration technologies assuming their technological learning. *GHC Contr. Technol*. **29**: 1095-1100.

RIBOLDI, L., & BOLLAND, O., 2017. Overview on pressure swing adsorption (PSA) as CO_2 capture technology: state-of-the-art, limits and potentials. *Energy Procedia*, **114:** 2390-2400.

ROCHELLE, G.T., 2009. Amine Scrubbing for CO_2 Capture. *Science*, **325**(5948):1652-1654.

ROSEN, M.J., & KUNJAPPU, J.T., 2012. *Surfactants and Interfacial Phenomena*, John Wiley & Sons, Inc., Hoboken, NJ, 4th edn.

ROUQUEROL, J., AVNIR, D., FAIRBRIDGE, C.W., EVERETT, D.H., HAYNES, J.M., PERNICONE, N., RAMSAY, J.D., SING, K.S.W. & UNGER, K.K., 1994. Recommendations for the characterization of porous solids (Technical Report). *Pure and appl. chem*, ***66***(8): 1739-1758.

RUBIN, E. S., MANTRIPRAGADA, H., MARKS, A., VERSTEEG, P., & KITCHIN, J., 2012. The outlook for improved carbon capture technology. Progress in Energy and Combustion *Science,* **38**(5): 630-67.

RYOO, R., JOO, S. H., & JUN, S., 1999. Synthesis of Highly Ordered Carbon Molecular Sieves via Template-Mediated Structural Transformation. *J. Phys. Chem. B*. **103** (37).

RYOO, R., JOO, S.H., KRUK, M., & JARONIEC, M., 2001. Ordered Mesoporous Carbons. *Adv. Mater*. **13**: 677–681.

SAHA, D., CONTESCU, C.I., & GALLEGO, N.C., 2012. Bimodal mesoporous carbon synthesized from large organic precursor and amphiphilic tri-block copolymer by self-assembly. *Microporous Mesoporous Mater*. **155**: 71–74.

SAHA, D., PAYZANT, E.A., KUMBHAR, A.S., & NASKAR, A.K., 2013. Sustainable Mesoporous Carbons as Storage and Controlled-Delivery Media for Functional Molecules. *ACS Appl. Mater. Interfaces*. **5**: 5868−5874.

SAHA, D., WARREN, K.E., & NASKAR, A.K., 2014. Soft-templated mesoporous carbons as potential materials for oral drug delivery. *Carbon*. **71:** 47–57.

SAHA, D., & KIENBAUM, M.J., 2019. Role of oxygen, nitrogen and sulfur functionalities on the surface of nanoporous carbons in CO_2 adsorption: A critical review. *Microporous and Mesoporous Materials*. **287**: 29–55.

SAIDUR, R., ABDELAZIZ, E. A., DEMIRBAS, A., HOSSAIN, M. S., & MEKHILEF, S. 2011. A review on biomass as a fuel for boilers. *Renew. Sustain. Energy Rev.* **15**(5): 2262-2289.

SAIKIA, D., WANG, T.H., CHOU, C.J., FANG, J., TSAI, L.D., & KAO, H.M., 2015. A comparative study of ordered mesoporous carbons with different pore structures as anode materials for lithium-ion batteries, *RSC Adv*. **5**: 42922-42930.

SAMANTA, A., ZHAO, A., SHIMIZU, G.K.H., SARKAR, P., & GUPTA, R., 2012. Post-Combustion CO2 Capture Using Solid Sorbents: *J Ind Eng Chem.* **51**: 1438-1463.

SANCHEZ-SANCHEZ, A., SUAREZ-GARCIA, F., MARTINEZ-ALONSO, A., TASCON, J.M.D., 2014. Aromatic polyamides as new precursors of nitrogen and oxygen-doped ordered mesoporous carbons, *Carbon* **70**: 119-129.

SANDI, G., THIYAGARAJAN, P., CARRADO, K. A., & WINANS, R. E., 1999. Small angle neutron scattering characterization of the porous structure of carbons prepared using inorganic templates, *Chem. Mater*. **11**: 235–240.

SATTERTHWAITE, D., 2008. Cities contribution to global warming: notes on the allocation of greenhouse gas emissions, *Environ. Urban*. **20**: 539–549.

SATYAPAL, S., FILBURN, T., TRELA, J., & STRANGE, J., 2001. Performance and Properties of a Solid Amine Sorbent for Carbon Dioxide Removal in Space Life Support Applications. *Energy Fuels*, **15**(2): 250-255.

SCHUSTER, J., HE, G., MANDLMEIER, B., YIM, T., LEE, K.T., BEIN T., & NAZAR, L.F., 2012. Spherical Ordered Mesoporous Carbon Nanoparticles with High Porosity for Lithium–Sulfur Batteries*. Angew. Chem., Int. Ed*. **51**: 3591–3595.

SCHMIDT-WINKEL, P., JR, W.W.L., YANG, P., MARGOLESE, D.I., LETTOW, J.S., YING, J.Y., & STUCKY., G.D., 2000. Microemulsion Templating of Siliceous Mesostructured Cellular Foams with Well-Defined Ultralarge Mesopores. *Chem. Mater.* **12**(3): 686-696.

SEVILLA, M., ALVAREZ, S., FUERTES, A.B., 2004. Synthesis and characterisation of mesoporous carbons of large textural porosity and tunable pore size by templating mesostructured HMS silica materials. *Microporous Mesoporous Mater*. **74**: 49–58.

SEVILLA, M., & FUERTES, A.B., 2011. Sustainable porous carbons with a superior performance for CO2 capture. *Energy Environ. Sci*., **4**: 1765.

SHAHEEN, S.M., NIAZI, N.K., HASSAN, N.E.E., BIBI, I., WANG, H.L., TSANG, D.C.W., OK, Y.S., BOLAN, N., & RINKLEBE, J., 2019. Wood-based biochar for the removal of potentially toxic elements in water and wastewater: a critical review. *Int. Mater. Rev.* **64**: 216–247.

SHAO, Y., HU, Z., YAO, Y., WEI, X., GAO, X., & WU, Z., 2022. Glycine-derived nitrogen-doped ordered mesoporous carbons with a bimodal mesopore size distribution for supercapacitors and oxygen reduction. *New Carbon Materials*, **37**(1): 259-276.

SHON, J.K., JIN, X., CHOI, S.Y., WON, J.G., HWANG, Y.K., YOU, D.J., LI, C., & KIM, J.M., 2016. Effect of acid catalysts on carbonization temperatures for ordered mesoporous carbon materials. *Carbon Letters*. **20**: 66-71.

SING, K., EVERETT, D., HAUL, R., MOSCOU, L., PIEROTTI, R., ROUQUÉROL, J. & SEIMEINIEWSKA, T. 1985. Reporting Physisorption Data for Gas/Solid Systems with Special Reference to the Determination of Surface Area and Porosity, *Int. res. j. pure appl. chem.*, **57(4)**: 603-619.

SING, K., 2001. The use of nitrogen adsorption for the characterization of porous materials. Colloids and Surfaces A: *Physicochem Eng. Asp* **187–188**: 3-9.

SIRIWARDANE, R.A., SHEN, M.N., FISHER, E.P., & POSTON, J.A., 2001. Adsorption of CO2 on Molecular Sieves and Activated Carbon. *Energ Fuel.***15**: 279-284.

SOLER-ILLIA, G.J.A.A., SANCHEZ, C., LEBEAU, B., & J. PATARIN, J., 2002. Chemical Strategies To Design Textured Materials: from Microporous and Mesoporous Oxides to Nanonetworks and Hierarchical Structures. *Chem. Rev*., **102**: 4093–4138.

SON, W.J., CHOI, J.S., & AHN, W.S., 2008. Adsorptive Removal of Carbon Dioxide using Polyethyleneimine-Loaded Mesoporous Silica Materials. *Microporous and Mesoporous Materials* **113**(1-3): 31–40.

SONG, Y., LI, L., WANG, Y., WANG, C., GUO Z., & XIA, Y., 2014. Nitrogen-Doped Ordered Mesoporous Carbon with a High Surface Area, Synthesized through Organic-Inorganic Coassembly, and Its Application in Supercapacitors. *Chem Phys Che.* **15**: 2084–2093.

SONG, Y., LIU, J., SUN, K., & XU, W., 2017. Synthesis of sustainable lignin-derived mesoporous carbon for supercapacitors using a nano-sized MgO template coupled with Pluronic F127. *RSC Adv.* **7**: 48324–48332.

SOTOMAYOR, F.J., & THOMMES, M.K.A.C, 2018. Characterization of Micro/Mesoporous materials by physisorption: concepts and case studies, *Acc. Mater. Surf. Res.* **3**: 34-50.

SPIGARELLI, B.P. & KAWATRA, S.K., 2013. Opportunities and challenges in carbon dioxide capture. *J. CO_2 Util.*, **1**: 69-87.

SPONZA, D. T., & GOK, O., 2010. Effect of rhamnolipid on the aerobic removal of polyaromatic hydrocarbons (PAHs) and COD components from petrochemical wastewater. *Bioresour. Technol.* **101**: 914–924.

SRIDHAR, M., REDDY, G.K., HU, N., MOTAHARI, A., SCHAEFER, D.W., THIEL, S.W., & SMIRNIOTIS, P.G., 2014. Preparation, characterization and lysozyme immobilization studies on siliceous mesocellular foams: Effect of precursor chemistry on pore size, wall thickness and interpore spacing. *Microporous and Mesoporous Materials* **190**:215–226.

SRIRAM, G., SUPRIYA, S., KURKURI, M., & HEGDE, G., 2020. Efficient CO_2 adsorption using mesoporous carbons from biowastes. *Mater. Res. Express* **7**: 015605.

SUBAGYONO, D.J, LIANG, Z., KNOWLES, G. P., & CHAFFEE, A. L., 2011. Amine modified mesocellular siliceous foam (MCF) as a sorbent for CO_2. *Chem Eng Res Des*, **89**(9):1647–57.

SUDHAGAR, P., RAMASAMY, E., CHO, W. H., LEE, J., & KANG, Y. S., 2011. Robust mesocellular carbon foam counter electrode for quantum-dot sensitized solar cells. *Electrochem. commun*. **13**: 34–37.

SUHAS, P.J.M., CAROTT, M.M.L., & CAROTT, R. 2007. Lignin – from natural adsorbent to activated carbon: A review. *Bioresour. Technol*. **98**(12): 2301–2312.

SUMIDA, K., ROGOW, D.L., MASON, J.A., MCDONALD, T.M., BLOCH, E.D., HERM, Z.R., BAE, T.H. & LONG, J.R., 2012. Carbon dioxide capture in metal–organic frameworks. *Chem reviews*, **112**(2): 724-781.

SUN, N., SUN, C., LIU, J., LIU, H., SNAPE, C.E., LI, K., WEI, W. & SUN, Y. 2015. Surface-modified spherical activated carbon materials for pre-combustion carbon dioxide capture. *RSC Advances*, **5**(42): 33681-33690.

SUN, Y., LIU, X., SUN, C., AL-SARRAF, W., KHAI ZHEN FOO, K. Z., MENG, Y., LEE, S., WANG, W., & LIU, H., 2018. Synthesis and functionalisation of spherical meso-,hybrid meso/macro- and macro-porous cellular silica foam materials with regulated pore sizes for CO_2 capture. *J. Mater. Chem. A*. **6**: 23587–23601.

SUN, Y. OUYANG, Y., LUO, J., CAO, H., LI, X., MA, J., LIU, J., WANG, Y., & LU, L.,2021. Biomass derived nitrogen self-doped porous activation carbon as an effective bifunctional electrocatalysts, *Chin. Chem. Lett*. **32**: 92-98.

SZEWCZYK, I., KOSYDAR, R., NATKAŃSKI, P., DURACZYŃSKA, D., GURGUL, J., KUŚTROWSKI, P., & DRELINKIEWIC, A., 2020. Effect of the type of siliceous template and carbon precursor on physicochemical and catalytic properties of mesoporous nanostructured carbon-palladium systems. *J. Porous Mater.* **27**:1287–1308.

TAKAMURA, Y., NARITA, S., AOKI, J., UCHIDA, S., 2001. Application of high-PSA process for improvement of CO_2 recovery system. *Can J Chem Eng,* **79**: 812–816.

TAMAI, H., KAKII, T., HIROTA, Y., KUMAMOTO, T., & YASUDA, H., 1996. Synthesis of Extremely Large Mesoporous Activated Carbon and Its Unique Adsorption for Giant Molecules*. Chem Mater* **8**:454–462.

TAN, S., ZOU, W., JIANG, F., TAN, S., LIU, Y., YUAN., D., 2010. Facile fabrication of copper-supported ordered mesoporous carbon for antibacterial behaviour. *Materials Letter*, **64**: 2163-2166.

TANAKA, S., NISHIYAMA, N., EGASHIRA, Y., & UEYAMA, K., 2005. Synthesis of ordered mesoporous carbons with channel structure from an organic–organic nanocomposite. *Chem. Commun*., 2125.

TANG, Z., HAN, Z., YANG, G., & YANG, J., 2013. Polyethylenimine loaded nanoporous carbon with ultra-large pore volume for CO_2 capture. *Appl. Surf. Sci.* **277**: 47– 52.

TANG, J., WANG, T., SALUNKHE, R.R., ALSHEHRI, S.M., MALGRAS V., & YAMAUCHI, Y., 2015. Three-Dimensional Nitrogen-Doped Hierarchical Porous Carbon as an Electrode for High-Performance Supercapacitors. *Chem. Eur. J*., **21**: 17293–17298.

TANG, D., HU, S., DAI, F., YI, R., GORDIN, M.I., CHEN, S., SONG, J., & WANG, D., 2016. Self-templated synthesis of mesoporous carbon from carbon tetrachloride precursor for supercapacitor electrodes. *ACS Appl. Mater. Interfaces*. **8**: 6779-6783.

TAY, T., UCAR, S. & KARAGOZ, S., 2009. Preparation and characterization of activated carbon from waste biomass. *J. Hazard. Mater*. **165**:481–485.

TENG, H., YEH, T.S., & HSU, L.Y., 1998. Preparation of activated carbon from bituminous coal with phosphoric acid activation. *Carbon* **36**(9): 1387–1395.

THOMMES, M., 2004. *Physical Adsorption Characterization of Ordered and Amorphous Mesoporous Materials. Nanoporous Materials: Science and Engineering* (Eds: G. Q. Lu, X. S. Zhao), Imperial College Press, Oxford, 317.

THOMMES, M. 2010. Physical Adsorption Characterisation of Nanoporous Materials, Chemie Ingenieur *Technik,* **82 (7)**: 1059-1073

THOMMES, M., & CYCHOSZ, K.A., 2014. Physical adsorption characterization of nanoporous materials: progress and challenges. *Adsorption*. **20**: 233-250.

THOMMES, M., KANEKO, K., NEIMARK, A.V., OLIVIER, J.P., RODRIGUEZ-REINOSO, F., ROUQUEROL, J., & SING, K.S.W., 2015. Physisorption of gases, with special reference to the evaluation of surface area and pore size distribution (IUPAC Technical Report). *Pure Appl. Chem*. **87**(9-10): 1051–1069.

THEO, W. L., LIM, J. S., HASHIM, H., MUSTAFFA, A. A., & HO, W. S., 2016. Review of precombustion capture and ionic liquid in carbon capture and storage. *Appl. Energy*, **183**: 1633-1663.

TIAN, W., ZHANG, H., DUAN, D., SUN, H., SHAO, G., & WANG., S., 2020. Porous Carbons: Structure-Oriented Design and Versatile Applications*. Adv. Funct. Mater.* **30**: 1909265.

TITIRICI, M., & ANTONIETTI, M., 2010. Chemistry and materials options of sustainable carbon materials made by hydrothermal carbonization, *Chem. Soc. Rev*. **39**: 103–116.

TITIRICI, M.M., WHITE, R.J., BRUN, N., BUDARIN, V.L., SU, D.S., MONTE, F., CLARK, J.H., & MACLACHLAN, M.J., 2015. Sustainable Carbon Materials. *Chem. Soc. Rev.*, 2015, **44**(1): 250-290.

TOLLEFSON, J., 2018. IPCC says limiting global warming to 1.5 [degrees] C will require drastic action. *Nature*, **562**(7726): 172-174.

TRICKETT, C.A., HELAL, A., AL-MAYTHALONY, B.A., YAMANI, Z.H., CORDOVA, K.E., & YAGHI, O.M., 2017. The chemistry of metal-organic frameworks for CO_2 capture, regeneration and conversion, *Nat. Rev. Mat*. **2**: 1–16.

UNDAVALLI, V.K., LING, C.X., & KHANDELWAL, B., 2021. Impact of alternative fuels and properties on elastomer compatibility. *Aviation Fuels*.113-132.

UNEP, 2019. *Emissions Gap Report* 2019.

UNVEREN, E. E., MONKUL, B. Ö., SAROGLAN, S., KARADEMIR, N. & ALPER, E. 2017. Solid amine sorbents for CO_2 capture by chemical adsorption: *A review. Petroleum*, **3:** 37-50.

VACLAV, S., 2017. Energy transitions: global and national perspectives. *BP Statistical Review of World Energy*.

VAN DER HEIDE, P. 2011. *X-ray photoelectron spectroscopy: an introduction to principles and practices*, John Wiley & Sons.

VAN DER HEIDE, P. 2014. *Secondary ion mass spectrometry: an introduction to principles and practices*, John Wiley & Sons , ISBN : 978-1-118-48048-9.

VASEGHI, M. R., ALI, A., & ALIREZA, P., 2012. *A review of energy efficiency and CO_2 emissions in the US cement industry*. Cement Industry Technical Conference, 2012 IEEE-IAS/PCA 53rd.

VASSILEV, S.V., BAXTER, D., ANDERSEN, L.K., & VASSILEVA, C.G. 2010. An overview of the chemical composition of biomass. *Fuel*, **89**: 913–933.

VENNA, S. R. & CARREON, M. A. 2015. Metal-organic framework membranes for carbon dioxide separation. *Chem. Eng. Sci.***, 124:** 3-19.

VINU, A., SRINIVASU, P., TAKAHASHI, M., MORI, T., BALASUBRAMANIAN, V.V., & ARIGA, K., 2007. Controlling the textural parameters of mesoporous carbon materials. *Microporous and Mesoporous Materials* **100**: 20-26.

VINU, A., 2008. Two-Dimensional Hexagonally-Ordered Mesoporous Carbon Nitrides with Tunable Pore Diameter, Surface Area, and Nitrogen Content*. Adv. Funct. Mater.* **18**: 816.

WALCARIUS, A., 2017. Recent Trends on Electrochemical Sensors Based on Ordered Mesoporous Carbon. *Sensors*. **17**: 1863.

WALL, T. F., 2007. Combustion processes for carbon capture. *Proc Combust Inst*, **31**: 31–47.

WAN, Y., SHI, Y., & ZHAO, D., 2008. Supramolecular Aggregates as Templates: Ordered Mesoporous Polymers and Carbons. *Chem. Mater*. **20** (3): 932-945.

WANG, X. X., SCHWARTZ, V., CLARK, J. C., MA, X. L., STEVEN H. OVERBURY., S. H., XU, X. C., & SONG, C., 2009. Infrared Study of CO_2 Sorption over "Molecular Basket" Sorbent Consisting of Polyethylenimine-Modified Mesoporous Molecular Sieve. *J. Phys. Chem. C*, **113**: 7260–7268.

WANG, D., SENTORUN-SHALABY, C., MA, X., & SONG, C., 2011. High-capacity and low-cost carbon-based "Molecular Basket" sorbent for CO_2 capture from flue gas, *Energy Fuels* **25**: 456 – 358.

WANG, Y., ZHANG, C., KANG, S., LI, B., WANG, Y., WANG, I, & LI, X., 2011a. Simple synthesis of graphitic ordered mesoporous carbon supports using natural seed fat, *J. Mater. Chem*. **21**:14420-14423.

WANG, D., SENTORUN-SHALABY, C., MA, X., SONG, C., 2011b. High-capacity and low-cost carbon-based "Molecular Basket" sorbent for CO_2 capture from flue gas, *Energy Fuels* **25**: 456-358.

WANG, L., & YANG, R.T., 2012. Significantly Increased CO_2 Adsorption Performance of Nanostructured Templated Carbon by Tuning Surface Area and Nitrogen Doping. *J. Phys. Chem*. **116**(1): 1099–1106.

WANG, J., KASKEL, S., 2012. KOH activation of carbon-based materials for energy storage. *J. Mater. Chem*. **22**(45): 23710–23725.

WANG, J., LONG, D., ZHOU, H., CHEN, Q., LIU, X., LING, L., 2012. Surfactant promoted solid amine sorbents for CO_2 capture, *Energy Environ. Sci*. **5**: 5742–5749.

WANG, D., MA, X., SENTORUN-SHALABY, C., & SONG, C., 2012a. Development of Carbon-Based "Molecular Basket" Sorbent for CO_2 Capture. *Ind. Eng. Chem. Res.* **51**: 3048−3057.

WANG, J., WANG, M., ZHAO, B., QIAO, W., LONG, D., LING, L., 2013. Mesoporous Carbon-Supported Solid Amine Sorbents for LowTemperature Carbon Dioxide Capture. *Ind. Eng. Chem. Res*. **52**: 5437−5444.

WANG, J., CHEN, H., ZHOU, H., LIU, X., QIAO, W., LONG, D., LING, L., 2013a. Carbon dioxide capture using polyethylenimine-loaded mesoporous carbons. *J. Environ. Sci.*. **25**(1): 124–132.

WANG, J., SENKOVSKA, I., OSCHATZ, M., LOHE, M.R., BORCHARDT, L., HEERWIG, A., LIU, Q., KASKEL, S., 2013b. Highly porous nitrogen-doped polyimine-based carbons with adjustable microstructures for CO2 capture. *J. Mater. Chem. A, **1**:* 10951.

WANG, X., LIU, C.G., NEFF, D., FULVIO, P.F., MAYES, R.T., ZHAMU, A., 2013c. Nitrogen enriched ordered mesoporous carbons through direct pyrolysis in ammonia with enhanced capacitive performance. *J. Mater. Chem. A* **1**(27): 7920-7926.

WANG, J., HUANG, L., YANG, R., ZHANG, Z., WU, J., GAO, Y., WANG, Q., O'HARE, D. & ZHONG, Z. 2014. Recent advances in solid sorbents for CO2 capture and new development trends. *Energy Environ. Sci.*, **7:** 3478-3518.

WANG, J.T., HUANG, H.H., WANG, M., YAO, L.W., QIAO, W.M., LONG, D.H., & LING, L.C., 2015. Direct capture of low-concentration CO_2 on mesoporous carbon-supported solid amine adsorbents at ambient temperature, *Ind. Eng. Chem. Res*. **54**: 5319–5327.

WANG, G., ZHANG, Z., WANG, J., LI, N., HAO, Z., 2015a. Study of the influence of pore width on the disposal of benzene employing tunable OMCs. *Ind Eng Chem Res* **54**(3):1074–1080.

WANG, M., LIWEN YAO, L., WANG, J., ZHANG, Z., QIAO, W., LONG, D., & LING, L., 2016. Adsorption and regeneration study of polyethylenimine-impregnated millimeter-sized mesoporous carbon spheres for post-combustion CO_2 capture. *Appl. Energy* **168**: 282–290.

WANG, L., LI, B., XU, F., SHI, X., FENG, D., WEI, D., LI, Y., FENG, Y., WANG, Y., JIA, D., ZHOU, Y., 2016a. High-yield synthesis of strong photoluminescent N-doped carbon nanodots derived from hydrosoluble chitosan for mercury ion sensing via smartphone APP. *Biosensors & Bioelectronics*. **79**: 1–8.

Wang, Y., Bai, X., Wang, F., Qin, H., Yin, C., Kang, S., Li, X., Zuo, Y., & Cui, L., 2016b. Surfactant-assisted Nanocasting Route for Synthesis of Highly Ordered Mesoporous Graphitic Carbon and Its Application in CO_2 Adsorption. Scientific Reports. **6**(1): 26673.

WANG, W.J.,ZHOU, M.,& YUAN, D.Q., 2017. Carbon dioxide capture in amorphous porous organic polymers. *J. Mater. Chem. A*. **5**(4):1334–1347.

WANG, X., PAN, H., LIN, Q., WU, H., JIA, S., & SHI, Y., 2019. One-Step Synthesis of Nitrogen-Doped Hydrophilic Mesoporous Carbons from Chitosan-Based Triconstituent System for Drug Release. *Nanoscale Res. Lett*.**14**:259.

WANG, S., SIMA, G., CUI, Y., CHANG, L., & GAN, L., 2020. Preparations of lignin-derived ordered mesoporous carbon by self-assembly in organic solvent and aqueous solution: Comparison in textural property. *Mater. Lett*.

WANG, Y., CHEN, J., IHARA, H., GUAN, M., & QIU, H., 2021. Preparation of porous carbon nanomaterials and their application in sample preparation: *A review. Trends Analyt Chem.* **143**:116421.

WEI, W., YU, C., ZHAO, Q., QIAN, X., LI, G., & WAN., Y., 2014. Synergy effect in photodegradation of contaminants from water using ordered mesoporous carbon-based titania catalyst. *Appl. Catal. B* **146**: 151–161.

WEI, F., HE, Y., QU, X., XU, Z., ZHENG, S., ZHU, D., & FU, H., 2019. In situ fabricated porous carbon coating derived from metal-organic frameworks for highly selective solid-phase microextraction, *Anal. Chim. Acta*. **1078**: 70-77.

WEN, J.J., GU, F.N., WEI, F., ZHOU, Y., LIN, W.G., YANG, J., YANG, J.Y., WANG, Y., ZOU, Z.G., & ZHU, J.H., 2010. One-pot synthesis of the amine-modified meso-structured monolith CO_2 adsorbent. *J. Mater. Chem*. **20**: 2840–2846.

WU, Z., PANG, J., LU, Y., 2009. Direct synthesis of ordered mesoporous carbons/silica nanocomposites and derivative hierarchically mesoporous carbon from a phenyl-bridged organosiloxane. *Nanoscale*. **1**: 245–249.

WU, Z.Y., LI, C., LIANG, H.W., CHEN, J.F., & YU, S.H., 2013. Ultralight, flexible, and fire-resistant carbon nanofiber aerogels from bacterial cellulose. *Angew Chem Int Ed*. **52**: 2925–2929.

WU, F., ARGYLE, M. D., DELLENBACK, P. A., & FAN, M., 2018. Progress in O_2 separation for oxy-fuel combustion-A promising way for cost-effective CO2capture: *a review. Prog. Energy Combust. Sci*, **67**: 188-205.

XIA, Y., YANG, Z., & MOKAYA, R., 2010. Templated nanoscale porous carbons. *Nanoscale*. **2**: 639–659.

XIA, K., WANG, G., ZHANG, H., LIU, L., YU, Y., WANG, L., & CHEN, A., 2017. Synthesis of bimodal mesoporous carbon nanospheres for methyl orange adsorption. *J Porous Mater*. **24**: 1605–1612.

XIE, W., YU, M., & WANG, R., 2017. CO_2 Capture Behaviors of Amine-Modified Resorcinol-Based Carbon Aerogels Adsorbents. *Aerosol and Air Quality Research*, **17**: 2715–2725.

XIN, W., & SONG, Y. 2015. Mesoporous carbons: recent advances in synthesis and typical applications*. RSC Adv*. **5**: 83239–83285.

XU, X., SONG, C., ANDRESEN, J.M., BRUCE, G., MILLER, B.G., & SCARONI, A.W., 2002. Novel Polyethylenimine-Modified Mesoporous Molecular Sieve of MCM-41 Type as High-Capacity Adsorbent for CO_2 Capture. *Energy & Fuels*, **16**: 1463-1469.

XUAN, H., LIN, G., WANG, F., LIU, J., DONG, X., & XI, F., 2017. Preparation of biomass-activated porous carbons derived from torreya grandis shell for high-performance supercapacitor. *J Solid State Electrochem*. **21**: 2241–2249.

XUE, B., WANG, X., FENG, Y., CHEN, Z., & LIU, X., 2020. Self-template synthesis of nitrogen-doped porous carbon derived from rice husks for the fabrication of high volumetric performance supercapacitors, *J. Energy Storage*. **30**: 101405.

YAMADA, H., NAKAMURA, H., NAKAHARA, F., MORIGUCHI, I., & KUDO, T., 2007. Electrochemical study of high electrochemical double layer capacitance of ordered porous carbons with both meso/macropores and micropores. *J. Phys. Chem. C*. **111**(1): 227-233.

YAN, X., ZHANG, L., ZHANG, Y., QIAO, K., YAN, Z., & KOMARNENI, S., 2011. Amine-modified mesocellular silica foams for CO2 capture. *Chem. Eng. J*. **168**: 918–924.

YAN, Y., LIU, S., HAO, F., LIU, P., & LUO, H. 2014. Nitrocyclohexane hydrogenation to cyclohexanone oxime over mesoporous carbon-supported Pd catalyst. *Catal Commun.* **50**: 9–12.

YANG, W., LIU, X., YUE, X., JIA, J., & GUO, S., 2015. Bamboo-like Carbon Nanotube/Fe3C Nanoparticle Hybrids and Their Highly Efficient Catalysis for Oxygen Reduction. *J. Am. Chem. Soc*. **137**: 1436−1439.

YANG, C.H., NGUYEN, Q.D., CHEN, T.H., HELAL, A.S., LI, J., & CHANG, J.K., 2017. Functional group-dependent supercapacitive and aging properties of activated carbon electrodes in organic electrolyte. *ACS Sustain. Chem. Eng*. **6**(1): 1208–1214.

YAZAYDIN, A.O., SNURR, R.Q., PARK, T.H., KOH, K., LIU, J., LEVAN, M.D., BENIN, A.I., JAKUBCZAK, P., LANUZA, M., GALLOWAY, D.B., LOW, J.J., & WILLIS, R.R., 2009. Screening of metal-organic frameworks for carbon dioxide capture from flue gas using a combined experimental and modeling approach*, J. Am. Chem. Soc*. **131**: 18198–18199.

YIN, C., & YAN, J., 2016. Oxy-fuel combustion of pulverized fuels: combustion fundamentals and modeling. *Appl. Energy*, **162**: 742-762.

YIN, L., LIJUN, X., YIYI, B., MENG, C., HONGPENG, W., SHENGDAO, S., RUIQIN, Y., & JIANWEI, M., 2018. Hydrothermal synthesis of mesoporous carbons for adsorption of two alkaloids. *J. Porous Mater*. **25:** 95-105.

YORGUN, S., & YILDIZ, D., 2015. Preparation and characterization of activated carbons from Paulownia wood by chemical activation with H3PO4. *J Taiwan Inst Chem Eng.* **53**: 122–131.

C. YU., J. FAN., B. TIAN., D. ZHAO., G.D. SNICKY., 2002. High-yield synthesis of periodic mesoporous silica rods and their replication to mesoporous carbon rods, *Adv. Mater* **14**: 1742-1745

YU, C., FAN, J., TIAN, B., ZHANG, F., STUCKY, G.D., & ZHAO, D., 2003. Morphological control of highly ordered mesoporous carbon, *Stud. Surf. Sci. Catal*. **146**: 45–48.

YU, C.-H. 2012. A Review of CO_2 Capture by Absorption and Adsorption. *Aerosol Air Qual. Res.*

YU, J., & BALBUENA, P.B., 2013. Water Effects on Post-combustion CO_2 Capture in Mg-MOF-74 *J. Phys. Chem. C*, **117**: 3383.

YU, J., GUO, M., MUHAMMAD, F., WANG, A., YU, G., MA H., & ZHU, G., 2014. Simple fabrication of an ordered nitrogen-doped mesoporous carbon with resorcinol–melamine–formaldehyde resin *Microporous Mesoporous Mater*. **190**: 117–127.

YU, X., FENG, Y., GUAN, B., LOU, X.W., & PAIK, U., 2016. Carbon coated porous nickel phosphides nanoplates for highly efficient oxygen evolution reaction. *Energy Environ Sci.* **9**: 1246–1250.

YU, J., XIE, L. H., Li, J. R., Ma, Y., SEMINARIO, J. M., BALBUENA, P. B., 2017. CO_2 capture and separations using MOFs: computational and experimental studies. *Chem. Rev*. **117**: 9674-9754.

YULIUSMAN, NASRUDDIN, A.M. KHAIRUL, H. FARANDY, A.R. ALFIA, H. AFDHAL, R.I. TAUFIQ, 2017. Production of Activated Carbon from Coffee Grounds Using Chemical and Physical Activation Method*. Adv. Sci. Lett.* **23**: 5751-5755.

YUE, L., XIA, Q., WANG, L., WANG, L., DA COSTA, H., YANG, J., & HU, X., 2018. CO_2 adsorption at nitrogen-doped carbons prepared by K_2CO_3 activation of urea-modified coconut shell. *J. Colloid Interface Sci*. **511**: 259–267.

ZAKZESKI, J., BRUIJNINCX, P.C.A., JONGERIUS, A.L., & WECKHUYSEN, B.M., 2010. The Catalytic Valorization of Lignin for the Production of Renewable Chemicals. *Chem. Rev*. **110**: 3552–3599.

ZDRAVKOV, B.D., CERMAK, J.J., SEFARA, M., JANK, J., 2007. Pore classification in the characterization of porous materials: A perspective. *Cent. Eur. J. Chem.* **5**(2): 385–395.

ZENG, M., WANG, Y., LIU, Q., YUAN, X., FENG, R., YANG, Z., QI, C., 2016. N-doped mesoporous carbons supported palladium catalysts prepared from chitosan/silica/palladium gel beads *Int. J. Biol. Macromol*. **89** 449–55.

ZHANG, L., XU, C. C., & CHAMPAGNE, P. 2010. Overview of recent advances in thermo-chemical conversion of biomass. *Energy Convers. Manag.*, ***51*(**5): 969-982.

ZHANG, W., LIU, H., SUN, C., DRAGE, T.C., SNAPE, C.E., 2014. Performance of polyethyleneimine–silica adsorbent for post-combustion CO2 capture in a bubbling fluidized bed. *J. Chem. Eng.* **251**: 293–303.

ZHANG, P.F., WANG, L., YANG, S.Z., SCHOTT, J.A., LIU, X.F., MAHURIN, S.M., HUANG, C.L., ZHANG, Y., FULVIO, P.F., CHISHOLM, M.F., DAI, S., 2017a. Solid-state synthesis of ordered mesoporous carbon catalysts via a mechanochemical assembly through coordination cross-linking. *Nat. Commun*. **8**: 15020.

ZHANG H, GOEPPERT A, OLAH G. A., & PRAKASH G. S., 2017. Remarkable effect of moisture on the CO_2 adsorption of nano-silica supported linear and branched polyethylenimine. *J CO_2 Util*, **19**: 91–9.

ZHANG, Z., BORHANI, T. N. G., & EL-NAAS, M. H., 2018. Carbon Capture, Exergetic, Energetic and Environmental Dimensions. *Elsevier*.

ZHANG, M., CHEN, M., REDDEPPA, N., XU, D., JING, Q., & ZHA, R., 2018a. Nitrogen self-doped carbon aerogels derived from trifunctional benzoxazine monomers as ultralight supercapacitor electrodes. *Nanoscale.* **10:** 6549−6557.

ZHANG, X.Q., & LU., A.H., 2020. *Porous Carbon Materials. Designed Synthesis and CO2 Capture. Materials for Carbon Capture*, First Edition. Edited by De-en Jiang, Shannon M. Mahurin and Sheng Dai. John Wiley & Sons Ltd. Published by John Wiley & Sons Ltd.

ZHANG, W., SUN, C., SNAPE, C.E., SUN, X., LIU, H., 2020a. Cyclic performance evaluation of a polyethylenimine/silica adsorbent with steam regeneration using simulated NGCC flue gas and actual flue gas of a gas-fired boiler in a bubbling fluidized bed reactor. *Int. J. Greenhouse. Gas Control.* **95**: 102975.

ZHANG, J., ZHANG, N., TACK, F.M.G., SATO, S., ALESSI, D.S., OLESZCZUK, P., WANG, H., WANG, X., & WANG, S., 2021. Modification of ordered mesoporous carbon for removal of environmental contaminants from aqueous phase: *A review. J. Hazard. Mater***. 418**: 126266.

ZHAO, D., QISHENG HUO, JIANGLIN FENG, BRADLEY F. CHMELKA, GALEN D. STUCKY. 1998. Nonionic triblock and star diblock copolymer and oligomeric surfactant syntheses of highly ordered, hydrothermally stable, mesoporous silica structures. *J. Am. Chem. Soc.,* **120:** 6024-6036.

ZHAO, J., SIMON, F., WANG, Y., LUO, G., & HATTON, T.A., 2012. Polyethylenimine-impregnated siliceous mesocellular foam particles as high capacity CO_2 adsorbents. *RSC Adv*. **2**: 6509-6519.

ZHAO, H., & LUO, X., 2018. Carbon-based adsorbents for post-combustion capture: *a review. Greenhouse Gas Sci Technol***, 8**: 11-36.

ZHAO, H., ZHANG, Y., LI, L., GENG, X., YANG, H., ZHOU, W., SUN, C., & AN, B., 2021. Synthesis of an ordered porous carbon with the dual nitrogen-doped interfaces and its ORR catalysis performance*, Chin. Chem. Lett*. **32**: 140-145.

ZHENG, F., YANG, Y., CHEN, Q., 2014. High lithium anodic performance of highly nitrogen-doped porous carbon prepared from a metal-organic framework. *Ncomms* 6261.

ZHONG, R., & SELS, B.F. 2018. Sulfonated mesoporous carbon and silica-carbon nanocomposites for biomass conversion. *Appl. Catal. B: Environ*. **236**: 518–545.

ZHOU, J., LUO, A., & ZHAO, Y., 2018. Preparation and characterization of activated carbon from waste tea by physical activation using steam. *J. Air Waste Manag. Assoc.* **68** (12): 1269-1277.

ZHOU, X.L., ZHANG, H., SHAO, L.M., LU, F., & HE, P.J., 2021a. Preparation and Application of Hierarchical Porous Carbon Materials from Waste and Biomass: *A Review. Waste and Biomass Valorization*. **12**: 1699–1724.

ZHOU, C., YU, S., MA, K., LIANG, B., TANG, S., LIU, C., & YUE, H., 2021. Amine-functionalized mesoporous monolithic adsorbents for post-combustion carbon dioxide capture. *J. Chem. Eng.* **413**: 127675.

ZHU, X., HOANG, T., LOBBAN, L. L., & MALLINSON, R. G., 2010. Low CO content hydrogen production from bio-ethanol using a combined plasma reforming–catalytic water gas shift reactor. *Appl Catal B*, **94**: 311–7.

ZHU, C.Y., AKIYAMA, T., 2016, Cotton derived porous carbon via an MgO template method for high performance lithium ion battery anodes. *Green Chem*. **18**,:2106.

ZHU, H., JING, Y., PAL, M., LIU, Y., LIU, Y., WANG, J., ZHANG, F., & ZHAO, D., 2017. Mesoporous TiO2 @ N-doped carbon composite nanospheres synthesized by the direct carbonization of surfactants after sol-gel process for superior lithium storage. *Nanoscale*. **9:** 1539-1546.

ZOU, L., SUN, Y., CHE, S., YANG, X., WANG, X., BOSCH, M., WANG, Q., LI, H., SMITH, M., YUAN, S., PERRY, Z., ZHOU, H.C., 2017. Porous organic polymers for post-combustion carbon capture. *Adv. Mater*, **29**: 1-35.

APPENDICES

APPENDIX A

LIST OF PUBLICATIONS

Published manuscripts during PhD:

1) Sani, Suleiman; Liu, Xin; Li, Mengbin; Stevens, Lee; Sun, Cheng-gong. Synthesis, and characterization of three-dimensional interconnected large-pore mesoporous cellular lignin carbon materials and their potential for CO_2 capture. *Microporous and Mesoporous Materials*. https://doi.org/10.1016/j.micromeso.2022.112334

2) Bai, F., Liu, X., Sani, S., Liu, Y., Guo, W., Sun, C., 2022. Amine functionalized mesocellular silica foam as highly efficient sorbents for CO_2 capture. *Separation and Purification Technology.* 121539. https://doi.org/10.1016/j.seppur.2022.121539

3) Liu, X., Wang, H., Liu, X., Yang, F., Guan, L., Sani, S., Sun, C., Wu, Y., 2022. Development of $MgSO_4$/mesoporous silica composites for thermochemical energy storage: the role of porous structure on water adsorption. *Energy Reports* **8**: 4913–4921. https://doi.org/10.1016/j.egyr.2022.03.137

Prepared manuscripts

1) Sani, Suleiman; Liu, Xin; Stevens, Lee; Sun, Cheng-gong. Amine functionalized sustainable lignin-derived mesoporous carbons for CO_2 adsorption. Fuel (Under Review).

APPENDIX B

Table B 1. Summary of binding energy distributions and relative contributions of CMC2 carbon sample at different carbonization temperatures.

Sample	Region	Binding energy (eV)	Relative contribution (at.%)
CMC2-700-1	N1s	398.5	26.6
		400.7	62.6
		402.8	5.8
		404.2	5.0
	C1s	284.9	44.1
		285.5	33.8
		287.2	13.1
		289.8	8.9
CMC2-800-1	N1s	398.4	26.6
		400.2	50.2
		401.6	18.8
		404.2	4.4
	C1s	284.6	49.9
		285.6	25.5
		286.7	15.6
		289.3	9.0
CMC2-900-1	N1s	398.3	25.8
		400.6	55.6
		402.4	10.0
		404.1	8.6
	C1s	284.7	51.6
		285.7	20.6
		286.7	16.1
		289.3	11.6

APPENDIX C

The textural properties of MCF1, MC2, and PQ-silica were repeated three times.

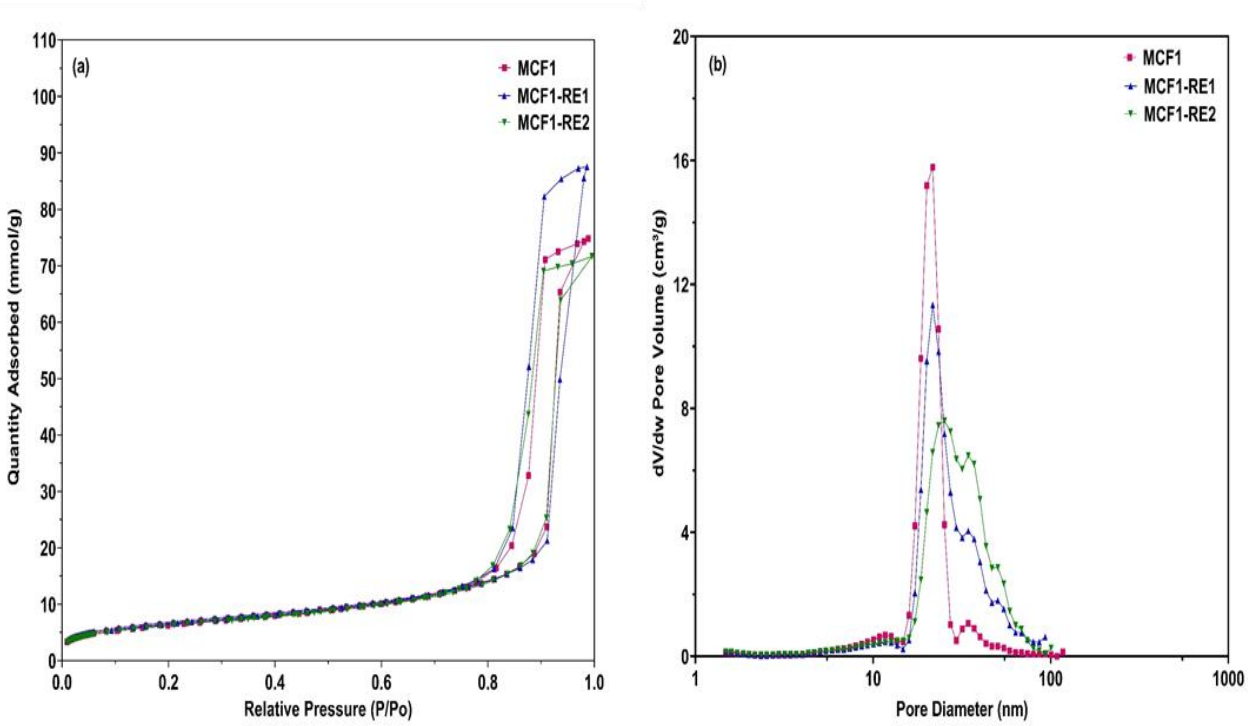

Figure C1 Nitrogen adsorption/desorption isotherms (a) and pore size distributions of MCF1 (b).

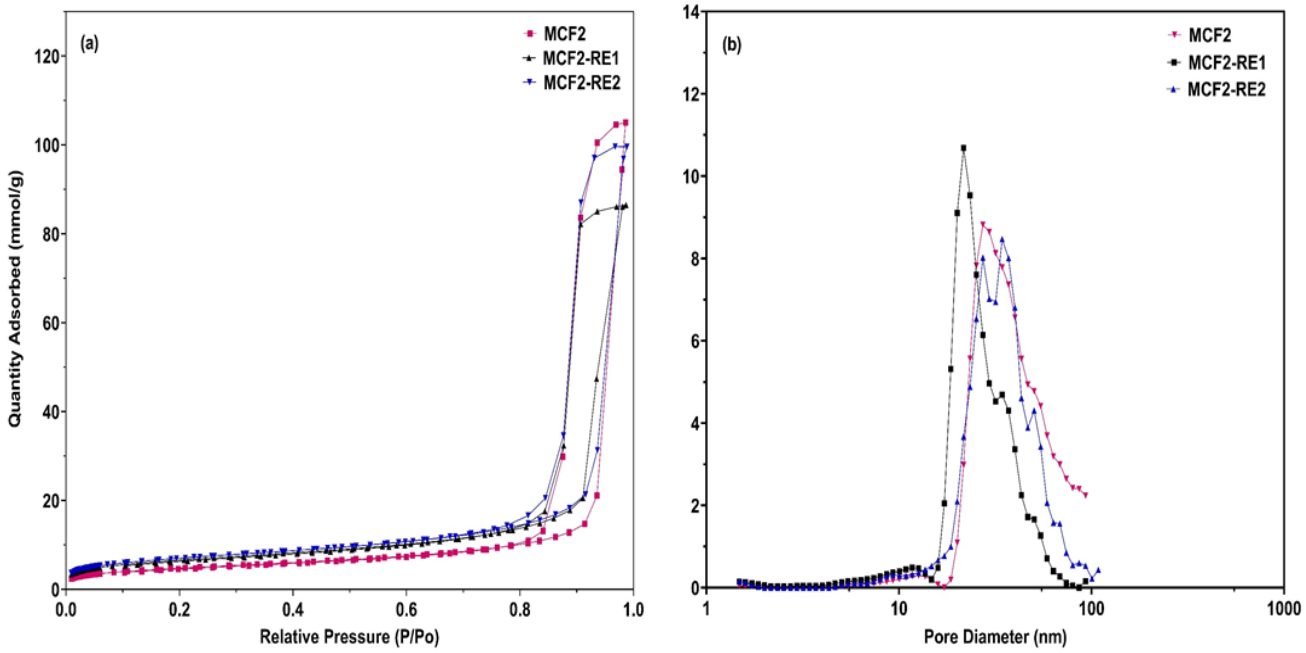

Figure C2 Nitrogen adsorption/desorption isotherms (a) and pore size distributions of MCF2 (b).

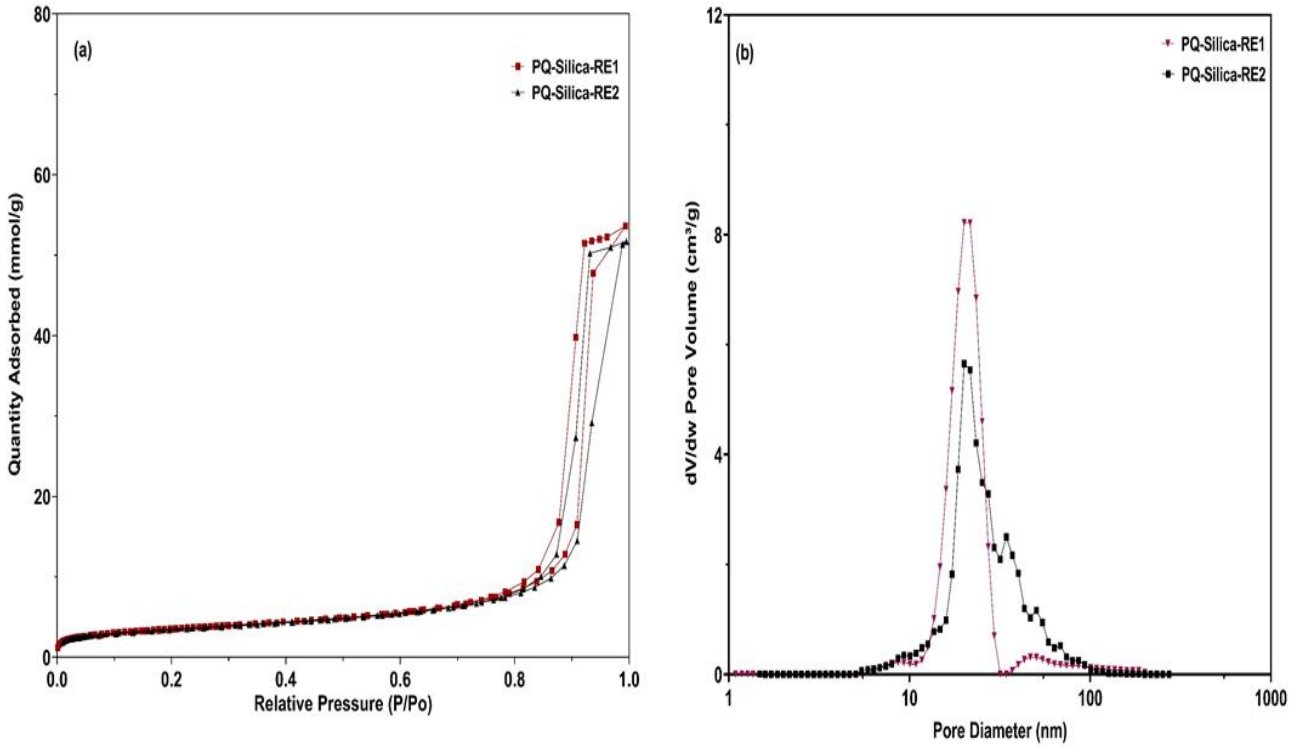

Figure C3 Nitrogen adsorption/desorption isotherms (a) and pore size distributions of MCF2 (b).

Table C1 Surface textural properties of MC2-800-1 tested twice.

The maximum and minimum difference of BET surface area was only 33 m^2/g and total pore volume, mesopore volume and micropore volume gave a difference of 0.04, 0.01, and 0.02 cm^3/g, respectively.

Test No.	S_{BET} (m^2/g)	V_{total} (cm^3/g)	V_{meso} (cm^3/g)	V_{micro} (cm^3/g)	Average pore size (nm)
A	960	1.80	1.50	0.17	12.4
B	913	1.75	1.48	0.20	11.4
	936.5±33.2	1.78±0.04	1.49±0.01	0.19±0.02	11.9±07

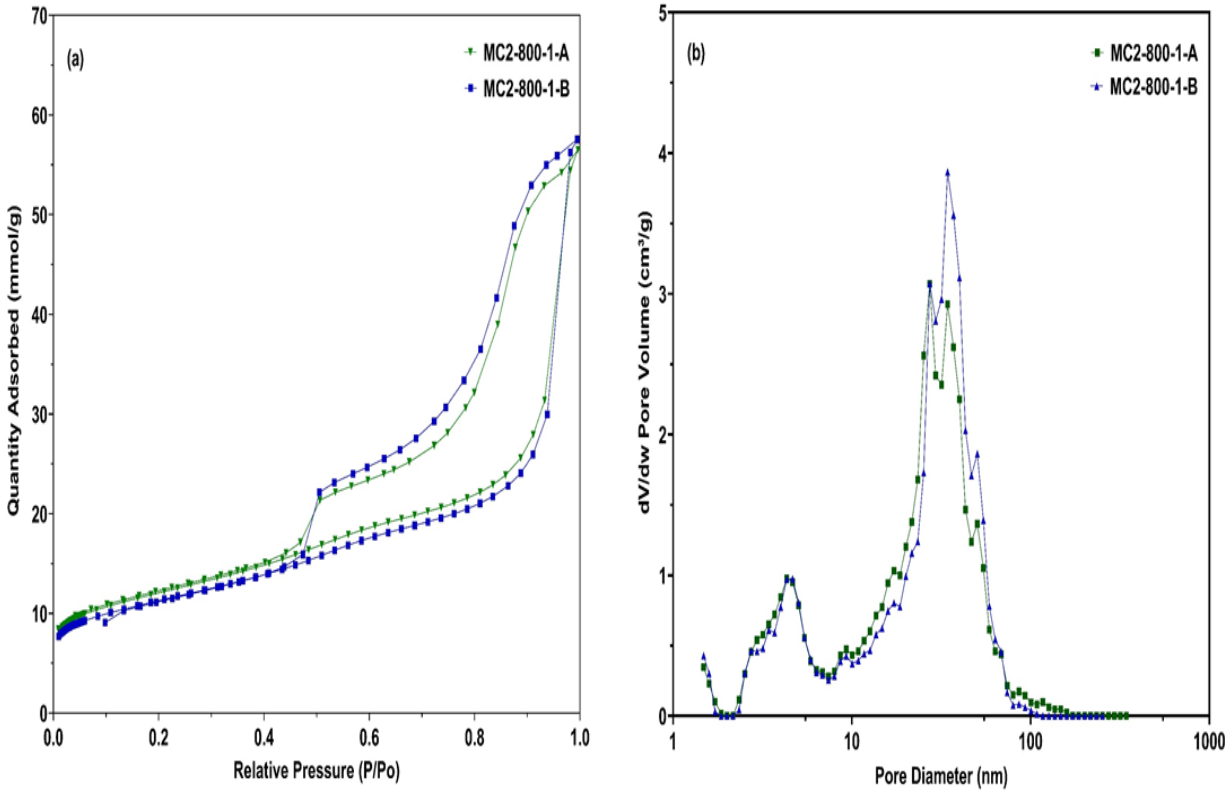

Figure C4 Nitrogen adsorption/desorption isotherms (a) and pore size distributions (b) of MC2-800-1 repeated twice.

Table C2 Adsorption capacities of MC2-800-1-60-75℃ and MC2-800-160-85℃ tested by TGA 3 times

Sample	CO_2 adsorption capacity (mmol/g)				
	1	2	3	Mean	Standard Deviation
MC2-800-1-60-75	2.94	2.88	2.83	2.88	0.05
MC2-800-1-60-85	3.13	3.06	3.06	3.08	0.04

Appendix D

This section shows the result of experiments that were carried out during the PhD project but were not included in the Chapters of the result.

Structural characterization and morphology of mesoporous silica templates.

MCF3 and MCF4 were produced using the same method as described in Section 3.1.2 but at an aging temperature of 120 and 160 ˚C, respectively. The nitrogen adsorption-desorption isotherms and pore size distributions of the mesoporous silica templates are shown in Figure D1.

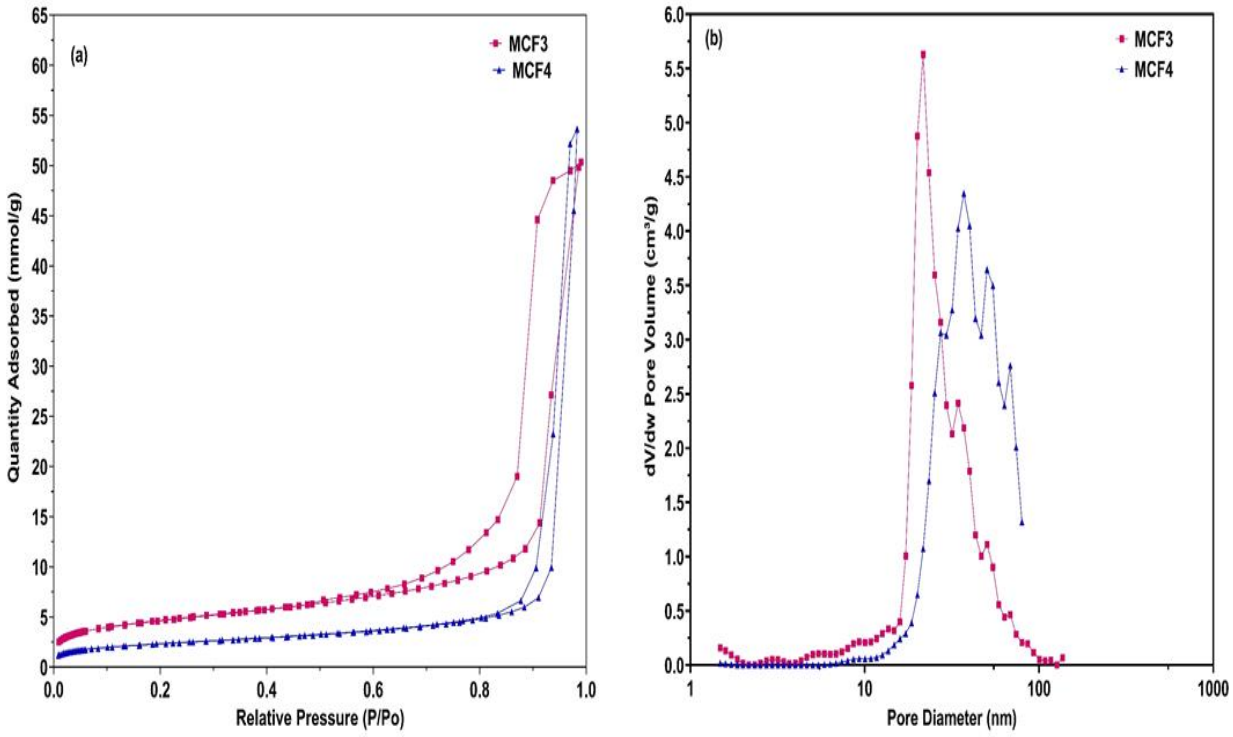

Figure D1 Nitrogen adsorption/desorption isotherms (a) and pore size distributions of silica templates (b).

The detailed textural properties of the mesoporous silica templates are summarized in Table D1

Table D1 Textural properties of the mesoporous silica templates

Hard templates	P123:TMB ratio	S_{BET} ($m^2\ g^{-1}$)	V_{total} ($cm^3\ g^{-1}$)	V_{meso} ($cm^3\ g^{-1}$)	V_{micro} ($cm^3\ g^{-1}$)	Pore size (nm)	Window size (nm)
MCF3	1:3	379	1.59	1.44	0.04	24.36	15.58
MCF4	1:1	187	1.81	1.31	0.01	39.10	31.10

The morphological structure of the MCF3 and PQ silica templates is displayed in Figures D2 and D3, respectively.

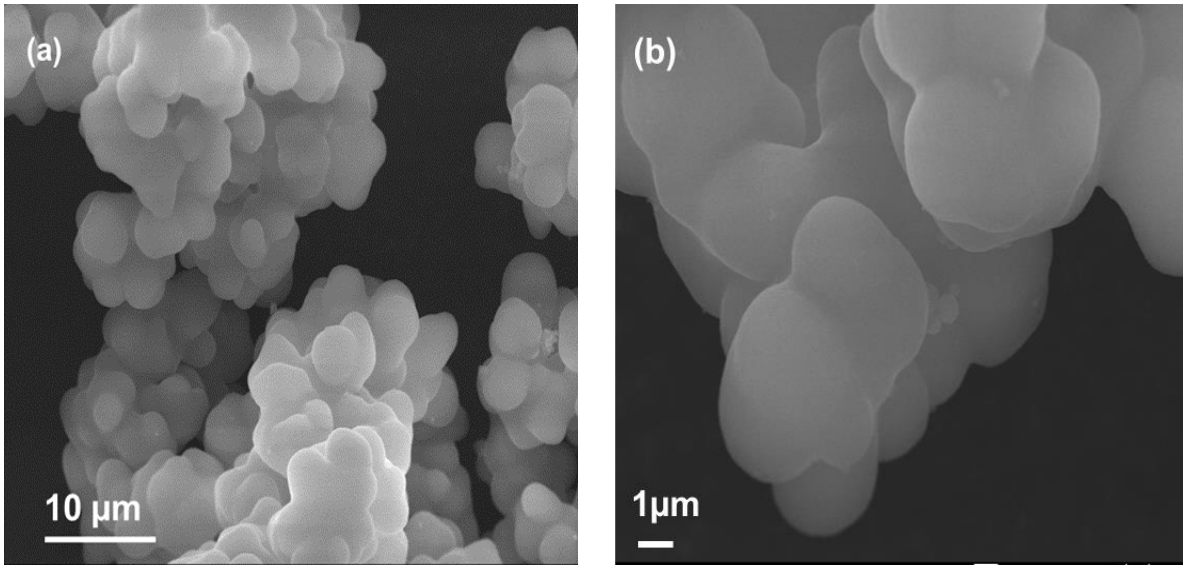

Figure D2 SEM images of MCF3 silica template.

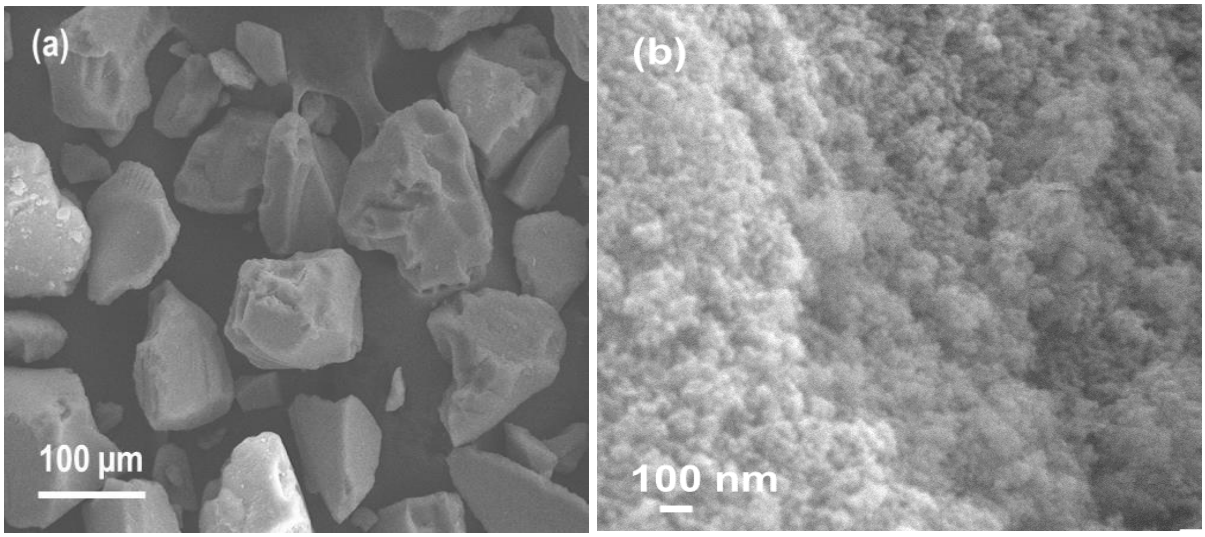

Figure D3 SEM images of PQ-silica silica template.

Structural characterization and morphology of mesoporous carbons.

Figure D4 shows the nitrogen adsorption-desorption isotherms and pore size distributions of the mesoporous carbons synthesized using MCF1, MCF2, and MCF3 silica templates at carbonization temperatures of 600, 900, and 1000 ˚C at a selected silica-to-lignin ratio of 1 and 2 by mass.

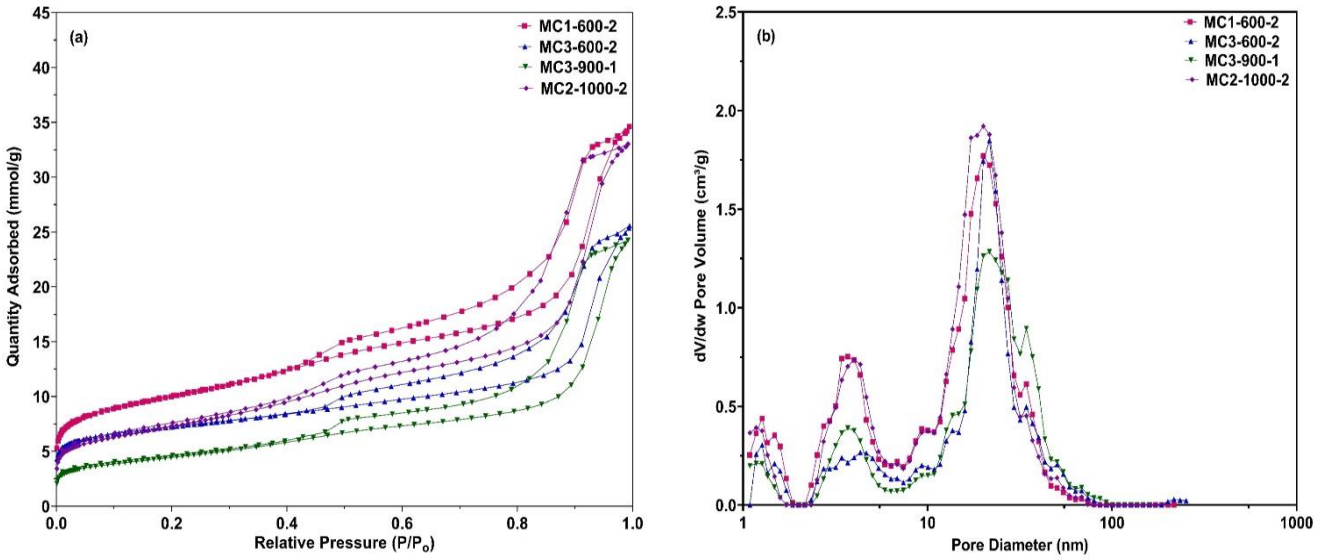

Figure D4 Nitrogen adsorption/desorption isotherms (a) and pore size distributions (b) of mesoporous carbons.

The textural properties of the carbon materials are shown in Table D2.

Table D2: Surface textural properties of mesoporous carbons.

Sample	S_{BET} (m^2g^{-1})	V_{total} (cm^3g^{-1})	V_{meso} (cm^3g^{-1})	V_{micro} (cm^3g^{-1})	Average pore size, (nm)
MC1-600-2	802	1.02	0.84	0.17	8.7
MC3-600-2	590	0.74	0.58	0.14	11.5
MC3-900-1	353	0.68	0.61	0.06	11.3
MC2-1000-2	577	0.99	0.88	0.09	9.2

CO_2 adsorption performance of PEI-impregnated mesoporous carbon adsorbents.

Figures D5 and D6 show the CO_2 adsorption capacities of PEI-impregnated carbon samples.

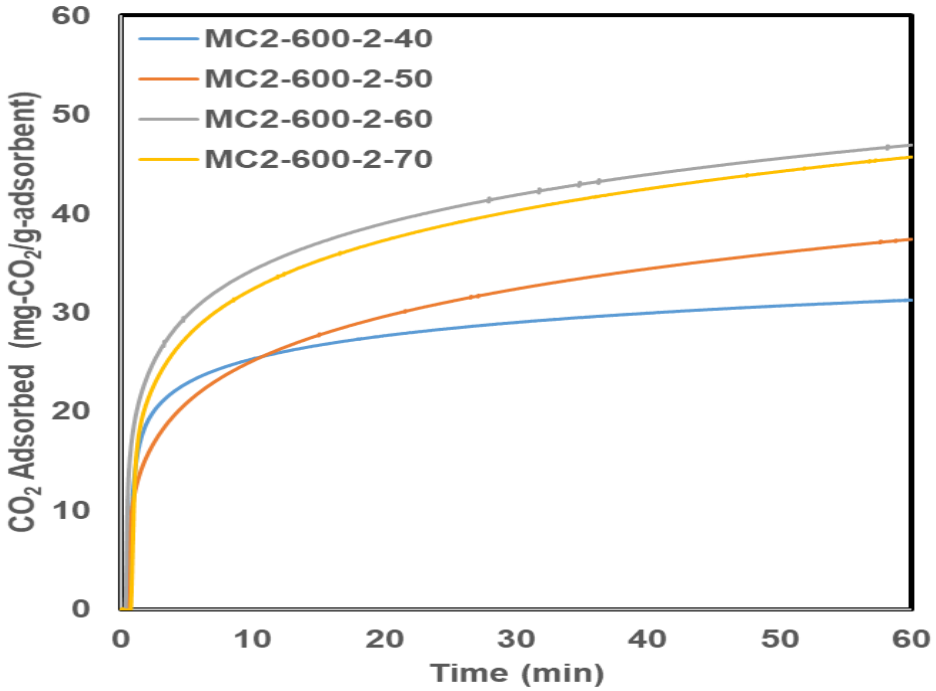

Figure D5 CO_2 adsorption performance of MC2-600-2 with different PEI loadings.

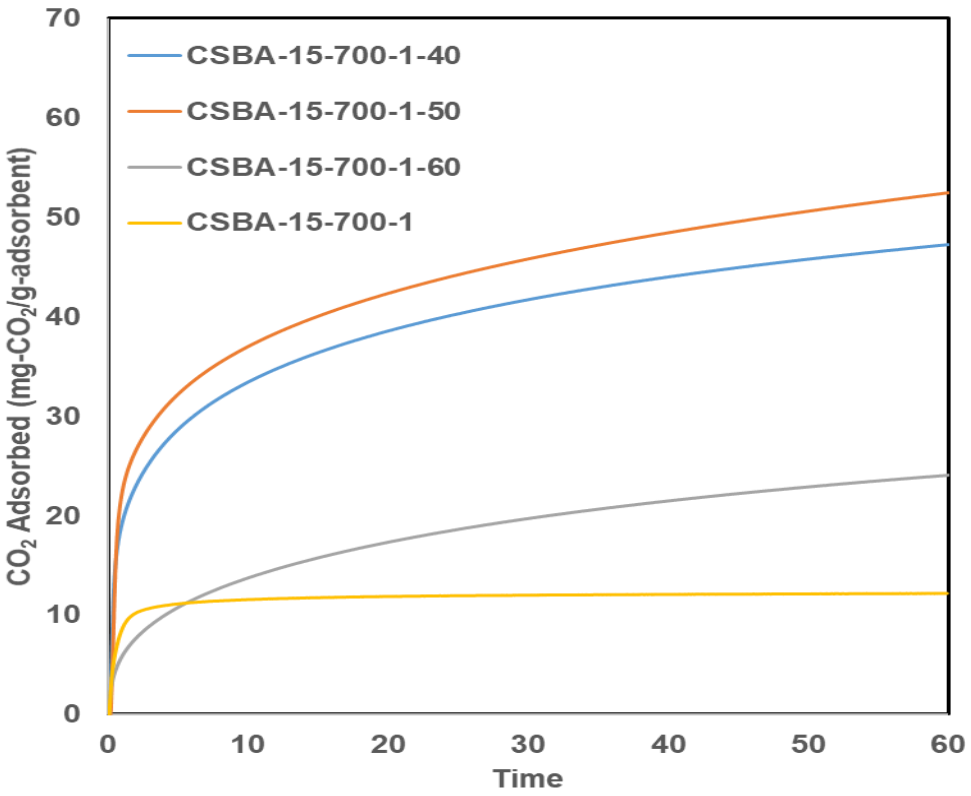

Figure D6 CO_2 adsorption performance of CSBA-15-700-1 and PEI-impregnated adsorbents.